UNED
Escuela
Internacional
de Doctorado
EIDUNED

TESIS DOCTORAL

2019

PRODUCCIÓN CATALÍTICA DE COMPUESTOS QUÍMICOS A PARTIR DE MATERIALES RENOVABLES

CRISTINA LÓPEZ OLMOS

PROGRAMA DE DOCTORADO
EN CIENCIAS

Directora: Dra. INMACULADA RODRIGUEZ RAMOS

Codirector: Dr. ANTONIO GUERRERO RUIZ

Programa de Doctorado en Ciencias

Madrid, Julio de 2019

PRODUCCIÓN CATALÍTICA DE COMPUESTOS QUÍMICOS A PARTIR DE MATERIALES RENOVABLES

CRISTINA LÓPEZ OLMOS

Memoria para optar al grado de
Doctor en Ciencias

Dirigida por:

Dra. Inmaculada Rodríguez Ramos
Profesora de Investigación
Instituto de Catálisis y
Petroleoquímica
CSIC

Dr. Antonio Guerrero Ruiz
Catedrático de Universidad
Dpto. Química Inorgánica
y Química Técnica
Facultad de Ciencias
UNED

AGRADECIMIENTOS

En primer lugar, quiero reconocer a las dos personas que, sin ninguna duda, se merecen mi mayor agradecimiento después de estos cuatro años junto a ellos: mis directores de Tesis, la Dra. Inmaculada Rodríguez-Ramos y el Dr. Antonio Guerrero-Ruiz. A los dos les agradezco por igual todo el conocimiento que me han transmitido, además del cariño y hospitalidad con el que me han tratado en todo momento. A Antonio le agradezco su capacidad para relativizar los problemas y sacar el lado positivo de todo, su total disponibilidad para ayudar y enseñar, así como por haber sido un constante proveedor de bombones y del fruto del árbol de la ciencia. Especialmente agradezco a Inmaculada, la que más me ha sufrido, su paciencia y afecto, el haberme dado la oportunidad de realizar la tesis y confiar en mí. He aprendido muchísimo gracias a ella y ha estado siempre ahí para todo, haciéndome sentir como en casa. Ha sido un placer trabajar con vosotros y teneros como jefes.

También quisiera expresar mi agradecimiento,

Al Ministerio de Educación, Cultura y Deporte por la financiación de este trabajo doctoral a través de la concesión de una Beca de formación de profesorado universitario (FPU).

A todo el personal del Instituto de Catálisis y Petroleoquímica, con mención especial a todos los miembros de la Unidad de Apoyo.

A todo el personal del departamento de Química Inorgánica y Química Técnica de la UNED, así como a todos los miembros del grupo de Diseño Molecular de Catalizadores Heterogéneos.

A Carolina, Nadia y Margarida, por todos los buenos momentos y haber sido las mejores compañeras de búnker.

Finalmente, agradezco a mis padres, Abel, mi familia y mis amigos Álvaro, Bea y Laura, por estar ahí y hacerme la vida más bonita.

TABLA DE CONTENIDOS

Tabla de contenidos

1. INTRODUCTION 3

1.1. Biomass valorization 3

1.2. 1-Butanol 7

1.3. Guerbet reaction 9

1.3.1. Guerbet reaction pathway 10

1.3.2. Heterogeneous catalysts for the Guerbet reaction 14

2. OBJECTIVES 31

3. EXPERIMENTAL 37

3.1. Catalysts synthesis 37

3.2. Characterization techniques 41

3.2.1. Temperature programmed reduction 41

3.2.2. X-ray diffraction 41

3.2.3. Nitrogen physisorption at 77 K 44

3.2.4. Temperature programmed desorption of NH_3 47

3.2.5. CO_2 chemisorption microcalorimetry 48

3.2.6. Transmission electron microscopy and X-ray energy dispersive spectroscopy 51

3.2.7. X-ray photoelectron spectroscopy 54

3.3. Catalytic reaction 57

3.3.1. Experimental system 57

4. RESULTS AND DISCUSSION 65

4.1. Continuous gas-phase condensation of bioethanol to 1-butanol over bifunctional Pd/Mg and Pd/Mg-carbon catalysts 65

4.1.1. Reaction results 65

4.1.2. Catalysts characterization 67

4.1.3. Discussion 75

4.1.4. Conclusions 80

4.2. Comparative study on the acidity and basicity of metal oxides for the catalytic conversion of ethanol into 1-butanol 81

4.2.1. Effect of reaction temperature on conversion and selectivity 81

4.2.2. Reaction results 84

4.2.3. Catalysts characterization 86

4.2.4. Discussion 101

4.2.5. Conclusions 105

4.3. Optimization of Cu-Ni-Mn-catalysts for the conversion of ethanol to butanol 106

4.3.1. Reaction results 106

4.3.2. Catalysts characterization 109

4.3.3. Discussion 126

4.3.4. Conclusions 131

4.4. Cu-Ni-MgO based catalysts for ethanol conversion into butanol: Optimization of the catalytic properties 133

4.4.1. Reaction results 133

  - 4.4.2. Catalysts characterization 135
  - 4.4.3. Discussion 160
  - 4.4.4. Conclusions 165

5. CONCLUSIONS 171

6. BIBLIOGRAPHY 177

LISTA DE CONTENIDOS

LISTA DE ABREVIATURAS

1,1-DEE: 1,1-diethoxyethane

1-Hex: 1-hexanol

ΔH^0: Standard enthalpy of reaction

Å: Amstrong

$\alpha'A$: Modified auger parameter

β: Corrected width of the diffraction peak in radians

λ: Wavelength of the X-rays

θ: Angle of incidence of the radiation

ρ: Density of the metal

Φ: Working function of the spectrometer

a.u.: Arbitrary units

ABE: Acetone–butanol–ethanol fermentation route

Ac: Acetaldehyde

B: Width of the diffraction peak of the sample

b: Instrumental broadening corresponding to a standard substance

BaO: Barium oxide

BE: Binding energy

BET: Brunauer-Emmett-Teller method

BJH: Barret-Joyner-Halenda method

ButOH: 1-Butanol

C%: Carbon balance

CH_4: Methane

CNF: Carbon nanofibers

CNT: Carbon nanotubes

CO: Carbon monoxide

CO_2: Carbon dioxide

D: Metal dispersion

d: Average particle size determined by TEM

d: distance between two lattice planes

DEE: Diethyl eter

DP: Deposition-precipitation method

Eb: Binding energy

Ec: Kinetic energy

EDXS: Energy dispersive X-ray spectroscopy

EU: European Union

FID: Flame ionization detector

GC: Gas chromatograph

hν: Incident energy of the photons

HSAG: High surface area graphite

IUPAC: International Union of Pure and Applied Chemistry

IWI: Incipient wetness impregnation

JCPDS: Joint Committe on Powder Difraction Standars

JRC: Joint Research Centre

L: Dimension of the crystallite in the direction perpendicular to the reflecting plane

MEK: Methyl ethyl ketone

MgO: Magnesium oxide

$Mg(OH)_2$: Magnesium hydroxide

MnO: Manganese oxide

MOx: Metal oxide

M_S: total number of metal atoms on the surface

M_t: Number of metal atoms

M_w: Atomic weight of the element

N_A: Avogadro’s constant

NH_3-TPD: Temperature programmed desorption of ammonia

NPs: Nanoparticles

NREL: National Renewable Energy Laboratory

N_s: Number of atoms at the surface per unit area

Qdiff: Differential heat of adsorption

R-: Samples after reaction.

S_{BET}: Surface area of the sample determined by BET method

SiC: Silicon carbide

S_i: Selectivity to a specific product

SEM: Scanning electron microscopy

STEM: Scanning transmission electron microscopy

STP: Standar temperature pressure

STY: Site time yield

TEM: Transmission electron microscopy

TCD: Thermal conductivity detector

TPR: Temperature programmed reduction

US: United States

X_{EtOH}: Ethanol conversion

XPS: X-ray photoelectron spectroscopy

XRD: X-ray diffraction

ZnO: Zinc oxide

LIST OF FIGURES

Figure 1.3.1 Ethanol condensation towards 1-butanol through the Guerbet reaction pathway. 11

Figure 1.3.2 Reaction scheme for ethanol condensation reaction. 13

Figure 3.2.1 Schematic representation of X-ray diffraction. 42

Figure 3.2.2 Classification of the isotherms according to IUPAC. 45

Figure 3.2.3 Volumetric equipment coupled to a microcalorimeter. 49

Figure 3.2.4 Glass reactor for adsorption microcalorimetry experiments and Tian Calvet microcalorimeter (Setaram C-80 II). 50

Figure 3.2.5 Type of signals generated in electron beam-sample interactions. 52

Figure 3.2.6 Photoelectric effect and Auger processes. 55

Figure 3.3.1 Detailed process flow scheme of the reactor set-up. 58

Figure 3.3.2 Reaction equipment used for the catalytic tests. 59

Figure 4.1.1 Conversion and 1-butanol selectivity through 24 hours of reaction.. 66

Figure 4.1.2 XRD pattern of Pd/Mg catalyst. 68

Figure 4.1.3 XRD pattern of Pd/Mg-HSAG catalyst.. 70

Figure 4.1.4 XRD patterns corresponding to A) Pd/Mg and B) Pd/Mg-HSAG catalysts a) reduced at 573 K and b) thermally treated at 723 K and reduced at 573 K. 71

Figure 4.1.5 Differential heats of CO_2 adsorption vs. coverage at 323 K. a) $Mg(OH)_2$ and MgO b) Pd bifunctional catalysts c) Pd bifunctional catalysts. 73

Figure 4.1.6 TEM images and particle size distribution of a) Pd/HSAG, b) Pd/Mg, c) Pd/Mg-HSAG, d) Pd/Mg*, e) Pd/Mg-HSAG* catalysts. 75

Figure 4.1.7 Site time yield (%) for bifunctional catalyst after 24 hours of reaction. 79

Figure 4.2.1 Variation of ethanol conversion and 1-butanol selectivity as a function of the reaction temperature on catalyst 5Cu-Mg/HSAG. 82

Figure 4.2.2 Analysis of the product distribution as a function of the reaction temperature on the catalyst 5Cu-Mg/HSAG.. 83

Figure 4.2.3 Conversion and 1-butanol selectivity through 24 hours of reaction for the bifunctional catalysts. 86

Figure 4.2.4 H_2-TPR profiles of the catalysts samples. 87

Figure 4.2.5 XRD patterns of the support HSAG and the metal oxide/HSAG catalysts......... 88

Figure 4.2.6 a) XRD patterns of the support HSAG, 5Cu/HSAG and the bifunctional catalysts reduced at 573 K, b) XRD patterns of the catalysts after reaction, where a) HSAG, b) 5Cu/HSAG, c) 5Cu-Mg/HSAG, d) 5Cu-Ba/HSAG, e) 5Cu-Zn/HSAG and f) Cu-Mn/HSAG... 90

Figure 4.2.7 NH_3-TPD profiles of the M/HSAG (left), 5Cu/HSAG and the bifunctional catalysts (right). 93

Figure 4.2.8 Differential heats of CO_2 adsorption vs. coverage at 323 K. a) M/HSAG, b) 5Cu-M/HSAG bifunctional catalysts, with M = Mg, Ba, Zn, Mn... 95

Figure 4.2.9 TEM images of catalysts reduced with hydrogen (left) and after reaction (right): a) 5Cu/HSAG, b) 5Cu-Mg/HSAG, c) 5Cu-Ba/HSAG, d) 5Cu-Zn/HSAG, e) 5Cu-Mn/HSAG... 99

Figure 4.2.10 EDX elemental mapping of catalysts reduced in hydrogen at 573 K: a) 5Cu-Mg/HSAG, b) 5Cu-Ba/HSAG, c) 5Cu-Zn/HSAG, d) 5Cu-Mn/HSAG.. 100

Figure 4.2.11 Site time yield (s^{-1}) for Cu/HSAG and the bifunctional catalyst after 7 hours of reaction. 105

Figure 4.3.1 Conversion and 1-butanol selectivity through 24 h of reaction......................... 108

Figure 4.3.2 H_2-TPR profiles of the catalysts samples. 110

Figure 4.3.3 XRD patterns of the support HSAG and the reduced catalysts........................ 112

Figure 4.3.4 XRD patterns of the support HSAG and the catalysts 4Cu1Ni-Mn/HSAG and 2.5Cu2.5Ni-Mn/HSAG, both reduced at 573 K with hydrogen, and after study in reaction (R-). 113

Figure 4.3.5 NH_3-TPD profiles of the Mn/HSAG, 5Cu/HSAG, 5Ni/HSAG and the the bifunctional catalysts reduced in situ. 115

Figure 4.3.6 Differential heats of CO_2 adsorption vs. coverage at 323 K. a) Mn/HSAG before and after thermal treatment b) Cu-Ni bifunctional catalysts c) 2.5Cu2.5Ni-Mn/HSAG before and after thermal treatment. 117

Figure 4.3.7 TEM images of catalysts reduced with hydrogen (left) and after reaction (right): a) 5Cu/HSAG, b) 5Ni/HSAG and c) 2.5Cu2.5Ni/HSAG. 119

Figure 4.3.8 TEM images of catalysts reduced with hydrogen (left) and after reaction (right): a) 5Cu-Mn/HSAG, b) 5Ni-Mn/HSAG, c) 2.5Cu2.5Ni-Mn/HSAG, d) 2.5Cu2.5Ni-Mn/HSAG*. 120

Figure 4.3.9 EDX elemental mapping of 5Cu-Mn/HSAG reduced in hydrogen at 573 K..... 122

Figure 4.3.10 EDX elemental mapping of 2.5Cu2.5Ni-Mn/HSAG reduced in hydrogen at 573 K (a) and after reaction (b). 122

Figure 4.3.11 Mn $2p_{3/2}$ (left), Cu $2p_{3/2}$ (center) and Ni $2p_{3/2}$ (right) XPS spectra of sample 2.5Cu2.5Ni-Mn/HSAG reduced in hydrogen at 573 K. 123

Figure 4.3.12 Site time yield (s^{-1}) for bifunctional catalyst after 7 h of reaction. 131

Figure 4.4.1 Conversion and 1-butanol selectivity through 24 hours of reaction for the bifunctional catalysts. 135

Figure 4.4.2 H_2-TPR profiles of the catalysts samples. 138

Figure 4.4.3 XRD patterns of the support HSAG and the reduced catalysts, where a) HSAG, b) Cu/HSAG, c) Ni/HSAG, d) 4Cu1Ni/HSAG, e) 5Cu-Mg/HSAG, f) 4.75Cu0.25Ni-Mg/HSAG, g) 4Cu1Ni-Mg/HSAG, h) 2.5Cu2.5Ni-Mg/HSAG, i) 5Ni-Mg/HSAG. 139

Figure 4.4.4 XRD patterns, where a) HSAG, b) 4Cu1Ni-Mg/HSAG, c) R-4Cu1Ni-Mg/HSAG, d) 4Cu1Ni-Mg/HSAG*, e) R-4Cu1Ni-Mg/HSAG*. 141

Figure 4.4.5 NH_3-TPD profiles of the Mg/HSAG, 5Cu/HSAG, 5Ni/HSAG and the bifunctional catalysts reduced in situ. 143

Figure 4.4.6 Differential heats of CO_2 adsorption vs. coverage at 323 K. a) Mg/HSAG before and after thermal treatment, b) Cu-Ni bifunctional catalysts, c) 4Cu1Ni-Mg/HSAG before and after thermal treatment. 146

Figure 4.4.7 TEM images of catalysts reduced with hydrogen (left) and after reaction (right): a) 5Cu/HSAG, b) 5Ni/HSAG, and c) 4Cu1Ni/HSAG. 149

Figure 4.4.8 TEM images of catalysts reduced with hydrogen (left) and after reaction (right): a) 5Cu-Mg/HSAG, b) 5Ni-Mg/HSAG, c) 2.5Cu2.5Ni-Mg/HSAG, d) 4Cu1Ni-Mg/HSAG, e) 4.75Cu0.25Ni-Mg/HSAG, f) 4Cu1Ni-Mg/HSAG*. 151

Figure 4.4.9 EDX elemental mapping of catalysts reduced in hydrogen at 573 K: a) 5Cu-Mg/HSAG, b) 5Ni-Mg/HSAG. 152

Figure 4.4.10 EDX elemental mapping of catalysts reduced in hydrogen at 573 K: a) 2.5Cu2.5Ni-Mg/HSAG, b) 4Cu1Ni-Mg/HSAG, c) 4.75Cu0.25Ni-Mg/HSAG. 154

Figure 4.4.11 EDX elemental mapping of catalysts after reaction at 503 K and 50 bar: a) 2.5Cu2.5Ni-Mg/HSAG, b) 4Cu1Ni-Mg/HSAG, c) 4.75Cu0.25Ni-Mg/HSAG. 155

Figure 4.4.12 Mg 2p (top left), Cu $2p_{3/2}$ (top right), Ni $2p_{3/2}$ (bottom left) and X-ray generated Cu LMM Auger (bottom right) XPS spectra of sample R-4Cu1Ni-Mg/HSAG* treated in helium at 723 K before reduction in hydrogen at 573 K. 156

Figure 4.4.13 Site time yield (s^{-1}) for bifunctional catalyst after 7 hours of reaction. 165

LIST OF TABLES

Table 3.1.1 Composition and preparation method of the catalysts. 40

Table 4.1.1 Catalytic activity and product selectivities obtained at 503 K and 50 bar after 24 h on stream. 66

Table 4.1.2 Textural and structural parameters of supports and catalysts. 69

Table 4.1.3 CO_2 chemisorption capacities at 323 K and type of basic sites. 73

Table 4.2.1 Catalytic activity and product selectivities obtained at 503 K and 50 bar after 24 h on stream. 85

Table 4.2.2 Textural parameters of support and reduced catalysts. 91

Table 4.2.3 Acidity distribution derived after deconvolution of the NH_3-TPD profiles. 94

Table 4.2.4 CO_2 chemisorption capacities at 323 K and type of basic sites. 96

Table 4.3.1 Catalytic activity and product selectivities obtained at 503 K and 50 bar after 24 h on stream. 107

Table 4.3.2 Textural parameters of support and reduced catalysts. 114

Table 4.3.3 Acidity distribution derived after deconvolution of the NH_3-TPD profiles of the bifunctional catalysts reduced in situ. 115

Table 4.3.4 CO_2 chemisorption capacities at 323 K and type of basic sites. 118

Table 4.3.5 Binding energies (eV) of core electrons and the Auger parameter (eV) of catalysts samples reduced in hydrogen at 573 K and after reaction (R-). 124

Table 4.3.6 Atomic ratios for catalysts samples reduced in hydrogen at 573 K and after reaction (R-). 126

Table 4.4.1 Catalytic activity and product selectivities obtained at 503 K and 50 bar after 24 h on stream. 134

Table 4.4.2 Textural parameters of support and reduced catalysts. 142

Table 4.4.3 Acidity distribution derived after deconvolution of the NH_3-TPD profiles. 145

Table 4.4.4 CO_2 chemisorption capacities at 323 K and type of basic sites. 148

Table 4.4.5 Binding energies (eV) of core electrons and the Auger parameter (eV) of catalysts samples reduced in hydrogen at 573 K and after reaction (R-). 158

Table 4.4.6 Atomic ratios for catalysts samples reduced in hydrogen at 573 K and after reaction (R-).. 160

RESUMEN-ABSTRACT

RESUMEN

Hoy en día, uno de los desafíos científicos más importantes es el desarrollo de procesos "verdes" que respeten el medio ambiente e involucren el uso de materias primas sostenibles y condiciones de operación moderadas. Por ello, muchos estudios actuales se centran en la optimización de rutas químicas para transformaciones de biomasa en productos químicos de mayor aplicabilidad, con el fin de disminuir la dependencia actual de los combustibles fósiles. La importancia de las moléculas plataforma obtenidas de la valorización de la biomasa radica en que se pueden convertir posteriormente a otros productos químicos o materiales de alto valor, lo que hará que la implementación de las biorrefinerías sea económicamente viable. Todavía es necesario seguir avanzando hacia la implementación industrial de la valorización de la biomasa cumpliendo con los objetivos de la química verde, la protección del medio ambiente y el beneficio económico. Esto podría lograrse mediante el desarrollo de catalizadores heterogéneos altamente selectivos que suponen bajo coste y alta estabilidad.

Esta tesis doctoral se centra en el estudio del proceso de valorización catalítica de bioetanol como molécula plataforma para obtener 1-butanol, conocido como la reacción de Guerbet. La producción del 1-butanol está despertando un gran interés, ya que se considera una alternativa prometedora al bioetanol y al biodiesel como combustible líquido o aditivo de gasolina, además de su aplicación como disolvente y materia prima en la fabricación de productos químicos. La condensación de bioetanol hacia 1-butanol a través del proceso Guerbet implica varias etapas que pueden resumirse como deshidrogenación de etanol a acetaldehído, condensación aldólica de acetaldehído a 3-hidroxibutanal, que se deshidrata fácilmente a 2-butenal y subsiguientes hidrogenaciones de 2-butenal a butiraldehído y finalmente a 1-butanol. Al ser un proceso multi-etapa, el diseño del sistema catalítico se convierte en una tarea bastante compleja, ya que las reacciones involucradas en el proceso son catalizadas por sitios activos de diferente naturaleza.

Hasta hace poco, el proceso industrial de Guerbet se ha llevado a cabo utilizando catalizadores homogéneos, aunque el objetivo de las tendencias de investigación actuales se centra en la heterogenización del sistema. La heterogenización del proceso de Guerbet es fácil de lograr para las etapas de hidrogenación/deshidrogenación, ya que los catalizadores metálicos heterogéneos son ampliamente conocidos por catalizar esos tipos de reacción. Sin embargo, la heterogenización de la base que cataliza la condensación aldólica, que consiste en óxidos metálicos selectivos, constituye una tarea más difícil.

Hasta ahora, los catalizadores heterogéneos descritos en la literatura, como los óxidos de metales básicos, zeolitas modificadas, hidrotalcitas o hidroxiapatitas modificadas, contienen sitios básicos o ácidos/bases y operan a temperaturas superiores a 573 K para obtener niveles aceptables de actividad y selectividad a 1-butanol. La incorporación de metales tales como Cu, Ni o Pd a los sistemas catalíticos mencionados anteriormente reduce considerablemente la temperatura de reacción necesaria para transformar satisfactoriamente etanol a 1-butanol. Aunque los catalizadores de cobre y níquel son generalmente conocidos por su interesante desempeño en la condensación de alcoholes de Guerbet, la combinación de ambos metales no ha sido estudiada en detalle.

Por lo tanto, el objetivo de esta Tesis Doctoral ha sido la optimización de diferentes formulaciones de catalizadores que combinan las ventajas del paladio, el cobre y/o el níquel como componentes deshidrogenante/hidrogenante y un óxido metálico que exhibe diferentes propiedades ácido/base (MgO, BaO, ZnO y MnO). Estos ingredientes se han depositado en un soporte carbonoso inerte y no poroso, grafito de alta área superficial (HSAG), que dispersaría las fases activas maximizando el número de centros superficiales expuestos y favoreciendo la interacción entre ellos. Todas las pruebas catalíticas se realizaron en un reactor de lecho fijo de flujo continuo operado en fase gaseosa a 503 K y 50 bar utilizando una corriente de helio y etanol. Previamente a su estudio los catalizadores se redujeron in situ en corriente de hidrógeno a su correspondiente temperatura de reducción. Los catalizadores se caracterizaron reducidos (frescos) y después de reacción mediante reducción a temperatura programada (TPR), difracción de rayos X (DRX), fisisorción de nitrógeno, desorción a temperatura programada de NH_3, microcalorimetría de quimiosorción de CO_2, microscopía electrónica de transmisión (TEM), espectroscopía de energía dispersiva de rayos X (EDX), y espectroscopía fotoelectrónica de rayos X (XPS).

En el capítulo 4.1, se estudió la condensación de etanol a 1-butanol en presencia de diferentes sistemas catalíticos basados en un componente de deshidrogenación/hidrogenación de Pd y materiales derivados de hidróxido de magnesio como ingrediente básico. También se estudió un catalizador bifuncional soportado consistente en un composite basado en Mg y HSAG. Los resultados catalíticos y la caracterización de los sitios activos sugieren que la conversión de etanol no solo depende del tamaño de las partículas de Pd, sino también de la eficiencia de la condensación aldólica y la hidrogenación en sitios básicos fuertes de MgO. Por lo tanto, el compromiso entre estos dos parámetros en los catalizadores, después de un tratamiento térmico adecuado, da lugar a los mayores rendimientos de 1-butanol.

El capítulo 4.2 comprende la modificación de catalizadores de cobre monometálicos soportados en HSAG con óxidos metálicos que exhiben diferentes propiedades de ácido/base (MgO, BaO, ZnO y MnO) y su evaluación en la reacción de Guerbet. También se evaluó el efecto de la temperatura sobre la conversión de etanol y la selectividad a 1-butanol, obteniendo que 503 K se consigue la reacción optimizada. Los resultados de la reacción y la caracterización de los catalizadores sugieren que los altos rendimientos de 1-butanol pueden atribuirse al efecto sinérgico entre los sitios ácido/base proporcionados por el óxido metálico, que catalizan la deshidratación del 3-hidroxibutanal y la condensación aldólica, respectivamente, así como las nanopartículas activas de cobre que catalizan las reacciones de deshidrogenación/hidrogenación. Se puso en evidencia que los sitios de cobre expuestos son óptimos para el catalizador con MgO, seguido muy de cerca por el catalizador con MnO, en contraste con aquellos sistemas que contienen BaO y ZnO como óxido metálico, y que se requiere un buen equilibrio entre los sitios de basicidad media-alta y los sitios de acidez media-débil.

En el capítulo 4.3, la reacción de Guerbet se estudió en diferentes sistemas catalíticos basados en Cu y/o Ni como componentes de hidrogenación/deshidrogenación, y óxido de manganeso que incorpora propiedades ácido/base sobre HSAG. La caracterización de los sitios activos y las pruebas catalíticas corroboraron la existencia de un efecto sinérgico entre el manganeso combinado con Cu y/o Ni que da lugar a un catalizador mejorado, en términos de alto rendimiento de 1-butanol. Aunque los sitios ácido/base tienen un impacto considerable en la selectividad a 1-butanol y la distribución de productos, parece que la función del metal desempeña un papel crucial en la reacción de condensación de etanol de Guerbet, ya que se observan claras diferencias en la conversión debidas a la sinterización de las partículas metálicas en las etapas de reducción, lo que conlleva una disminución de la actividad catalítica. Además, los catalizadores bimetálicos demostraron que combinan las mejores características de ambos metales, siendo 2.5% en peso de Cu y 2.5% en peso de Ni la carga de metal óptima.

En el capítulo 4.4, se evaluó el rendimiento en la reacción de Guerbet de diferentes sistemas catalíticos bifuncionales basados en Cu y/o Ni y óxido de magnesio soportados en HSAG. Los resultados catalíticos y la caracterización de los sitios catalíticos respaldaron el efecto sinérgico entre los sitios ácido/base proporcionados por el óxido de magnesio y las nanopartículas de Cu-Ni para la condensación de etanol hacia 1-butanol, mostrándose que la función del metal tiene efectos significativos en la acidez y basicidad resultantes del catalizador bifuncional y, por lo tanto, en la selectividad a 1-butanol y en la distribución de subproductos.

Finalmente, se concluye que una función metálica y especialmente una carga apropiada de cobre y níquel combinada con la presencia de sitios básicos de fuerza media-alta y una concentración moderada de sitios ácidos aportados también por el óxido metálico, especialmente MgO y MnO, dan como resultado un catalizador mejorado para la producción de 1-butanol y, al mismo tiempo se reduce la formación de productos no deseados. Para todos los catalizadores estudiados en esta Tesis Doctoral, el análisis de los productos de reacción indica que las etapas del mecanismo coinciden con las propuestas previamente para el proceso Guerbet: cabe destacar que los mejores materiales catalíticos desarrollados en esta investigación, presentan una adecuada estabilidad durante su trabajo en el proceso, permaneciendo activos durante 24 h en reacción.

ABSTRACT

Nowadays, one of the most crucial scientific challenges is the development of ‘’green’’ processes that respect the environment and involve the use of sustainable raw materials and moderate operation conditions. Thus, many current studies are focused on the optimization of chemical routes for biomass transformations into added-value chemicals, in order to diminish the current dependence on fossil fuels. The importance of potential platform molecules obtained from biomass valorization is that they can be subsequently converted to other high-value chemicals or materials, thus making the implementation of the biorefineries economically viable. Further progress is still needed towards the industrial implementation of biomass valorization while addressing the goals of green chemistry, environmental protection and economic benefit. This could be accomplished by the development of highly selective heterogeneous catalysts that comprise low cost and sufficient stability.

This Doctoral Thesis focuses on the study of the catalytic valorization process of bio-ethanol as a platform molecule towards the high value product 1-butanol, known as the Guerbet reaction. The production of 1-butanol is attracting widespread interest since it is considered a promising alternative to bio-ethanol and biodiesel as a liquid fuel or gasoline additive in addition to its application as a solvent and raw material in the manufacture of chemical products. The condensation of bio-ethanol towards 1-butanol through the Guerbet process involves several steps that can be summarized as dehydrogenation of ethanol to acetaldehyde, aldol condensation of acetaldehyde to 3-hydroxybutanal, which readily dehydrates to 2-butenal and subsequent hydrogenations of 2-butenal to butyraldehyde and finally to 1-butanol. Being a multi-step process, the design of the catalytic system becomes a rather complex task since the reactions involved in the process are catalyzed by active sites of different nature. Until recently, the industrial Guerbet process has been performed using homogeneous catalysts, even though

the aim of current research trends is focused on the heterogenization of the system. The heterogenization of the Guerbet process is easy to accomplish for the hydrogenation/dehydrogenation steps, since heterogeneous metal catalysts are widely recognized for catalyzing those types of reaction. Nevertheless, the heterogenization of the base catalyzed aldol condensation over selective acidic/basic metal oxides constitutes a more challenging task.

So far, the heterogeneous catalysts reported in literature, such as basic metal oxides, modified zeolites, hydrotalcites and modified hydroxyapatites, contain basic or acid/base sites and operate at temperatures above 573 K to obtain acceptable levels of activity and 1-butanol selectivity. The incorporation of metals such as Cu, Ni or Pd to the above mentioned catalytic systems considerably reduce the reaction temperature necessary to satisfactorily upgrade ethanol to 1-butanol. Although copper and nickel catalysts are generally known for their interesting performance in the Guerbet coupling of alcohols, the combination of both metals has not been extensively studied.

Thus, the aim of this Doctoral Thesis has been the optimization of different catalytic systems combining the advantages of palladium, copper and/or nickel as the dehydrogenating/hydrogenating component and a metal oxide exhibiting different acid/base properties (MgO, BaO, ZnO and MnO), supported on an inert and non-porous carbonaceous support, high surface area graphite (HSAG), that would disperse the active phases maximizing the number of surface centers exposed and favoring the interaction between them. All the catalytic tests were performed in a continuous-flow fixed bed reactor operated in gas phase at 503 K and 50 bar using a stream of helium and ethanol, while the catalysts were previously reduced in-situ with hydrogen at their corresponding reduction temperature for 1 h. The catalysts were characterized reduced and after reaction by temperature-programmed reduction

(TPR), X-ray diffraction (XRD), nitrogen physisorption, NH_3 temperature-programmed desorption, CO_2 chemisorption microcalorimetry, transmission electron microscopy (TEM), energy-dispersive X-ray spectroscopy (EDX), and X-ray photoelectron spectroscopy (XPS).

In chapter 4.1, the condensation of ethanol to 1-butanol was studied in the presence of different catalyst systems based on a Pd dehydrogenating/hydrogenating component and magnesium hydroxide-derived materials as basic ingredient. A bifunctional catalyst supported on a synthetic composite based on Mg and HSAG was also studied. The catalytic results and the characterization of the active sites suggest that ethanol conversion is not only dependent on the size of Pd particles, but also on the efficiency of aldol condensation and hydrogenation on more strong basic MgO sites. Thus, the compromise between the two parameters in the catalysts, after adequate thermal treatment, gives rise to higher 1-butanol yields.

The chapter 4.2 comprises the modification of monometallic copper catalysts supported on HSAG with metal oxides exhibiting different acid/base properties (MgO, BaO, ZnO and MnO) and their evaluation on the Guerbet reaction. The effect of temperature on ethanol conversion and 1-butanol selectivity was also evaluated, obtaining that 503 K is considered the optimal reaction temperature. Reaction results and catalysts characterization suggest that high 1-butanol yields can be ascribed to the synergistic effect between the acid/base sites provided by the metal oxide, which catalyze the dehydration of 3-hydroxybutanal and the aldol condensation, respectively, and the active copper nanoparticles, that catalyze the dehydrogenation/hydrogenation reactions. It was founded that the exposed copper sites are optimal for the catalyst with MgO, closely followed by the catalyst with MnO, in contrast with their counterparts with BaO and ZnO as the metal oxide, thanks to a good equilibrium between medium-high strength basic sites and medium-weak strength acid sites.

In chapter 4.3, the Guerbet reaction was studied over different catalytic systems based on Cu and/or Ni as hydrogenating/dehydrogenating components, and manganese oxide incorporating acid/base properties on HSAG. The characterization of the active sites and the catalytic tests corroborated the existence of a synergistic effect between manganese combined with Cu and/or Ni that gives place to an improved catalyst, in terms of high 1-butanol yield. Although acid/base sites have a considerably impact on 1-butanol selectivity and product distribution, it seems that the metal function plays a crucial role in the Guerbet ethanol condensation reaction since clear differences in conversion are attributed to the sintering of particles that leads to decreasing conversion. In addition, bimetallic catalysts proved to combine the best characteristics of both metals, being 2.5 wt% Cu and 2.5 wt% Ni the optimal metal loading.

In chapter 4.4, it was evaluated the performance on the Guerbet reaction of different bifunctional catalytic systems based on Cu and/or Ni and magnesium oxide supported on HSAG. The catalytic results and the characterization of the catalytic sites endorsed the synergistic effect between the acid/base sites provided by magnesium oxide and the Cu-Ni nanoparticles for the upgrading of ethanol towards 1-butanol, obtaining that the metal function have significant effects on the resulting acidity and basicity of the bifunctional catalyst and therefore on the 1-butanol selectivity and product distribution.

All things considered, a metal function and especially an appropriate copper and nickel loading combined with the presence of medium-high strength basic sites and moderate concentration of acid sites provided by a metal oxide, specially MgO or MnO, result in an improved catalyst for the production of 1-butanol and at the same time reducing the formation of undesired products. For all the catalysts studied throughout this Doctoral Thesis, the analysis of the product streams indicated that the reaction pathway follows the Guerbet route and demonstrated good stability, remaining active for 24 h on stream.

INTRODUCTION

1. INTRODUCTION

1.1. Biomass valorization

Currently, biomass is the renewable energy source with the highest growth potential, and one of the most widely used renewable resources in the world. Several factors, such as the increase in the price of fossil fuels and the growing concern for climate change, have contributed to its rapid development, becoming a source of alternative energy that is non-polluting and highly competitive [1]. Therefore, the biomass conversion into liquid fuels, hydrogen and raw chemicals has endured great technological development in recent years as a result of the rising concern of the governments and the chemical industry to develop more environmentally sustainable processes [2]. This has led to the movement commonly known as "Green Chemistry", which is based on the design, development and implementation of energy efficient processes that use renewable material feedstock as well as safer substances for the environment and the human health, avoiding or minimizing the production of waste [1,3]. In this sense, the biomass valorization represents an interesting chemical route that allows the use of a sustainable source for replacing the conventional fossil fuels.

The term ‘’biomass’’ refers to the organic matter of vegetable or animal origin that can be used as an energy source. Biomass originates from dedicated crops for energy, herbaceous residues or by-products from agriculture, wood from forests, organic waste and residues of forest harvest and wood industry. A report by the Joint Research Centre (JRC), the European Commission’s science and knowledge service, estimated that the total agricultural biomass produced annually in the European Union (EU) was 956 Mt of dry matter per year, of which 54% corresponds to grains, fruits, roots, tubers, etc., and the remaining 46% is above ground biomass from by-products and residues (such as leaves, husks and stems) [4]. In addition, the lignocellulosic biomass residues are estimated to exceed $2 \cdot 10^{11}$ t/year worldwide [5]. Biomass residues can have an economic value when used for bioenergy production, animal bedding, maintaining organic carbon levels in soil or preventing soil erosion, among other applications. Nevertheless, although its use as an energy source is growing worldwide, the biomass replacement of petrol as a raw material for obtaining chemical products is not an easy or immediate task. In this sense, while the EU uses 1 billion tonnes of dry matter of biomass per year, only the 18.8% is destined for the synthesis of chemical products. In addition, the biomass market is currently concentrated mainly in the feed and food sector (more than 60%) and the production of bioenergy (19.1%) [4]. However, in the same way that occurs in the refineries of the petrochemical industry, there are studies that indicate that the simultaneous use of biomass as a source of energy and as a precursor of added-value chemical products is also feasible [6]. Regarding the use of crops for energy production instead of nutrition purposes, there is an ongoing public discussion about the ethics of such application since it is not clear if there will be sufficient food crops to fulfill all the demands threatening food supplies and biodiversity [7,8]. Others consider that it would be convenient to use agricultural residues that cannot be used for food such as lignocellulosic substrates or algae biomass for energy applications, even though the complexity and thus the total costs of pretreatment and downstream processing would increase [9]. Nevertheless, it is estimated by the World Bioenergy Association that by 2035, 240 million ha of land can be used for dedicated crops to produce energy and that there is enough land on the planet Earth to feed 9 billion people besides producing more biomass for energy and material use [10]. In this context, the concepts of second and third generation biorefineries are born to ensure sustainability without threatening food supplies and biodiversity. Whereas first generation biorefineries use sources such as starch, sugar, animal fats and vegetable oil to produce fuels, the raw material of second generation biorefineries comprises agricultural and forests residues, namely non-food parts of crops (stems, leaves or husks, among others), crops that are not used for food applications (such as switchgrass or cereals with more fibre than grain), as well as industry waste (wood chips, skins and pulp from fruit pressing, etc.), to produce biofuels, materials and added-value fine chemicals [11,12]. On the other hand, third generation considers the use of algae and microalgae as feedstocks [12].

Even though biomass research is accelerating and chemical companies are showing increased interest in renewable feedstock, there is still a long path before replacing oil as a source of chemical products. This substitution implies the development of biorefineries, that are complex industries that process biomass as raw material, for a variety of bio-compound products (food, chemicals) and bioenergy (biofuels and electric power). In this way, the products derived from biomass, known as platform molecules, would provide viable routes to produce chemical products and consequently lightening the strong dependence on fossil fuels [1,11,13,14]. All in all, it is clear that further progress is still needed towards the industrial implementation of biomass valorization into fuels and platform chemicals while addressing the goals of green chemistry, environmental protection and economic benefit.

Regarding the production of chemicals, biomass is considered an important renewable substitute of petrol since in general (changes with the type of raw material) it is formed by 75% of carbohydrates (cellulose, hemicellulose, starch, etc.), 20% of aromatic compounds (lignin) and 5% of minor products such as proteins or fats, therefore based mainly on carbon [15]. Depending on the biomass valorization route, some of the possible products or potential platform molecules obtained are bio-ethanol, 1-butanol and other alcohols, synthesis gas, bio-oil, bio-hydrocarbons, polyols (sorbitol, xylitol, glycerol), furans (furfural, 5-hydroxymethylfurfural) and acids (succinic acid, levulinic acid, hidroxypropionic acid, and lactic acid) [2,16,17]. The importance of these products is that they can be subsequently converted to other high-value chemicals or materials, thus making the implementation of the biorefineries economically viable [18]. The scientific and technological fields must make a significant effort in the search for suitable processes or the optimization of the existing ones to obtain compounds with high added value from these organic molecules. This could be accomplished by the development of highly selective heterogeneous catalysts that comprise low cost and sufficient stability.

The catalytic routes are receiving special attention since the principles of Green Chemistry identify catalysis as one of the most important tools for implementing industrial sustainable processes [19]. The use of catalysts offers economic and environmental benefits besides lower energy consumption, rate enhancement, improved selectivity that minimizes the use of processing and separation agents, allowing the use of less toxic materials [20]. Particularly, the study and design of new heterogeneous catalysts is of great interest in the field of biomass valorization to enable the implementation of Green Chemistry goals by facilitating the separation of products from the reaction mixture, the purification of intermediates and thus eliminating the need for separation through distillation or extraction [3,19]. This Doctoral Thesis focuses on the study of the catalytic valorization process of bio-ethanol as a platform molecule towards the high value product 1-butanol, known as the Guerbet reaction.

1.2. 1-Butanol

The production of 1-butanol is attracting widespread interest since it is considered a promising alternative to bio-ethanol and biodiesel as a liquid fuel or gasoline additive in addition to its application as a solvent and raw material in the manufacture of chemical products such as butyl acetate, butyl acrylate, acrylic acid and acrylic esters, glycol ethers, resins and plasticizers [21,22,23]. Butanol is widely used in the US for the synthesis of butyl acrylate and methacrylate, which are subsequently used in the polymer, paint and textile industries [24,25]. The main use of 1-butanol in the EU is as a solvent in the manufacture of paints, coatings, resins, waxes, as well as in the pharmaceutical industry [26]. In some countries, 1-butanol is also used as a flavor modifier or food additive in ice cream, cheeses, candy, and baked goods [7,25].

Some of the 1-butanol advantages with respect to bio-ethanol are the hydrophobic nature of 1-butanol, its higher energy density, lower volatility, lower solubility with water, fewer corrosion problems in combustion engines and mainly its higher heat of combustion, similar to that of gasoline [7,27,28,29]. The comparable properties of 1-butanol and gasoline, such as the air-fuel ratio, would permit the use of the existing refinery and transportation infrastructures as well as car engines with no modification since they can be blended to any ratio or used separately [7,30,31,32]. Companies like BP and DuPont are joining efforts in the production of advanced biofuel, with an emphasis on bio-butanol, even though they recognize that 1-butanol will be more expensive than conventional gasoline in the near future. To overcome this problem, they are focusing on the improvement of the biomass conversion into bio-butanol using crops such as sugar cane and sugar beet [33,34]. However, the National Renewable Energy Laboratory (NREL) considers that, although the potential is real, a significant technological advance will be necessary to overcome the lack of competitiveness of 1-butanol production from starches, sugars and lignocellulosic biomass, due to its high production cost and low yield obtained [35].

Traditionally, 1-butanol has been produced since the 1920s by the acetone–butanol–ethanol (ABE) fermentation route that uses the bacterium Clostridium acetobutylicum to produce a mixture of acetone, butanol and ethanol, which is then subjected to a separation procedure, using starches and molasses as substrates [7,30,31]. This process was used in many countries until the 1950s when the ABE fermentation industry became non-profitable due to the increasing substrate costs and the lack of competitiveness with the petrochemical industry that produced large quantities of much cheaper acetone and butanol through petrochemical processes such as the ‘’oxo process’’ [36,37]. Other limitations of the ABE process are the low butanol yield and the formation of by-products such as acetone, ethanol, acetic acid, butyric acid, etc. [38]. In turn, the oxo process is based on the homogeneous catalyzed hydroformylation reaction of propylene with syn-gas (mixture of carbon monoxide and hydrogen) at 383-453 K and 50-350 bar, forming the intermediate isomeric aldehyde mixture of 1-butanal and 2-methylpropanal, which is subsequently hydrogenated to produce butanol and 2-methyl-1-propanol, using a coordination complex of Co, Rh or Ru as catalyst [9,25,37]. However, this process recently became less attractive due to economic and environmental aspects, such as the depleting of oil reserves, the highly fluctuating crude oil price and the carbon dioxide emissions [36]. Hence, the ABE process regained the interest of the scientific community and industry in recent decades, now focusing on genetic manipulation, the development of new metabolic engineering and the improvement of the separation process of 1-butanol from the fermentation broth [7,31].

Other petrochemical route for 1-butanol production is the Reppe synthesis or BASF process, that is the catalytic carbonylation of propene, with one unit operating in Japan. In this process, propene, carbon monoxide and water react at 373 K and 5-20 bar producing 1-butanol and 2-methyl-1-propanol in the presence of a homogeneous catalyst, usually tertiary ammonium salts or polynuclear iron carbonyl hydrides [9,37]. Although the reaction conditions were milder than that of the oxo process, the Reppe synthesis was not as successful due to the more expensive process technology required [38].

All things considered, it is clear that the design and optimization of economic and energy efficient processes to synthesize 1-butanol are of great interest due to its many applications in the industrial and energy sector. The available information suggests that the 1-butanol production using bio-ethanol as raw material would help to solve two critical issues for the governments and chemical companies, that is the energy crises and environment pollution. Since recent trends focus on ‘’green’’ processes and the use of renewable materials, the Guerbet process or catalytic condensation of bio-ethanol has emerged as a more desirable route for 1-butanol production, since the reaction is faster when compared to the ABE process and fewer steps are necessary to get to the product.

1.3. Guerbet reaction

The organic Guerbet reaction consists in the catalytic conversion of primary aliphatic alcohols into their β-alkylated dimer alcohol with the release of water [39,40]. The reactant alcohol can be coupled with itself (self-condensation) or with another alcohol (cross-condensation) resulting in the final ‘‘Guerbet’’ alcohol that contains the sum of the carbon atoms of the reactants, being 1-butanol the simplest alcohol that can be obtained by the condensation of ethanol. This reaction is of great interest, since it allows to produce higher alcohols that maintain the functional groups of the initial alcohol and, therefore, being potential chemical precursors for the production of more complex molecules. This process was first described by Marcel Guerbet in the 1890s, using a strong base and metal oxide for the conversion of 1-butanol to 2-ethyl-1-hexanol at high temperature [41,42].

Traditionally, the industrial production of 1-butanol through the Guerbet process has been based on homogeneous catalysis using metal alkaline salts or transition metal complexes [39,42,43]. However, the heterogeneous catalytic Guerbet process is gaining more attention due to the reusability of a solid catalyst, the reduction of waste formation and energy necessary to separate the products from the reaction mixture, in contrast to the disadvantages that the use of homogeneous catalysts implies, namely the production discontinuity and the environmental problems related to the use of soluble strong bases and organic solvents [19,43]. The design of the most suitable heterogeneous catalyst in terms of activity and selectivity is not an easy task since the condensation of ethanol towards 1-butanol involves several steps that determine the properties of the catalytic system required [41].

1.3.1. Guerbet reaction pathway

Although the Guerbet process was described more than 100 years ago, the scientific community has not reached yet an agreement regarding the mechanism of the reaction since two main pathways have been suggested by the literature towards 1-butanol [44,45,46,47]. One of the mechanisms proposed for the Guerbet reaction is the ‘’direct route‘’ based on the direct condensation of two ethanol molecules to give 1-butanol, which has been reported using basic zeolites and hydroxyapatite catalysts at temperatures higher than 623 K [48,49,50]. The other proposed mechanism known as the ‘’Guerbet route’’ consists of several steps: dehydrogenation of ethanol to give acetaldehyde (R1), aldol condensation of two molecules of acetaldehyde to 3-hydroxybutanal (R2), dehydration of 3-hydroxybutanal to 2-butenal (R3) and subsequent hydrogenations of 2-butenal to butyraldehyde and finally to 1-butanol (R4 and R5) [24,51,52]. A schematic representation of the Guerbet route is shown in Figure 1.3.1. The hydrogen used for the hydrogenation steps is formed through hydrogen transfer reactions [45,46].

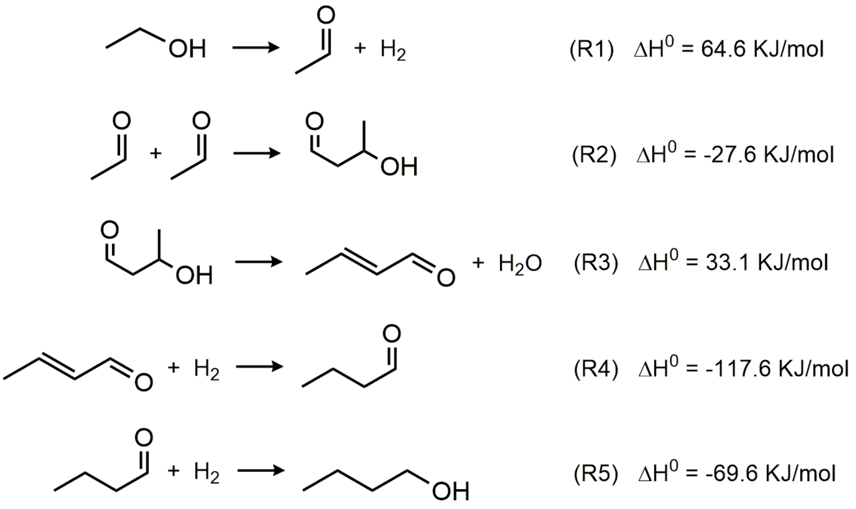
(R1) ΔH^0 = 64.6 KJ/mol
(R2) ΔH^0 = -27.6 KJ/mol
(R3) ΔH^0 = 33.1 KJ/mol
(R4) ΔH^0 = -117.6 KJ/mol
(R5) ΔH^0 = -69.6 KJ/mol

Figure 1.3.1 Ethanol condensation towards 1-butanol through the Guerbet reaction pathway.

Some discrepancies can be found in literature regarding the ethanol condensation mechanism towards 1-butanol. For example, according to Scalbert et al., 1-butanol is produced through both mechanisms (direct coupling and the multi-step Guerbet route) simultaneously on hydroxyapatite catalysts in the temperature range 623–683 K, being the dominant route the direct condensation pathway [50]. On the other hand, Ho et al. also studied the ethanol coupling to n-butanol on hydroxyapatite at 573−613 K and their work suggests that the Guerbet pathway is the predominant route [46]. Nevertheless, there appears to be a general consensus in most of the literature that the multi-step mechanism is the main Guerbet pathway at lower temperatures

(<523 K) and on metal-containing catalysts since intermediate products such as 2-butenal and butyraldehyde are often observed, besides the rate of product formation has been found to be proportional to the concentration of acetaldehyde [39,51,53].

Since several steps are involved in the Guerbet process, some undesired reactions have been reported depending on the catalyst used. For instance, the most common by-products according to literature are 1,1-diethoxyethane which is formed through acid catalyzed acetylation of acetaldehyde with two ethanol molecules [54], ethyl acetate that is a dehydrogenation product of the hemiacetal intermediate formed by reaction of ethanol and acetaldehyde [23,39], as well as diethyl ether and ethylene which are formed via acid catalyzed ethanol dehydration [23,55]. Other by-products often appear when the reaction proceeds at temperatures higher than 500 K, when 1-butanol can go through condensation reactions giving place to other higher alcohols such as 1-hexanol and 1-octanol [52]. In addition, methane and carbon monoxide can be produced via metal-catalyzed acetaldehyde decarbonylation, while acetone can be formed via ethyl acetate hydrolysis that produces acetic acid and subsequent ketonization of this compound [23,56]. Other by-products such as propane, pentane, butane and butenes have been reported for this reaction [50,55,57]. All in all, the main reactions involved in the production of 1-butanol as well as the side reactions more often reported in literature are summarized in Figure 1.3.2.

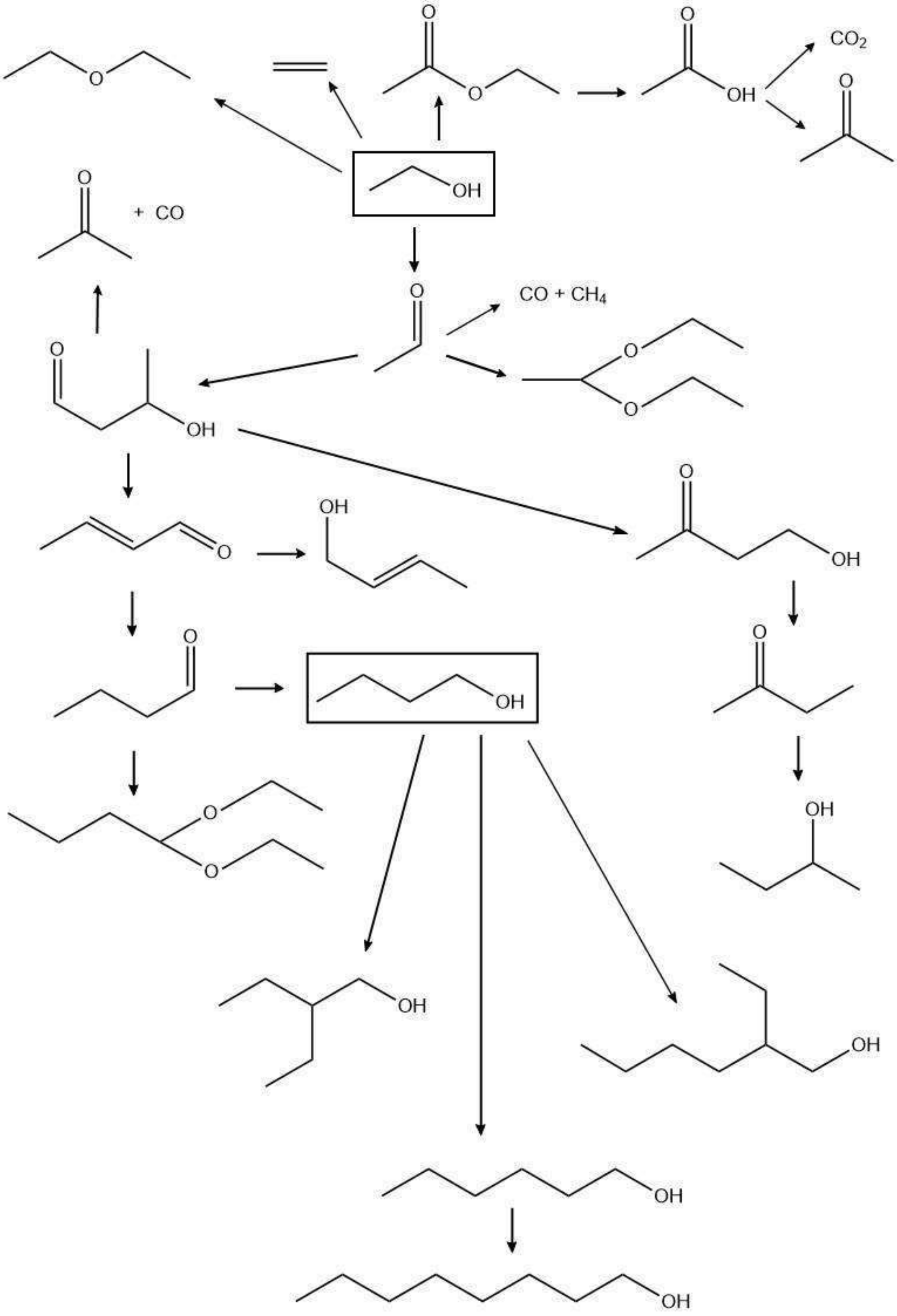
O
CO₂
OH
+ CO
CO + CH₄

Figure 1.3.2 Reaction scheme for ethanol condensation reaction.

1.3.2. Heterogeneous catalysts for the Guerbet reaction

As it was previously stated, the generally accepted Guerbet pathway comprises several steps, and as a result the design of the catalytic system becomes a rather complex task that must be carefully approached. The selection of a suitable catalytic system constitutes a challenge since the reactions involved in the process are catalyzed by active sites of different nature. For example, the aldol condensation reaction is catalyzed by basic sites, whereas the dehydration of 3-hydroxybutanal is catalyzed by acid sites [21,39,58]. Since dehydrogenation/hydrogenation reactions are also involved in the process, the active sites of the catalytic system needed for those reactions to take place must exhibit at the same time acidic, basic and a metal function with dehydrogenation/hydrogenation properties [23,51,59]. As mentioned in the chapter 1.1, the heterogenization of a process is considered by Green Chemistry a more environmentally sustainable approach, so recent studies are focused on the design of heterogeneous bifunctional catalysts with appropriate active sites in the same solid for replacing the homogeneous catalysts such as alkali metal hydroxides and the transition metal complexes that have been extensively used in the industrial Guerbet process [39]. From the point of view of industrial applicability, the use of purely heterogeneous catalytic systems has the advantage of eliminating problems associated to homogeneous catalysts such as corrosion of the reactor vessel, metal leaching, expensive catalyst separation from the reaction mixture (including filtration, centrifugation, extraction or distillation steps), waste formation and wastewater purification treatment, as well as limiting the detrimental effect of the co-produced water on the thermodynamic equilibrium of the reaction pathway, particularly inconvenient when working in liquid phase [39,60]. In addition, a heterogeneous catalyst can be reused multiple times without extensive regeneration and used in continuous-flow fixed-bed catalytic reactors.

Regarding the reactions involved in the Guerbet process, the dehydrogenation/hydrogenation steps are easily catalyzed by heterogeneous metal catalysts which are widely known for catalyzing those types of reaction [61,62,63]. However, it is not as straightforward as it might first appear to design a heterogeneous bifunctional catalyst containing a metal function as well as acid/base sites that selectively catalyze the multiple reactions that must take place for successfully convert ethanol to 1-butanol. It must be taken into account that an inappropriate tuning of the catalytic properties would result in the production of side reactions giving place to undesired by-products.

1.3.2.1. Heterogeneous catalysts with acid-base properties for the Guerbet reaction

The use of different heterogeneous catalysts with acid-base properties has been reported in literature on the Guerbet reaction, including metal oxides, zeolites, hydrotalcites and hydroxyapatites. For instance, the basic magnesium oxide has been extensively studied due to its well-known basic character, even though 573 K seems the minimum temperature necessary to obtain detectable activity for this reaction [51,64,65,66,67]. Some publications describing the use of MgO in gas phase reactions are those of Ndou et al. [64], which reported an ethanol conversion of 56% with 1-butanol selectivity of 18% at 723 K and atmospheric pressure, and Birky et al. [66], who achieved 23% of ethanol conversion and 34% of 1-butanol selectivity at 673 K and 1.3 bar. In contrast, Chieregato et al. [67] produced traces of 1-butanol at 523 K and atmospheric pressure with an ethanol conversion of approximately 10%. Moreover, MgO has been dispersed on metal oxides (Mg/SiO_2) as well as modified with basic metals (Ba, Ca) or transition metals (Zn, Ce, Zr, Pb, Sn, Cu) in order to enhance the catalyst performance by increasing the surface basicity of the final catalyst but with no improvement in terms of 1-butanol yield [64,68].

Another approach to improve the catalytic performance of magnesium oxide is the incorporation of acidic metals into the MgO structure. For example, the system formed by Mg-Al mixed oxides synthesized by calcination of hydrotalcites is attracting wide attention, due to the tunable combination of the basic sites of magnesia and the acid sites of alumina, their high surface area and structural stability [39,69,70]. The number and strength of their acid and basic sites can be tuned by adjusting the Mg/Al ratio or by substituting the Mg or Al atoms with transition, noble or lanthanide atoms, which provides great versatility to selectively catalyze the Guerbet reaction steps [65,71,72]. It has been reported that higher contents of Al, that is higher density of strong acid sites, favor the dehydration of ethanol instead of the dehydrogenation and condensation reactions, while adjacent Lewis acid and medium basic sites are required for a good catalytic performance [73].

Bifunctional catalysts containing the basic barium oxide would be an interesting option for selectively catalyze the aldol condensation step of the Guerbet process, even though only Patel et al. [74] have reported the use of BaO catalysts for this reaction. In this study, alkaline earth metal oxide nanoparticles, such as MgO and BaO, supported on carbon nano-fibers (CNF) were prepared and tested for the Guerbet reaction starting from ethanol at 573 K in a plug flow quartz reactor. The authors obtained nearly 40% of 1-butanol selectivity after 1 h of reaction time with an ethanol conversion of 5% for the catalyst BaO/CNF, showing that barium oxide is capable of catalyzing all the consecutive Guerbet steps including dehydrogenation/hydrogenation reactions at 573 K. They also observed that the higher basicity of BaO compared to MgO leads to increased production of higher alcohols such as 2-ethyl-1-hexanol and 1-octanol. In addition, the basic nature of barium oxide has demonstrated good catalytic performance in terms of activity and selectivity for base-catalyzed reactions such as the self-condensation of acetone and the dehydrogenation of ethanol [75,76,77].

The use of ZnO-based catalysts for the Guerbet reaction has not been widely studied, even though its amphoteric properties make it an attractive catalyst choice for the Guerbet process. Some of the few studies found in literature address the use of zinc oxide as heterogeneous catalyst for the synthesis of Guerbet alcohols [39] as well as a promotor of MgO [51], whereas Onyestyák et al. [21] studied ZnO supported on activated carbon at 623 K and 21 bar obtaining approximately 15% of 1-butanol yield. In addition, zinc oxide is assumed to catalyze the dehydrogenation of ethanol [78].

Manganese based catalysts have not been extensively studied on the Guerbet condensation reaction, being most of this studies homogeneous catalyzed in presence of a base and only a few studies have been of heterogeneous catalysis [45,79,80,81]. Among the heterogeneous catalyzed studies described in literature, Ghaziaskar et al. [45] reported a conversion of 18.7% for the condensation of ethanol on mixed catalysts of $Mn_2O_3/\gamma\text{-}Al_2O_3$ and $Ni/\gamma\text{-}Al_2O_3$ in a fixed-bed reactor reaching 64% of 1-butanol selectivity at supercritical conditions (523 K and 176 bar). Additionally, Marcu et al. [79] carried out this reaction in an autoclave at 473 K and autogenic pressure with MMgAlO mixed oxide catalysts (M = Pd, Ag, Mn, Fe, Cu, Sm, Yb). In particular, the catalyst Mn-Mg-AlO mixed oxide produced 1-butanol with high selectivity (53.3%) but with a very low conversion. This selectivity towards 1-butanol was attributed to the surface basicity of the catalyst, which presented mostly medium and high strength basic sites. All in all, the authors concluded that the presence of high strength basic sites is required to obtain higher selectivities towards n-butanol. Moreover, manganese oxide has been reported to improve the activity of the dehydrogenation step to acetaldehyde resulting in an increased ethanol conversion at temperatures about 573-673 K, so its use as a Guerbet catalyst would be an interesting choice [57,82,83,84].

It has also been described the production of 1-butanol from ethanol using the mineral hydroxyapatite, that is $Ca_{10}(PO_4)_6(OH)_2$, synthetized with different Ca/P ratios by controlling the pH during the precipitation step [85,86]. As it was described for the Mg/Al ratio of the hydrotalcites, the tuning of the hydroxyapatite’s Ca/P ratio has a direct impact on the surface distribution of the acid/base sites and therefore on the rates of dehydration and dehydrogenation reactions. Tsuchida et al. [86] reported that low contents of Ca leads to a higher density of acid sites, whereas a higher Ca/P ratio leads to more surface basic sites and that pure hydroxyapatite catalysts, that is without the addition of metals, are capable of synthetize 1-butanol with high selectivity at temperatures higher than 573 K. Moreover, Ogo et al. [87,88] modified the hydroxyapatite structure by replacing Ca with Sr, which led to an increase of both the amount of basic sites and the 1-butanol selectivity, and also by replacing the phosphate with vanadate ions, which strongly decreased the 1-butanol selectivity due to extensive dehydration of ethanol. Finally, they concluded that the more density of surface basic sites, the higher the 1-butanol selectivity.

Additionally, it has been also investigated the use of alkali metal supported zeolites as well as the amphoteric zirconium oxide, pure and doped with sodium [48,89,90]. The acidic nature of the zeolites and ZrO_2 was successfully reduced by addition of alkaline compounds, but the dehydration of ethanol was still favored as the formation of by-products such as ethylene and diethyl ether revealed. Hence, these materials are not considered ideal candidates for ethanol upgrading to butanol [91].

Other catalysts reported are alkaline compounds supported on activated carbon, Mg/Ce mixed oxide doped with potassium, La-promoted alumina impregnated with alkaline earth compounds, as well as catalysts containing copper oxide mixed with Mg_2SiO_4, $Zn_6Al_2O_9$ or boehmite [21,92,93,94]. Although the above mentioned catalysts contain acid/base sites necessary for the condensation of ethanol, their main drawback is that they need to operate at temperatures of 573-673 K to exhibit proper catalytic performances, due to the high activation energy of the dehydrogenation reaction, usually considered the limiting step of the Guerbet process [48,85,88,90,95].

1.3.2.2. Active metals for the Guerbet reaction

In order to reduce the reaction temperature necessary to reach proper levels of activity and 1-butanol selectivity, the addition of metals to the above mentioned catalytic systems has been widely reported in literature [62,79,96,97]. It should be taken into account that being able to operate at low temperature is considered an improvement of the reaction conditions since at high temperatures side reactions can occur, giving place to the formation of undesired by-products. This enhancement of the reaction conditions is due to the dehydrogenation/hydrogenation properties of the metal function, which can speed up the dehydrogenation of ethanol and the hydrogenation of reaction intermediates at lower temperatures than the ones reported for the same catalysts without metals [53,74,92,98]. Since the dehydrogenation of ethanol is considered the limiting step of the process, especially at temperatures as low as 403-413 K, and the subsequent hydrogenations of 2-butenal and butyraldehyde lead to 1-butanol, the incorporation of a metal to a catalytic system containing acidic and basic sites would increase both conversion and selectivity of the global reaction [74,99,100]. Examples of metal supported catalysts found in literature comprise noble and transition metals (Ru, Rh, Pd, Pt, Au, Ag, Cu, Ni, Co) deposited on different types of oxides such as alumina, ceria and Mg-Al mixed oxides [101,102,103]. It is widely recognized that the Guerbet condensation is improved by the use of active metals acting as hydrogenation catalysts such as Cu, Ni and Pd in combination with a base [99,104,105].

Copper containing catalysts have been widely studied for the Guerbet reaction due to the availability and low cost of the metal source, as well as their high selectivity in the dehydrogenation of alcohols to aldehydes or ketones and specially in the ethanol dehydrogenation towards acetaldehyde [60,106,107,108,109,110]. Consequently, this reaction can take place in relatively mild conditions when copper is present in the catalytic system [111,112]. Petrolini et al. [113] recently studied the impact in the catalytic activity at elevated pressures and 598 K of Cu addition to porous mixed oxide catalysts of AlMgO and AlCaO. These authors observed that the addition of copper promoted the dehydrogenation step for all catalysts increasing the conversion from 7.1 to 19.7% and the selectivity to higher alcohols and aldehydes from 30.7 to 54.8% upon addition of Cu to AlMgO. Besides, Marcu et al. [54] carried out the ethanol condensation towards 1-butanol at 473 K on Cu/Mg/Al mixed oxides obtaining a 1-butanol selectivity of 40.3% with an ethanol conversion of ~4%, while the performance of the Cu-free catalyst (MgAlO) at the same temperature was very similar to the blank test, that is 0.3% of conversion and no traces of 1-butanol. Moreover, Earley et al. [112] produced 1-butanol with a selectivity of 60% and an ethanol conversion of 16% at 463 K using copper supported on high surface CeO_2 catalyst in a continuous flow reactor. Another study confirming the advantages of incorporating copper to the catalyst composition was performed by Perrone et al. [62], which obtained 1-butanol at temperature as low as 423 K on mixed oxides derived from hydrotalcites modified with copper, palladium or indium. The best catalytic result was attained at 443 K using In-CuMgAl as catalyst obtaining 65% of 1-butanol selectivity with 3% of ethanol conversion. To further illustrate the positive effect of the Cu-In phase, it should be highlighted that the Guerbet reaction requires temperatures above 573 K to occur using only MgAl oxides.

Many studies describe the advantages of using nickel as the metal phase for the Guerbet reaction, mainly its good activity for alcohol dehydrogenation reactions as well as the availability and low cost of the metal source [61,99,101,102,103,114]. For example, Riittonen et al. [103] screened a large selection of metal heterogeneous catalysts (Ru, Rh, Pd, Pt, Au, Ni, Ag) supported on alumina for the direct one-pot liquid-phase conversion of ethanol at 523 K and 70 bar. The authors observed variations in the catalytic activity and product distribution derived from the use of different metals, obtaining the best catalytic result with (20.7%)Ni/Al_2O_3, that is 25% ethanol conversion and 80% selectivity to 1-butanol. Using also alumina as support, Yang et al. [115] obtained 64% selectivity towards 1-butanol with 19.1% of ethanol conversion on (8%)Ni/γ-Al_2O_3 in a fixed-bed reactor at 473 K and 1 atm. Kourtakis et al. [116,117] published two patents describing the benefits of the incorporation of nickel to Mg/Al hydrotalcites in the gas phase condensation of ethanol, obtaining conversions between 45 and 67% and a selectivity to higher alcohols of 75% at 488 K. Another nickel catalyst on a hydrotalcite support was reported by Pang et al. [61], who prepared highly dispersed (19.5%)Ni-MgAlO catalysts exhibiting 55.2% selectivity to n-butanol with 18.7% ethanol conversion at 523 K and 30 bar. High reaction pressure was applied to increase the catalysts activity. The authors affirm that metallic Ni promoted ethanol dehydrogenation and that the released hydrogen spilled over the catalyst lead to in situ hydrogenation of reaction intermediates. Since the majority of the reported studies are performed with very high metal loadings (15–20 %), Quesada et al. [114] prepared Ni/Mg-Al catalyst with only 1 wt.% of metal, but their best catalytic result is obtained under reductive conditions at 623 K (33% 1-butanol selectivity, ~20% conversion) since at low temperature, conversions obtained with and without metal were very similar. Although the literature reported that nickel catalysts show relatively high activity and selectivity towards 1-butanol, one major drawback of Ni containing catalysts is the large amount of gaseous carbon products such as CO, CO_2 and CH_4 formed due to the strong cracking ability of C-C bonds over Ni metal [103,104].

Although copper and nickel catalysts are generally known for their interesting performance in the Guerbet coupling of alcohols, the combination of both metals has not been extensively studied. It has been reported that the combination of copper and nickel improves copper stability, the reducibility of nickel as well as the catalytic performance in terms of selectivity to the required Guerbet alcohols and particularly 1-butanol [52,118,119]. Examples of Cu-Ni catalysts described in the patent literature are Ni-Cu/Al_2O_3 and Ni-Cu metal powder, which have been patented as highly versatile and efficient catalysts for the production of Guerbet alcohols, producing yields up to 90% depending on the starting alcohol and the nature of the base [120,121,122]. The effect of Cu-Ni catalysts has also been investigated in homogeneous/heterogeneous catalytic systems for the self-condensation of 1-octanol using Ni−Cu hydrotalcite-derived mixed oxides as dehydrogenation/hydrogenation catalysts and KOH as a homogeneous base [119]. The authors claim that copper ensure good reaction kinetics and the dehydrogenation of the starting alcohol, while nickel favors the production of the totally hydrogenated Guerbet alcohol (2-hexyl-1-decanol). Using pure heterogeneous catalytic system, Sun et al. [52] reported that copper and nickel doped porous metal oxides increase 1-butanol yield up to 22% with an ethanol conversion of 56% at 583 K and 80 bar for 6 h in a stainless steel batch minireactor, outperforming the monometallic as well as the metal-free Mg-Al porous metal oxides catalysts.

Palladium-based catalysts, characterized for their dehydrogenating/hydrogenating properties, are reported to have a positive effect on the Guerbet reaction [99,104]. Regarding pure heterogeneous catalytic systems, the performance of several transition metals including Pd have been tested for the ethanol condensation on MMgAlO mixed oxide catalysts (M = Pd, Ag, Mn, Fe, Cu Sm, Yb) in a steel autoclave at 473 K and autogenic pressure, obtaining the highest selectivity and 1-butanol yield (3.8% of ethanol conversion and 72.7% 1-butanol selectivity) with the Pd-containing mixed oxide, which also exhibited a remarkable stability during three successive reactions [79]. High level of 1-butanol selectivity was also reported for Pd coated hydrotalcites (Pd-Mg/Al oxide), obtaining 54% of ethanol conversion and 63% of 1-butanol selectivity at supercritical conditions, 563 K and 340 bar [123]. Riittonen et al. [103] also studied the catalytic performance of Pd/Al_2O_3 at 523 K and 70 bar for the liquid phase Guerbet reaction obtaining 21% of 1-butanol selectivity with 9% of ethanol conversion. Nevertheless, the major product obtained with this catalyst was diethyl ether with a selectivity of 64%. Although Pd has been used in homogeneous-heterogeneous catalytic systems as the dehydrogenating/hydrogenating component next to a base, significant leaching of palladium was observed reducing the interest for industrial application [124,125].

1.3.2.3. Supported metal catalysts

In a patent report, Wick et al. [125] stabilized and protected the hydrogenation catalyst from leaching, by the confinement of the metal (e.g. Pd) in a hydrophobic environment. That is to say, by immobilization of the metals on hydrophobic supports like carbon, hydrophobized silica, zeolites, hydrotalcites or silicates. Bounding the metals into a hydrophobic environment substantially protects them from being leached out by water or from deactivation by alkaline compounds.

Moreover, the metal-support interaction can also restrict the mobility of the disperse phase delaying its sintering [126]. For example, the application of copper catalysts is usually limited by their fast deactivation mainly caused by sintering due to the relatively low melting point of metallic copper. Therefore, copper is commonly supported on carbon materials and/or oxide compounds, which are considered to prevent copper sintering and, consequently, the catalyst deactivation [127]. Particularly, the chemically inert nature and hydrophobic properties of carbon materials make them more attractive supports compared to conventional oxides such as SiO_2, Al_2O_3 or ZrO_2 [128,129]. These properties are especially important taking into account that the Guerbet reaction involves several steps and that undesired secondary reactions may be catalyzed by acid and/or basic sites present on the support surface and thereby negatively affecting the 1-butanol selectivity. For example, Wang et al. [129] claim that the surface characteristics of the carbon support show great advantages in the ethanol dehydrogenation reaction, which the authors associate to the excellent selectivity obtained toward acetaldehyde on a mesoporous-carbon-supported Cu catalyst compared with Cu/SBA-15, whose abundant surface Si-OH groups promote undesired reactions. In addition, carbon materials present great versatility of their textural properties, surface area, porosity, and in their surface chemical nature, which can be modified by different chemical treatments in order to introduce different surface groups that provide the material desired characteristics in terms of acidity, hydrophilicity and surface charge [130,131].

All things considered, a carbonaceous support, high surface area graphite (HSAG) has been selected in this doctoral thesis to disperse and combine the advantages of palladium, copper and/or nickel as the metal phase with the acid/base properties of several metal oxides (MgO, BaO, ZnO and MnO). This inert and non-porous carbonaceous support would disperse the active phases (metal oxide and reduced metallic precursors) maximizing the number of surface centers exposed and favoring the interaction between them [132,133]. HSAG would improve the catalytic performance of the bifunctional catalysts for the ethanol condensation towards 1-butanol, since its surface inertness may inhibit secondary undesired reactions and its hydrophobic surface would exhibit more affinity for organic molecules than water, which is a by-product of the Guerbet reaction. In particular, their advantageous properties make carbon supports the most suitable material for the coupling of ethanol since they are reported to increase the concentration of basic sites exposed of MgZr oxides [128,134].

OBJECTIVES

2. OBJECTIVES

The main objective of this thesis is the synthesis and characterization of solid materials and further optimization for their application as heterogeneous catalysts in the production of chemical compounds of energetic interest from platform molecules obtained from biomass, specifically, the ethanol condensation into butanol. These catalysts are supported on a carbonaceous material and contain catalytic functions consisting of acid/base sites and metal centers. The combination of these two functions make it possible to catalyze aldol condensation reactions as well as hydrogenation/dehydrogenation reactions. More specifically, the objectives of the work are detailed in the following points:

1. Synthesis of bifunctional catalysts using an acid/base phase (metal oxides such as MgO, BaO, ZnO or MnO) and a metallic phase (Pd, Cu, Ni or Cu-Ni) using a graphite support with a high surface area.

2. Characterization of the prepared catalysts to obtain information about the structural, textural and surface characteristics of the solid catalysts that can explain their catalytic properties and therefore their performance on the Guerbet reaction. The characterization techniques used comprise transmission electron microscopy (TEM), X-ray energy dispersive spectroscopy (EDX), X-ray diffraction, CO_2 chemisorption microcalorimetry, temperature programmed reduction (TPR) or temperature programmed desorption of NH_3 (NH_3-TPD).

3. Evaluate the catalytic activity of the catalysts in the transformation of bio-ethanol to obtain 1-butanol in the Guerbet reaction, in order to study the effects of the support, metallic and metal oxide phase nature, and the acid/base interaction with the metallic nanoparticles, as well as the

effect of the Cu and Ni loading for the bimetallic catalysts. The reaction tests were performed in a gas phase continuous flow reactor operated at 503 K and 50 bars of pressure.

EXPERIMENTAL

3. EXPERIMENTAL

This chapter describes the synthesis of the studied catalysts, as well as the foundations of the characterization techniques employed over the development of this work to determine their most relevant structural and surface properties to achieve further understanding on the role of the active phases in the catalytic performance in the Guerbet reaction. It also includes the description of the experimental reaction set up and the analytical methods employed in the evaluation of the catalytic activity.

3.1. Catalysts synthesis

As it was previously introduced in the chapter 1, almost all the studied catalysts were supported on a carbonaceous support, a high surface area graphite (HSAG) supplied by Timcal. The specific surface area of the HSAG was S_{BET} = 396 m^2/g. The support MgO was obtained by calcination at 723 K of a commercial $Mg(OH)_2$ from Fluka, that has a specific surface area of S_{BET}=17 m^2/g.

Two preparation methods have been applied for the synthesis of the M/HSAG catalysts (M = Mg, Ba, Zn, Mn), generally incipient wetness impregnation (IWI) except one Mg/HSAG sample that was prepared by a deposition-precipitation method (DP). The incorporation of copper, nickel and palladium was done by IWI in all cases. The precursor salts used were $Mg(NO_3)_2·6H_2O$, $Ba(NO_3)_2$, $Pd(NO_3)_2·2H_2O$ and $Cu(NO_3)_2·3H_2O$ from Sigma-Aldrich, $Mn(NO_3)_2·4H_2O$ and $Zn(NO_3)_2·6H_2O$ from Panreac, and $Ni(NO_3)_2·6H_2O$ from Alfa Aesar. For the IWI method, the necessary quantity of the corresponding metal nitrate salt was dissolved in distilled water to achieve the specified weight percent (wt%) that is tabulated in Table 3.1.1 In the case of the M/HSAG samples, which are used to prepare the bifunctional catalysts, the weight percent of the metallic element (M) of each metal oxide was calculated to achieve an atomic proportion Metal (Cu or Ni)/M 2:1. Regarding the monometallic and bimetallic catalysts, the adequate concentration of the corresponding precursor was used to incorporate a metal loading of 5 wt% on HSAG or M/HSAG: 5wt.% Cu; 5wt.% Ni; 5wt.% Pd; 2.5wt.% Cu and 2.5wt.% Ni; 4wt.% Cu and 1wt.% Ni; and 4.75wt.% Cu and 0.25wt.% Ni for each case.

In the case of the Mg/HSAG sample prepared by a DP method, the HSAG support was suspended by constant stirring in a solution containing the necessary quantity of nitrate magnesium precursor to incorporate a 50 wt% of final MgO (30.2 wt% of Mg) loading to the support. The pH was adjusted to 11 with NaOH and the final solution was kept stirring for 1 h.

After each preparation method, the resulting material was dried overnight in an open recipient at room temperature. The M/HSAG samples were then treated at 873 K for 3 h in a quartz tube reactor under helium atmosphere or in a horizontal furnace using a N_2 flow with a heating rate of 5 K/min to obtain the corresponding metal oxide, except Mn/HSAG which was treated at 673 K. The calcination temperature applied was chosen after extensive literature review [135,136,137,138,139,140,141,142]. The monometallic Cu or Pd catalysts as well as the bimetallic Cu-Ni were reduced in-situ under flowing hydrogen (20 mL_{STP}/min) for 1 h at 573 K, whereas 5Ni/HSAG and 5Ni-Mg/HSAG were reduced at 723 K. The reduction temperature of each sample were set as a result of the temperature programmed reduction (TPR) profiles. The reduced catalysts were exposed and stored under air up to their evaluation in reaction or the characterization studies.

To sum up, Table 3.1.1 summarizes all the studied catalysts, indicating in each case their composition and the preparation method used to incorporate the metal oxide and the Pd, Cu and/or Ni nanoparticles.

Table 3.1.1 Composition and preparation method of the catalysts.

Catalyst	Metal oxide preparation method	Wt% Element of the MOx	Metal preparation method	Wt% Cu	Wt% Ni	Wt% Pd
5Cu/HSAG	-	-	IWI	5	-	-
5Ni/HSAG	-	-	IWI	-	5	-
2.5Cu2.5Ni/HSAG	-	-	IWI	2.5	2.5	-
4Cu1Ni/HSAG	-	-	IWI	4	1	-
5Pd/HSAG	-	-	IWI	-	-	5
Mg/HSAG	DP	30.2	IWI	-	-	-
Mg/HSAG	IWI	1	IWI	-	-	-
Ba/HSAG	IWI	5	IWI	-	-	-
Zn/HSAG	IWI	2.4	IWI	-	-	-
Mn/HSAG	IWI	2	IWI	-	-	-
5Pd/Mg	IWI	-	IWI	-	-	5
5Pd/Mg-HSAG	DP	30.2	IWI	-	-	5
5Cu-Mg/HSAG	IWI	1	IWI	5	-	-
5Ni-Mg/HSAG	IWI	1	IWI	-	5	-
2.5Cu2.5Ni-Mg/HSAG	IWI	1	IWI	2.5	2.5	-
4Cu1Ni-Mg/HSAG	IWI	1	IWI	4	1	-
4.75Cu0.25Ni-Mg/HSAG	IWI	1	IWI	4.75	0.25	-
5Cu-Mn/HSAG	IWI	2	IWI	5	-	-
5Cu-Ba/HSAG	IWI	5	IWI	5	-	-
5Cu-Zn/HSAG	IWI	2.4	IWI	5	-	-
5Ni-Mn/HSAG	IWI	2	IWI	-	5	-
4Cu1Ni-Mn/HSAG	IWI	2	IWI	4	1	-
2.5Cu2.5Ni-Mn/HSAG	IWI	2	IWI	2.5	2.5	-

3.2. Characterization techniques

3.2.1. Temperature programmed reduction

This technique (abbreviated TPR) provides useful information on the temperatures needed for the complete reduction of a catalyst as well as the interaction between the metal phases and the support [126]. The reduction of the catalyst is monitored while the temperature increases linearly in time in a reducing atmosphere, in our case hydrogen atmosphere. The gases consumed and produced during the reduction are continuously analyzed on-line with a gas chromatograph, which depicts the variation of the hydrogen concentration and the appearance of other compounds released during the decomposition of the precursor or the decomposition of thermally unstable groups. The reduction profile of the catalyst is obtained plotting the hydrogen consumption as a function of the temperature.

The experiments were performed placing 150 mg of catalyst in a U-shaped quartz reactor under 30 mL/min of a mixture of 5 vol.% hydrogen in helium (Air Liquide 99.999% purity). For each TPR experiment, the sample was heated from room temperature up to 973 K with a ramp of 10 K/min. The equipment used comprises a programmable oven where the quartz reactor is introduced, and a thermal conductivity detector to measure changes in the thermal conductivity of the gas stream.

3.2.2. X-ray diffraction

X-ray diffraction (XRD) is a technique used to obtain structural information from the catalyst, such as identify crystalline phases (employing Bragg’s law) and to obtain an indication of the particle size (employing Scherrer formula) [126]. X-rays are short-wavelength electromagnetic radiation produced by the deceleration of high-energy electrons or by electronic electron transitions found in the internal orbitals of atoms.

When a monochromatic X-ray radiation is applied to a solid sample, the crystalline planes of regularly spaced atoms act like a diffraction grating, giving rise to a pattern of diffraction lines specific to each material, where each line corresponds to a spacing between specific planes of the material [143]. Figure 3.2.1 represents a narrow beam of radiation that hits the surface of a crystal at an angle θ. Two requirements are necessary in order to take place the diffraction of the X-rays: that the spacing between the planes of atoms has to be approximately the same as the wavelength of the radiation, and that the dispersion centers are regularly distributed in space. The spacing between the lattice planes can be estimated with Bragg's law, which says that X-rays are reflected by the crystal only if the angle of incidence satisfies the condition:

$$n\lambda = 2d\sin\theta \qquad \text{Equation 3.1}$$

Where λ is the wavelength of the X-rays, d is the distance between two lattice planes, θ is the angle of incidence of the radiation, and n is an integer called the order of the reflection.

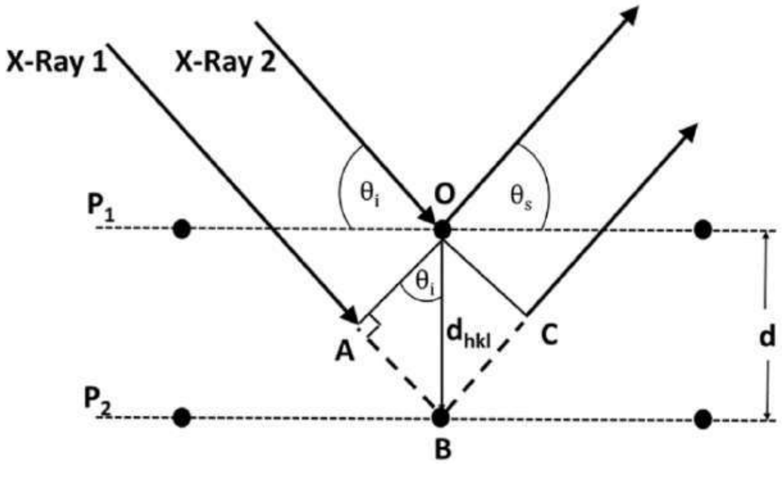

Figure 3.2.1 Schematic representation of X-ray diffraction [144].

In catalyst characterization, the diffraction patterns are mostly used to identify the crystallographic phases present in the catalyst. The representation of the intensity of the radiation after interacting with the sample as a function of the angle of incidence (2θ), is called a diffractogram, which is characteristic of each crystalline material. The identification of crystalline phases is accomplished by comparison with the X-ray diffraction database of the JCPDS (Joint Committee on Powder Difraction Standars, 1971).

The diffraction peaks from perfect crystals are very narrow, for example the reflections corresponding to large metal nanoparticles. However, for crystallite sizes below 100 nm, the peaks become broader due to incomplete destructive interference in the scattering directions where the X-rays are out of phase [126]. Scherrer's formula relates the size of the crystallite with the peak width:

$$L = \frac{K\lambda}{\beta cos\theta} \qquad \text{Equation 3.2}$$

Where L is the dimension of the crystallite in the direction perpendicular to the reflecting plane, λ is the X-ray wavelength, K is a constant often taken as 0.9 for spherical crystallites, θ is the angle between the beam and the normal to the reflecting plane, and β is the width of the diffraction peak in radians corrected by the broadening effects produced by the instrumental equipment measured at half the height of the maximum intensity. It is corrected by the equation $\beta = \sqrt{B^2 - b^2}$, where B is the width of the diffraction peak of the sample and b is the instrumental broadening corresponding to a standard substance.

The experiments were carried out in a Polycristal X'Pert Pro PANalytical diffractometer equipped with a graphite monochromator and using Cu Kα radiation (λ = 1.54 Å) and a Ni filter. The catalysts were previously reduced in hydrogen atmosphere at their corresponding reduction temperature. The experimental conditions used with our materials were 45 kV and 40 mA. Data were collected in the 2θ range between 4º and 90º at a rate of 0.04º/s and the qualitative analysis was done using PANalytical X'Pert HighScore Plus software.

3.2.3. Nitrogen physisorption at 77 K

This technique is employed to determine the specific surface area, that is the exposed area of a solid per unit mass (m^2/g), as well as the distribution of pore sizes of a porous material. It is based on the adsorption phenomena that takes place at the interface between the solid analyzed (adsorbent) and the fluid (gas or liquid) used to carry out the adsorption, commonly known as adsorbate.

First, the sample is degasified with or without heating in order to clean the surface and remove adsorbed species. Then, the sample is cooled to cryogenic temperature (77 K) and then exposed to a ramp of controlled pressures in the presence of N_2. As the pressure increases, the number of gas molecules adsorbed on the surface increases. The amount of gas adsorbed can be determined applying the universal laws of the gases and knowing the pressure at which the adsorption reach the equilibrium. From this point on, the desorption process begins, in which the release of the adsorbed molecules occurs as the pressure is reduced. The quantity of gas adsorbed or desorbed on the surface is quantified by gravimetric or volumetric techniques, according to the characteristics of the equipment. At the end of the analysis, the adsorption along with the desorption phenomenon are described by means of their isotherms, that is the representation of the volume of N_2 physisorbed on the solid as a function of the relative equilibrium pressure of nitrogen. The analysis of these isotherms offers great information about the surface area of the solid, as well as its porosity.

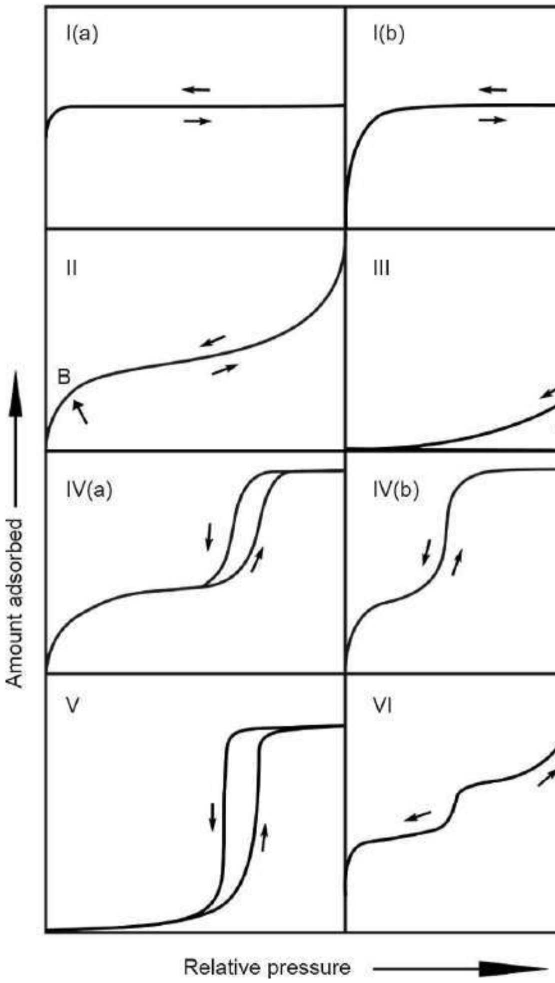

Figure 3.2.2 Classification of the isotherms according to IUPAC [145].

There are six types of isotherms according to IUPAC (Figure 3.2.2), where the Type I corresponds to microporous solids such as activated carbons, molecular sieve zeolites and certain porous oxides [145,146], which are characterized by an increase in the amount adsorbed at low pressure, corresponding to the filling of the micropores, followed by a distinctive plateau.

Type II corresponds to non-porous or macroporous solids, whereas Type III is ascribed to non-porous or macroporous solids with weak adsorbent-adsorbate interactions. Mesoporous solids give rise to Type IV isotherms, while the uncommon Type V isotherm is related to mesoporous solids with weak adsorbent-adsorbate interactions. The Type VI represents multilayer adsorption on a uniform non-porous surface such as graphite systems. The hysteresis loops observed for the Type IVa and Type V isotherms correspond to a capillary condensation phenomena associated with the mesoporosity.

The total surface area is determined calculating the volume of the monolayer, which is multiplied by the area occupied by each adsorbed molecule. The volume of the monolayer is calculated with the BET method (Brunauer-Emmett-Teller) using the equation that describes the isotherm:

$$\frac{p}{V(p^o - p)} = \frac{1 + (c-1)}{Vm\,c}\,\frac{p}{p^o} \qquad \text{Equation 3.3}$$

Where Vm is the volume of the monolayer, c is a constant, p is the equilibrium pressure, and p^o is the saturation pressure of the gas. Vm and c can be obtained by representing p/V(p°– p) versus p/p°. The resulting figure has a linear part corresponding to the monolayer adsorption. With the slope (s) and the ordinate in the origin (i), the volume of the monolayer and the constant c can be calculated:

$$V_m = \frac{1}{s+i} \qquad \text{Equation 3.4}$$

$$c = \frac{s}{i} + 1 \qquad \text{Equation 3.5}$$

The surface area (S) of the sample is determined from the expression:

$$S = A_m V_m \frac{N_A}{22414} \qquad \text{Equation 3.6}$$

Where Am is the section area occupied by each molecule of adsorbate, which according to IUPAC it is 0.162 nm^2 for nitrogen [147], and N_A is the Avogadro's constant.

For non-porous and mesoporous materials, the BET equation is valid for the linear region in the BET plot between $p/p^o = 0.05$ and 0.35 approximately. For microporous solids, the BET equation is only valid for the linear region below $p/p^o = 0.05$ [148].

The BJH method is used to calculate the pore size and volume from the N_2 desorption curve [149], assuming that the equilibrium between the gas phase and the adsorbed phase during desorption is determined by two mechanisms: (1) physical adsorption on the pore walls, and (2) capillary condensation in the inner capillary volume. It applies only to the mesopore and small macropore size range. The size of the pores is classified by IUPAC according to: i) micropores if the dimensions are less than 2 nm; ii) mesopores if the dimensions are between 2 and 50 nm; and iii) macropores if the dimensions are greater than 50 nm [150].

The experiments were carried out using an automatic volumetric adsorption Micromeritics ASAP 2010 instrument where the N_2 adsorption-desorption isotherms were collected at 77 K. Prior to nitrogen adsorption, the samples were outgassed for 5 h at 423 K to remove all physisorbed species retained in the pores and external surface.

3.2.4. Temperature programmed desorption of NH_3

Temperature-programmed desorption (TPD) is widely applied for catalyst characterization, generally using previously chemisorbed NH_3, H_2, CO or CO_2 as probe molecules. The sample is subjected to a temperature program while the desorbed gaseous products from the surface are analyzed on-line. Useful information can be obtained from the desorption patterns to characterize the surface of the catalyst, such as the adsorption states and the kinetics of desorption. Qualitative interpretation of the TPD is based on the fact that the higher the desorption temperature, the stronger the adsorbate is bonded to the surface. Determination of relative coverages can be accomplished since the area under the curve of a TPD spectra is proportional to the coverage of the surface [126].

All in all, this technique determines the adsorbate layer and the number of molecules desorbed as a function of temperature. Ammonia is employed as the molecule adsorbed/desorbed for acidity measurements and characterization of the acid centers of the catalysts: acid strength, superficial acidity and strength distribution of the active centers.

The experiments were carried out in a chemisorption Micromeritics Autochem II 2920 apparatus connected to a thermal conductivity detector. The in-situ reduced samples were previously saturated with ammonia gas 5% at 323 K, swept with He at 373 K and then heated from 373 to 623 K at 10 K/min.

3.2.5. CO_2 chemisorption microcalorimetry

Calorimetry is the process of measuring the amount of heat released or absorbed during a certain process, which can be exothermic (releases heat) or endothermic (absorbs heat). In the adsorption microcalorimetry technique, the sample is kept at a constant temperature while a probe molecule is adsorbed on the surface, while a thermal flow detector emits a signal proportional to the amount of heat transferred per unit of time. Therefore, the adsorption microcalorimetry describes the thermodynamic of the gas-solid interaction phenomena and provides useful information for the characterization of solid surfaces. In this thesis, the CO_2

adsorption microcalorimetry is applied to obtain information about the density of basic surface centers and their strength distribution.

The experimental system used in this study is schematized in Figure 3.2.3 and consists in a Tian-Calvet microcalorimeter (C80 II-Setaram) with a CS32 control unit associated to a volumetric gas adsorption line built in Pyrex glass. The volumetric equipment consists of two pumps (one rotary and another turbomolecular), a liquid nitrogen trap to improve the vacuum, a set of taps used to introduce the gas doses, and two pressure gauges: one Alcatel CF2P to measure the residual pressure 10^{-2}-10^{-7} Torr, and another Baratron capacitance manometer (MKS Instruments) to control the doses of the gas probe with a working range of 1^{-10} Torr and an accuracy of 10^{-3} Torr.

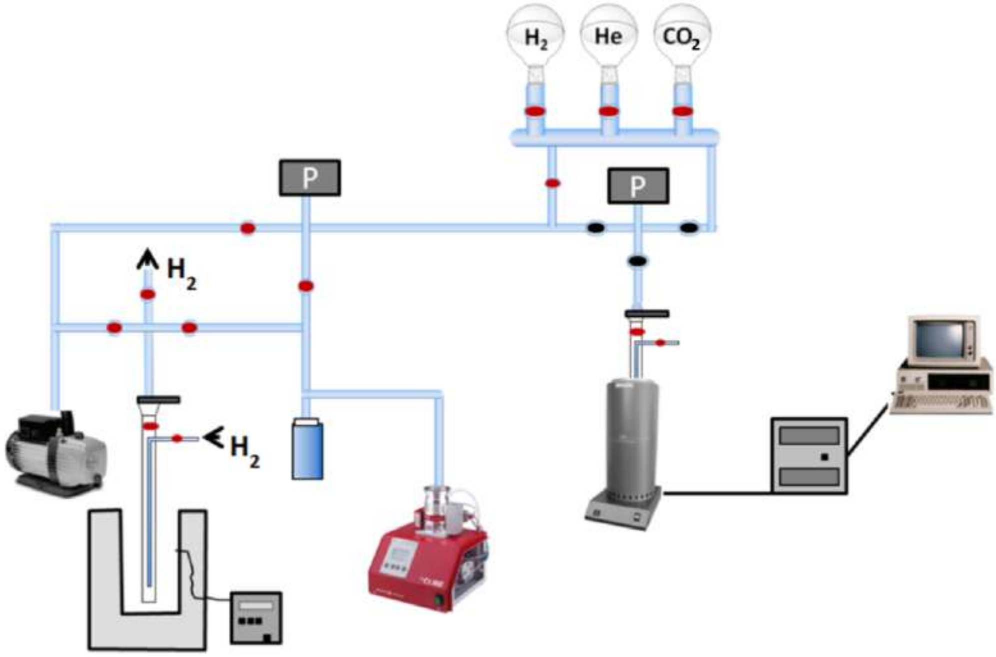

Figure 3.2.3 Volumetric equipment coupled to a microcalorimeter.

Approximately 200 mg of sample are introduced into an adsorption bulb or glass reactor (Figure 3.2.4), where it is first reduced in a flow of H_2 (30 mL/min) for 1 hour at the corresponding reduction temperature. Subsequently, the sample is pretreated for 10 hours at 623 K under high vacuum and outgassed overnight while it is cooled to room temperature. Then, the bulb is placed in the calorimeter cell, where it is left in dynamic vacuum until the heat flow signal is stabilized (generally, about 90 minutes), that is, until there is no heat flow between the reference cell and the measurement cell since both are at the same temperature, 323 K in our case. The CO_2 chemisorption is then initiated by introducing successive doses of gas to the adsorption bulb at a constant temperature of 323 K, with initial pressures ranging from 0.5 to 10 Torr. For a particular pulse, the adsorption is considered complete when the heat flow of the calorimeter and the pressure remain constant. The total CO_2 chemisorbed at the monolayer is considered to be attained when the adsorption heat is lower than 40 kJ/mol, since below this value the heats of adsorption are considered a consequence of physical adsorption phenomena [151,152].

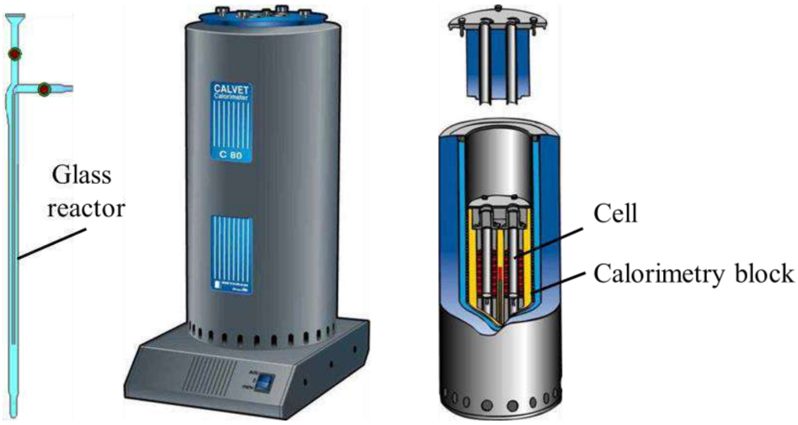

Figure 3.2.4 Glass reactor for adsorption microcalorimetry experiments and Tian Calvet microcalorimeter (Setaram C-80 II) [153].

The adsorption microcalorimetry profile is obtained by representing the differential heat of adsorption (Q_{diff}) that is released when a given amount of CO_2 is adsorbed (for example in kilojoules per mole of adsorbed gas) versus the amount adsorbed per gram of catalyst or the surface coverage (θ), which is defined as the monolayer's fraction of chemisorbed gas. The analysis of the calorimetric profile, characteristic of each catalyst, provides information about the type and number of adsorption centers, as well as their energy distribution.

3.2.6. Transmission electron microscopy and X-ray energy dispersive spectroscopy

Transmission electron microscopy is a widely used technique for the structural and chemical characterization of materials, since it provides direct information on the morphology, size and spatial distribution of the metallic nanoparticles (NPs), as well as the chemical composition and crystalline phase identification applicable to a wide range of materials [154]. It is important to determine the size of the NPs in order to understand their activity, since the number of surface atoms, which can act as active sites during the catalytic process, increases with decreasing particle size. Moreover, the atoms located in edges and corners are more active than those located in the planes and their number also increases when decreasing the particle size [155].

This technique is based on the interaction of the material with an electron beam that is generated in a gun and accelerated under a differential electric potential of 100-400 kilovolts to acquire kinetic energy. The electron beam is collimated, focused and guided through a series of electromagnetic lenses and condensers. The interaction of a high energy electron beam with the specimen will produce various effects resulting in a range of signals being emitted (Figure 3.2.5). Depending on how the beam is projected onto the sample, it can be obtained the transmission electron microscopy (TEM) which occurs when a beam is projected in parallel, or the scanning electron microscopy (STEM) which takes place when the beam converges in a point of 1nm, obtaining a scan of the sample.

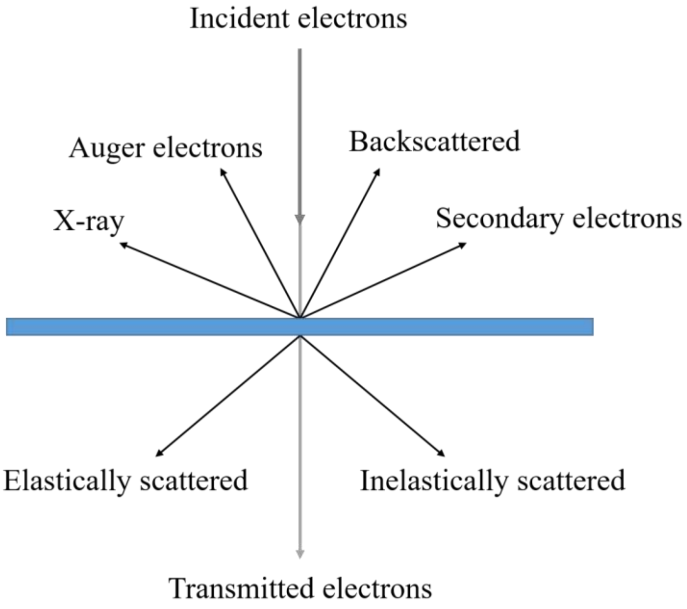
Incident electrons
Auger electrons
Backscattered
X-ray
Secondary electrons
Elastically scattered
Inelastically scattered
Transmitted electrons

Figure 3.2.5 Type of signals generated in electron beam-sample interactions.

The signal obtained by TEM microscopy, corresponds to the transmitted and undispersed electrons that penetrate the material without interacting with it; while the signal obtained by STEM microscopy corresponds to the dispersed electrons during the collision with the sample atoms. Afterwards, a series of magnetic lenses deliver the signal to a detector, generating a two-dimensional image of the sample. The higher the atomic number of the elements that constitute the sample, the higher the number of electrons that are dispersed. There is also a direct relationship between angle of measurement and atomic number, that is, the higher the atomic number, the higher the number of electrons scattered at high angles, which generates a greater contrast in the final photograph.

A spectrometer of X-ray dispersive energies (Energy-dispersive X-ray spectroscopy, EDXS) can be indexed to the microscope, which can collect and analyze the characteristic X-rays emitted from the specimen as a result of its interaction with a high-energy electron beam. The incident beam may excite and eject an electron from its discrete energy level, creating an electron hole that is occupied by an electron from an outer, higher-energy level. The difference in energy between the higher-energy level and the lower energy level may be released in the form of an X-ray. As the energies of the X-rays are characteristic of the difference in energy between the two levels and of the atomic structure of the emitting element, EDXS provides qualitative and quantitative analysis of the elemental composition of the specimen. The EDX spectrometer connected with the STEM scan mode offers the possibility to obtain X-ray mapping of elements, where the positions of specific elements emitting characteristic X-rays within an inspection field can be indicated by unique color.

To carry out the analysis, the catalysts must be previously reduced and then grounded before suspending the fine powder in a volatile solvent (ethanol). After that, a couple of drops are added to the copper or gold grid (Lacey carbon, 200 mesh, Aname) that is placed in the sample holder and then introduced into the microscope for degassing and subsequent analysis. TEM images and mappings were obtained on a JEOL JEM-2100F microscope operating at 200 kV and a JEM 3000F microscope at 300 kV, both equipped with an Energy-Dispersive X-Ray detector from Oxford Instruments with a maximum resolution of 0.17 nm and with a minimum size of beam convergence of 0.2 nm for the STEM mode.

The average diameter (d) of the metal NPs (Pd, Cu and/or Ni) was calculated based on a minimum of 300 particles, using the following equation:

$$d = \frac{\sum n_i d_i^3}{\sum n_i d_i^2} \qquad \text{Equation 3.7}$$

Where n_i is the number of particles with diameter d_i. This equation is used when there are particles of similar shapes, but with different sizes.

3.2.7. X-ray photoelectron spectroscopy

The X-ray photoelectron spectroscopy technique is one of the most useful characterization tools used to determine the surface composition, the oxidation state of the elements and, in favorable cases, the dispersion of one phase over another [156]. It is based on the photoelectric effect represented in Figure 3.2.6 (left): when a catalyst is irradiated with X-ray photons, an atom absorbs a photon of energy hυ while a core or valence electron with binding energy E_b is ejected. A hemispherical detector detects the electrons emitted and records their energy to obtain the X-ray photoelectron emission spectrum. The incident photons have a higher binding energy than the electrons in the sample, since this energy must be overcome in order to pull them out. The kinetic energy of the emitted electron E_c must fulfill the equation of the photoelectric effect:

$$E_C = h\upsilon - E_b - \phi \qquad \text{Equation 3.8}$$

Where hυ is the incident energy of the photons, E_b is the binding energy of the excited electron, and Φ is the working function of the spectrometer, a correction factor which represents the minimum energy required to impulse one electron towards the highest level occupied in the vacuum.

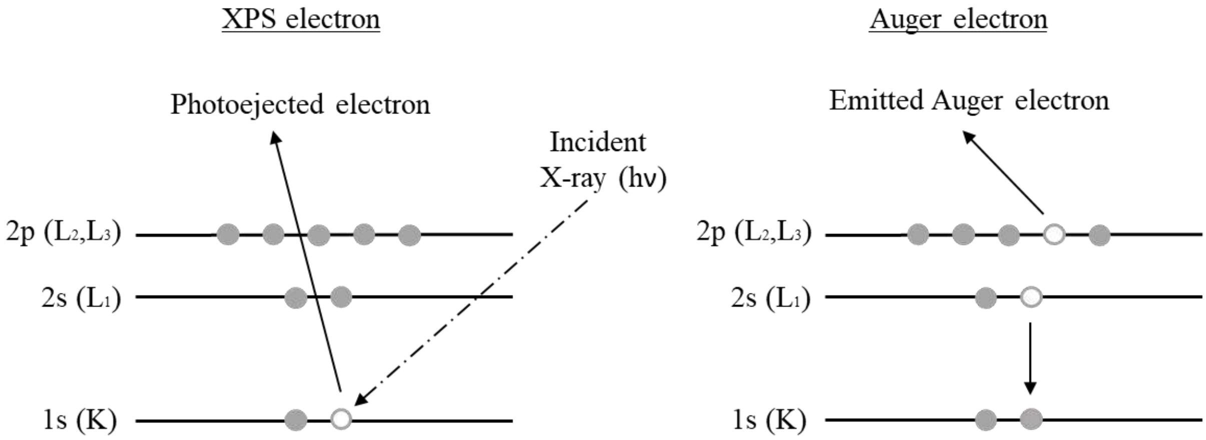

Figure 3.2.6 Photoelectric effect and Auger processes.

When an electron is photoejected, the atom becomes an unstable ion with a hole in one of the core levels. The excited ion relaxes by filling the core hole with an electron from a higher shell (Figure 3.2.6, right). The energy released by this transition is taken up by another electron, known as the Auger electron, which leaves the sample with a kinetic energy specific of the element [157]. Auger electrons have fixed kinetic energies that are independent of the energy that created the initial core hole. The label $KL_1L_{2,3}$ corresponds to an Auger electron that originates from a transition with the initial core hole in the K shell, which is filled by an electron from the L_1 shell, whereas the Auger electron is emitted from the $L_{2,3}$ shell.

An XPS spectrum is the representation of the intensity of the flow of emitted electrons recorded by the detector as a function of their kinetic energy or, more frequently, as a function of their binding energy. As stated by Eq. 8, the kinetic energy of the emitted electrons is related to their binding energy (BE), which is characteristic of the elements present in the sample from the photoelectron originates and the electronic interactions between them. The binding energies of a particular electron level and the spin–orbit splittings increase with increasing atomic number.

The intensity ratio of the peaks from a spin doublet is determined by the multiplicity of the corresponding levels. Consequently, photoelectron peaks from core levels appear as doublets or paired peaks except for s levels, which normally give a single peak [157]. In addition, the binding energy increases with increasing oxidation state, and for a fixed oxidation state with the electronegativity of the ligands.

To perform the experiments, the material must be pelletized to provide a flat and homogeneous surface, which prevents the loss of material as a result of the high vacuum. The pelletized sample is placed in the sample holder and introduced into the pre-treatment chamber, where it must be degassed until reaching a vacuum close to $1.3 \cdot 10^{-6}$ mbar. Then, the sample is transferred to the analysis chamber where the pressure is always kept below 10^{-10} mbar. The equipment used for the analyzes was a PHOIBOS 150 9MCD SPECS GmbH. The X-ray radiation sources used were non-monochromatic Al radiation (200 W, 1486.61 eV) and Mg radiation (200 W, 1253.6 eV).

The spectral data for each sample were analyzed using CASA XPS software. The resulting spectra were deconvoluted and fitted to a mix of Gaussian and Lorentzian curves. The peak corresponding to C 1s (BE = 284.6 eV) was used as the reference standard for the peak's displacements due to the charges effect. The equipment error in the energy determinations was less than 0.01 eV.

3.3. Catalytic reaction

3.3.1. Experimental system

The catalytic condensation of ethanol was carried out in a stainless-steel fixed-bed reactor operated in gas phase at 50 bar in a continuous flow. The equipment has a gas supplier system and a HPLC-pump for the injection of ethanol. The fixed bed reactor is a tube of stainless steel 316 L (52.5 cm long, 0.049” wall diameter and 3/8” outer diameter). The reaction set-up and the detailed process flow scheme are shown in Figure 3.3.1 and Figure 3.3.2. The gas flow rates were controlled using Bronkhorst High-Tech Series mass flow controllers. The reactor was held within a furnace equipped with a temperature controller. The reaction temperature was measured with a K-type thermocouple inserted directly in the catalytic bed.

For each experiment, the reactor was filled with 0.5 g of the catalyst, and silicon carbide (SiC) was added to obtain 4 cm length. Prior to the catalytic test, the catalysts were reduced in situ with hydrogen at 573 K for 1 h before reaction, except the monometallic nickel catalysts introduced in the chapter 3.1, which were reduced at 723 K. After reduction, the catalyst was cooled to the reaction temperature in helium atmosphere. For all experiments, helium flow rate during reaction was 50 mL_{STP}/min and ethanol (absolute extra pure, Scharlau) flow rate was adjusted to 0.02 mL/min with a HPLC-pump.

In a preliminary study, a set of experiments were performed to assess the impact of temperature on conversion and 1-butanol selectivity using 5Cu-Mg/HSAG as catalyst in the range 443-573 K, concretely at 443, 483, 503, 523, 548 and 573 K. After establishing the optimized reaction temperature, it was set to 503 K. With the purpose of studying the influence of thermal pretreatment temperature, the catalysts 4Cu1Ni-Mg/HSAG and 2.5Cu2.5Ni-Mn/HSAG were also tested after treatment in helium at 723 K for 1 h prior reduction with hydrogen.

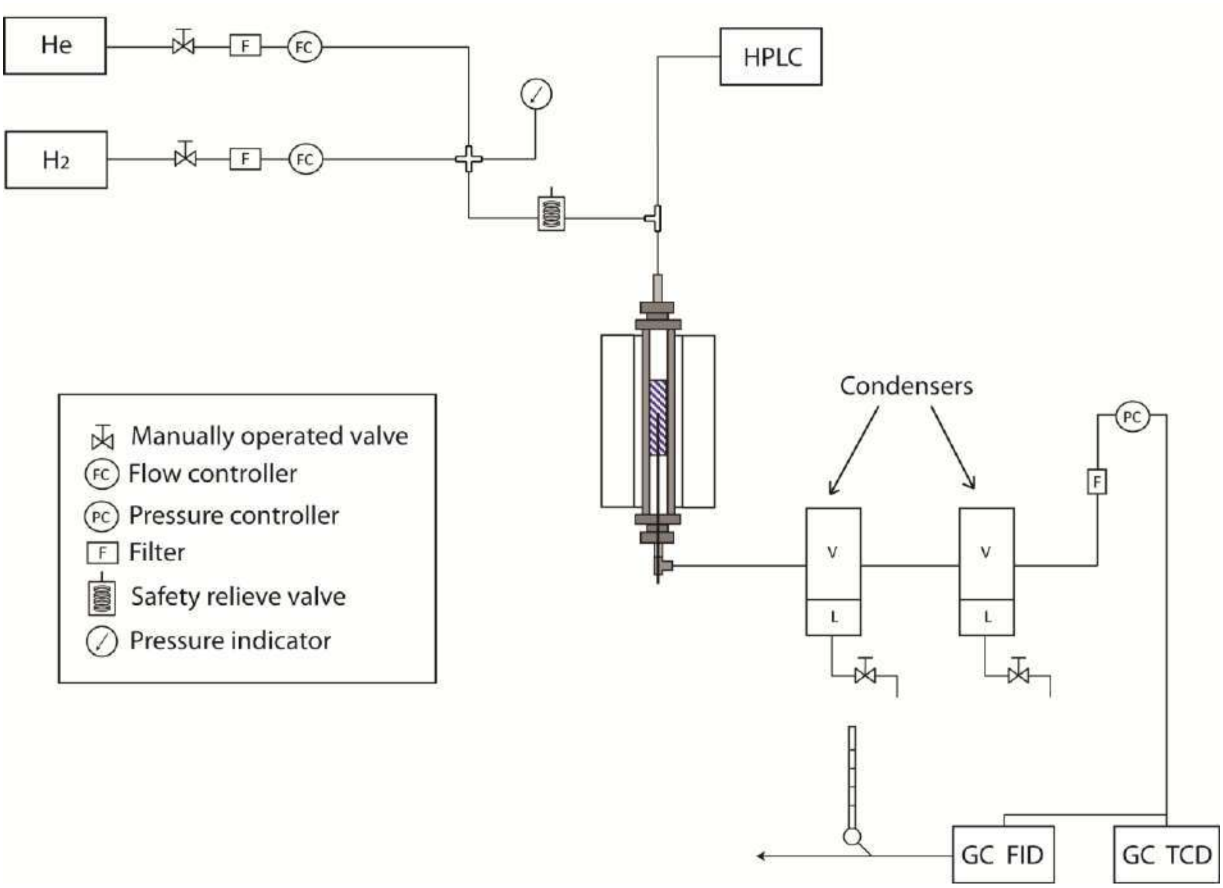
He
H2
F
FC
HPLC
Condensers
PC
V
L
GC FID
GC TCD
Manually operated valve
Flow controller
Pressure controller
Filter
Safety relieve valve
Pressure indicator

Figure 3.3.1 Detailed process flow scheme of the reactor set-up.

The gaseous products were analyzed with two on-line gas chromatographs (GC, Varian CP 3380) fitted with a flame ionization detector (FID) and a thermal conductivity detector (TCD), while the condensed reaction products were collected and analyzed with a GC equipped with a FID detector. The FID and TCD detectors were configured with a capilar column SupelQ Plot and 60/80 Carboxen-1000 column, respectively. The temperature program for GC-FID separation was ramp from 35 to 51ºC at 2ºC/min and hold at 51ºC for 1 min, then ramp to 200ºC at 16ºC/min and hold at 200ºC for 7 min. For the GC-TCD, the temperature program was hold at 50ºC for 3 minutes, ramp to 150 at 5ºC/min and then to 225 at 20 ºC/min (total = 26.75 min). Calibration of the possible reaction products was done with commercial standards.

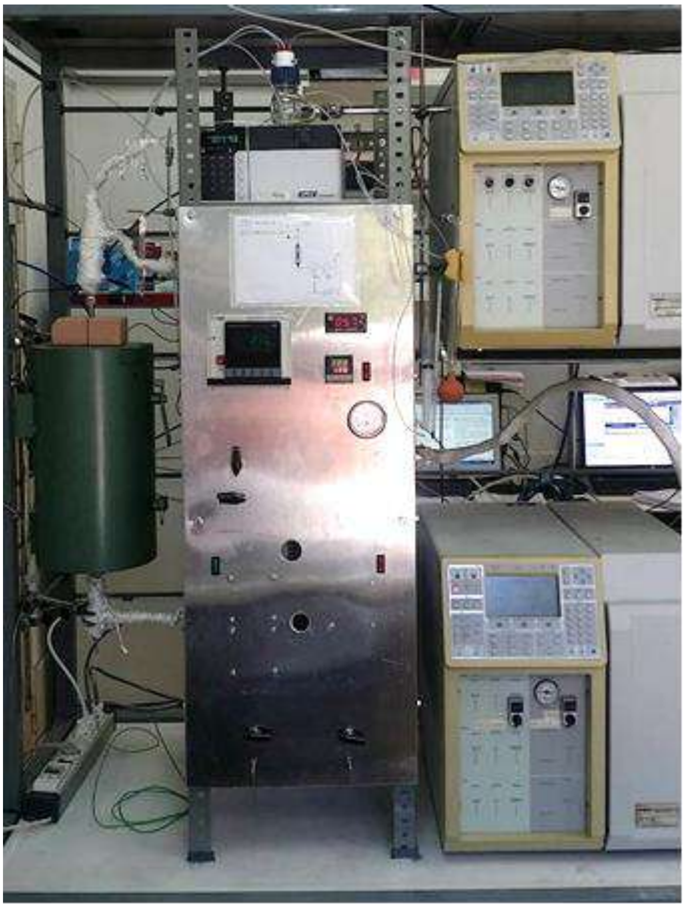

Figure 3.3.2 Reaction equipment used for the catalytic tests.

3.3.1.1. Data analysis

After 24 hours of reaction time, the ethanol conversion X_{EtOH} is calculated using the following equation:

$$X_{EtOH}\,(\%) = \frac{\Sigma_i n_i mol_i}{2mol'_{EtOH} + \Sigma_i n_i mol_i} \cdot 100 \qquad \text{Equation 3.9}$$

Where n_i is the number of carbon atoms of the product i, mol_i is the number of mol of the product i, and mol'_{EtOH} is the number of mol of unconverted ethanol.

The selectivity to a specific product was defined as follows:

$$S_i\,(\%) = \frac{n_i mol_i}{\Sigma_i n_i mol_i} \cdot 100 \qquad \text{Equation 3.10}$$

The carbon balance (C%), which resulted higher than 90%, was defined as:

$$C\,(\%) = \frac{\Sigma_i n_i mol_i + 2mol'_{EtOH}}{2mol_{EtOH}} \cdot 100 \qquad \text{Equation 3.11}$$

Additionally, site time yield STY (h^{-1} or s^{-1}) of 1-butanol was calculated as the number of µmol of 1-butanol produced per unit time and per active site of the catalyst. The active sites were considered the number of µmol CO_2 absorbed per gram of catalyst with heat of adsorption superior than 90 KJ/mol, which correspond to the strong basic sites, and the total number of metal atoms on the surface M_S, which was defined for each metal as a function of the number of metal atoms, M_t, and the metal dispersion, D:

$$M_s = M_t \cdot D \qquad \text{Equation 3.12}$$

Where the metal dispersion was calculated by $D=(6\cdot N_s\cdot M_w)/(\rho\cdot N\cdot d)$, where N_s is the number of atoms at the surface per unit area ($1.47\cdot10^{19}$ m^{-2} for Cu and $1.54\cdot10^{19}$ m^{-2} for Ni) [158], M_w is the atomic weight of the element, ρ is the density of the metal (8.96 g/cm^3 for Cu and 8.9 g/cm^3 for Ni), N is the Avogadro constant and d is the average particle size of the reduced samples (determined by TEM, assuming that particles are spherical). Therefore, the metal dispersion for each element was calculated as:

$$D = \frac{a}{d} \qquad Equation\ 3.13$$

With a=1.04 for copper and a=1.01 for nickel.

RESULTS AND DISCUSSION

4. RESULTS AND DISCUSSION

4.1. Continuous gas-phase condensation of bioethanol to 1-butanol over bifunctional Pd/Mg and Pd/Mg-carbon catalysts

The condensation of ethanol to 1-butanol in the presence of different catalyst systems based on a Pd dehydrogenating/hydrogenating component and magnesium hydroxide-derived materials as basic ingredient was studied in a fixed-bed reactor. A bifunctional catalyst supported on a synthetic composite based on Mg and high surface area graphite (HSAG) was also studied.

4.1.1. Reaction results

First, a blank experiment without catalyst, which showed no ethanol conversion after 6 h at 503 K, indicated that the reaction can barely take place in absence of a catalyst. Table 4.1.1 summarizes the catalytic parameters obtained with the Mg-HSAG support, as well as with the bifunctional catalysts reduced at 573 K and those samples previously treated in helium at 723K. In general, the main products detected were 1-butanol (ButOH), acetaldehyde (Ac), diethyl ether (DEE), carbon monoxide and methane. Other products such as acetone and 1,1-diethoxyethane, ethyl acetate, 2-butanona, diethoxybutane, butanal, 2-butenal, 2-butanol, 2-ethyl-1-butanol, 1-hexanol, 1-octanol, 2-ethyl-1-hexanol were observed in small quantities. The detection of 1,1-diethoxyethane, ethyl acetate and other higher alcohols (>C4), is in agreement with other reports on the continuous condensation of ethanol [50,52,73,101,102].

Table 4.1.1 Catalytic activity and product selectivities obtained at 503 K and 50 bar after 24 h on stream.

Sample	Average particle size (nm)	Conv. (%)	Selectivity (%)						
			ButOH	Ac	DEE	CO	CH$_4$	Acetone	Others^a
Mg-HSAG	-	0.5	0	8	73	-	-	0	19
Pd/HSAG	2.6	4.5	0	2	37	10	14	30	7
Pd/Mg	3.5	17	34	13	27	4	5	0.0	17
Pd/Mg-HSAG	3.8	19	41	15	25	5	6	0.9	7
Pd/Mg*	5.9	22	43	13	1	6	7	1	29
Pd/Mg-HSAG*	6.4	17	54	13	< 1	4	6	<1	22

Ac – Acetaldehyde, DEE – Diethyl ether, ButOH – 1-Butanol. ^{a} Other products also detected in small quantities: 1,1-diethoxyethane, ethyl acetate, 1-hexanol, 2-butanona, diethoxybutane, 1-octanol, butanal, 2-butenal, 2-butenol, 2-butanol, 2-ethyl-1-butanol, 1-octanol, 2-ethyl-1-hexanol. The ``*`` indicates that the material was thermally treated in helium at 723 K prior to reduction with hydrogen.

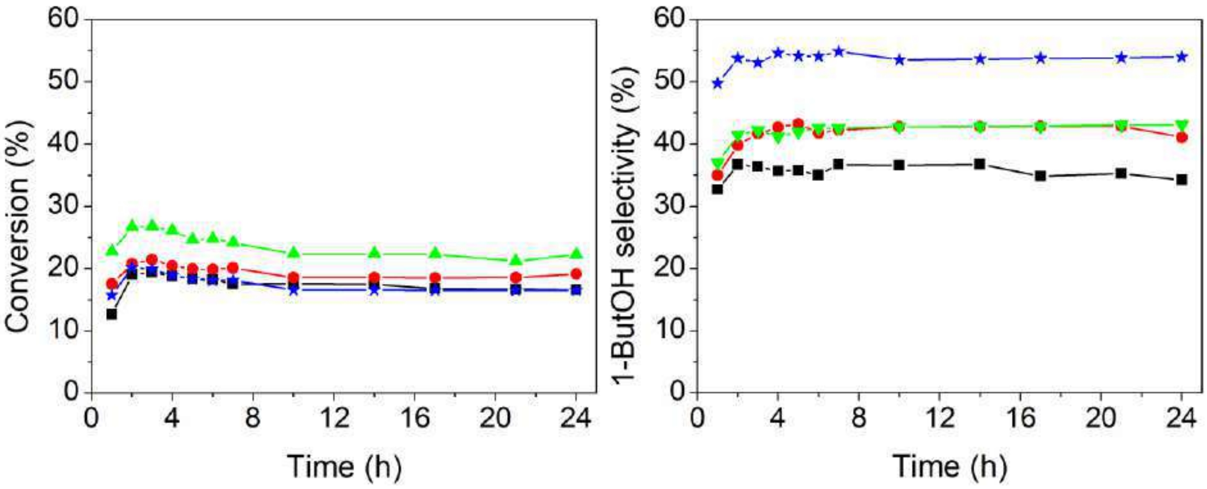

Figure 4.1.1 Conversion and 1-butanol selectivity through 24 hours of reaction. The ``*`` indicates that the material was thermally treated in helium at 723 K prior to reduction with hydrogen. (■) Pd/Mg, (●) Pd-Mg/HSAG, (▲) Pd/Mg*, (★) Pd/Mg-HSAG*.

The bifunctional catalyst proved to be very stable during 24 hours of reaction in terms of conversion and selectivity (Figure 4.1.1). After the maximum in conversion is reached at 2–3 h, the catalysts suffer slight deactivation, but after 10 h the reaction reaches steady-state conditions.

4.1.2. Catalysts characterization

4.1.2.1. Structural and textural features

The X-ray diffraction patterns of the commercial $Mg(OH)_2$, the MgO support, and the resulting Pd/Mg catalyst are represented in Figure 4.1.2. The diffractogram of $Mg(OH)_2$ can be indexed as the hexagonal brucite phase (JCPDS card 084-2164), while the thermal dehydration process at 723 K gave rise to the characteristic periclase structure of MgO (JCPDS card 45-946). The crystallite size of MgO was estimated from line broadening of the (200) diffraction peak (2θ=42.9º) by using the Scherrer formula, while for $Mg(OH)_2$ the peak at 2θ =58.8º corresponding to the (110) reflection plane was used to determine the mean crystallite size. The values are listed in Table 4.1.2, together with some other parameters related to textural and structural properties. As expected, the thermal decomposition of $Mg(OH)_2$ resulted in the formation of MgO particles of a much smaller size, in good agreement with other reported observations [159,160]. This was also reflected in the increase in the measured surface area (from 17 to 105 m^2/g, Table 4.1.2). The subsequent incorporation of metal NPs to the MgO support caused some evident changes in the structure and texture of the material (Figure 4.1.2, Table 4.1.2). The bifunctional Pd/Mg catalyst showed the characteristic peaks of the brucite structure of $Mg(OH)_2$, which confirmed that aqueous impregnation transformed MgO back to $Mg(OH)_2$ as a consequence of its interaction with water [161], although the main peak at about

43º corresponding to residual MgO was also present. It should be noted that the conversion of MgO into $Mg(OH)_2$ during the impregnation procedure to incorporate the metal caused a decrease in the surface area as well as in the pore volume with respect to the starting MgO and this is in agreement with the findings of other authors [160] (Table 4.1.2). The distinct peaks of the Pd NPs (JCPDS card 001-1201) were detected at 2Ө values of 40.4, 46.8, 68.4 and 82.4º.

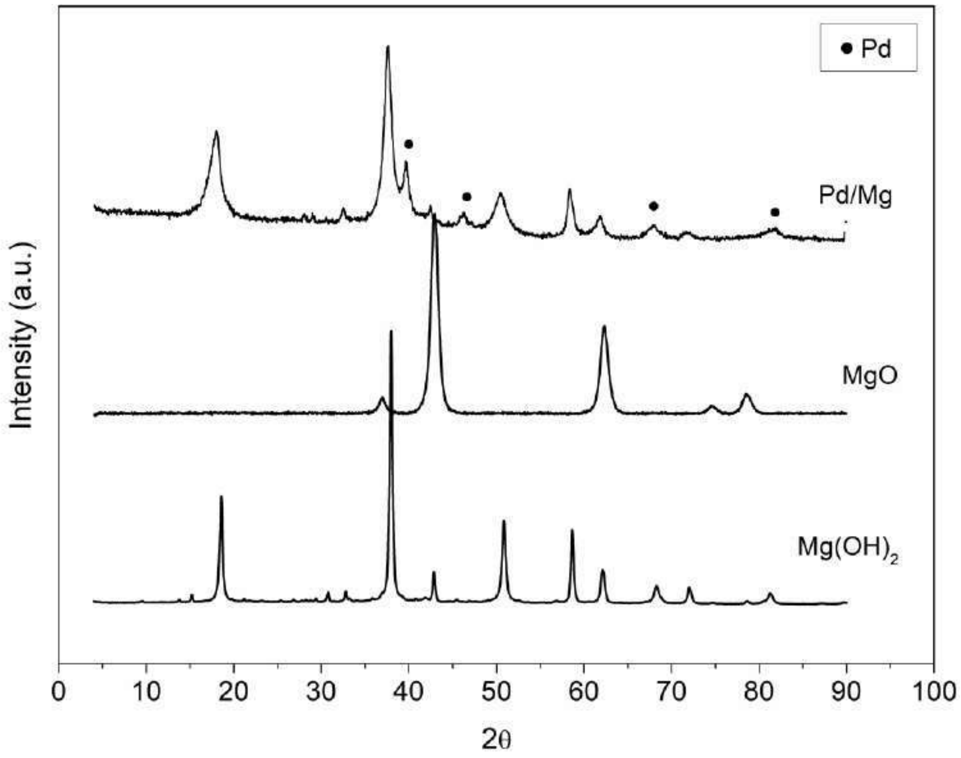

Figure 4.1.2 XRD pattern of Pd/Mg catalyst. For comparison the patterns of the starting $Mg(OH)_2$ and MgO are also shown.

Table 4.1.2 Textural and structural parameters of supports and catalysts.

SUPPORTS					**CATALYSTS**			
Sample	**S_{BET} (m^2/g)**	**Pore volume[a] (cm^3/g)**	**MgO loading[b] (wt %)**	**Crystal size (nm)**	**Sample**	**S_{BET} (m^2/g)**	**Pore volume (cm^3/g)**	**$Mg(OH)_2$ Crystal size[c] (nm)**
$Mg(OH)_2$	17	0.11	-	44[c]	**Pd/Mg**	41	0.23	17
MgO	105	0.39	-	9.9[d]	**Pd/Mg-HSAG**	224	0.54	22
Mg-HSAG	234	0.56	45	20[d]	**Pd/Mg***	166	-	-
					Pd/Mg-HSAG*	215	-	-

[a] BJH desorption pore volume, [b] determined from thermogravimetric analysis in air. Crystallite size was determined applying Scherrer formula to [c] peak at $2\Theta=58.8^{\circ}$ corresponding to $Mg(OH)_2$, [d] peak at $2\Theta=42.9^{\circ}$ corresponding to MgO. The ``*`` indicates that the material was thermally treated in helium at 723 K prior to reduction with hydrogen.

Figure 4.1.3 shows the XRD pattern of the Pd/Mg-HSAG catalyst. As can be observed, reflections corresponding to metallic Pd were detected and the diffractogram confirmed that incorporation of Pd NPs during the synthesis procedure converted the MgO in $Mg(OH)_2$, as was previously observed with the bulk Pd/Mg catalyst.

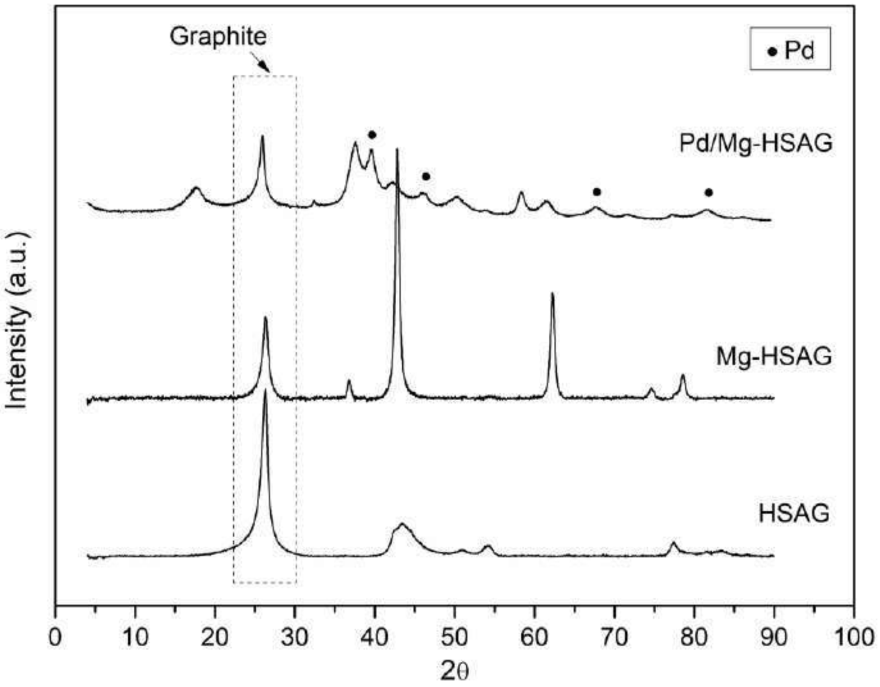

Figure 4.1.3 XRD pattern of Pd/Mg-HSAG catalyst. For comparison the patterns of the Mg-HSAG and HSAG supports are also shown.

Figure 4.1.4 shows the XRD patterns of Pd/Mg and Pd/Mg-HSAG with and without pretreatment in helium at 723 K prior to reduction with hydrogen at 573 K. For both catalysts, the thermal treatment at 723 K after deposition of Pd NPs decomposed $Mg(OH)_2$ to MgO, as the reflections corresponding to $Mg(OH)_2$ disappear. The diffraction patterns show sharper palladium peaks after thermal treatment, implying an increase in particle size, which is more evident for the Pd/Mg-HSAG catalyst.

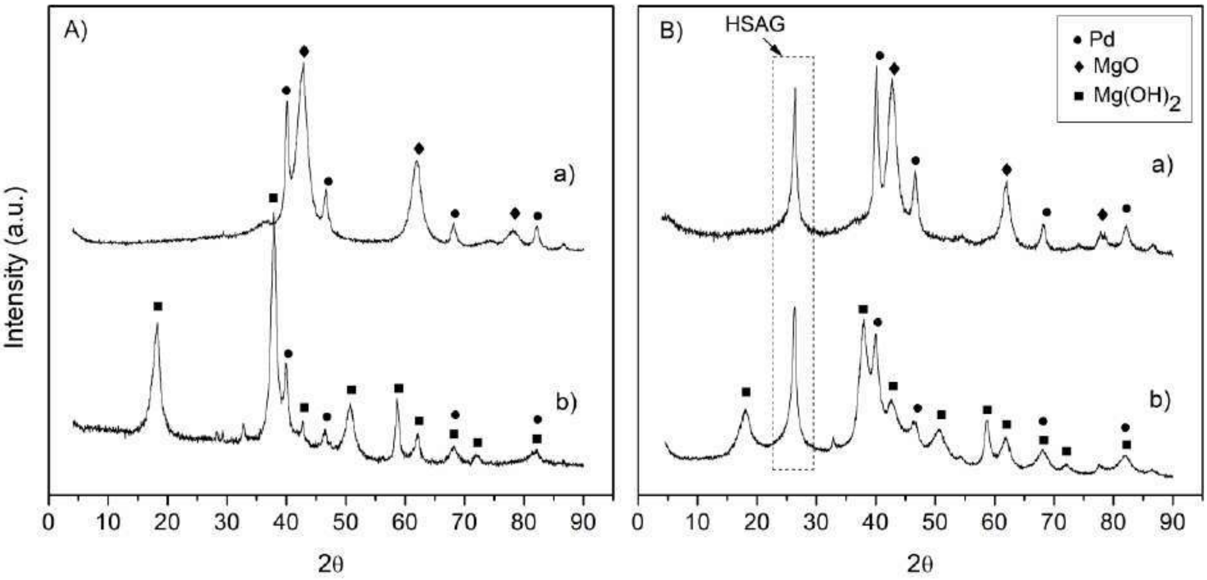

Figure 4.1.4 XRD patterns corresponding to A) Pd/Mg and B) Pd/Mg-HSAG catalysts a) reduced at 573 K and b) thermally treated at 723 K and reduced at 573 K.

4.1.2.2. Surface properties

Figure 4.1.5a shows the evolution of the differential heat of adsorption Q_{diff} of CO_2 with the surface coverage of $Mg(OH)_2$ and MgO. The increase in the CO_2 uptake is accompanied by a continuous decrease in Q_{diff} from initial values around 125 kJ/mol to about 40 kJ/mol; the latter value is attributed to the boundary between chemical and physical CO_2 adsorption [151,152]. The Q_{diff} values indicate the basic strength of the adsorption sites; thus, this value indicates a heterogeneous strength distribution of the basic sites. Considering the differences in the strength of the adsorption sites of CO_2, three types of basic sites have been established: strong basic sites ($Q_{diff} > 90$ KJ/mol), medium-strength basic sites ($90 > Q_{diff} > 60$ KJ/mol) and weak basic sites ($Q_{diff} < 60$ KJ/mol). The total amount of basic sites and the corresponding percentage of each type for each sample are summarized in Table 4.1.3. $Mg(OH)_2$ and MgO have the same total quantity of basic sites and quite similar strength distributions and heats of adsorption, presumably because $Mg(OH)_2$ was degasified at 623 K for 10 h prior to calorimetric measurements, conditions that lead to the formation of MgO, as reveled in the XRD patterns (not shown for the sake of brevity). Although the evolution of the differential heat of adsorption was quite comparable to that of MgO, a decrease in the total amount of basic sites was observed for materials containing Pd (Figure 4.1.5b), which may be due to the hydroxylation of the MgO surface that takes place during incipient wetness impregnation with the acidic aqueous palladium nitrate solution [162]. However, a calorimetry study on Pd/Mg and Pd/Mg-HSAG after thermal treatment at 723 K (Figure 4.1.5c) showed higher heats of adsorption at initial values of surface CO_2 coverage, which implies considerable strengthening of strong basic sites compared with the other samples and even MgO. Probably this effect is due to metal-support interaction at high temperatures, as was previously reported [163,164,165,166,167]. In particular, Ueda et al. [163,164,165] observed that the addition of metals has a remarkable effect on the basic surface of MgO, in which the incorporation of metal atoms causes a distortion in the lattice, an expansion of Mg-O bond length, and localization of electrons on the oxygen atom. As a result, the M-MgO combination exhibits higher basicity.

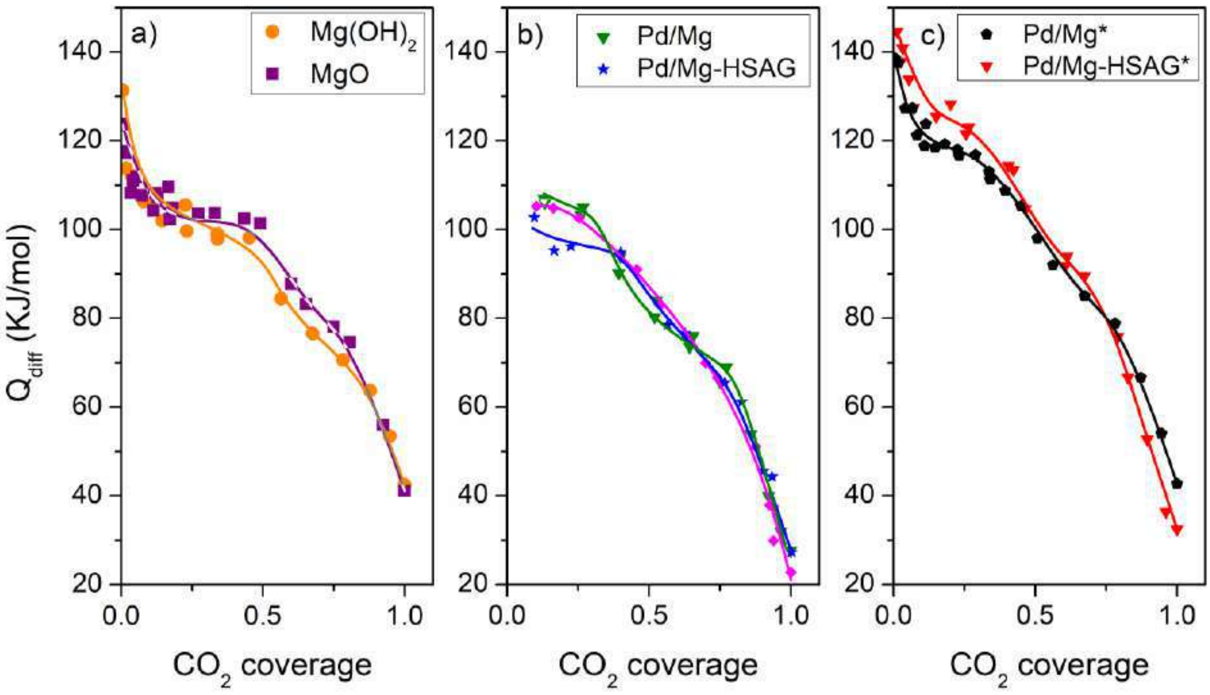

Figure 4.1.5 Differential heats of CO_2 adsorption vs. coverage at 323 K. a) $Mg(OH)_2$ and MgO b) Pd bifunctional catalysts c) Pd bifunctional catalysts. The ``*`` indicates that the material was thermally treated in helium at 723 K prior to reduction with hydrogen.

Table 4.1.3 CO_2 chemisorption capacities at 323 K and type of basic sites.

Sample	Total µmol CO_2/g ($Q_{diff} > 40$ kJ/mol)	Basic sites distribution (%)		
		Strong sites ($Q_{diff} > 90$ kJ/mol)	Medium-strength ($90 > Q_{diff} > 60$ kJ/mol)	Weak-strength ($60 > Q_{diff} > 40$ kJ/mol)
$Mg(OH)_2$	487	51	38	11
MgO	488	58	32	10
Pd/Mg	374	47	41	12
Pd/Mg-HSAG	295	47	38	15
Pd/Mg*	411	61	29	10
Pd/Mg-HSAG*	214	68	22	10

Figure 4.1.6 shows TEM images of the Pd catalysts and the corresponding histograms of the particle size distributions. The TEM images confirmed the formation of metal NPs during the activation process with hydrogen. The Pd catalysts supported on Mg have a Gaussian particle size distribution in which the maximum of the peak coincides with the average Pd particle size. The combination of Pd and Mg gave rise to larger average Pd particle sizes (d=3.5-3.8, Figure 4.1.6b and 4.1.6d) compared with Pd/HSAG (d=2.6 nm, Figure 4.1.6a). Interestingly, Pd/HSAG shows a non-Gaussian particle size distribution, and approximately 45% of the Pd particles have a diameter smaller than 2 nm (Figure 4.1.6a). Additionally, the TEM study confirmed the conclusions drawn from the XRD study, in which Pd peaks of higher intensity were observed for catalysts treated in helium at 723 K. This thermal treatment has a remarkable effect on the particle size and its distribution, considering that both catalysts studied lost their Gaussian particle size distribution and suffered an increase in the average particle size, such that approximately 15% of the particles had a diameter larger than 9 nm.

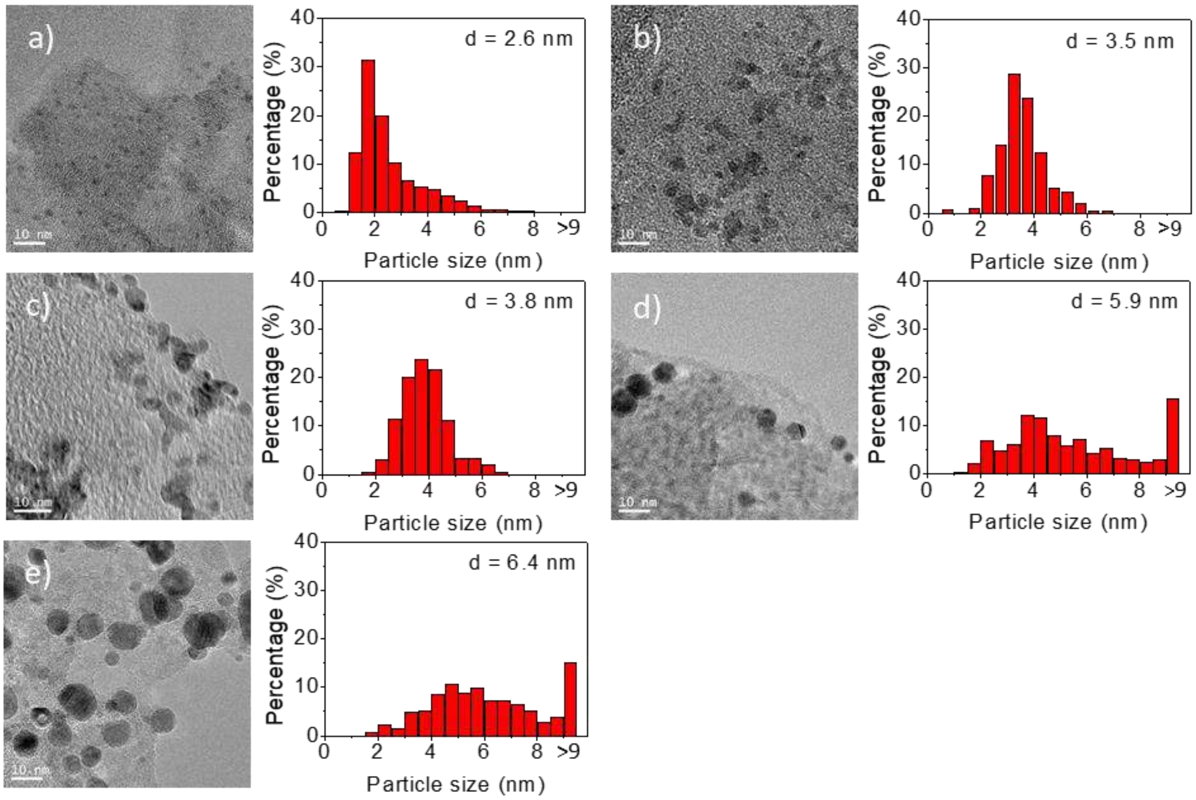

Figure 4.1.6 TEM images and particle size distribution of a) Pd/HSAG, b) Pd/Mg, c) Pd/Mg-HSAG, d) Pd/Mg*, e) Pd/Mg-HSAG* catalysts. The ``*`` indicates that the material was thermally treated in helium at 723 K prior to reduction with hydrogen.

4.1.3. Discussion

The presence of the main reaction products can be explained by the different reaction pathways shown in Figure 1.3.1 and 1.3.2. Briefly, acetaldehyde is the primary dehydrogenation (R1) product which can undergo subsequent condensation reactions: reaction with another two ethanol molecules to form 1,1-diethoxyethane or with another acetaldehyde molecule yielding 3-hydroxybutanal (R2), which is readily dehydrated to 2-butenal (R3). According to the literature, the first condensation is an acid-catalyzed acetylation reaction, [168] while the second is a base-catalyzed aldol condensation [7,57,161]. Subsequent hydrogenation of 2-butenal give rise to the desired product 1-butanol (R4, R5).

1-Butanol can also react with unconverted ethanol to form C6 alcohols such as 1-hexanol, [169] whose presence in our product stream increased with increasing selectivity to 1-butanol. Thus, Pd/Mg, Pd/Mg-HSAG, Pd/Mg* and Pd/Mg-HSAG* show 2, 4, 4 and 5% hexanol selectivity, respectively, whereas the corresponding 1-butanol selectivities are 34, 41, 43 and 54% (Table 4.1.1).

Diethyl ether is the product of the acid-catalyzed direct dehydration of ethanol, [57,103,170] whereas methane and carbon monoxide are obtained by metal-catalyzed decarbonylation of acetaldehyde [56]. The presence of Mg in the Pd catalysts reduces considerably the formation of diethyl ether, methane and carbon monoxide, as can be seen in Table 4.1.1, presumably because the acid sites of the HSAG support are covered by Mg. Moreover, the selectivity for diethyl ether decreases remarkably with Pd catalysts thermally treated in helium at 723 K prior to hydrogen reduction (Table 4.1.1), which is in agreement with the XRD and calorimetry studies, in which it was observed that the interaction of Pd and MgO at this temperature involves strengthening of the basic sites. Thus, the MgO covering the acid sites of the HSAG plays an important role in the decreased acetone formation. This undesired product can be obtained by i) decarbonylation and dehydrogenation of 3-hydroxybutanal, which also leads to formation of carbon monoxide and hydrogen, and ii) ketonization of acetic acid, a hydrolysis product of ethyl acetate [57]. The former reaction is unlikely to take place, as dehydration of 3-hydroxybutanal should predominate. The second route is plausible since carbon dioxide carbon dioxide (the other product of acetic acid ketonization) was detected, whereas acetic acid could not be observed owing to the low sensitivity of the FID detector. Acetone formation is favored with the Pd-HSAG catalyst, whereas the presence of Mg in Pd/Mg-HSAG reduces considerably the amount of this by-product (Table 4.1.1).

The first step in the Guerbet mechanism is dehydrogenation. According to the literature [65,86,116], dehydrogenation of ethanol to acetaldehyde on metal oxides takes place at medium-strength basic Mg^{2+}-O^{2-} pairs, which are predominant in MgO with respect to $Mg(OH)_2$. Aldol condensation of adsorbed acetaldehyde is faster than dehydrogenation [90,171] and also implies acid-base pairs as well as a large quantity of basic sites [65]. The presence of trace amounts of 2-butenal, crotyl alcohol, and butanal among the reaction products suggests that with our catalysts the reaction pathway follows the Guerbet route.

As shown in Table 4.1.1, Mg-HSAG showed negligible conversion, while Pd-HSAG exhibited no selectivity to 1-butanol. According to the catalytic tests, the metal/Mg combination is compulsory to obtain good 1-butanol yields. The incorporation of Pd into MgO greatly improved the catalytic performance in the condensation of ethanol, because transition metals have better dehydrogenation properties than metal oxides [100]. The differences in catalytic performance between Pd/Mg and Pd/Mg-HSAG cannot be ascribed to different basicity properties determined by CO_2 chemisorption, as the two catalysts have similar percentages of strong surface basic sites (47 %). Moreover, the average Pd particle sizes of the two materials are very similar (3.5 and 3.8 nm for Pd/Mg and Pd/Mg-HSAG, respectively). Therefore, we can speculate about some additional effect of the graphite support that was not identified by the characterization techniques used but is observed in the increased catalytic selectivity towards 1-butanol. Likely, the graphite support makes it possible to maximize the interaction between Pd atoms and the strong basic sites of the MgO to form cooperative sites for the tandem reaction. In addition, the Pd/Mg-HSAG catalyst shows a 2-butenal selectivity of 3 %, whereas the selectivity with Pd/Mg is 1 %. This confirms the greater tendency of Pd/Mg-HSAG to catalyze reactions that require coupled Pd atoms and stronger basic surface sites, since 2-butenal is the product of the base-catalyzed aldol condensation of acetaldehyde and an intermediate in the formation of 1-butanol.

Catalyst treated in helium at 723 K, in particular Pd/Mg-HSAG, exhibited the best catalytic behavior in terms of 1-butanol selectivity, which coincides with the tendency observed in Table 4.1.3 whereby these catalysts showed larger amounts of strong basic sites than their counterparts. The selectivity towards 1-butanol increased from 34% with Pd/Mg to 43% after thermal treatment in helium. This effect is even more pronounced with Pd/Mg-HSAG, for which 1-butanol selectivity increases from 41% to 54%, and it is in accordance with results reported for Ni-MgAlO catalysts, [61] which exhibit conversion and selectivity of 19 and 55%, respectively. To rationalize these findings, the type and quantity of active sites involved in the reaction must be analyzed. Concerning basic sites, quite similar distributions of basic strength were found in both catalysts after thermal treatment, as revealed by the Q_{diff} profiles (Figure 4.1.5c), which suggest that both catalysts preserve the nature of the active sites (same strength of basic sites) for the aldol-condensation step. However, the total quantity of strong basic sites measured as chemisorbed CO_2 was 42 % lower in Pd/Mg-HSAG than in Pd/Mg after treatment in helium (Table 4.1.3) at 723 K.

On the basis of the microscopy results and catalytic tests, Pd particle size is not critical to achieve Pd-Mg bifunctionality, but it possibly has an effect on ethanol conversion. It is often claimed that dehydrogenation of ethanol to acetaldehyde is the limiting step in Guerbet reactions, so this would explain the differences between the Pd catalysts. TEM images (Figure 4.1.6) show quite comparable average particle sizes for Pd/Mg and Pd/Mg-HSAG catalysts, which also have fairly similar particle size distributions and ethanol conversion results (Table 4.1.1). Nevertheless, the catalyst treated at 723 K showed a higher average particle size than its counterparts and considerably different conversions: Pd/Mg* has smaller particle size (5.9 nm) than Pd/Mg-HSAG* (6.4 nm), whereas ethanol conversion is higher for the former (25%) than the latter (19%). On the other hand, our Pd catalysts are able to dehydrogenate ethanol at lower reaction temperatures (503 K) than nonmetallic catalysts, for instance, hydroxyapatite, which requires a minimum temperature of 573 K [46].

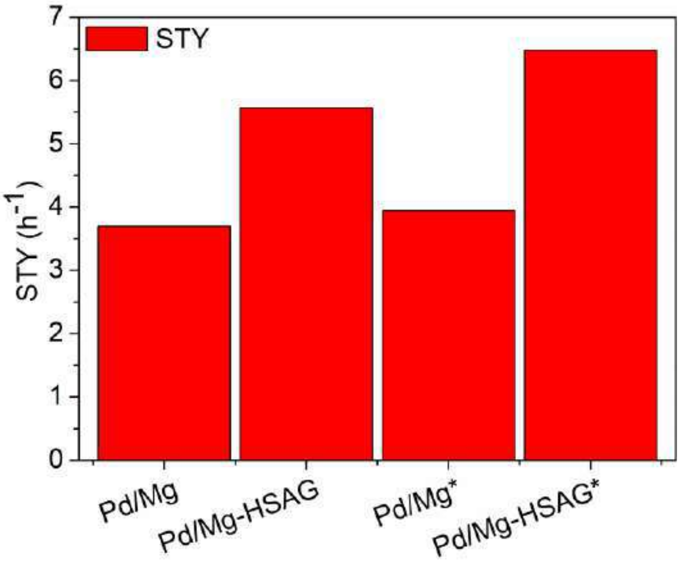

Figure 4.1.7 Site time yield (%) for bifunctional catalyst after 24 hours of reaction. The ``*`` indicates that the material was thermally treated in helium at 723 K prior to reduction with hydrogen.

Figure 4.1.7 shows site-time yields for Pd-Mg catalysts based on the number of strong basic sites per gram. Considerable increase of this parameter is observed when catalysts are supported on HSAG or treated in helium at 723 K in comparison with their counterparts. These tendencies are consistent with 1-butanol selectivity, which has great dependence on the distribution of strong basic sites of the catalyst.

4.1.4. Conclusions

The synthesis of 1-butanol from ethanol by acetaldehyde condensation was studied in a fixed-bed continuous gas-phase reactor with bifunctional heterogeneous catalysts based on Pd NPs and magnesium oxide, which incorporated basic properties and were unsupported or supported on HSAG. Pd/Mg catalysts supported on graphite were the most selective to 1-butanol, and thermal treatment in helium at 723 K played an important role in the selectivity of the catalysts for the Guerbet condensation reaction of ethanol. Characterization of the active sites by microcalorimetric CO_2 chemisorption (revealing basic sites provided by MgO) and TEM analysis (revealing dehydrogenating/hydrogenating properties related to Pd particle size) allowed us to explain the differences in catalytic performance. Catalysts treated in helium at 723 K exhibited the best catalytic behavior in terms of 1-butanol selectivity, in particular Pd/Mg–HSAG*, which has the highest amount of strong basic sites among the catalysts studied, whereas its larger Pd particles have a slightly negative impact on ethanol conversion. As the condensation of ethanol to 1-butanol is a tandem reaction, ethanol conversion is not only dependent on the size of Pd particles, but also on the efficiency of aldol condensation and hydrogenation over more strong basic MgO sites. Thus, the compromise between the two parameters in the catalysts, after adequate thermal treatment, gives rise to higher 1-butanol yields.

4.2. Comparative study on the acidity and basicity of metal oxides for the catalytic conversion of ethanol into 1-butanol

The modification of monometallic copper catalysts supported on high surface area graphite with metal oxides exhibiting different acid/base properties (MgO, BaO, ZnO and MnO) has been studied in order to enhance the yield of 1-butanol in the continuous flow catalytic condensation of ethanol through the Guerbet reaction pathway. The Guerbet reaction is a multi-step process that involves hydrogenation/dehydrogenation reactions as well as base catalyzed aldol condensation and acid catalyzed dehydration, so a bifunctional catalyst that comprise copper as the hydrogenating/dehydrogenating component and a metal oxide with acid/base properties is needed in order to successfully upgrade ethanol to 1-butanol.

4.2.1. Effect of reaction temperature on conversion and selectivity

The influence of temperature on conversion and 1-butanol selectivity in the range 443-573 K is depicted in Figure 4.2.1 for the catalyst 5Cu-Mg/HSAG. The results show that ethanol conversion increases with increasing reaction temperature reaching a value of 70% at 573 K. Nevertheless, 1-butanol selectivity slightly decreases to 14 % at this temperature. It should be noticed that the highest selectivity value (26 %) is achieved at 503 K.

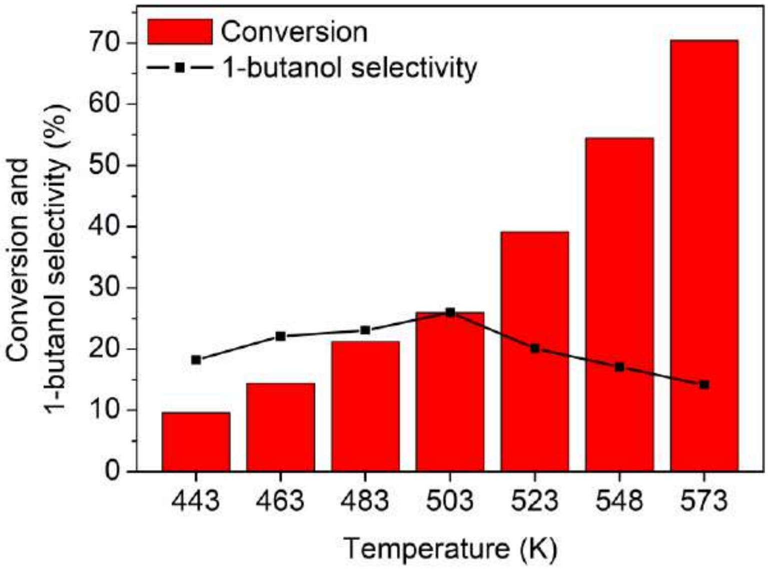

Figure 4.2.1 Variation of ethanol conversion and 1-butanol selectivity as a function of the reaction temperature on catalyst 5Cu-Mg/HSAG.

In order to achieve more insight on the influence of temperature on the product distribution, Figure 4.2.2 illustrates the selectivities of the main products detected for the catalyst 5Cu-Mg/HSAG for each temperature studied: 1-butanol, acetaldehyde, 1,1-diethoxyethane, 2-butanone, 1-hexanol and diethyl ether.

The profiles of the different product selectivities are very similar with others found in literature at a temperature range close to 443-573 K on copper and nickel doped porous oxides and M-Mg-Al mixed oxide catalysts (M = Pd, Ag, Mn, Fe, Cu, Sm, Yb) [52,79]. The 1-butanol selectivity profile reaches a maximum of 26% at 503 K and then decreases to less than 15% at 573 K. This performance was also observed by Quesada et al. [114] and it can be ascribed to the progress of a primary product obtained after successive steps of a global reaction that continues producing undesired by-products at higher temperatures. This study also addressed a decreasing trend of acetaldehyde similar to the profile depicted in Figure 4.2.2 above 503 K, which was also attributed to the evolution of a primary product. On the other hand, the selectivity to 1,1-diethoxyethane increased up to 23% at the expense of acetaldehyde, since it is formed via the acid catalyzed acetylation of acetaldehyde and ethanol [103].

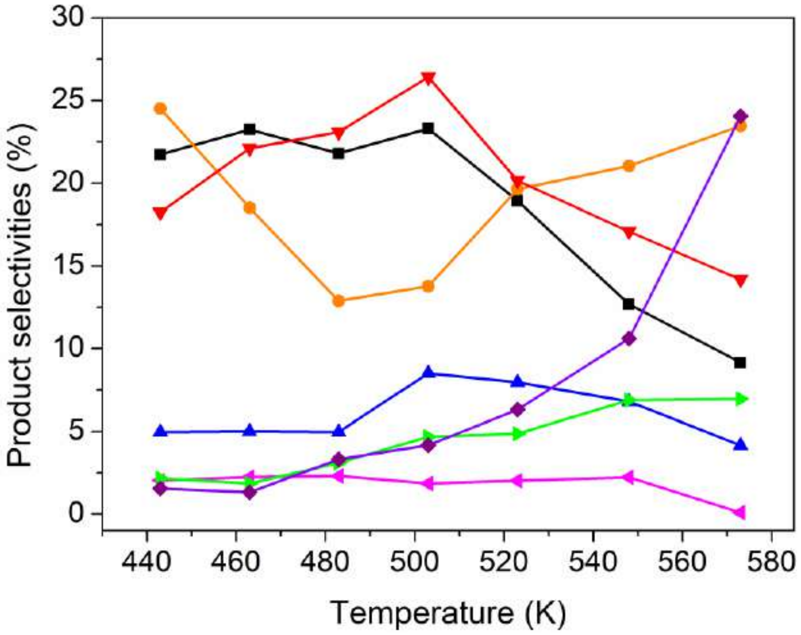

Figure 4.2.2 Analysis of the product distribution as a function of the reaction temperature on the catalyst 5Cu-Mg/HSAG. (▼) 1-butanol, (■) acetaldehyde, (●) diethoxyethane, (▲) 2-butanone, (◀) 1-hexanol, (▶) diethyl ether, (♦) unknowns.

Other minor side products with selectivity values lower than 10% are 2-butanone, 1-hexanol or diethyl ether. The first two exhibit a decreasing trend above 523 K, while the selectivity of diethyl ether increases with reaction temperature as the temperature range studied is not high enough to favor the dehydration of ethanol to ethylene instead of diethyl ether [172].

On the other hand, the selectivity of unknown products, which is lower than 5% at temperatures below 503 K, sharply increases up to 24% at 573 K. Nevertheless, the distribution of products at temperatures below 503 K suggest that the reaction follows the main pathway proposed (Figure 1.3.1).

4.2.2. Reaction results

Given the maximum of 1-butanol selectivity achieved at 503 K with good values of conversion and carbon balance (Figure 4.2.1), the subsequent catalyst screening was therefore performed at this temperature. Before evaluating the performance of the prepared samples in the ethanol condensation, blank experiments in the absence of any catalyst were carried out with the reactor filled with silicon carbide at 503 K. No ethanol conversion was observed, implying that a catalyst is needed for the reaction to take place at this temperature. Preliminary tests with the HSAG support and with the samples Mg/HSAG, Ba/HSAG, Zn/HSAG and Mn/HSAG showed negligible conversion under the reaction conditions used. The catalytic performance of the different samples after 24 hours is summarized in Table 4.2.1. It should be noted that carbon balances for all catalysts were above 90%.

The product distribution strongly depends on the nature of the catalyst used, as can be seen in Table 4.2.1, where 1-butanol, acetaldehyde, 1,1-diethoxyethane and methyl ethyl ketone were the main products detected. The product 1,1-diethoxyethane is formed by the acid catalyzed acetylation of acetaldehyde with two ethanol molecules [54], whereas methyl ethyl ketone could result from crotyl alcohol isomerization or could be the product of deoxygenated 3-hydroxybutanal with subsequent rearrangement [57]. Other products observed in small quantities were 1-hexanol, ethyl acetate, ethylene, diethoxy butane, butanal, 2-butenal, 2-butanol, 2-ethyl-1-butanol, 1-octanol, and 2-ethyl-1-hexanol, which is in good agreement with the reaction pathway and the possible by-products mentioned in the introduction (Figures 1.3.1 and 1.3.2).

Table 4.2.1 Catalytic activity and product selectivities obtained at 503 K and 50 bar after 24 h on stream.

Sample	d (nm)		Conv. (%)	Selectivity (%)					
	Fresh[a]	Used[b]		ButOH	Ac	1,1-DEE	MEK	1-Hex	Others[c]
5Cu/HSAG	4.7	11.1	17	4	52	31	7	0	6
5Cu-Mg/HSAG	7.5	8.9	26	26	23	15	9	2	25
5Cu-Ba/HSAG	7.8	8.9	28	13	23	14	11	1	38
5Cu-Zn/HSAG	7.6	9.6	25	11	25	36	11	1	16
5Cu-Mn/HSAG	8.3	11.7	27	33	26	16	3	4	18

ButOH – 1-Butanol, Ac – Acetaldehyde, 1,1-DEE – 1,1-diethoxyethane, MEK – Methyl ethyl ketone, 1-Hex – 1-hexanol, d – average particle size, determined by TEM of fresh catalysts reduced at 573 K and after 24 hours in reaction. [a] Catalysts reduced at 573 K, [b] After 24 h in reaction. [c] Other products also detected in small quantities: diethyl ether, ethyl acetate, diethoxy butane, 1-octanol, butanal, 2-butenal, 2-butanol, 2-ethyl-1-butanol, 1-octanol, 2-ethyl-1-hexanol, ethylene.

The catalysts were very stable upon 24 hours of reaction in terms of ethanol conversion and 1-butanol selectivity, as it can be observed in Figure 4.2.3. Interestingly, both conversion and selectivity stabilize for all catalysts at hour 3-4, which presumably means that the catalyst undergoes a structural change at early stages of the reaction at 503 K and 50 bar. Afterwards, the reaction achieves the steady state conditions.

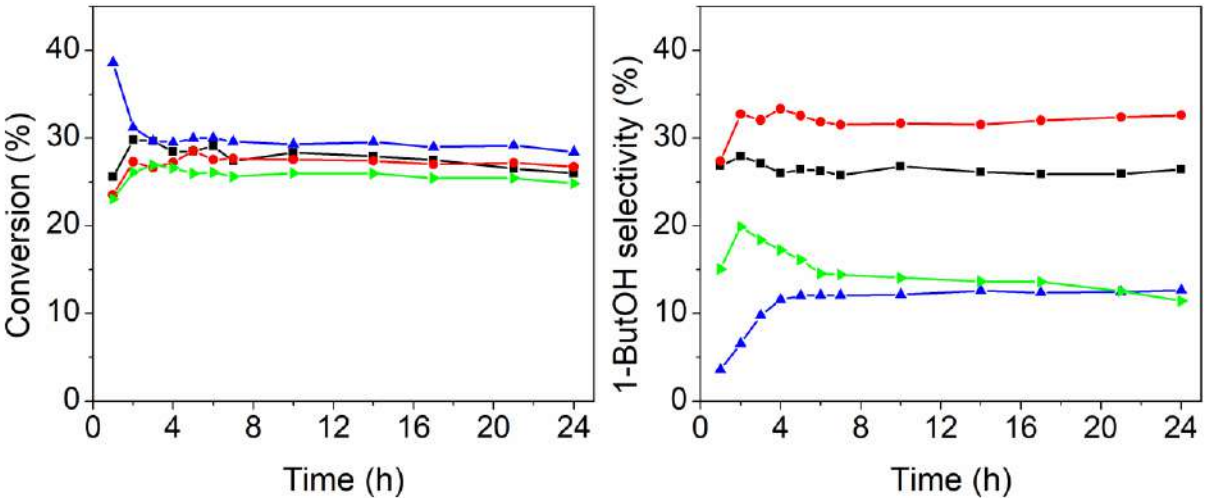

Figure 4.2.3 Conversion and 1-butanol selectivity through 24 hours of reaction for the bifunctional catalysts. (■) 5Cu-Mg/HSAG, (▲) 5Cu-Ba/HSAG, (▶) 5Cu-Zn/HSAG, (●) 5Cu-Mn/HSAG.

4.2.3. Catalysts characterization

4.2.3.1. Structural and textural features

Figure 4.2.4 shows the H_2-TPR profiles of the monometallic Cu catalysts. It should be noted that these analyses were carried out with the fresh catalysts, without any thermal treatment like calcination, therefore the TPR profiles include the reduced products derived from the copper nitrate decomposition. The sample 5Cu/HSAG shows a reduction peak at ca 485 K, whereas the reduction of copper occurs at higher temperatures for the catalysts containing a metal oxide, in the range 515-535 K. According to literature, the reduction of the precursor $Cu(NO_3)_2$ takes place at 535-565 K while the reduction of Cu^{2+} to Cu^0 occurs at 485-520 K [173,174]. Furthermore, the shift to higher temperatures observed for the catalysts containing a metal oxide suggest that copper has stronger interaction with the support when a metal oxide is present since it is known that species harder to reduce are those with stronger interaction with the support

[175]. The sample 5Cu-Ba/HSAG shows an H_2 uptake at 550-700 K that could reflect the decomposition of the barium carbonate formed during ambient exposition as discussed below. Thus, considering the H_2-TPR analysis, the reduction temperature of the catalysts was set at 573 K.

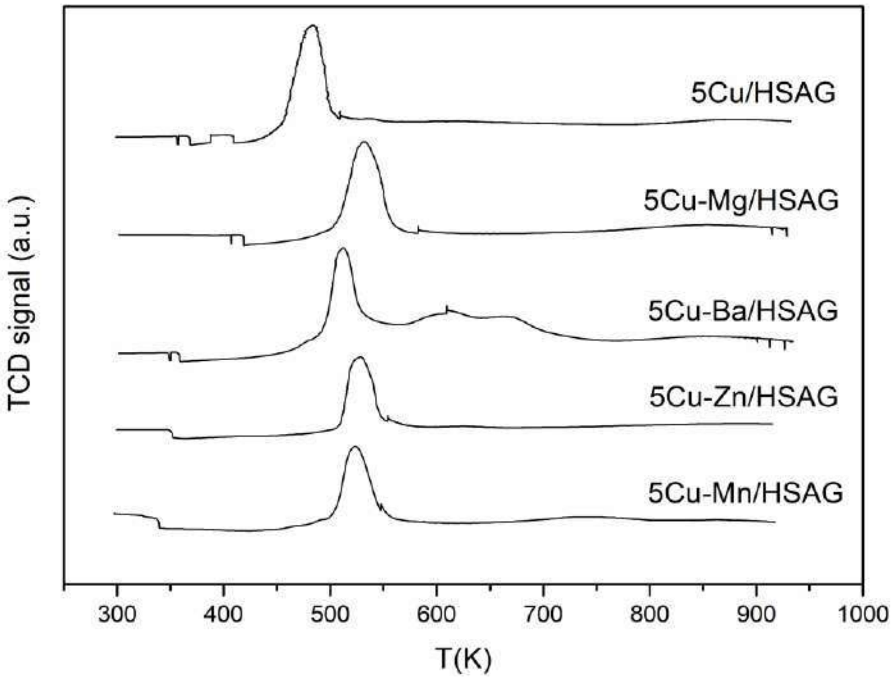

Figure 4.2.4 H_2-TPR profiles of the catalysts samples.

Figure 4.2.5 shows the X-ray diffractograms of the HSAG support and the Mg/HSAG, Ba/HSAG, Zn/HSAG and Mn/HSAG catalysts after thermal treatment. It can be observed that the reflections corresponding to HSAG were detected at 2ϴ of 26.2, 43.9, 54.6 and 77.6º for all samples, whereas no diffraction peak could be ascribed to any magnesium or manganese oxide. However, the peaks corresponding to ZnO (31.8, 34.3, 36.4, 47.5, 57.2, 63.2 and 67.8º) and $BaCO_3$ (23.6, 34.2, 41.6 and 46.5º) were detected for the samples Zn/HSAG and Ba/HSAG, respectively. Barium carbonate was presumably formed upon exposure to moisture in the air at ambient conditions over a prolonged period of time or upon contact with carbonic acid dissolved in liquid H_2O during the incipient wetness impregnation process with the copper nitrate solution, since the reduction temperature applied afterwards, that is 573 K, is not enough to completely decompose the carbonate [140,176,177]. Taking into account that Mg/HSAG, Ba/HSAG, Zn/HSAG and Mn/HSAG contain approximately 1.5wt% of Mg, 5.5wt% of Ba, 3wt% of Zn and 2wt% of Mn, respectively, the results suggest that MgO and MnOx crystallites are either too small or in low concentration to be detected by XRD.

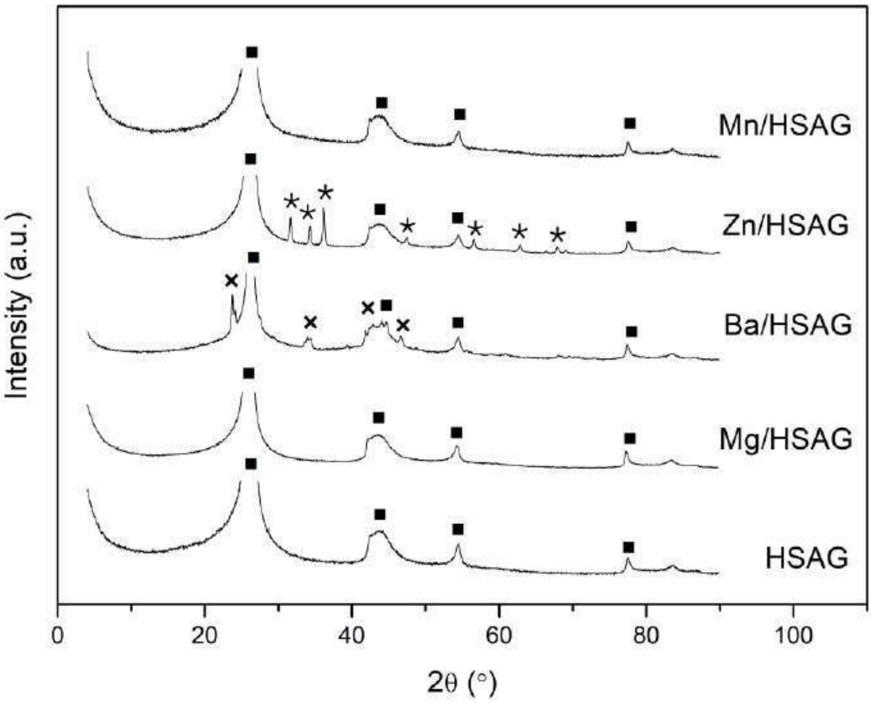

Figure 4.2.5 XRD patterns of the support HSAG and the metal oxide/HSAG catalysts. (■) HSAG, (★) ZnO, (✕) $BaCO_3$.

X-ray diffractograms of the HSAG support and the resulting 5Cu/HSAG and 5Cu-M/HSAG (M = Mg, Ba, Zn, Mn) catalysts reduced at 573 K with hydrogen are shown in Figure 4.2.6a. This time, no reflections corresponding to the metal oxides could be detected except the peaks ascribed to ZnO (31.8, 34.3 and 36.4º) for the sample Zn/HSAG. The diffraction peaks corresponding to HSAG were once again detected for all samples, which implies some uncertainty for the XRD analysis of copper since the main peak characteristic of metallic copper (43.5º) is overlapped by the broad HSAG peak at 2ϴ=43.9º. Nevertheless, the main peak attributed to metallic Cu was detected for all the samples, whereas the characteristic reflections at 2ϴ of 50.4 and 74º could only be detected for the 5Cu-M/HSAG samples (Figure 4.2.6a). It should be noted that the peak at 43.5º is bigger and sharper for the samples containing a metal oxide, especially for 5Cu-Zn/HSAG and 5Cu-Mn/HSAG. The sharpening of a XRD reflection is attributed to bigger size and worse dispersion of the crystallites, so the results suggest that copper nanoparticles seem to become bigger and worse dispersed when a metal oxide is present, especially for ZnO and MnOx, compared to the copper nanoparticles supported on HSAG alone (5Cu/HSAG). However, the reflections corresponding to CuO (35.7º, 38.9º) are perceptible to some extent, especially for the 5Cu-Mg/HSAG sample, indicating that all reduced samples might have suffered a slight surface oxidation due to ambient exposition.

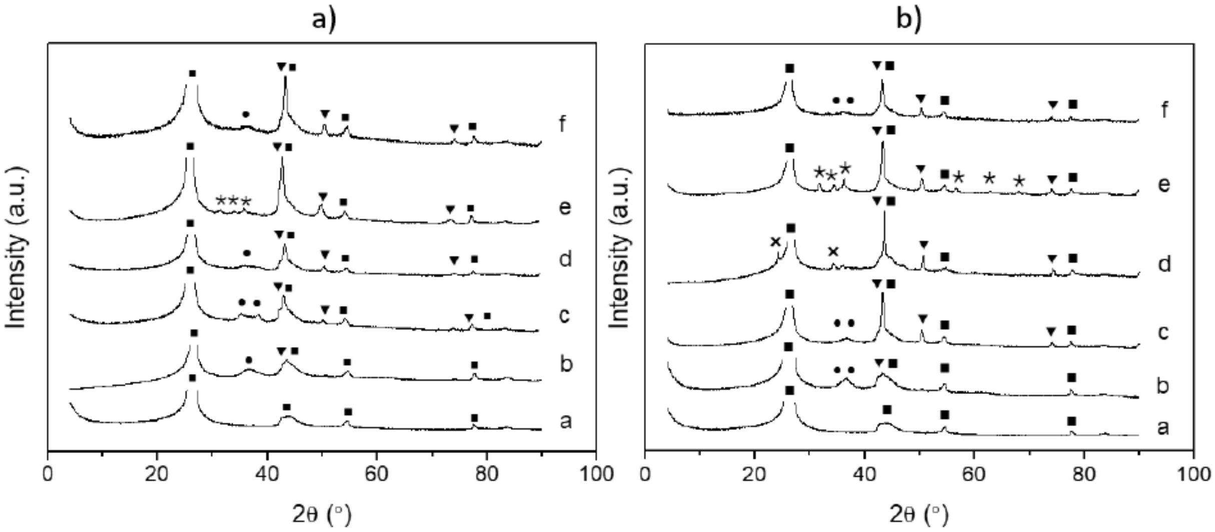

Figure 4.2.6 a) XRD patterns of the support HSAG, 5Cu/HSAG and the bifunctional catalysts reduced at 573 K, b) XRD patterns of the catalysts after reaction, where a) HSAG, b) 5Cu/HSAG, c) 5Cu-Mg/HSAG, d) 5Cu-Ba/HSAG, e) 5Cu-Zn/HSAG and f) Cu-Mn/HSAG. (■) HSAG, (▼) Metallic Cu, (●) CuO, (★) ZnO, (x) $BaCO_3$.

The XRD patterns of the samples after reaction are shown in Figure 4.2.6b. It can be observed that the reflections corresponding to Cu^0 (43.5, 50.4 and 74º) become sharper for the catalysts R-5Cu-Mg/HSAG and R-5Cu-Ba/HSAG compared to their counterparts only reduced in hydrogen at 573 K, which may suggest that the reaction conditions have a negative effect on copper nanoparticles' size and dispersion for those catalysts. On the other hand, the reflections corresponding to CuO (35.7º, 38.9º) for the 5Cu-Mg/HSAG sample become almost imperceptible, which is in agreement with the intensification of the Cu^o main peak. Interestingly, the reflections corresponding to ZnO (31.8, 34.3, 36.4, 57.2, 63.2 and 67.8º) and $BaCO_3$ (23.6 and 34.2º) were detected for the samples Zn/HSAG and Ba/HSAG, respectively, which indicates that ZnO and $BaCO_3$ crystallites become bigger or worse dispersed after reaction.

The specific surface area of the support HSAG, the M/HSAG (M=Mg, Ba, Zn, Mn) after thermal treatment and the 5Cu-M/HSAG catalysts reduced at 573 K are listed in Table 4.2.2. The presence of a metal oxide decreases the BET area in all cases from 396 m^2/g of HSAG to 317 m^2/g of Mg/HSAG, 301 m^2/g of Ba/HSAG, 315 m^2/g of Zn/HSAG and 321 m^2/g of Mn/HSAG. Additionally, the catalysts containing copper present further decrease of the BET area, especially 5Cu-Ba/HSAG (143 m^2/g). Previous studies found in literature [77,178,179] have reported analogous decrease of the specific surface area related to the formation of agglomerates species or large particles covering the support.

Table 4.2.2 Textural parameters of support and reduced catalysts.

Sample	**S_{BET} (m^2/g)**	**Sample**	**S_{BET} (m^2/g)**
HSAG	399	-	-
Mg/HSAG	317	5Cu-Mg/HSAG	270
Ba/HSAG	301	5Cu-Ba/HSAG	143
Zn/HSAG	315	5Cu-Zn/HSAG	294
Mn/HSAG	321	5Cu-Mn/HSAG	236

4.2.3.2. Surface properties

The distribution of acidic sites of the M/HSAG and the bifunctional copper catalysts was determined by temperature-programmed desorption (TPD) of NH_3. All samples were reduced in situ with hydrogen at 573 K. Figure 4.2.7 shows the resulting desorption curves, which where deconvoluted assuming three contributions that peaked at 450, 540 and 625 K, indicating the presence of acid sites with different strengths taking into account that the higher the NH_3 desorption temperature, the stronger the acid sites. In this way, the weak acid sites give rise to a signal between 350-500 K, the peak corresponding to medium strength acid sites appears at 550-550 K, whilst the strong acid sites are associated to a signal at 550-675 K. The association of the acid strength with temperature is in agreement with other scales found in literature for Cu/ZnO catalysts and for Al_2O_3 and SiO_2 as supports [59,178,180]. The deconvoluted peaks of the NH_3-TPD profiles fitted the experimental data quite satisfactorily as depicted in Figure A1.1, which show the fitted curve of the samples. The distribution of acid strength derived from the fitted curves, considering the area of each TPD curve and the ones of the deconvoluted peaks, is shown in Table 4.2.3, as well as the normalized area of each curve in arbitrary units to compare the total acidity of the catalysts.

It is not surprising that the catalyst 5Cu/HSAG shows some acidity since the adsorption of ammonia at copper surfaces has been previously described on literature and metallic Cu nanoparticles are reported to act as a Lewis acid due to their electron-deficient nature [181,182]. Nevertheless, 5Cu/HSAG shows less total acidity, that is the normalized area per gram of sample under each curve in arbitrary units, than the bifunctional catalysts due to the combination of acid sites from the metal oxide and the copper nanoparticles in these latter. Comparing the acid sites distribution of the M/HSAG and the copper bifunctional catalysts (Table 4.2.3), it could be observed that the addition of copper has a direct impact on the strength of the acid sites. For instance, the catalysts Mg/HSAG and 5Cu-Mg/HSAG show relatively uniform acid sites distribution, even though the presence of copper seems to favor the creation of strong acid sites in detriment of the medium and the weak ones (5Cu-Mg/HSAG shows 35% strong acid sites and 34% weak acid sites, while Mg/HSAG shows 29% strong acid sites and 38% weak acid sites, Table 4.2.3). This strengthening of the acid sites when copper is present is also observed for Zn/HSAG and 5Cu-Zn/HSAG, since the percentage of medium-strong acid sites increases from 27-35% for Zn/HSAG to 33-37% for 5Cu-Zn/HSAG. In contrast, the percentage of strong acid sites decreases from 44% for Ba/HSAG to 39% for 5Cu-Ba/HSAG, in benefit of the medium-strength acid sites that increase from 20 to 28%. Interestingly, the addition of copper to the catalyst Mn/HSAG, which shows relatively uniform acid sites distribution with 39% of weak acid sites, considerably weakens the acidity of the catalyst surface since 5Cu-Mn/HSAG exhibits mainly weak acid sites (51%). Although the samples studied exhibit diverse proportions of weak, medium and strong acid sites, their most relevant difference lays on the total acidity. It could be concluded after the observation of Figure 4.2.7 that the bifunctional catalysts have considerably more total amount of acid sites than their counterparts without copper, except 5Cu-Mn/HSAG which exhibits less amount of acid sites than Mn/HSAG. In terms of total acidity, the catalyst with the highest amount of acid sites among the M/HSAG samples is Mn/HSAG followed by Mg/HSAG, Ba/HSAG and Zn/HSAG; while 5Cu-Mg/HSAG shows the highest total acidity among the bifunctional catalysts, followed by 5Cu-Mn/HSAG, 5Cu-Ba/HSAG and 5Cu-Zn/HSAG (Figure 4.2.7 and Table 4.2.3).

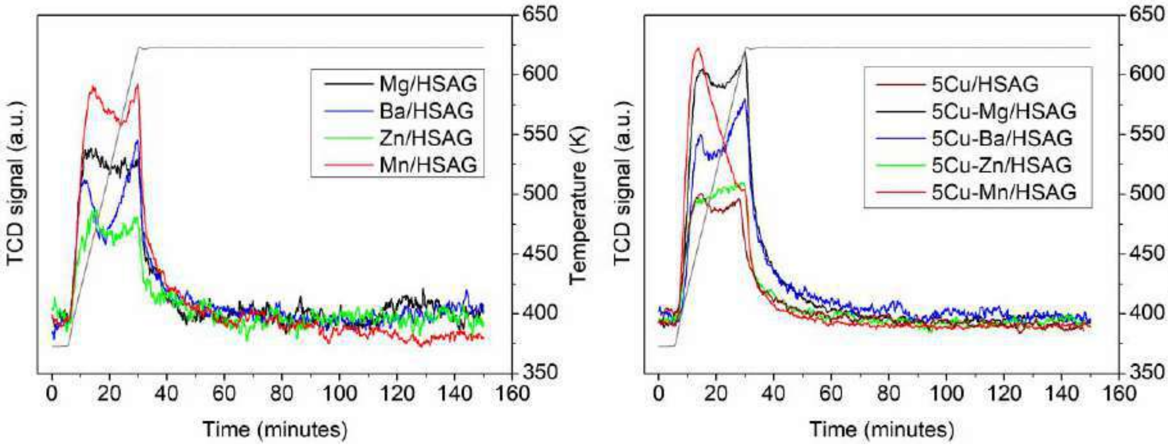

Figure 4.2.7 NH_3-TPD profiles of the M/HSAG (left), 5Cu/HSAG and the bifunctional catalysts (right), where M = Mg, Ba, Zn, Mn.

Table 4.2.3 Acidity distribution derived after deconvolution of the NH_3-TPD profiles.

Sample	NH_3-TPD Area[a] (a.u.)	% Weak acid sites	% Medium acid sites	% Strong acid sites
Mg/HSAG	1.6	38	33	29
Ba/HSAG	1.4	36	20	44
Zn/HSAG	1.0	38	27	35
Mn/HSAG	2.4	39	26	35
5Cu/HSAG	1.3	35	31	34
5Cu-Mg/HSAG	2.6	34	31	35
5Cu-Ba/HSAG	2.0	33	28	39
5Cu-Zn/HSAG	1.4	30	33	37
5Cu-Mn/HSAG	2.0	51	27	22

[a] Normalized per gram of sample.

CO_2 microcalorimetry measurements were conducted to examine the strength and the amount of surface basic sites of the catalysts, in order to determine the effect of the basic properties on the catalytic performance of the bifunctional catalysts in the Guerbet reaction. For comparison purposes and to achieve further understanding on the role of the copper NPs and the metal oxides on the basic properties of the resulting catalysts, the samples 5Cu/HSAG and M/HSAG were also analyzed. Figure 4.2.8 shows the differential heat of adsorption Q_{diff} (KJ/mol) as a function of surface coverage, which can be divided into three regions corresponding with the strength distribution of the basic sites, that is strong (Q_{diff}>90 KJ/mol), medium (90>Q_{diff}>60 KJ/mol) and weak (Q_{diff}<60 KJ/mol), whereas 40 KJ/mol is considered the boundary between chemical and physical CO_2 adsorption [151,152]. Consequently, the amount and the strength distribution of the basic sites are summarized in Table 4.2.4. There was no CO_2 chemisorption and therefore no surface basic sites on 5Cu/HSAG since the obtained Q_{diff} was below 40 KJ/mol for each pulse of CO_2, revealing that physisorption was the only adsorption phenomenon that took place and, for the sake of brevity, the adsorption profile of the sample 5Cu/HSAG is not shown.

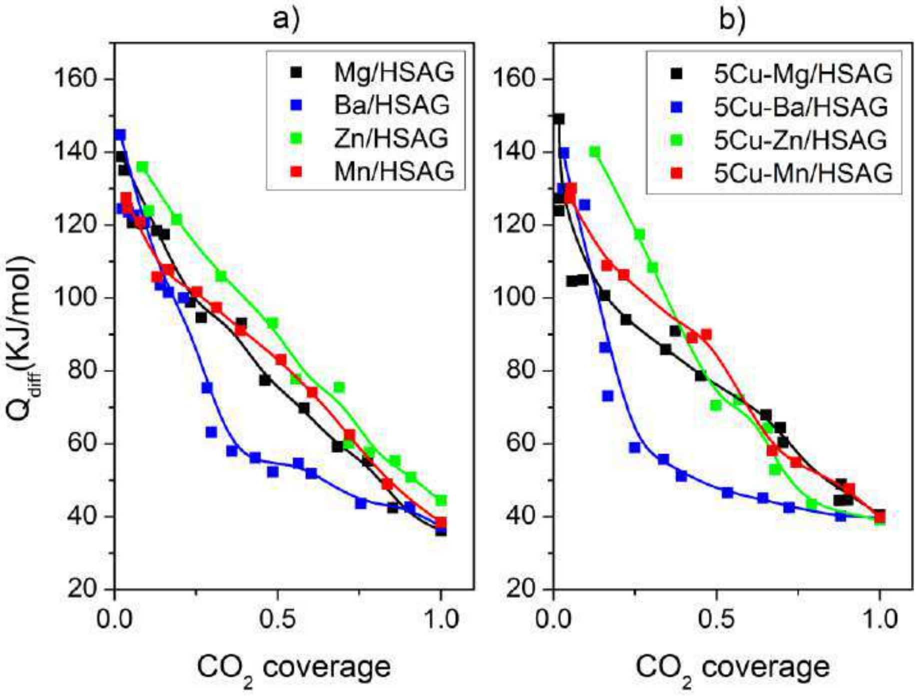

Figure 4.2.8 Differential heats of CO_2 adsorption vs. coverage at 323 K. a) M/HSAG, b) 5Cu-M/HSAG bifunctional catalysts, with M = Mg, Ba, Zn, Mn.

From the analysis of both Figure 4.2.8a and Table 4.2.4, it could be observed that the Mg/HSAG, Zn/HSAG and Mn/HSAG samples present similar strength distribution and heats of adsorption, independently of the total amount of CO_2 adsorbed, with predominance of strong and medium-strength basic sites. However, the strength distribution of Ba/HSAG is completely different, with predominance of weak-strength basic sites (43%) against the low presence of strong basic sites (17%), that might be already carbonated due to the formation of surface

$BaCO_3$ revealed by the XRD analysis. Nevertheless, in terms of total basicity (µmol CO_2 adsorbed/g), the catalysts are ordered as follows: Ba/HSAG > Mg/HSAG > Mn/HSAG > Zn/HSAG. Interestingly, the total amount of basic sites decreases for all the bifunctional catalysts compared with their counterparts without copper, even though their strength distribution remains practically unaltered, except for 5Cu-Mg/HSAG that exhibits predominantly medium-strength basic sites. The decrease of basicity related to the incorporation of copper to the catalyst composition has been reported by Cheng et al. [109], who obtained that the amount of basic sites is much lower on the copper-containing catalysts than on the Cu-free catalyst, namely a MgAlOx mixed oxide. These results point to a surface coverage of the metal oxide nanoparticles by the copper.

Table 4.2.4 CO_2 chemisorption capacities at 323 K and type of basic sites.

Sample	Total µmol CO_2/g (Q_{diff}> 40 kJ/mol)	Basic sites distribution		
		Strong sites µmol CO_2/g (Q_{diff}>90 kJ/mol)	Medium-strength µmol CO_2/g (90>Q_{diff}>60 kJ/mol)	Weak-strength µmol CO_2/g (60>Q_{diff}>40 kJ/mol)
Mg/HSAG	65	26	22	17
Ba/HSAG	71	17	11	43
Zn/HSAG	18	9	5	4
Mn/HSAG	39	16	13	10
5Cu-Mg/HSAG	54	16	24	14
5Cu-Ba/HSAG	32	5	4	22
5Cu-Zn/HSAG	5	2	1	2
5Cu-Mn/HSAG	21	9	5	7

TEM and EDX analysis were also conducted with the aim of identifying the interaction between copper and the metal oxide, the distribution of the nanoparticles on the support and the particle size in 5Cu-M/HSAG catalysts. The obtained TEM images and the corresponding histograms of the particle size distribution are shown in Figure 4.2.9, while the mean particle sizes are collected in Table 4.2.1. For comparison purposes, the sample 5Cu/HSAG was also analyzed. The formation of metallic copper nanoparticles is evidenced for all reduced catalysts, with a diameter that varies from 4.7 nm of 5Cu/HSAG to the range 7.5-8.3 nm for the bifunctional catalysts. Therefore, the TEM analysis confirmed the conclusion derived from the XRD study, that the presence of a metal oxide has a negative impact on the copper particle size, since the bifunctional catalysts present bigger particle size than the reduced 5Cu/HSAG. On the other hand, the average particle size increases for all samples after reaction (Figure 4.2.9, right), irrespective of the catalysts composition, with diameters that range between 8.9 and 11.7 nm. This is in agreement with the XRD results, according to which the XRD patterns of the catalysts after reaction show sharper Cu^0 reflections than the reduced ones.

From the histograms in Figure 4.2.9 it should be highlighted that approximately 10% of the 5Cu/HSAG and 5Cu-Mg/HSAG particles after reaction have a diameter bigger than 15 nm; percentage that escalates to 20-25% for 5Cu-Ba/HSAG, 5Cu-Zn/HSAG and 5Cu-Mn/HSAG. Regarding the reduced catalysts, only the bifunctional ones show copper particles bigger than 15 nm, with a percentage of approximately 5%. Some of these larger copper nanoparticles can be seen in both TEM (Figure 4.2.9) and EDX images (Figure 4.2.10). As expected, the EDX elemental mappings of the reduced bifunctional catalysts show well-defined copper nanoparticles that coincide in space with the corresponding metal oxide on the carbonaceous support, supporting the conclusions drawn from the CO_2 adsorption microcalorimetry measurements.

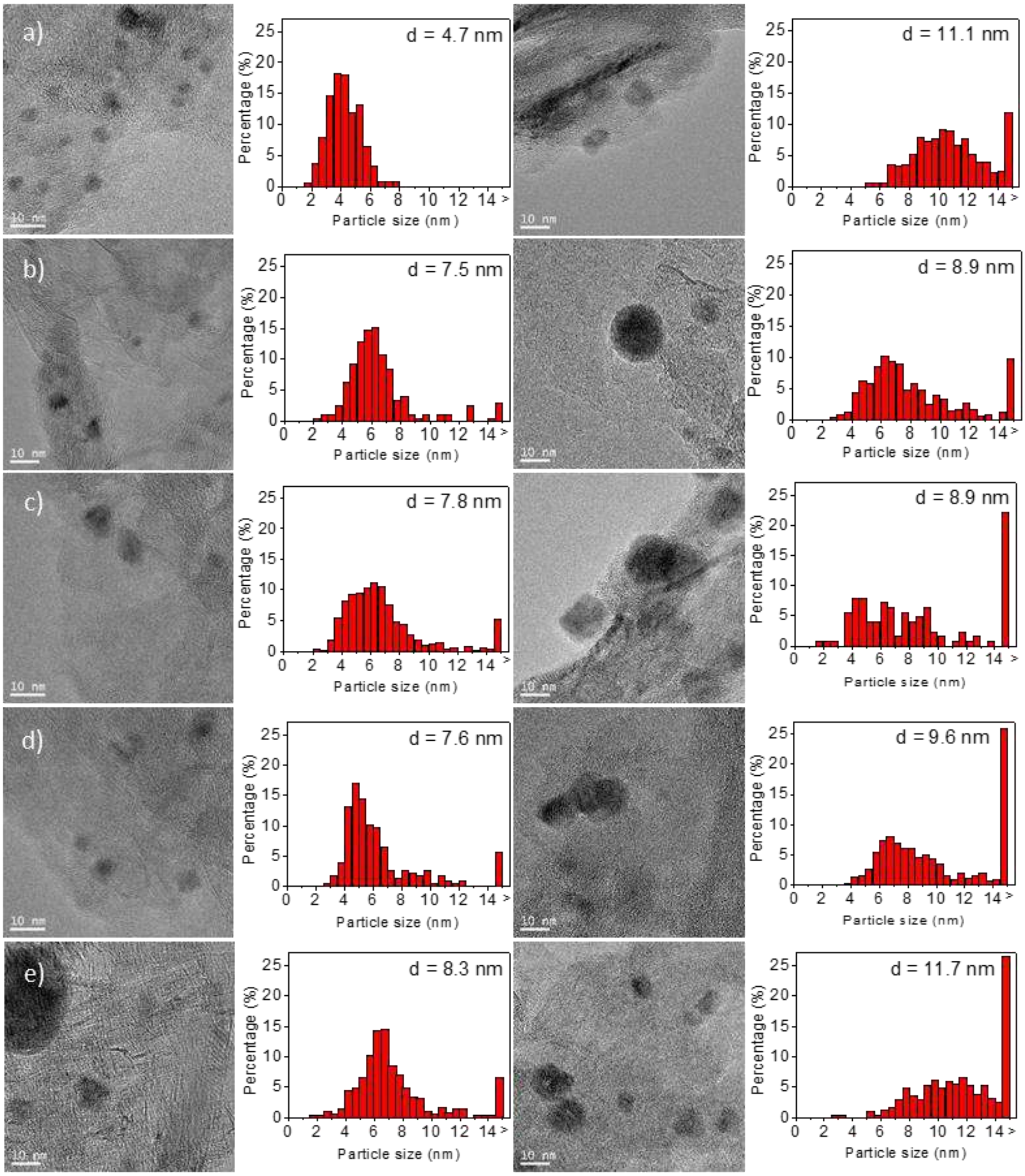

Figure 4.2.9 TEM images of catalysts reduced with hydrogen (left) and after reaction (right): a) 5Cu/HSAG, b) 5Cu-Mg/HSAG, c) 5Cu-Ba/HSAG, d) 5Cu-Zn/HSAG, e) 5Cu-Mn/HSAG.

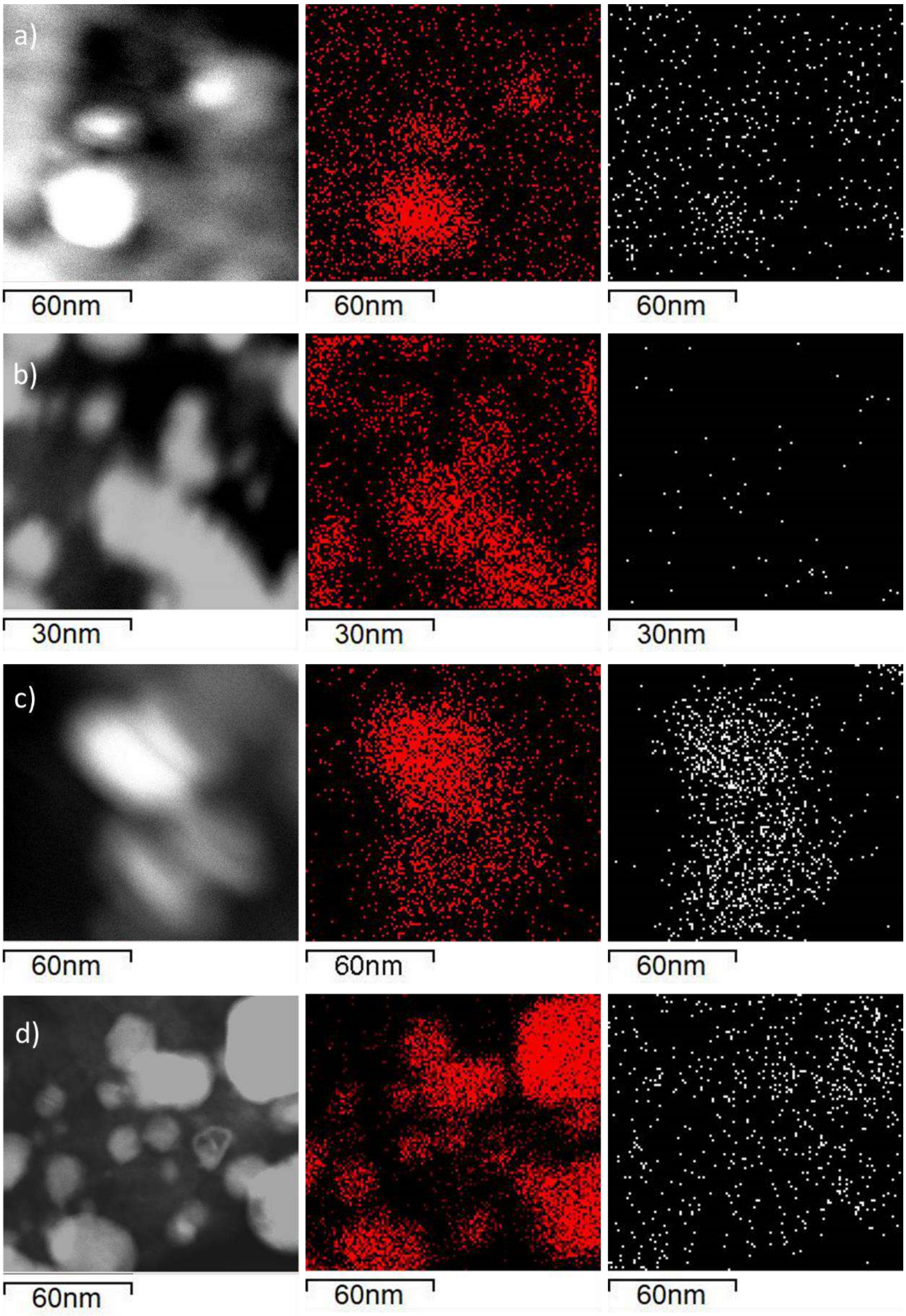

Figure 4.2.10 EDX elemental mapping of catalysts reduced in hydrogen at 573 K: a) 5Cu-Mg/HSAG, b) 5Cu-Ba/HSAG, c) 5Cu-Zn/HSAG, d) 5Cu-Mn/HSAG. Color code refers to the distribution of elements (Cu, red; Metal oxide, white).

4.2.4. Discussion

Henceforth, the reaction results and the extensive analysis derived from the characterization techniques will be discussed in order to evaluate the benefits of tuning the catalysts composition with a metal oxide, regarding the ethanol condensation towards 1-butanol. Since the synergistic interaction between copper as a metallic function and metal oxides with acid/base properties has been previously demonstrated [39,54,108,109], the aim of the discussion is to discern which metal oxide is the most suitable among the studied ones considering their acid/base sites and the copper particle size of the resulting catalyst. First of all, it should be noted that all bifunctional 5Cu-M/HSAG catalysts studied present similar conversion levels, in the range 25-28%, which constitutes an improvement against the 17% obtained with 5Cu/HSAG. Moreover, it is concerning 1-butanol selectivity where the presence of a metal oxide in the catalyst composition significantly improves the catalytic performance from the selectivity level of 11% obtained with 5Cu-Zn/HSAG to the 33% with 5Cu-Mn/HSAG, whereas the catalyst Cu/HSAG only reach a modest 4% (Table 4.2.1). It is therefore clear that both copper and the acid/base sites of the metal oxide need to work cooperatively, since neither function is capable of effectively upgrade ethanol to 1-butanol on their own.

In the light of the results, there is no doubt that the bifunctional catalysts have improved the catalytic performance in the Guerbet reaction compared to their counterpart without a metal oxide. Previous studies have attributed the reasons behind this synergistic behavior to the exposed copper sites that catalyze the dehydrogenation/hydrogenation reactions, in unison with the acid/base sites provided by the metal oxide, which catalyze the dehydration of 3-hydroxybutanal (Figure 1.3.1, R3) and the aldol condensation (R2), respectively [67,183]. Furthermore, copper is widely recognized for catalyzing the dehydrogenation of ethanol towards acetaldehyde [52], the first step of the Guerbet reaction, which is consistent with the acetaldehyde selectivity of 52% obtained with the catalyst Cu/HSAG. However, the observed sintering of copper particles (Figure 4.2.9) does not seem to be crucial to significantly influence on the ethanol conversion, since all bifunctional catalysts present similar conversion levels despite exhibiting different values of copper particle size, whereas the sample 5Cu/HSAG undergoes the most substantial change in its particle size at early stages of the reaction which reflects on a conversion decrease to 17%.

Regarding which metal oxide is the most suitable for the Guerbet reaction, the results evidence that manganese oxide and magnesium oxide further improve the catalytic performance among the metal oxides studied, with conversion levels of 27 and 26% and 1-butanol selectivity levels of 33 and 26%, respectively (Table 4.2.1). Interestingly, the 1-butanol selectivity increases for the catalysts with the highest total acidity (5Cu-Mg/HSAG, 5Cu-Mn/HSAG and 5Cu-Ba/HSAG, Table 4.2.3). Although 5Cu-Mn/HSAG and 5Cu-Ba/HSAG present the same total acidity, their differences in the 1-butanol selectivity could be ascribed to their strength distribution, since the former has predominantly weak acid sites (51%, Table 4.2.3) while the latter shows relatively uniform acid sites distribution with 39% of strong acid sites. Considering the acid strength distribution of the bifunctional catalysts, it seems that a high concentration of weak acid sites has a beneficial effect on the 1-butanol selectivity, since the catalyst 5Cu-Mn/HSAG has the highest percentage of weak acid sites (51%, Table 4.2.3) and also exhibits the greatest 1-butanol selectivity (33%), followed by 5Cu-Mg/HSAG (26% 1-butanol selectivity, 34% weak acid sites), 5Cu-Ba/HSAG (13% 1-butanol selectivity, 33% weak acid sites) and 5Cu-Zn/HSAG (11% 1-butanol selectivity, 30% weak acid sites). Therefore, it could be concluded that the presence of medium-weak strength acid sites seems compulsory for catalyzing the ethanol dehydration of 3-hydroxybutanal and thus improving the 1-butanol yield.

On the other hand, after analyzing the basic properties and the catalytic performance of each catalyst, some correlations can be found regarding the amount of basic sites and their strength with the 1-butanol selectivity. In this sense, the catalyst 5Cu-Zn/HSAG contains an insignificant amount of basic sites (5 µmol CO_2 chemisorbed/g, 2 µmol/g of high strength, Table 4.2.4), being also the least selective catalyst (11%), whereas 5Cu-Mg/HSAG has the highest amount of basic sites (54 µmol CO_2 chemisorbed/g, 16 µmol/g of high strength), followed by 5Cu-Ba/HSAG (32 µmol CO_2 chemisorbed/g, 5/g µmol of high strength) and 5Cu-Mn/HSAG (21 µmol CO_2 chemisorbed/g, 9 µmol/g of high strength). Although 5Cu-Ba/HSAG is the second catalyst with the largest amount of basic sites, its 1-butanol selectivity is practically as low (13%) as the one achieved with 5Cu-Zn/HSAG. This apparent contradiction is in fact a revealing indication of the relevance that the basic strength has along with the total amount of basic sites, since 22 µmol/g, that is, the 71% of the 5Cu-Ba/HSAG basic sites, have weak strength. Moreover, the catalysts 5Cu-Mn/HSAG and 5Cu-Mg/HSAG contain 9 µmol/g (44%) and 16 µmol/g (29%) of strong basic sites, respectively, which might explain their differences on the 1-butanol selectivity. Therefore, it could be concluded that the metal function combined with a good equilibrium between medium-high strength basic sites and medium-weak strength acidity is compulsory to satisfactorily upgrade ethanol towards 1-butanol, even though it is commonly acknowledged that the increase of 1-butanol selectivity is related to the presence of high strength basic sites [21,54,55,169].

The metal oxide and the acid/base properties of the resulting catalyst not only have an impact on the selectivity towards 1-butanol but also on the product distribution and potential undesired compounds. For example, the formation of 1,1-diethoxyethane is generally attributed to acid sites [54], which is in agreement with the 31 and 36% of selectivity achieved with Cu/HSAG and 5Cu-Zn/HSAG, respectively, while the rest of the bifunctional catalysts reduce its formation by half. Bearing in mind the results derived from the NH_3-TPD and CO_2 chemisorption techniques, the fact that the bifunctional catalysts considerable reduced the formation of 1,1-diethoxyethane compared to Cu/HSAG, might be ascribed to the introduction of basic sites and that the metal oxide covers the acid sites of the HSAG that catalyze the acetylation of acetaldehyde with two ethanol molecules that leads to 1,1-diethoxyethane. Given that the catalyst 5Cu-Zn/HSAG has an insignificant amount of basic sites and therefore is constituted predominantly by acid sites, it is not surprising that its selectivity towards 1,1-diethoxyethane was very similar to that of Cu/HSAG.

To sum up, although the acid/base sites of the final catalyst play a relevant role on the Guerbet reaction, there is no doubt about the importance of the metal function on the 1-butanol yields, since all of the M/HSAG catalysts ended up showing negligible ethanol conversion. Therefore, the site time yield towards 1-butanol was calculated (Figure 4.2.11) for Cu/HSAG and the bifunctional catalysts based on the number of copper atoms on the surface per gram. Figure 4.2.11 clearly illustrates that the copper sites exposed are optimal for the catalysts 5Cu-Mn/HSAG and 5Cu-Mg/HSAG followed by their counterpart with BaO and ZnO as the metal oxide, whereas the copper sites exposed are not enough to satisfactorily upgrade ethanol towards 1-butanol in the absence of a metal oxide.

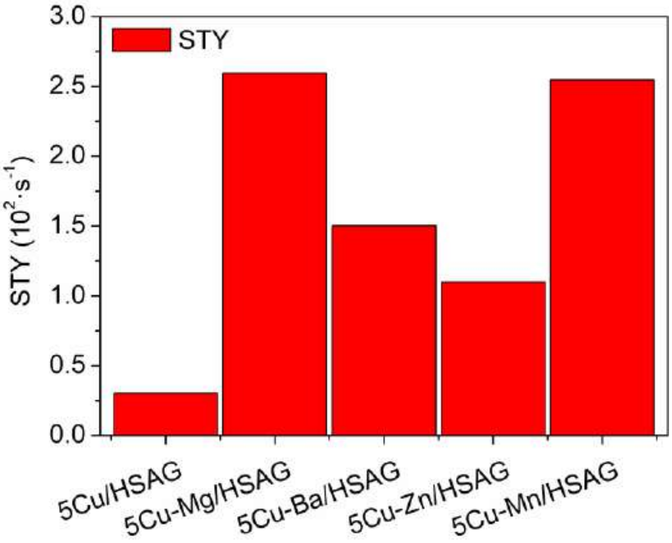

Figure 4.2.11 Site time yield (s^{-1}) for Cu/HSAG and the bifunctional catalyst after 7 hours of reaction.

4.2.5. Conclusions

Heterogeneous bifunctional catalysts based on copper nanoparticles and a metal oxide, namely MgO, BaO, ZnO or MnO, supported on high surface area graphite were tested in the continuous gas phase ethanol conversion towards 1-butanol, commonly known as Guerbet reaction. The catalysts showed different catalytic behavior which was tried to be explained by characterization of the active copper nanoparticles along with the acidity and basicity properties of the resulting catalysts by TEM/EDX analysis, temperature-programmed desorption of NH_3 and microcalorimetry of CO_2 chemisorption. All in all, high 1-butanol yields can be ascribed to the synergistic effect between the acid/base sites provided by the metal oxide, which catalyze the dehydration of 3-hydroxybutanal and the aldol condensation, respectively, and the active copper nanoparticles, that catalyze the dehydrogenation/hydrogenation reactions. In this sense, the exposed copper sites are optimal for the catalyst 5Cu-Mg/HSAG, with a site time yield towards 1-butanol of $2.6\cdot10^{2}$ s^{-1}, closely followed by 5Cu-Mn/HSAG, with a site time yield towards 1-butanol of $2.55\cdot10^{2}$ s^{-1}, in contrast to their counterparts with BaO and ZnO as the metal oxide, thanks to a good equilibrium between medium-high strength basic sites and medium-weak strength acid sites. The catalytic enhancement achieved with the bifunctional catalysts and the low performance of Cu/HSAG in terms of 1-butanol selectivity suggest that the presence of a metal oxide seems compulsory to efficiently upgrade ethanol towards 1-butanol. Finally, all catalysts remained active for 24 h on stream, verifying their stability, while the analysis of the product distributions showed that the reaction follows the Guerbet route.

4.3. Optimization of Cu-Ni-Mn-catalysts for the conversion of ethanol to butanol

In this chapter, the catalytic coupling of ethanol into 1-butanol through the Guerbet reaction was studied in a fixed bed reactor over different catalytic systems based on Cu and/or Ni as a hydrogenating/dehydrogenating components, and manganese oxide incorporating acid/base properties on a carbonaceous support, high surface area graphite (HSAG).

4.3.1. Reaction results

Blank experiments verified the absence of reaction at 503 K either with the empty reactor or filled with silicon carbide, hence a catalyst is needed for the reaction to take place. For the different samples, the results obtained in the catalytic reaction, once the steady state was reached, are shown in Table 4.3.1. Carbon balances for all samples were above 90%. Preliminary tests with the HSAG support and with Mn/HSAG sample show that these are inactive under the reaction conditions used.

Table 4.3.1 Catalytic activity and product selectivities obtained at 503 K and 50 bar after 24 h on stream.

Sample	d (nm)[a]		Conv. (%)	Selectivity (%)					
	Fresh	Used		ButOH	Ac	CO	CH_4	1,1-DEE	Others[b]
Mn/HSAG	-	-	0.1	0	2	0	0	0	98
Cu/HSAG	4.7	11.1	17	4	52	0	0	31	13
Ni/HSAG	4.9	8.9	23	7	24	15	25	1	28
2.5Cu2.5Ni/HSAG	3.9	6.7	20	4	37	12	18	6	23
5Cu-Mn/HSAG	8.3	11.7	27	33	26	0	0	16	25
5Ni-Mn/HSAG	5.3	6.0	45	21	11	10	21	2	35
4Cu1Ni-Mn/HSAG	5.3	8.0	36	35	16	6	8	8	27
2.5Cu2.5Ni-Mn/HSAG	7.6	7.8	37	36	13	7	10	3	31
2.5Cu2.5Ni-Mn/HSAG*	7.4	11.5	30	39	19	5	6	4	27

Ac – Acetaldehyde, 1,1-DEE – 1,1-diethoxyethane, ButOH – 1-Butanol. [a]Average particle size determined by TEM of fresh catalysts reduced at 573 K, except Ni/HSAG and 5Ni-Mn/HSAG that were reduced at 723 K, and after 24 h in reaction. [b] Other products also detected in small quantities: diethyl ether, ethyl acetate, 2-butanona, diethoxybutane, 1-octanol, butanal, 2-butenal, 2-butanol, 2-ethyl-1-butanol, 1-octanol, 2-ethyl-1-hexanol, ethylene, ethane, acetone, propane, pentane. The ``*`` indicates that the material was thermally treated in helium at 723 K prior to reduction with hydrogen.

As a general trend, the main products detected were 1-butanol, acetaldehyde, 1,1-diethoxyethane, carbon monoxide and methane, while other products observed in small quantities were ethyl acetate, 2-butanone, acetone, ethylene, ethane, pentane, propane, diethoxybutane, butanal, 2-butenal, 2-butanol, 2-ethyl-1-butanol, 1-hexanol, 1-octanol and 2-ethyl-1-hexanol. The proposed reaction pathways leading to these compounds can be found in Figure 1.3.2. The presence of these compounds in the product stream is quite common for this condensation reaction, as can be seen by reviewing literature, although the relative amount of these compounds in the product distribution presents strong variations depending on the catalyst used. For example, 1,1-diethoxyethane, ethyl acetate and other higher alcohols such as 1-hexanol and 1-octanol are the most common by-products [50,52,83,101], although acetone, ethylene, propane, pentane, butane and butenes are also reported for this reaction [51,52,57,72,78,170].

The catalysts were studied during 24 h of reaction and proved to be very stable in terms of conversion and 1-butanol selectivity. Figure 4.3.1 shows that all catalysts reach a maximum in conversion at hour 3-4, followed by a slight deactivation. Nevertheless, after 10 h the reaction achieves the steady state conditions.

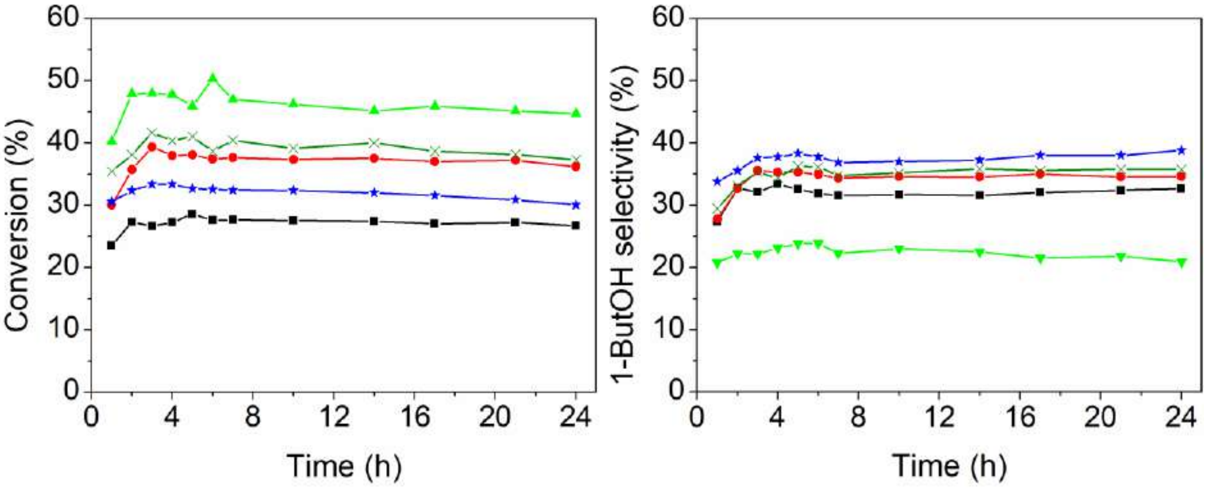

Figure 4.3.1 Conversion and 1-butanol selectivity through 24 h of reaction. The ``*`` indicates that the material was thermally treated in helium at 723 K prior to reduction with hydrogen. (■) 5Cu-Mn/HSAG, (▲) 5Ni-Mn/HSAG, (●) 4Cu1Ni-Mn/HSAG, (x) 2.5Cu2.5Ni-Mn/HSAG, (★) 2.5Cu2.5Ni-Mn/HSAG*.

4.3.2. Catalysts characterization

4.3.2.1. Structural and textural features

The H_2-TPR profiles of the catalysts are represented in Figure 4.3.2. These samples were not subjected to any pretreatment like calcination and therefore it must be taken into account that these profiles also include the reduction of some products derived from the metal precursor decomposition. The samples 5Cu/HSAG and 5Cu-Mn/HSAG show a reduction peak at 485 K and 520 K, respectively, corresponding to the reduction of Cu^{2+} to Cu^0 [174,184,185]. Interestingly, the presence of manganese shifts the reduction of copper at higher temperatures, suggesting close interaction between the copper and the manganese oxide since species harder to reduce are those with stronger interaction with metal oxides, according to literature [174,186,187,188]. On the other hand, catalysts 5Ni/HSAG and 5Ni-Mn/HSAG show the opposite behavior with two reduction peaks, the first one sharper at 540 K and the second one in the range 585–685 K for 5Ni/HSAG, while 5Ni-Mn/HSAG shows the first peak at 525 K and the second one in the range 595–780 K. These TPR profiles are in accordance with others studies found in literature with Ni supported on CNT [185] and HSAG [189,190], where the first sharp peak is due to the reduction of dispersed Ni^{2+} and the second broad one is attributed to the reduction of remaining Ni^{2+} in addition to gasification of carbon atoms in the vicinity of the nickel particles, which catalyze this reaction producing methane. Catalysts containing both copper and nickel show the first sharp peak at lower temperatures the more %wt of copper is present, meanwhile the second broad peak is smoother and almost indistinguishable for 4Cu1Ni-Mn/HSAG. There is no appreciable contribution of manganese oxide reduction since the TPR profiles of samples 5Cu/HSAG, 5Ni/HSAG and 2.5Cu2.5Ni/HSAG and their counterparts with manganese are practically identical in shape although they are displaced in the X axis as a result of changes in the dispersion state when supported on Mn/HSAG. Given that manganese (II) nitrate was used as a precursor and that Mn/HSAG was treated in helium at 673 K, the oxidation state expected for manganese is Mn^{2+} and therefore no reduction profile could be attributed to higher oxidation states of manganese. Bearing in mind these profiles, reduction temperature was set at 573 K for the catalysts containing copper and 723 K for those containing only nickel.

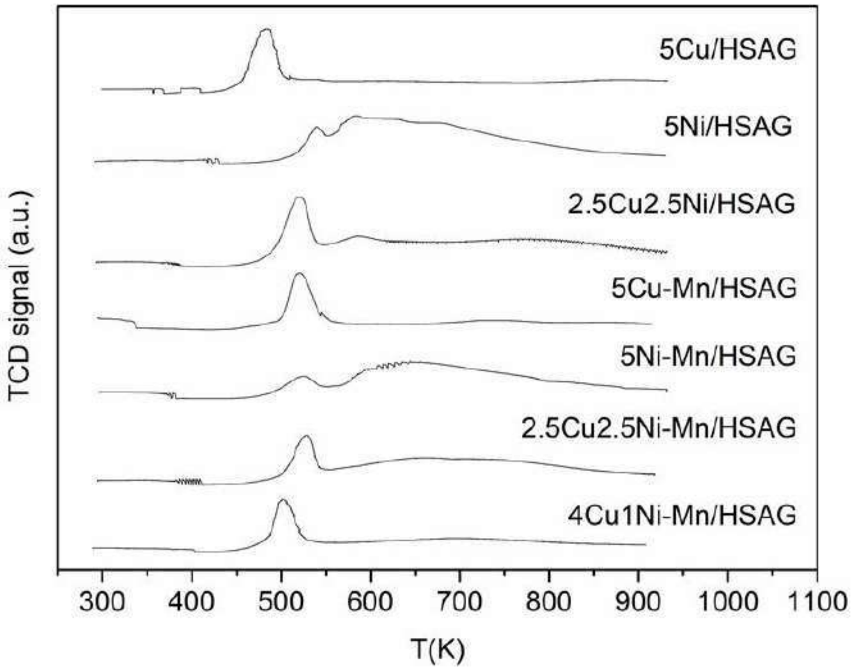

Figure 4.3.2 H_2-TPR profiles of the catalysts samples.

Figure 4.3.3 represents the X-ray diffraction patterns of the HSAG support and the resulting metal/HSAG and metal-Mn/HSAG catalysts reduced at 573 K with hydrogen, except 5Ni/HSAG and 5Ni-Mn/HSAG catalysts that were reduced at 723 K. Sample 2.5Cu2.5Ni-Mn/HSAG was also studied after thermal treatment at 723 K and reduction with hydrogen, even though its XRD pattern is not shown for the sake of brevity since the diffractogram is practically identical to the same sample only reduced in hydrogen. As can be observed in Figure 4.3.3, no diffraction peak could be ascribed to any manganese oxide suggesting that MnOx crystallites are either too small or in low concentration to be detected by XRD. These results are expected since all samples contain approximately 2 wt% of Mn. The reflections corresponding to HSAG were detected at 2θ of 26.2, 43.9, 54.6 and 77.6° for all samples. It must be taken into account that the broad peak at $2\theta = 43.9°$ overlaps the highest distinct peaks of metallic copper (43.5°) and nickel (44.4°). However, reflections corresponding to metallic Cu were detected in the metal-Mn/HSAG catalysts and they were only discernible in the 5Cu/HSAG and 2.5Cu2.5Ni/HSAG samples, whereas the peak of higher intensity corresponding to metallic Ni is slightly perceptible in the samples with Ni alone (5Ni/HSAG and 5Ni-Mn/HSAG), implying that the incorporation of manganese to the carbonaceous support produce bigger particle size and worse dispersion of the copper nanoparticles than the HSAG alone. XRD patterns of reduced 5Cu/HSAG, 5Cu-Mn/HSAG and 5Ni-Mn/HSAG catalysts suggest that these samples might have suffered a slight surface oxidation due to ambient exposition since the peaks of CuO (35.7°, 38.9°) and NiO (37.4°, 43.5°) are perceptible to some extent.

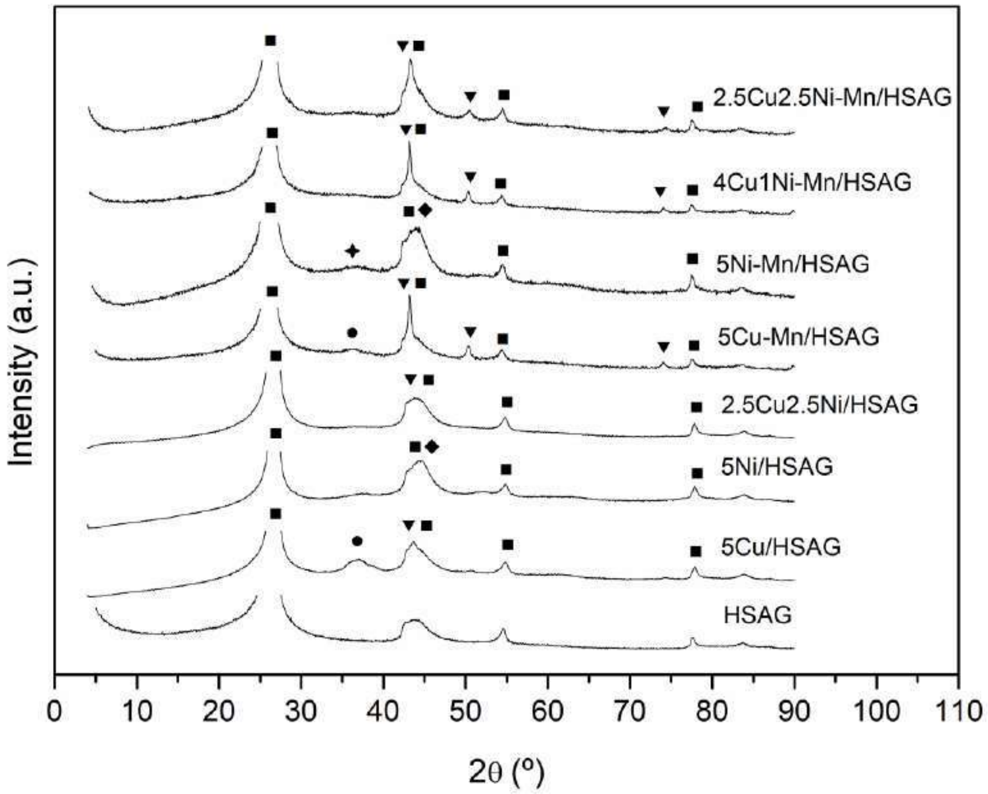

Figure 4.3.3 XRD patterns of the support HSAG and the reduced catalysts. (■) HSAG, (▼) Metallic Cu, (●) CuO, (♦) Metallic Ni, (✦) NiO.

Figure 4.3.4 shows XRD patterns of the bimetallic catalysts 4Cu1Ni-Mn/HSAG and 2.5Cu2.5Ni-Mn/HSAG reduced in hydrogen at 573 K and after reaction. For simplicity, samples after reaction are denoted with R-. XRD patterns corresponding to the rest of catalysts samples after reaction at 503 K and 50 bar can be found in the Annex section A2 (Figure A2.1). The results show that the samples remained practically unchanged after reaction, although it can be observed that the peak corresponding to Cu^0 appears sharper for the samples after reaction, evidencing the sintering of copper particles.

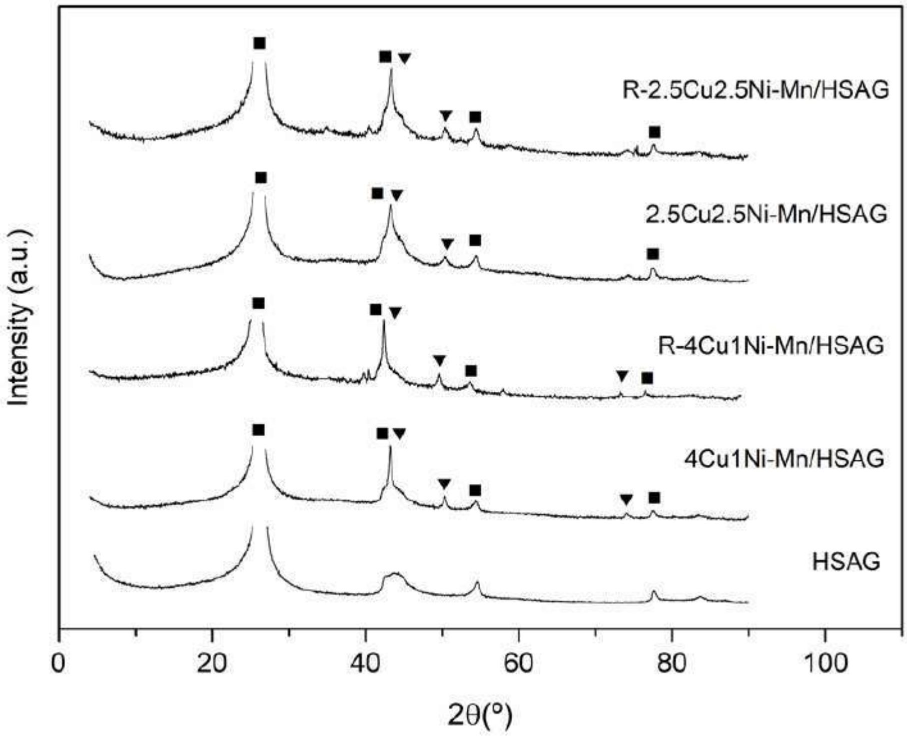

Figure 4.3.4 XRD patterns of the support HSAG and the catalysts 4Cu1Ni-Mn/HSAG and 2.5Cu2.5Ni-Mn/HSAG, both reduced at 573 K with hydrogen, and after study in reaction (R-). (■) HSAG, (▼) Metallic Cu.

For the study of the specific surface area, BET measurements were performed for the support HSAG, the sample Mn/HSAG and the M-Mn/HSAG catalysts reduced at their corresponding temperature. As shown in Table 4.3.2, BET areas of the supported catalysts decrease with the addition of manganese (321 m^2/g) and specially after the addition of metal compared to that of HSAG (396 m^2/g). In addition, the pore volume is reduced by half for 2.5Cu2.5Ni-Mn/HSAG (0.23 cm^3/g) compared to that of HSAG (0.51 cm^3/g), presumably also due to the addition of manganese oxide and the reduced metal nanoparticles that form crystallites (especially copper) that block the space formed by the aggregation of the graphite grains.

Table 4.3.2 Textural parameters of support and reduced catalysts.

Sample	S_{BET} (m^2/g)	Pore volume[a] (cm^3/g)
HSAG	399	0.51
Mn/HSAG	321	-
5Cu-Mn/HSAG	236	-
5Ni-Mn/HSAG	278	-
2.5Cu2.5Ni-Mn/HSAG	230	0.23

[a] BJH desorption pore volume

4.3.2.2. Surface properties

The distributions of acidic sites were determined by temperature-programmed desorption (TPD) of NH_3 for selected samples (Figure 4.3.5). All samples were reduced in situ with hydrogen at 573 K except 5Ni/HSAG and 5Ni-Mn/HSAG, which were reduced at 723 K. The shape of the NH_3-TPD profiles obtained suggest the existence of three main constituent peaks with maximums at about 470, 540 and 625 K, respectively, which implies the presence of acid sites with different strengths. Therefore, the strength of acid sites was classified as weak (350–500 K), medium (500–550) and strong (550–675 K), in accordance with other scales found in literature with Al_2O_3 and SiO_2 as supports [59,180]. To obtain the distribution of acid strength, NH_3-TPD profiles of all samples were deconvoluted into three components corresponding to weak, medium and strong acid sites. The fitted curves of the samples are shown in the Annex section A2 (Figure A2.2). Moreover, the acidity distribution derived after deconvolution of the NH_3-TPD profiles is presented in Table 4.3.3, taking into account the area of each TPD curve and the ones of the deconvoluted peaks. The normalized area of each curve in arbitrary units is also showed in Table 4.3.3 to compare the total acidity of the catalysts.

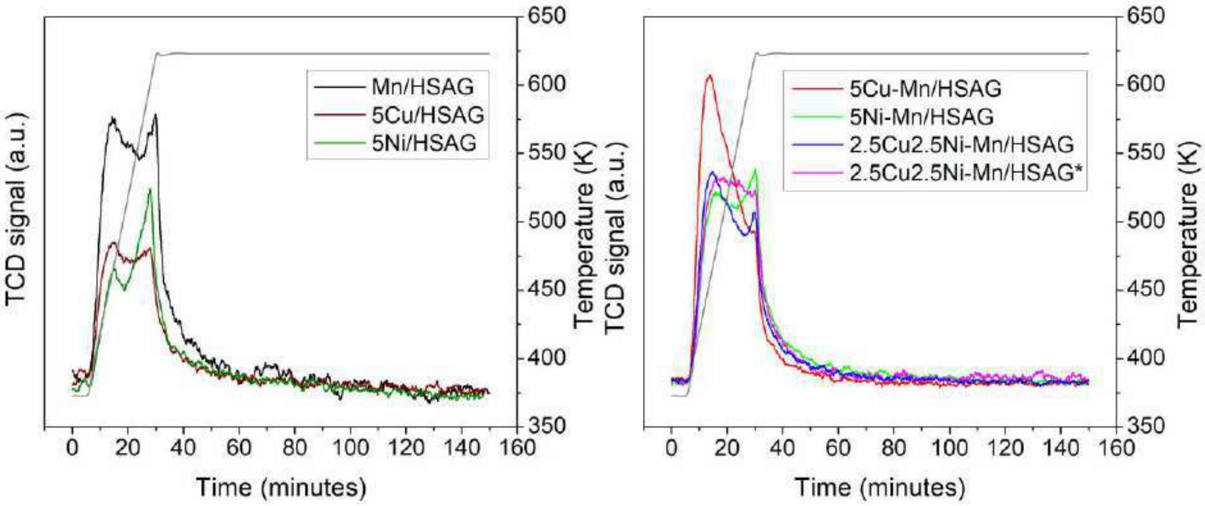

Figure 4.3.5 NH_3-TPD profiles of the Mn/HSAG, 5Cu/HSAG, 5Ni/HSAG and the the bifunctional catalysts reduced in situ. The ``*`` indicates that the material was thermally treated in helium at 723 K prior to reduction with hydrogen.

Table 4.3.3 Acidity distribution derived after deconvolution of the NH_3-TPD profiles of the bifunctional catalysts reduced in situ.

Sample	NH_3-TPD Area (a.u.)	% Weak acid sites	% Medium acid sites	% Strong acid sites
Mn/HSAG	2.4	39	26	35
5Cu/HSAG	1.3	35	31	34
5Ni/HSAG	1.3	31	26	43
5Cu-Mn/HSAG	2.0	51	27	22
5Ni-Mn/HSAG	1.9	35	27	38
2.5Cu2.5Ni-Mn/HSAG	1.8	44	24	32
2.5Cu2.5Ni-Mn/HSAG*	1.9	39	32	29

The ``*`` indicates that the material was thermally treated in helium at 723 K prior to reduction with hydrogen.

Table 4.3.3 shows a decrease in the amount of surface acid sites for the bifunctional catalysts with respect to the Mn/HSAG sample, whereas the monometallic 5Cu/HSAG and 5Ni/HSAG show the lowest total acidity. All samples (Figure 4.3.5 and Table 4.3.3) show relatively uniform acid sites distribution while the acidity of 5Cu-Mn/HSAG and 2.5Cu2.5Ni-Mn/HSAG is predominantly associated to weak acid sites (51 and 44%, respectively). Interestingly, the presence of copper in 5Cu-Mn/HSAG noticeably increases the percentage of weak acid sites compared with the free-metal sample, while the addition of nickel in 2.5Cu2.5Ni-Mn/HSAG seems to decrease the amount of weak sites associated to copper and increase the amount of strong sites associated to Ni since the samples 5Ni/HSAG and 5Ni-Mn/HSAG show predominantly strong acid sites (43 and 38 %, respectively). The bimetallic catalyst treated in helium at 723 K shows an increase in the amount of medium-strength acid sites compared to its counterpart without thermal treatment, while exhibiting quite uniform acid sites distribution, probably due to the incorporation of copper and nickel into the structure of manganese oxide after this thermal treatment.

Strength and number of surface basic sites and their distribution were estimated for the catalysts by determination of CO_2 chemisorption heats. Figure 4.3.6 shows the evolution of the differential heat of adsorption with the surface coverage for the studied catalysts. The strength of basic sites can be classified as strong (Q_{diff}>90 KJ/mol), medium ($90 > Q_{diff} > 60$ KJ/mol) and weak ($Q_{diff} < 60$ KJ/mol), whereas a differential heat of 40 kJ/mol is considered the limit between chemical and physical CO_2 adsorption [191].

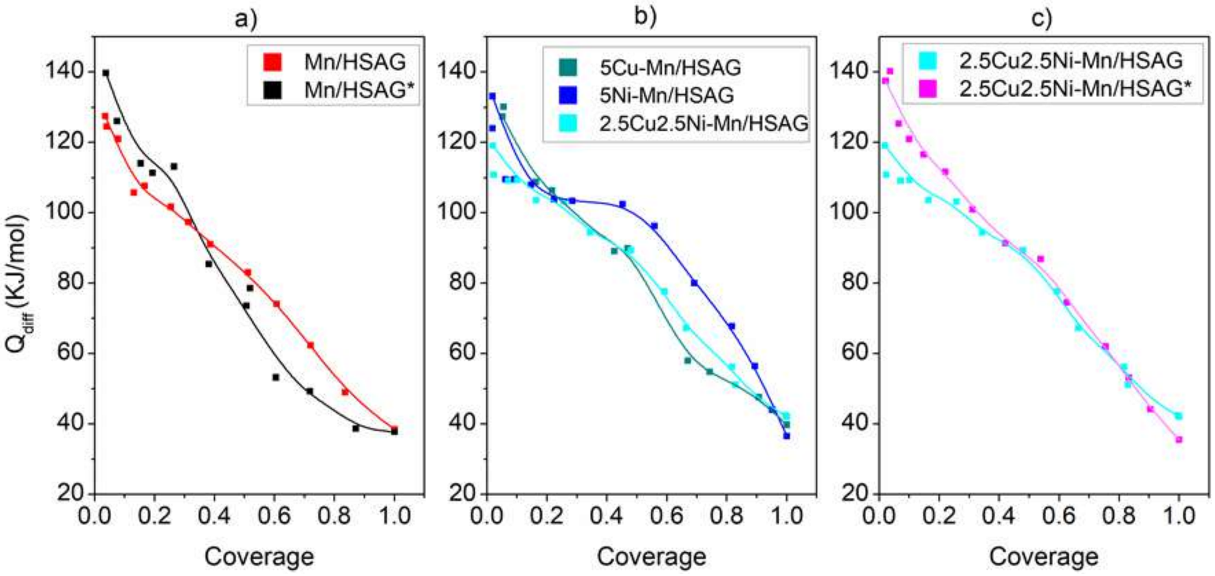

Figure 4.3.6 Differential heats of CO_2 adsorption vs. coverage at 323 K. a) Mn/HSAG before and after thermal treatment b) Cu-Ni bifunctional catalysts c) 2.5Cu2.5Ni-Mn/HSAG before and after thermal treatment. The ``*`` indicates that the material was thermally treated in helium at 723 K prior to reduction with hydrogen.

Figures 4.3.6a) and b) show similar distribution profiles of basic sites, although there are some significant differences that must be taken into account. First of all, it is quite noticeable that the addition of copper to the sample Mn/HSAG drops the total amount of basic sites to a half, while the percentage of strong basic sites remains practically the same (Table 4.3.4). This latter finding is in agreement with the results of Shi et al., that assessed the basicity of CuO, α-MnO_2 and Cu-Mn samples by CO_2-TPD and observed that the high temperature bands corresponding to strong basic sites of the single metal oxides shifted to slightly lower temperatures for the Cu-Mn samples accompanied with a decrease in the intensity of the signal, indicating that the total basicity was reduced for those catalysts [142]. On the other hand, the addition of nickel has the opposite response: the total amount and the percentage of strong basic sites are higher than those of the Mn/HSAG sample. The combination of copper and nickel (2.5Cu2.5Ni-Mn/HSAG) remarkably increases the total amount of basic sites (Table 4.3.4) compared to the samples with copper and nickel alone, even though the percentage of strong basic sites is lower (43%) than the one achieved with 5Ni-Mn/HSAG (62%). In addition, Figure 4.3.6a) and c) show higher initial heats of adsorption of CO_2 for the samples Mn/HSAG and 2.5Cu2.5Ni-Mn/HSAG after thermal treatment at 723 K than the same samples only reduced at 573 K, which implies a strengthening of basic sites even though the total amount remains practically unchanged. Although there are few studies approaching the effect of metal-manganese oxide interaction on the resulting material basicity, previous studies of our group [183] and others [163,164,165,166,167] regarding this effect on metal-MgO, suggest that the incorporation of metals in the MgO lattice has an improving effect in the basic surface of MgO. Hence, the same interpretation could be applied to explain the effect of thermal treatment when metal is added on manganese containing catalysts.

Table 4.3.4 CO_2 chemisorption capacities at 323 K and type of basic sites.

Sample	**Total μmol CO_2/g (Q_{diff}> 40 kJ/mol)**	**Basic sites distribution**		
		% Strong sites (Q_{diff}>90 kJ/mol)	**% Medium-strength (90>Q_{diff}>60 kJ/mol)**	**% Weak-strength (60>Q_{diff}>40 kJ/mol)**
Mn/HSAG	39	42	34	24
Mn/HSAG*	41	43	25	32
5Cu-Mn/HSAG	21	44	24	32
5Ni-Mn/HSAG	49	62	26	12
2.5Cu2.5Ni-Mn/HSAG	55	43	31	26
2.5Cu2.5Ni-Mn/HSAG*	56	49	33	18

The ``*`` indicates that the material was thermally treated in helium at 723 K prior to reduction with hydrogen.

TEM images of the catalysts and their corresponding histograms representing the particle size distribution are depicted in Figure 4.3.7 and Figure 4.3.8. For the sake of brevity, TEM images corresponding to 4Cu1Ni-Mn/HSAG are shown in the Annex section A2 (Figure A2.3). TEM images show Gaussian particle size distribution for all catalysts where the maximum of the peak coincides with the average particle size. Metallic particles supported on Mn/HSAG have bigger average particle sizes (d = 8.3, 5.3 nm and 7.6 nm, Figure 4.3.8a, b and c) than that of Cu/HSAG, Ni/HSAG and 2.5Cu2.5Ni/HSAG (d = 4.7, 4.9 and 3.9 nm, Figure 4.3.7a, b and c), confirming the conclusions drawn from the X-ray study.

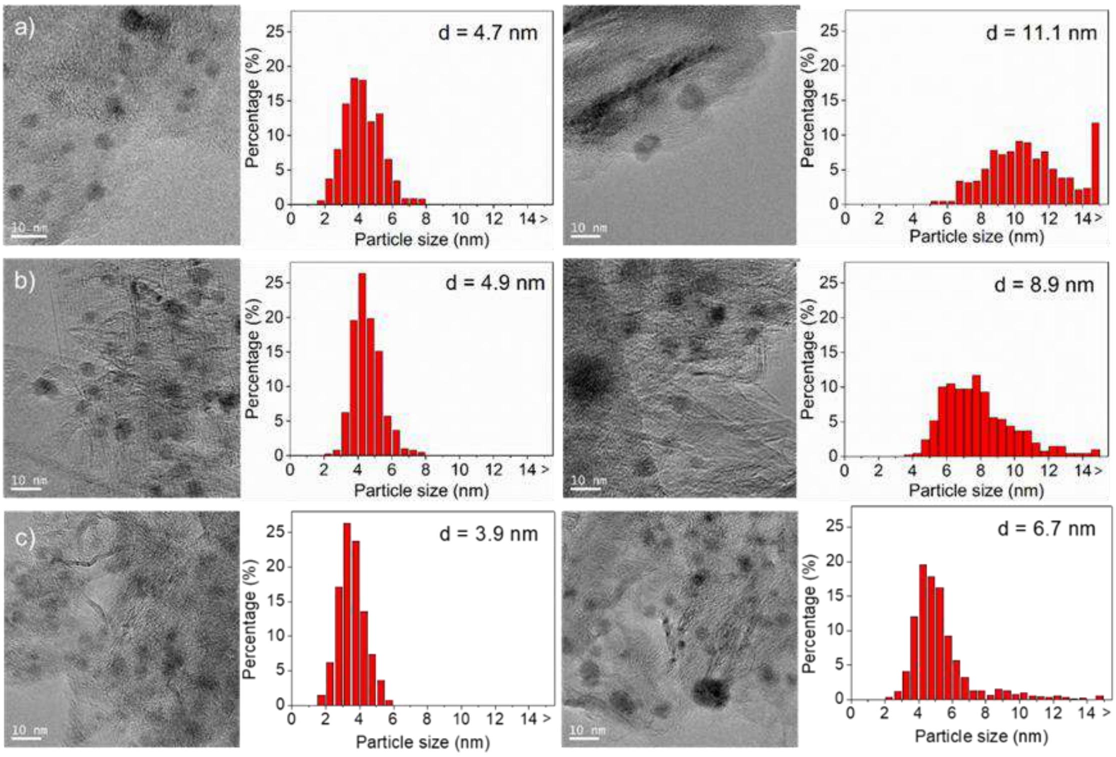

Figure 4.3.7 TEM images of catalysts reduced with hydrogen (left) and after reaction (right): a) 5Cu/HSAG, b) 5Ni/HSAG and c) 2.5Cu2.5Ni/HSAG.

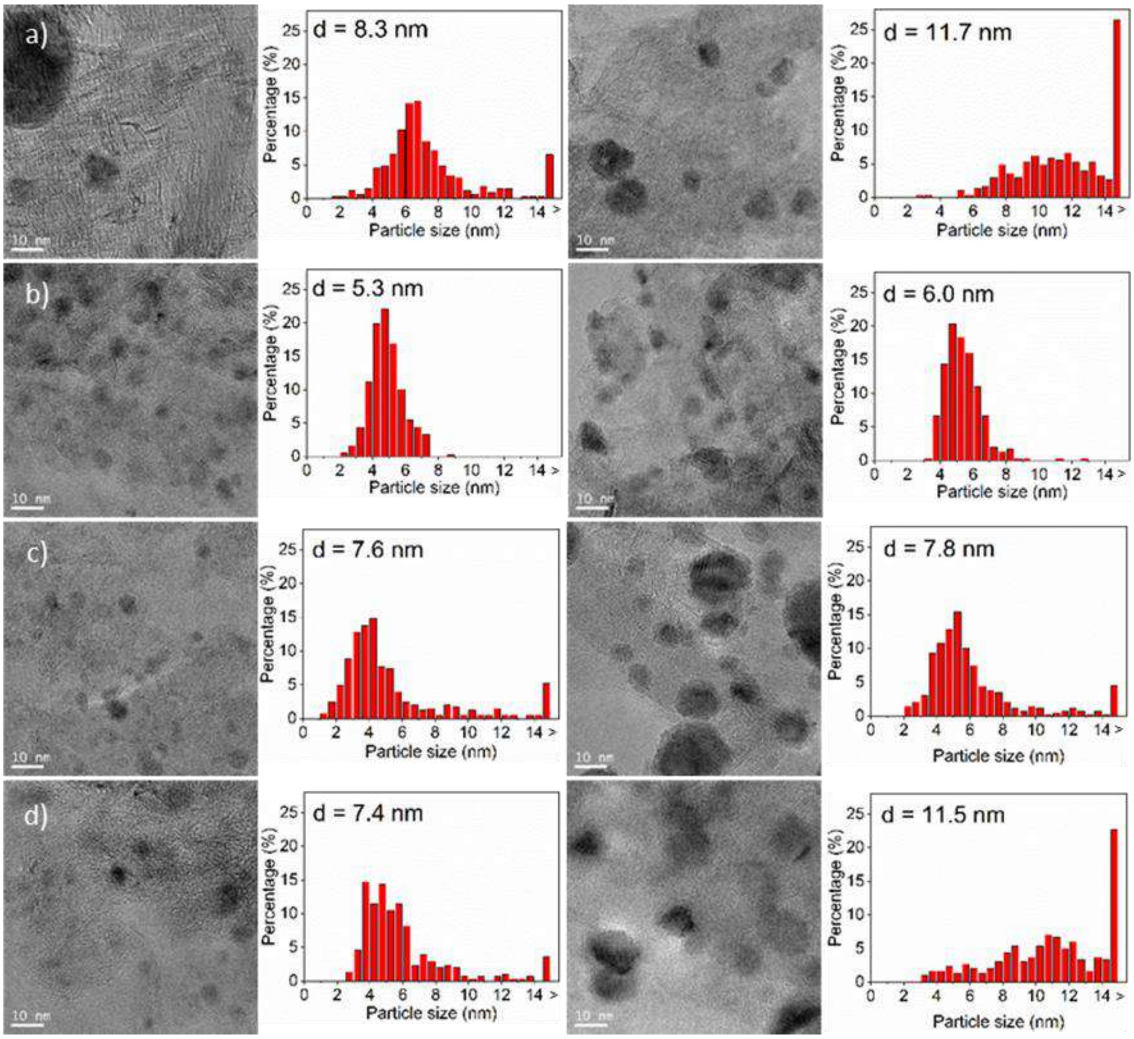

Figure 4.3.8 TEM images of catalysts reduced with hydrogen (left) and after reaction (right): a) 5Cu-Mn/HSAG, b) 5Ni-Mn/HSAG, c) 2.5Cu2.5Ni-Mn/HSAG, d) 2.5Cu2.5Ni-Mn/HSAG*. The ``*`` indicates that the material was thermally treated in helium at 723 K prior to reduction with hydrogen.

Additionally, average particle size determined by TEM increases for all catalysts after reaction (Figure 4.3.7, Figure 4.3.8, right), especially for the samples containing copper, where the proportion of particles with a diameter bigger than 15 nm reaches approximately 10% and 25% for 5Cu/HSAG and 5Cu-Mn/HSAG, respectively. On the other hand, the proportion of particles bigger than 15 nm after reaction is irrelevant for samples containing nickel alone and for

2.5Cu2.5Ni/HSAG. XRD and TEM results seem to conclude that the increase of particle size after reaction is due mainly to the sintering of copper particles, especially for manganese oxide containing catalyst. Sun et al. also observed an agglomeration of smaller nanoparticles to form bigger nanoparticles after reaction for catalysts containing copper and nickel [52]. It is interesting to note that 2.5Cu2.5Ni-Mn/HSAG treated in helium at 723 K loses its Gaussian distribution after reaction and that approximately more than 20% of the particles have a diameter superior than 15 nm. Moreover, Figure 4.3.10b clearly showed an agglomeration of nickel and manganese for the sample 2.5Cu2.5Ni-Mn/HSAG after reaction at 503 K, which combined with the fact that Figure 4.3.1 showed stable conversion after reaching a maximum at 3-4 h, all seems to indicate that nickel and specially copper suffered superficial re-accommodation and agglomeration at early stages of the reaction prior to reaching the steady state conditions.

EDX elemental mapping of the catalysts showed that manganese was highly dispersed on the support (Figure 4.3.9, Figure 4.3.10a) and confirmed the formation of copper and nickel nanoparticles, which coincided in space with manganese evidencing well dispersion of the active phases over the carbonaceous support. The samples 5Cu-Mn/HSAG and 2.5Cu2.5Ni-Mn/HSAG reduced at 573 K showed copper particles of heterogeneous size (Figure 4.3.9, Figure 4.3.10a) in agreement with the size distribution determined by TEM (Figures 4.3.8a and c), while nickel and manganese remained well dispersed after reduction.

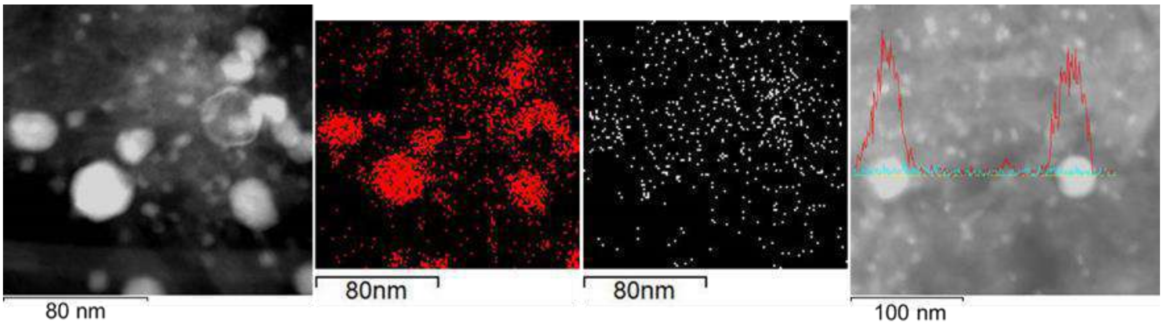
80 nm
80nm
80nm
100 nm

Figure 4.3.9 EDX elemental mapping of 5Cu-Mn/HSAG reduced in hydrogen at 573 K. Color code refers to the distribution of elements (Cu, red; Mn, white).

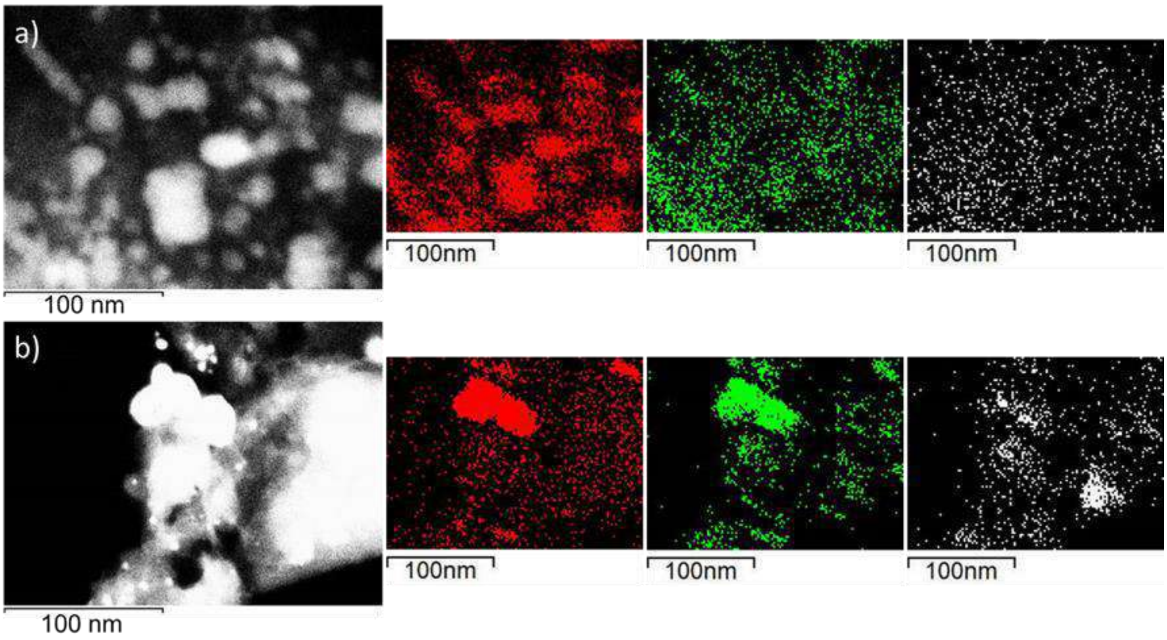
a)
100nm
100nm
100nm
100 nm
b)
100nm
100nm
100nm
100 nm

Figure 4.3.10 EDX elemental mapping of 2.5Cu2.5Ni-Mn/HSAG reduced in hydrogen at 573 K (a) and after reaction (b). Color code refers to the distribution of elements (Cu, red; Ni, green; Mn, white).

In order to identify and quantify the different surface species of the catalysts, a surface analysis was carried out by XPS. All samples present essentially the same XPS spectra. For simplicity, Figure 4.3.11 shows Mn 2p$_{3/2}$, Cu 2p$_{3/2}$ and Ni 2p$_{3/2}$ core level spectra of catalyst 2.5Cu2.5Ni-

Mn/HSAG after reduction in hydrogen at 573 K as an example. The rest XPS spectra is shown in the Annex section 4.3 (Figures A2.4-A2.8). The oxidation state observed for Mn $2p_{3/2}$ after its spectrum analysis is Mn^{2+}, having this species significant multiplet splitting according to literature [192,193]. Nevertheless, curve fitting of this species requires extremely good signal/noise of the spectra, therefore the Mn $2p_{3/2}$ peak could only be deconvolved into three peaks corresponding with the peaks of maximum intensity representatives of Mn^{2+} and its characteristic shake-up. Binding energies of the three contributions observed for Mn $2p_{3/2}$ were practically constant for all the reduced samples (Table 4.3.5). Therefore, a shoulder is evident on the Mn 2p spectra at ca 646 eV, evidencing the presence of Mn^{2+}, whose main peak appears at lower BE (641.1 eV) [192,193,194].

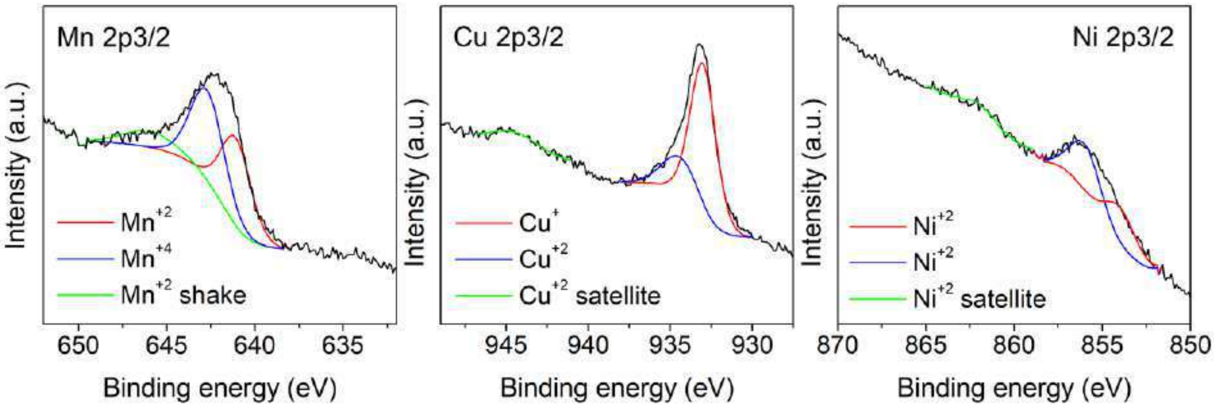

Figure 4.3.11 Mn $2p_{3/2}$ (left), Cu $2p_{3/2}$ (center) and Ni $2p_{3/2}$ (right) XPS spectra of sample 2.5Cu2.5Ni-Mn/HSAG reduced in hydrogen at 573 K.

Table 4.3.5 Binding energies (eV) of core electrons and the Auger parameter (eV) of catalysts samples reduced in hydrogen at 573 K and after reaction (R-).

	BE (eV) Mn 2p 3/2			BE (eV) Cu 2p 3/2		Auger param.	BE (eV) Ni 2p 3/2	
	Mn^{+2}	Mn^{+2}	Mn^{+2} shake	Cu^{+}	Cu^{+2}		Ni^{+2}	Ni^{+2}
5Cu-Mn/HSAG	641.2	642.8	646.0	932.9	934.3	1849.9	-	-
5Ni-Mn/HSAG	641.3	642.9	644.2	-	-	-	853.9	855.8
2.5Cu2.5Ni-Mn/HSAG	641.1	642.7	646.0	932.9	934.4	1849.7	853.7	855.6
R-5Cu-Mn/HSAG	641.4	643.1	646.0	932.8	934.8	1849.9	-	-
R-5Ni-Mn/HSAG	641.0	642.7	646.0	-	-	-	853.1	855.8
R-2.5Cu2.5Ni-Mn/HSAG	641.1	642.6	646.0	932.9	-	1849.9	853.7	856.0

The catalysts studied showed two contributions for the Cu $2p_{3/2}$ peak corresponding to Cu^{+} (ca 932.9 eV) and Cu^{2+} (ca 934.5 eV) with its characteristic satellite at the high binding energy side [195,196,197]. Cu^{+} was identified and differentiated from Cu^{0} through observation of the L3VV X-ray induced Auger parameter of copper and the calculation of the modified Auger parameter, α'A, which was defined as:

$$\alpha'_A = hv + KE_{LMM} - KE\ Cu2p_{3/2} \qquad Equation\ 4.1$$

Where KE_{LMM} and KE Cu$2p_{3/2}$ are the kinetic energies of the L3VV X-ray induced Auger-emitted electrons and the Cu $2p_{3/2}$ photo-emitted electrons, respectively [195]. The Auger parameters determined for all catalysts containing copper (Table 4.3.5) are characteristic of Cu^{+} since α'A is approximately 1849.8 eV. The formation of metallic copper nanoparticles was confirmed by XRD and TEM analysis, therefore the presence of Cu^{2+} is attributed to surface oxidation of the reduced sample under ambient air at room temperature, while the core must remain Cu^0. Cu^+ might be formed in the XPS chamber due to the reductive atmosphere which induces the reduction of surface Cu^{2+}.

Ni $2p_{3/2}$ spectra of all samples exhibit a main peak at ca 855 eV corresponding to Ni^{2+} and a satellite peak at 861–862 eV. No peak could be ascribed to Ni^0 since its characteristic peak is associated to lower BE (852.6 eV). The Ni $2p_{3/2}$ envelope was fitted into two contributions at 853–854 eV and ca 855.9 eV, in agreement with other studies found in literature [192,198,199]. Absence of Ni^0 could be attributed to surface oxidation to Ni^{2+}, as in the case of copper.

XPS atomic ratios of Metal/C, Mn/C, Cu/Ni, and Metal/Mn for the samples studied are given in Table 4.3.6. Interestingly, the bimetallic sample reduced and after reaction shows higher Cu/Ni atomic ratio obtained by XPS (2.28 and 1.47, respectively, Table 4.3.6) than the nominal atomic ratio (Cu/Ni = 0.92). These results are consistent with literature, where surface copper enrichment is observed for Cu-Ni nanostructured alloys [200] and Cu-Ni supported on Al_2O_3, ZrO_2 and CeO_2/ZrO_2 [201,202], due to the lower heat of sublimation of copper compared to nickel that induce the former to occupy the surface sites of the particles.

Moreover, atomic ratios (Table 4.3.6) extracted from the XPS analysis are in agreement with the conclusions drawn from the preceding characterization techniques. The decrease of the Metal/C and Metal/Mn ratios clearly illustrates how nickel and especially copper particles have bigger particle size after the chemical reaction at 503 K and 50 bar. This effect is also observed for manganese comparing Mn/C ratios and the Mn mappings (Figure 4.3.10b) where this element seems to agglomerate after reaction. These results confirm the conclusion derived from XRD, EDX and TEM analysis, given that some sintering of copper nanoparticles was observed after reaction for 5Cu/HSAG and 5Cu-Mn/HSAG samples, while less sintering or agglomeration of nickel particles was observed in the 5Ni-Mn/HSAG sample studied after reaction (Figure 4.3.8b).

Table 4.3.6 Atomic ratios for catalysts samples reduced in hydrogen at 573 K and after reaction (R-).

	Cu/C	Ni/C	Mn/C	Cu/Ni	Cu/Mn	Ni/Mn
5Cu-Mn/HSAG	0.0013		0.0011		1.16	
5Ni-Mn/HSAG		0.0004	0.0012			0.34
2.5Cu2.5Ni-Mn/HSAG	0.0006	0.0003	0.0012	2.28	0.47	0.21
R-5Cu-Mn/HSAG	0.0010		0.0010		0.95	
R-5Ni-Mn/HSAG		0.0002	0.0009			0.26
R-2.5Cu2.5Ni-Mn/HSAG	0.0002	0.0002	0.0009	1.47	0.26	0.17

4.3.3. Discussion

In order to understand the synergystic behavior of the metals and manganese, it is of interest to analyze how both functions work separately. Despite showing negligible conversion, the main products with the sample Mn/HSAG were acetaldehyde, butane, 2-butenone, 1-butene, ethylene and ethane. Although these compounds were found in traces since more than 99% percent of the product stream was unconverted ethanol, the information deduced from these results is enough to conclude that Mn/HSAG sample is not capable of upgrading ethanol to 1-butanol, but it is promising as support since it contains acid/base sites of homogeneous strength distribution (Table 4.3.3, Table 4.3.4) that are able to produce ethylene (formed by dehydration of ethanol on acid sites) and acetaldehyde (dehydrogenation of ethanol on basic sites), among others.

Cu/HSAG, Ni/HSAG and 2.5Cu2.5Ni/HSAG show high activity for the conversion of ethanol but with low selectivity towards 1-butanol (4, 7 and 4%, respectively), most likely due to the absence of basic sites provided by manganese (Table 4.3.4). The principal by-products for Cu/HSAG were acetaldehyde and 1,1-dyethoxyethane, which is formed by acid-catalyzed acetylation of acetaldehyde with two ethanol molecules [168]. On the other hand, Ni-HSAG tends to other undesired products such as methane, carbon monoxide, diethyl ether, and acetone, whereas the bimetallic catalyst 2.5Cu2.5Ni/HSAG shows an intermediate behavior between the monometallic Cu and Ni catalysts in terms of conversion and product distribution. Metal-catalyzed acetaldehyde decarbonylation produces methane and carbon monoxide [56]; diethyl ether is the product of the acid-catalyzed ethanol dehydration [57]; acetone is formed through ethyl acetate hydrolysis that produce acetic acid and subsequent ketonization of this compound [23]. Interestingly, the three catalysts are very selective towards acetaldehyde, especially 5Cu/HSAG and 2.5Cu2.5Ni/HSAG with a selectivity of 52 and 37%, respectively, which is consistent with literature since it is reported that copper considerably speeds up the rate of ethanol dehydrogenation that leads to acetaldehyde [52]. The presence of basic sites would continue the reaction towards the aldol condensation of acetaldehyde that forms 3-hydroxybutanal, which readily dehydrates to 2-butenal on acid sites and finally give rise to 1-butanol after subsequent hydrogenations [103]. Since it was previously remarked that 1-butanol selectivities are insufficient with metal/HSAG, it seems that a good combination of metal with acid/base sites like those of Mn/HSAG (Figure 4.3.5 and Table 4.3.3, Table 4.3.4) would be a promising combination for the upgrading of ethanol towards 1-butanol.

Indeed, 1-butanol selectivities rise considerably when copper and nickel are combined with manganese supported on HSAG presumably due to the combination of both functionalities: metal and acid/base sites. This enhancement is mainly observed with copper since 1-butanol selectivity rises from 4 to 33% with 5Cu/HSAG and 5Cu-Mn/HSAG, respectively, while it increases from 7 to 21% with 5Ni/HSAG and 5Ni-Mn/HSAG, respectively. Interestingly, despite containing more amount of basic sites (49 μmol CO_2 chemisorbed/g, 62% of high strength, Table 4.3.4) and more percentage of strong acid sites (38%, Table 4.3.3) than 5Cu-Mn/HSAG (21 μmol CO_2 chemisorbed/g, 44% of high strength, Table 4.3.4; 22% of strong acid sites, Table 4.3.3), 5Ni-Mn/HSAG is the worst catalyst in terms of 1-butanol selectivity (21%) among the bifunctional catalysts studied. Therefore, it seems that the upgrading of ethanol to 1-butanol requires a good equilibrium of acidic and basic sites similar to that of 5Cu-Mn/HSAG, which is one of the samples studied that presented more acidity (Table 4.3.3 and Figure 4.3.5), mainly of weak strength (51%, Table 4.3.3), and less basicity, mainly of high strength (44%, Table 4.3.4). It should be noted that ethanol conversion rises remarkably for both catalysts compared to their counterparts without manganese, and especially for 5Ni-Mn/HSAG which reaches 45% of ethanol conversion. These clear differences in conversion may be attributed to the surface metal sites of the catalysts after reaction, since 5Ni-Mn/HSAG undergoes mild sintering (from 5.3 to 6 nm) compared to 5Cu-Mn/HSAG (from 8.3 to 11.7 nm). All things considered, acid/base sites are definitely necessary to catalyze the dehydration of 3-hydroxybutanal and the aldol condensation, respectively. But these centers do not seem to be as crucial as the number of exposed metal sites, which catalyzes dehydrogenation/hydrogenation reactions, for achieving good conversion and consequently high 1-butanol yields.

Furthermore, both catalysts present particularly different product distribution due to the before mentioned tendency of nickel to produce side reactions that lead to undesired by-products. Nevertheless, 5Ni-Mn/HSAG constitutes an enhancement in the suppression of these side reactions since carbon monoxide, methane and acetone selectivities decrease from 15, 25 and 9% with 5Ni/HSAG to 10, 21 and 0.8% with 5Ni-Mn/HSAG, presumably because manganese covers the acid sites of the HSAG support and introduce basic sites. This is confirmed by Figure 4.3.5 and data in Table 4.3.3, Table 4.3.4, which showed that this sample presented less total amount of acid sites and a total amount of basic sites higher than Mn/HSAG and 5Cu-Mn/HSAG. In addition to these by-products not found in the same catalyst with copper instead of nickel, 5Ni-Mn/HSAG also produces small quantities of ethane, propane and pentane. On the other hand, 5Cu-Mn/HSAG produces more 1,1-diethoxyethane than 5Ni-Mn/HSAG (16 and 2%, respectively), but at the same time the presence of manganese reduces its formation compared to 5Cu/HSAG (31%). As the formation of 1,1-dyethoxyethane requires acid sites, the different selectivities achieved for each catalyst are then consistent on the basis of their acidity, since the absence of manganese and the acid character of HSAG make 5Cu/HSAG more acid than 5Cu-Mn/HSAG, which in turn presents more acidity than 5Ni-Mn/HSAG (Table 4.3.3 and Figure 4.3.5). Therefore, to inhibit the formation of undesired by-products and enhance the conversion and the selectivity towards 1-butanol, a catalyst combining the best characteristics attributed to copper and nickel should improve the ethanol condensation route to 1-butanol.

In fact, the bimetallic catalysts studied present higher 1-butanol selectivities compared to the monometallic catalysts, especially 2.5Cu2.5Ni-Mn/HSAG (36%), which is the least acid (mostly of weak strength, 44%) and the most basic (43% of strong basic sites) compared to the other samples (Table 4.3.3 and Table 4.3.4). As it was expected, the catalytic behavior of the bifunctional and bimetallic catalyst 2.5Cu2.5Ni-Mn/HSAG is considerably better than that of its counterpart without manganese, 2.5Cu2.5Ni/HSAG, in terms of 1-butanol selectivity (that rises from 4 to 36%) and the formation of undesired by-products, whose selectivities decrease when manganese is present in the catalyst formulation. This once again demonstrates that the presence of acid/base sites provided by manganese oxide is compulsory to satisfactorily upgrade ethanol towards 1-butanol. Moreover, ethanol conversion is higher (37 and 36% with 2.5Cu2.5Ni-Mn/HSAG and 4Cu1Ni-Mn/HSAG, respectively) than the one achieved with 5Cu-Mn/HSAG (27%) but lower than that of 5Ni-Mn/HSAG (45%), which is consistent with the previous mentioned hypothesis that particle sintering during reaction severely affects ethanol conversion, since 5Ni-Mn/HSAG presents smaller final particle size after reaction (6 nm) than 2.5Cu2.5Ni-Mn/HSAG (7.8 nm), 4Cu1Ni-Mn/HSAG (8 nm) and 5Cu-Mn/HSAG (11.7 nm). However, considering both conversion and selectivity, it can be observed that the bimetallic catalysts improve the 1-butanol yield comparing to the monometallic and that the 2.5 wt.% Cu and 2.5 wt.% Ni is the optimal Cu-Ni load, thanks to the above mentioned compromise between medium-weak strength acid sites, homogeneous strength distribution of basic sites and mild sintering. In addition, the presence of nickel enabled the 2.5Cu2.5Ni-Mn/HSAG catalyst to especially reduce the formation of CO, CH_4, 1,1-diethoxyethane and acetone, with selectivities of 7, 10, 3 and 0.5, respectively.

The 2.5Cu2.5Ni-Mn/HSAG catalyst treated in helium at 723 K slightly improved 1-butanol selectivity, but reduced considerably the ethanol conversion. This behavior was expected due to the strong metal sintering observed after reaction (11.5 nm) and the reduction of its high strength acidity after thermal treatment, with mostly weak and medium strength acid sites (39 and 32%, respectively, Table 4.3.3).

As above discussed, in addition to the favorable contribution of acid/base sites, the production of 1-butanol is strongly influenced by the metal function of the catalyst. So, given the observed role of the metal phase, the site time yield towards 1-butanol was calculated (Figure 4.3.12) for the bifunctional catalysts based on the number of metal atoms on the surface per gram for the catalysts after reaction, since the superficial re-accommodation and agglomeration of nickel and specially copper seems to be produced at early stages of the reaction prior to reaching the steady state conditions. In this way, Figure 4.3.12 clearly illustrates how the combination of copper and nickel in the 2.5Cu2.5Ni-Mn/HSAG and especially in the 2.5Cu2.5Ni-Mn/HSAG* catalysts is the optimum among those studied to favor the reaction pathway towards 1-butanol.

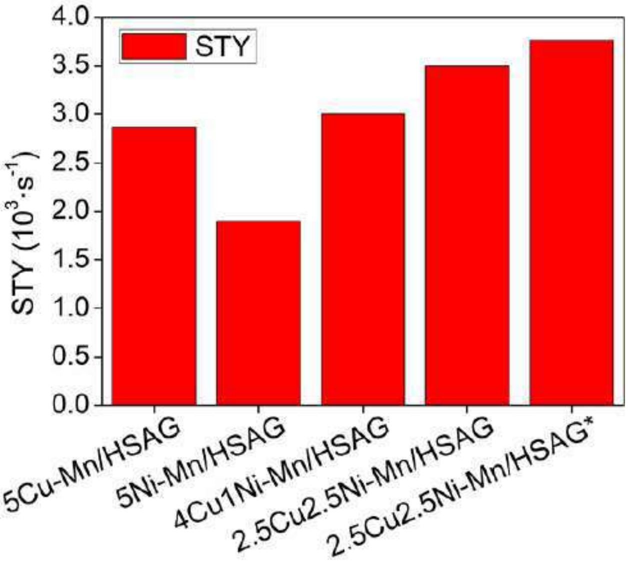

Figure 4.3.12 Site time yield (s^{-1}) for bifunctional catalyst after 7 h of reaction.

4.3.4. Conclusions

Several heterogeneous bifunctional catalysts based on Cu-Ni nanoparticles and manganese oxide supported on high surface area graphite were screened in a fixed-bed gas continuous reactor to study the conversion of ethanol to 1-butanol. Their catalytic performance showed substantial differences that were tentatively explained by characterization of the active sites by temperature programmed desorption of NH_3, microcalotrimetry of CO_2 chemisorption and TEM/EDX analysis, which provided information about the acid/base sites related to manganese oxide and its interaction with the metal particles, and the dehydrogenating/hydrogenating properties associated to Cu-Ni particle size and distribution. These analysis and catalytic tests suggested the existence of a synergistic effect between manganese combined with Cu and/or Ni dispersed on high surface area graphite that gives place to an improved catalyst, in terms of high 1-butanol yield, when applied in the Guerbet process. Copper is needed since it considerably speeds up the rate of ethanol dehydrogenation that leads to acetaldehyde, while nickel's activity and less disposition to sintering favored the ethanol conversion, although more undesired products and mostly gases were produced. Bimetallic catalysts proved to combine the best characteristics of both metals. The most promising catalyst, 2.5Cu2.5Ni-Mn/HSAG* treated in helium at 723 K prior reduction with hydrogen, exhibited an ethanol conversion of 30% and selectivity to 1-butanol of 39%, whose high amounts of weak acid sites and strong basic sites constitute the optimal acid/base site strength distribution, even though its higher metal particle size after reaction seems to provide a slightly negative impact in ethanol conversion. Moreover, this catalyst remarkably reduces the formation of unwanted products. For all catalysts, the analysis of the product streams indicated that the reaction pathway follows the Guerbet route and demonstrated good stability, remaining active for 24 h on stream. Although acid/base sites have a considerably impact on 1-butanol selectivity and product distribution, it seems that the metal function plays a crucial role in the Guerbet ethanol condensation reaction since clear differences in conversion are attributed to the sintering of particles that leads to decreasing conversion. However, a compromise between both parameters must be reached to further optimize these catalysts.

4.4. Cu-Ni-MgO based catalysts for ethanol conversion into butanol: Optimization of the catalytic properties

This chapter studies the performance for the ethanol condensation into 1-butanol through the Guerbet reaction pathway of different bifunctional catalytic systems based on Cu and/or Ni as a hydrogenating/dehydrogenating component and magnesium oxide incorporating acid/base properties, supported on a high surface area graphite (HSAG).

4.4.1. Reaction results

In the first place, reaction blank tests were performed with the reactor filled with silicon carbide and no activity was observed at 503 K, therefore a catalyst is needed for the reaction to take place. Table 4.4.1 summarizes the catalytic performance of the different samples after 24 hours, namely once the steady state was reached. It should be mentioned that carbon balances for all catalysts were above 90 %.

Preliminary tests with the HSAG support and with the sample Mg/HSAG showed negligible conversion under the reaction conditions used. As can be seen in Table 4.4.1, the catalyst used has a strong influence on the product distribution. Generally, the main products detected were 1-butanol, acetaldehyde, 1,1-diethoxyethane, carbon monoxide and methane, whereas other products observed in small quantities were ethyl acetate, 2-butanone, ethylene, diethoxybutane, butanal, 2-butenal, 2-butanol, 2-ethyl-1-butanol, 1-hexanol, 1-octanol, 2-ethyl-1-hexanol and acetone, which is in good agreement with the reaction pathway and the possible by-products mentioned in the introduction (see Figure 1.3.1 and the detailed version Figure 1.3.2). In addition, methane and carbon monoxide can be produced via metal-catalyzed acetaldehyde decarbonylation, while acetone can be formed via ethyl acetate hydrolysis that produces acetic acid and subsequent ketonization of this compound [23,56].

Table 4.4.1 Catalytic activity and product selectivities obtained at 503 K and 50 bar after 24 h on stream.

Sample	**d (nm)**		**Conv. (%)**	**Selectivity (%)**					
	Fresh[a]	**Used[b]**		**ButOH**	**Ac**	**CO**	**CH_4**	**1,1-DEE**	**Others[c]**
Cu/HSAG	4.7	11.1	17	4	52	0	0	31	13
Ni/HSAG	4.9	8.9	23	7	24	15	25	1	28
4Cu1Ni/HSAG	4.2	7.1	20	5	39	8	12	13	23
5Cu-Mg/HSAG	7.5	8.9	26	26	23	0	0	15	36
5Ni-Mg/HSAG	4.5	5.5	23	24	12	15	25	2	22
2.5Cu2.5Ni-Mg/HSAG	5.8	9.3	28	32	13	11	15	2	27
4Cu1Ni-Mg/HSAG	6.6	7.1	24	39	22	4	6	4	25
4.75Cu0.25Ni-Mg/HSAG	6.8	8.5	28	31	23	2	2	10	32
4Cu1Ni-Mg/HSAG*	8.8	9.7	20	44	21	3	2	3	27

ButOH – 1-Butanol, Ac – Acetaldehyde, 1,1-DEE – 1,1-diethoxyethane, d – average particle size, determined by TEM of fresh catalysts reduced at 573 K, except Ni/HSAG and 5Ni-Mg/HSAG that were reduced at 723 K, and after 24 h in reaction. [a] Catalysts reduced at 573 K, [b] After 24 h in reaction. [c] Other products also detected in small quantities: diethyl ether, ethyl acetate, 1-hexanol, 2-butanona, diethoxybutane, 1-octanol, butanal, 2-butenal, 2-butanol, 2-ethyl-1-butanol, 1-octanol, 2-ethyl-1-hexanol, ethylene, ethane, acetone, propane, pentane. The ``*`` indicates that the material was thermally treated in helium at 723 K prior to reduction with hydrogen.

After 24 hours of reaction, the catalysts showed high stability with regard to 1-butanol selectivity, as it can be observed in Figure 4.4.1. It should be highlighted that all catalysts reach a maximum in conversion at hour 3-4, followed by a slight deactivation, except catalysts 2.5Cu2.5Ni-Mg/HSAG and 4Cu1Ni-Mg/HSAG*, whose deactivation is a bit more accentuated. Presumably, this means that the catalysts undergo a structural change at early stages of the reaction at 503 K and 50 bar. Once the catalyst is finally transformed, the reaction achieves the steady state conditions after 10 hours as Figure 4.4.1 shows.

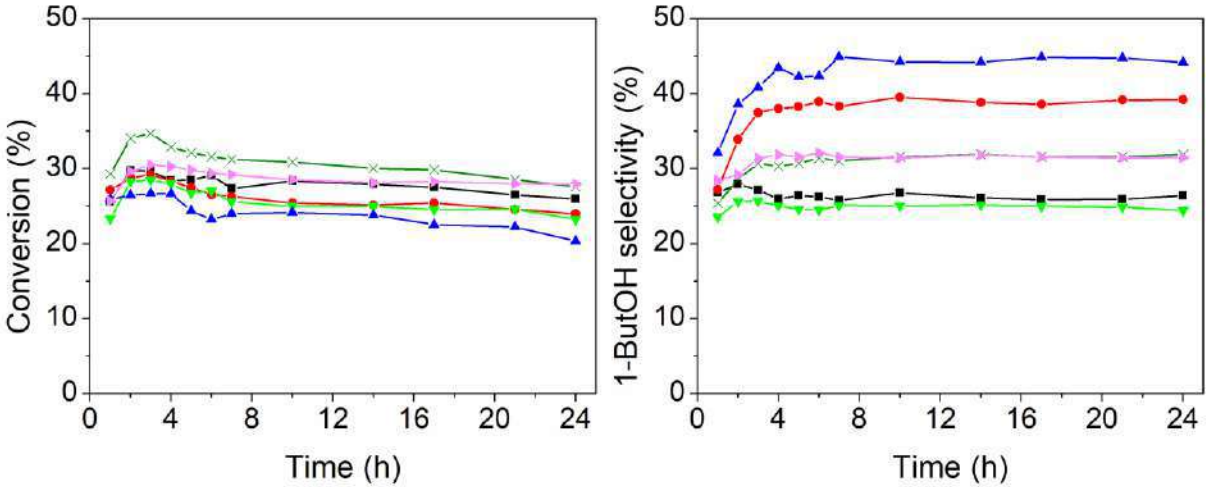

Figure 4.4.1 Conversion and 1-butanol selectivity through 24 hours of reaction for the bifunctional catalysts. The ``*`` indicates that the material was thermally treated in helium at 723 K prior to reduction with hydrogen. (■) 5Cu-Mg/HSAG, (▼) 5Ni-Mg/HSAG, (●) 4Cu1Ni-Mg/HSAG, (x) 2.5Cu2.5Ni-Mg/HSAG, (▶) 4.75Cu0.25Ni-Mg/HSAG, (▲) 4Cu1Ni-Mg/HSAG*.

4.4.2. Catalysts characterization

4.4.2.1. Structural and textural features

Figure 4.4.2 shows the H_2-TPR profiles of the monometallic Cu and Ni and the bimetallic Cu-Ni catalysts. It is important to note that these profiles include the reduced products derived from the metal precursor decomposition since these analyses were carried out with the fresh catalysts, without any thermal treatment like calcination. The sample 5Cu/HSAG shows a reduction peak at ca 485 K, while 5Ni/HSAG exhibits two reduction peaks, the first one sharper at 540 K and the second one in the range 585-685 K. Interestingly, the sample 4Cu1Ni/HSAG presents an intermediate behavior with a sharp single reduction peak at 515 K. These results are consistent with literature, since the reduction of the precursor $Cu(NO_3)_2$ and particularly Cu^{2+} to Cu^0 has been found to take place at 535-565 K and 485-520 K, respectively [173,174,184,185]. In addition, the H_2-TPR profiles of carbon supported Ni reported in the literature [185,189,190] present the same first sharp peak attributed to the reduction of dispersed Ni^{2+} and the second broad one, which is ascribed to the reduction of remaining Ni^{2+} as well as the metal catalyzed gasification of carbon atoms around the nickel particles.

On the other hand, the H_2-TPR profiles of the monometallic catalysts containing magnesium show that the reduction of copper and nickel occurs at higher temperatures compared with their counterparts without magnesium. The shift to higher temperatures is especially significant for the 5Cu-Mg/HSAG sample, with a reduction peak at 530 K, whereas the 5Ni-Mg/HSAG sample shows the main reduction peak at 560 K and the broad one in the range 600-700 K. Remarkably, the broad peak characteristic of nickel is undiscernible in the H_2-TPR profiles of the bimetallic catalysts, showing only one sharp peak that shifts to higher temperatures the more %wt of nickel is present: 530 K for 4.75Cu0.25Ni-Mg/HSAG, 540 K for 4Cu1Ni-Mg/HSAG, and 555 K for 2.5Cu2.5Ni-Mg/HSAG. However, the reduction peak of the bimetallic catalysts always appears at temperatures lower than that of 5Ni-Mg/HSAG (560 K), which is in agreement with previous findings in the literature involving Cu and Ni nanoparticles [203,204,205,206]. In particular, Lv et al. [204] characterized multi-walled carbon nanotubes (MWCNT) supported nickel nanoparticles doped with magnesia and copper catalysts and observed that bimetallic Ni-Cu-Mg/MWCNT catalysts reduced at lower temperatures than the monometallic Ni-Mg/MWCNT ones, leading to the conclusion that the introduction of copper enables the reduction of nickel at lower temperatures. It is commonly acknowledged that species harder to reduce are those with stronger interaction with the support [203], therefore these results suggest that both metals have stronger interaction with the support when magnesium oxide is present. There is no appreciable contribution of magnesium oxide reduction since the TPR profiles of samples 5Cu/HSAG, 5Ni/HSAG and 4Cu1Ni/HSAG and their counterparts with magnesium are practically identical in shape although they are displaced in the X axis as a result of changes in the dispersion state when supported on Mg/HSAG. Given that magnesium (II) nitrate was used as a precursor and that Mg/HSAG was treated in helium at 873 K, the oxidation state expected for magnesium is Mg^{2+} and therefore no reduction profile could be attributed to lower oxidation states of magnesium. All things considered, the reduction temperature was set at 573 K for the catalysts containing copper and 723 K for those containing only nickel.

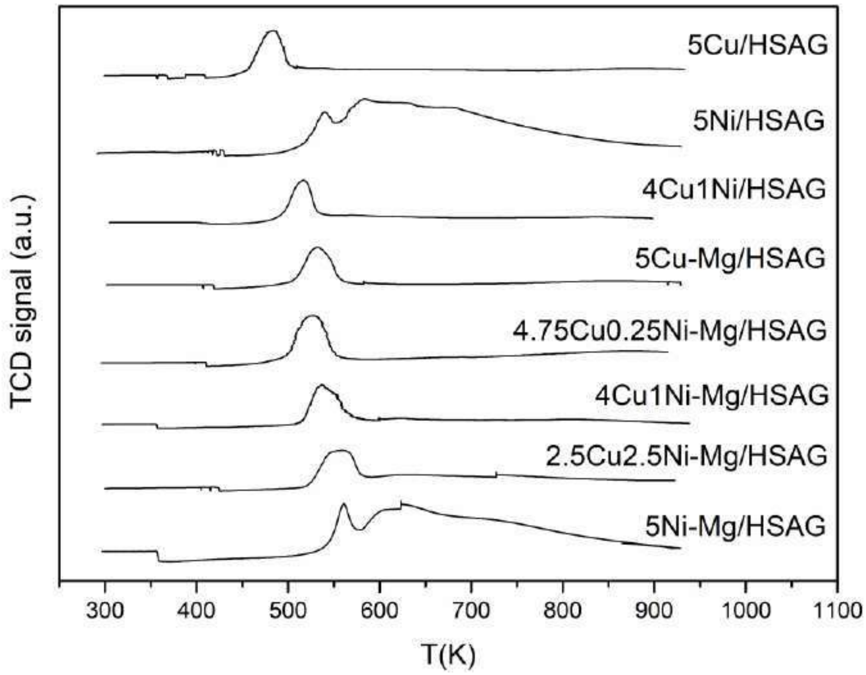

Figure 4.4.2 H_2-TPR profiles of the catalysts samples.

Figure 4.4.3 shows the X-ray diffractograms of the HSAG support and the resulting Metal/HSAG and Metal-Mg/HSAG catalysts reduced at 573 K with hydrogen, except 5Ni/HSAG and 5Ni-Mg/HSAG catalysts that were reduced at 723 K. The diffractograms show no reflections corresponding to magnesium oxide, which was expected since all samples contain approximately 1.45wt% of Mg. On the other hand, the diffraction peaks attributed to HSAG were detected at 2Θ of 26.2, 43.9, 54.6 and 77.6º for all samples. Unfortunately, the XRD analysis of copper and nickel involves some uncertainty since the broad HSAG peak that appears at 2Θ=43.9º overlaps the main peaks characteristic of metallic copper (43.5º) and nickel (44.4º). Despite this limitation, the highest reflection of metallic Cu was discerned in the 5Cu/HSAG and 4Cu1Ni/HSAG samples (Figure 4.4.3b and 4.4.3d), while the reflections at 2Θ of 43.5, 50.4 and 74º were detected in all the copper containing samples supported on

Mg/HSAG (Figure 4.4.3e-h). On the other hand, no diffraction peak corresponding to metallic Ni could be detected except for the 5Ni/HSAG sample (Figure 4.4.3c), even though the peak at 2Θ=44.4º was only slightly perceptible. These differences may be attributed to the presence of magnesium and its influence on the dispersion and size of metal nanoparticles. While nickel appears well dispersed and immutable regardless of the catalyst composition, copper nanoparticles seems to become bigger and worse dispersed when magnesium oxide is present.

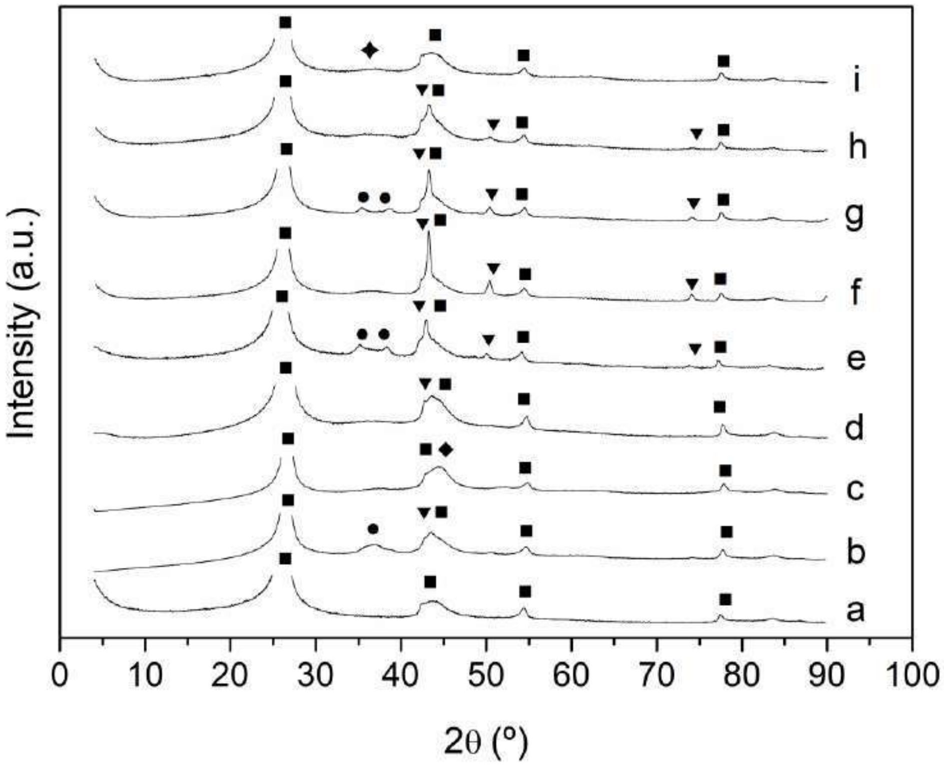

Figure 4.4.3 XRD patterns of the support HSAG and the reduced catalysts, where a) HSAG, b) Cu/HSAG, c) Ni/HSAG, d) 4Cu1Ni/HSAG, e) 5Cu-Mg/HSAG, f) 4.75Cu0.25Ni-Mg/HSAG, g) 4Cu1Ni-Mg/HSAG, h) 2.5Cu2.5Ni-Mg/HSAG, i) 5Ni-Mg/HSAG. (■) HSAG, (▼) Metallic Cu, (●) CuO, (♦) Metallic Ni, (✦) NiO.

The peaks of CuO (35.7º, 38.9º) and NiO (37.4º, 43.5º) are perceptible to some extent in the XRD patterns of reduced 5Cu/HSAG, 5Cu-Mg/HSAG, 4Cu1Ni-Mg/HSAG and 5Ni-Mg/HSAG catalysts, indicating that these samples might have suffered a slight surface oxidation due to ambient exposition.

The 4Cu1Ni-Mg/HSAG catalyst and its counterpart treated in helium at 723 K were studied by XRD after reduction in hydrogen at 573 K and after reaction (-R) (Figure 4.4.4). Interestingly, the reflections corresponding with CuO (35.7º, 38.9º) observable for the reduced sample 4Cu1Ni-Mg/HSAG (Figure 4.4.4b), disappear after reaction (Figure 4.4.4c), after the reduction of its counterpart thermally treated in helium (Figure 4.4.4d) and after the reaction with this latter catalyst (Figure 4.4.4e). In contrast, the reflections corresponding with Cu^0 (43.5, 50.4 and 74º) become sharper, which suggest that copper is severely affected by temperature and the reaction conditions. The rest of catalysts were also studied after reaction but, for the sake of brevity, their XRD patterns can be found in the Annex section A3 (Figure A3.1). The latter assumption that copper seems to form aggregates after reaction at 503 K is once again confirmed since Figure A3.1 shows that the Cu^0 peak is more intense for the samples containing copper than for their counterparts only reduced in hydrogen (Figure 4.4.3) and that the CuO peaks disappear except for the samples 5Cu/HSAG and 5Cu-Mg/HSAG. Moreover, the peaks corresponding with Ni^0 and NiO are imperceptible for all the samples containing nickel, evidencing that nickel particles do not suffer the same sintering effect that the copper particles do.

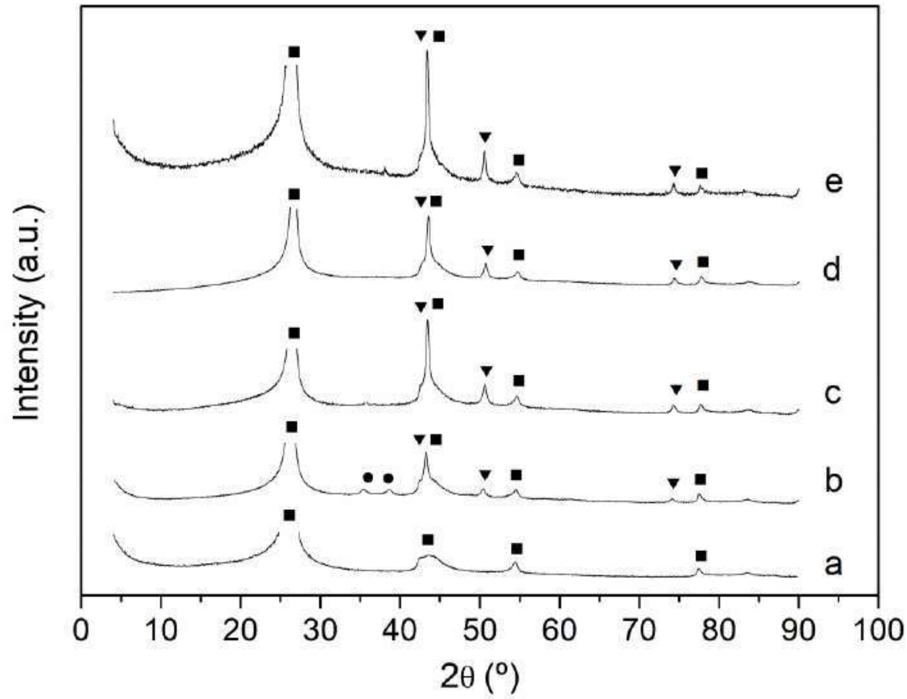

Figure 4.4.4 XRD patterns, where a) HSAG, b) 4Cu1Ni-Mg/HSAG, c) R-4Cu1Ni-Mg/HSAG, d) 4Cu1Ni-Mg/HSAG*, e) R-4Cu1Ni-Mg/HSAG*. (■) HSAG, (▼) Metallic Cu, (●) CuO.

The specific surface area of the support HSAG, and the Mg/HSAG and M-Mg/HSAG catalysts reduced at their corresponding temperature are listed in Table 4.4.2. The presence of magnesium oxide decreases the BET area from the 396 m^2/g of HSAG to the 317 m^2/g of Mg-HSAG. Moreover, the addition of metal further decreases the specific surface area, especially for the 5Cu-Mg/HSAG (270 m^2/g) and 4Cu1Ni-Mg/HSAG (243 m^2/g) samples, presumably due to the incorporation of magnesium oxide and the reduced metal NPs that form crystallites (especially copper) that block the space formed by the aggregation of the graphite grains. Thus, it was not surprising that the 4Cu1Ni-Mg/HSAG sample treated in helium at 723 K prior reduction with hydrogen, showed further decrease of the BET area (214 m^2/g) compared with the 4Cu1Ni-Mg/HSAG sample only reduced in hydrogen at 573 K, presumably due to the formation of crystallites of bigger size as it was observed by XRD.

Table 4.4.2 Textural parameters of support and reduced catalysts.

Sample	S_{BET} (m^2/g)
HSAG	399
Mg/HSAG	317
5Cu-Mg/HSAG	270
5Ni-Mg/HSAG	303
4Cu1Ni-Mg/HSAG	243
4Cu1Ni-Mg/HSAG*	214

The ``*`` indicates that the material was thermally treated in helium at 723 K prior to reduction with hydrogen.

4.4.2.2. Surface properties

Temperature-programmed desorption (TPD) of NH_3 was performed for selected samples in order to obtain the distributions of acidic sites that can be seen in Figure 4.4.5. All samples were reduced in situ with hydrogen at 573 K except 5Ni/HSAG and 5Ni-Mg/HSAG, which were reduced at 723 K. After detailed observation of the NH_3-TPD profiles, it can be concluded that the samples studied present acid sites with different strengths, since each profile can be deconvoluted into three components with a maximum at 450, 540 and 625 K, corresponding to weak (350-500 K), medium (500-550) and strong (550-675 K) acid sites. This correlation between temperature and acid strength is in accordance with other scales found in literature for Cu/ZnO and other catalysts with Al_2O_3 and SiO_2 as supports [59,178,180]. Therefore, the distribution of acid strength was obtained after deconvolution of the NH_3-TPD profiles of all samples as can be seen in the Annex section A3 (Figure A3.2). The acidity distribution resulting after deconvolution of the NH_3-TPD profiles is shown in Table 4.4.3, considering the area under each TPD curve and the ones of the deconvoluted peaks. The normalized area under each curve in arbitrary units is also showed in Table 4.4.3 to compare the total acidity of the catalysts.

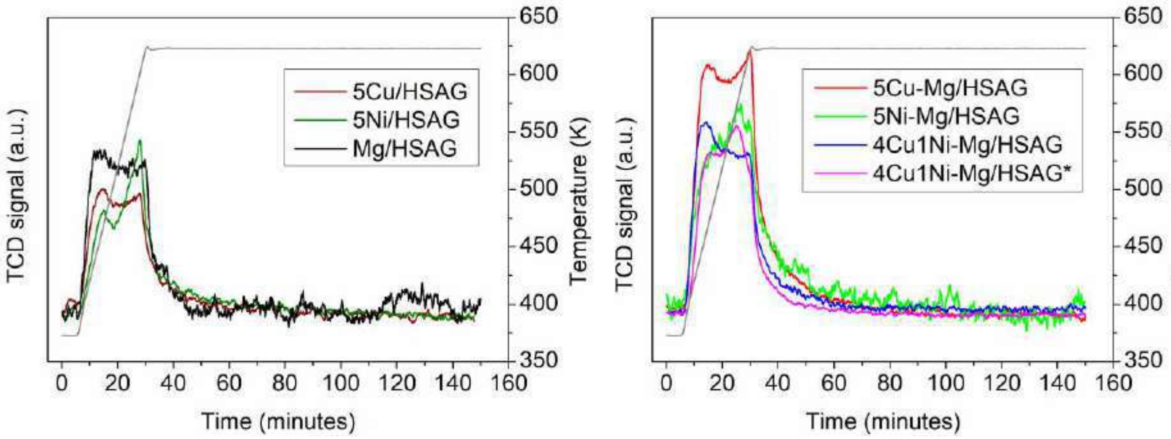

Figure 4.4.5 NH_3-TPD profiles of the Mg/HSAG, 5Cu/HSAG, 5Ni/HSAG and the bifunctional catalysts reduced in situ. The ``*`` indicates that the material was thermally treated in helium at 723 K prior to reduction with hydrogen.

Table 4.4.3 shows an increase in the amount of surface acid sites for the bifunctional catalysts with respect to the monometallic 5Cu/HSAG and 5Ni/HSAG as well as the Mg/HSAG sample. The adsorption of ammonia at metal surfaces such as copper and nickel has been previously reported on literature [181,182,207] and there is a general consensus on the nature of the metal-ammonia bonding, in which the NH_3 molecule is bound through its nitrogen atom. Biemolt et al [181] reported that the ammonia-metal bond involves a relatively weak orbital interaction between the metal valence electrons and the lone pair of ammonia, and a strong electrostatic interaction between the permanent dipole of NH_3 and the positive charge of the copper nucleus. Moreover, metallic Cu nanoparticles are reported to act as a Lewis acid due to their electron-deficient nature [208]. The samples 5Cu-Mg/HSAG and 5Ni-Mg/HSAG show similar NH_3-TPD profiles than their counterparts without magnesium oxide, 5Cu/HSAG and 5Ni/HSAG, even though the areas and therefore the total acidity are superior when supported on Mg/HSAG since the bifunctional samples combine the metallic and the exposed MgO centers, the latter partially covered by copper and nickel NPs. The sample 5Cu-Mg/HSAG presents the most total acidity (Figure 4.4.5 and Table 4.4.3) even though it shows relatively uniform acid sites distribution (35% strong acid sites and 34% weak acid sites). The percentage of weak acid sites seems to predominate for the samples Mg/HSAG and 4Cu1Ni-Mg/HSAG (38 and 40%, respectively), while the percentage of strong acid sites predominates for the samples 5Ni-Mg/HSAG and 4Cu1Ni-Mg/HSAG* (39 and 41%, respectively). In addition, it can be observed in Figure 4.4.5 and Table 4.4.3 that the presence of nickel in the bimetallic catalysts (4Cu1Ni-Mg/HSAG and 4Cu1Ni-Mg/HSAG*) decrease the total acidity with respect to the monometallic bifunctional catalysts, specially 5Cu-Mg/HSAG. The bimetallic catalyst treated in helium at 723 K shows an increase in the amount of strong acid sites compared to its counterpart without thermal treatment, probably due to the incorporation of copper and nickel into the structure of magnesium oxide after this thermal treatment.

Table 4.4.3 Acidity distribution derived after deconvolution of the NH_3-TPD profiles.

Sample	NH_3-TPD Area (a.u.)	% Weak acid sites	% Medium acid sites	% Strong acid sites
5Cu/HSAG	1.3	35	31	34
5Ni/HSAG	1.3	31	26	43
Mg/HSAG	1.6	38	33	29
5Cu-Mg/HSAG	2.6	34	31	35
5Ni-Mg/HSAG	2.0	29	32	39
4Cu1Ni-Mg/HSAG	1.9	40	31	29
4Cu1Ni-Mg/HSAG*	1.7	29	30	41

The ``*`` indicates that the material was thermally treated in helium at 723 K prior to reduction with hydrogen.

The strength distribution and number of surface basic sites were estimated by adsorption microcalorimetry measurements using carbon dioxide as molecular probe. Figure 4.4.6 illustrates the distribution of basic sites representing the differential heat of adsorption as a function of surface coverage for the studied catalysts, whereas Table 4.4.4 summarizes the results obtained. Foremost, the strength of basic sites can be classified as strong (Qdiff>110 KJ/mol), medium (110>Qdiff>60 KJ/mol) and weak (Qdiff<60 KJ/mol), while a differential heat of 40 kJ/mol is considered the boundary between chemical and physical CO_2 adsorption [151,152].

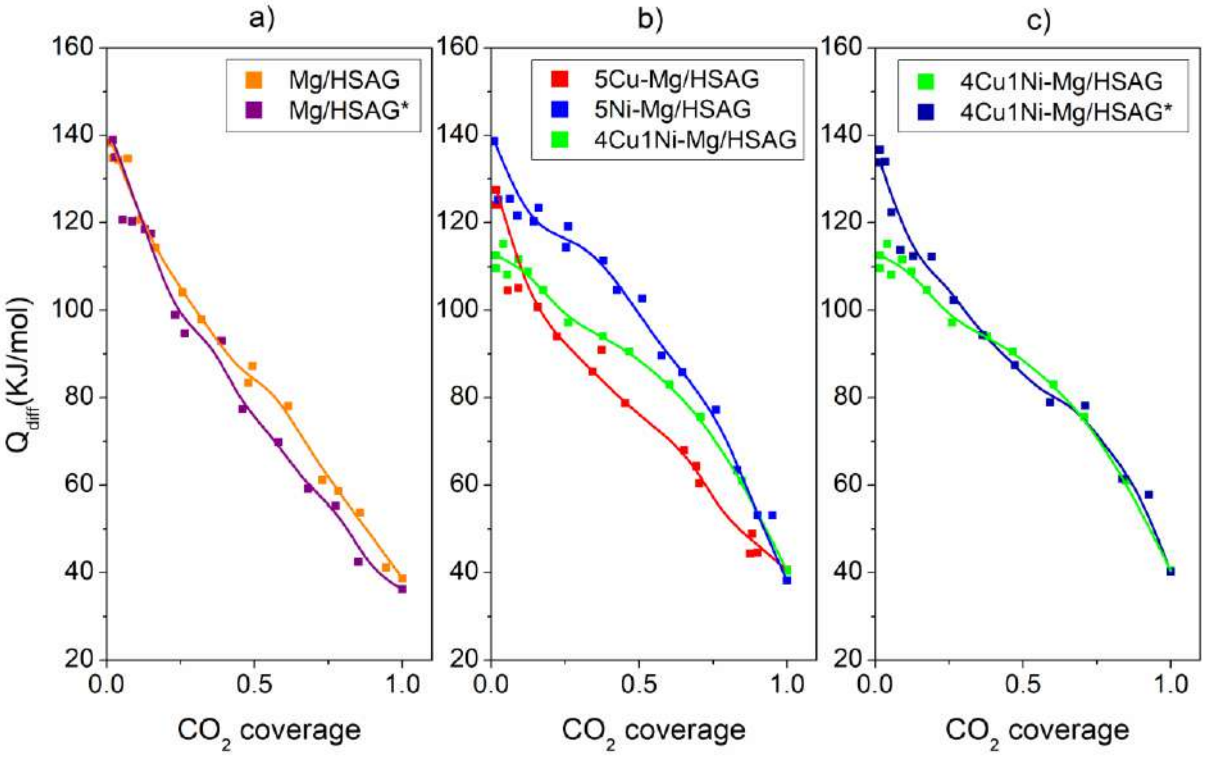

Figure 4.4.6 Differential heats of CO_2 adsorption vs. coverage at 323 K. a) Mg/HSAG before and after thermal treatment, b) Cu-Ni bifunctional catalysts, c) 4Cu1Ni-Mg/HSAG before and after thermal treatment. The ``*`` indicates that the material was thermally treated in helium at 723 K prior to reduction with hydrogen.

Interestingly, the sample Mg/HSAG presents similar strength distribution and heats of adsorption after thermal treatment at 723 K (Mg/HSAG*, Figure 4.4.6a), although the total amount of CO_2 adsorbed is higher for the latter (Table 4.4.4). The lower total amount of basic sites observed for Mg/HSAG may be due to the water and CO_2 adsorbed after ambient exposition that disappear when the sample is treated in situ at 723 K, giving rise to enhanced basicity. Remarkably, the total amount and the percentage of strong basic sites decrease for the sample 5Cu-Mg/HSAG compared to Mg/HSAG. However, the percentage of strong sites is noticeably higher for 5Ni-Mg/HSAG with a total amount of basic sites similar to that of Mg/HSAG after thermal treatment, since the former is reduced at 723 K. In order to understand the different basicity displayed by both metals supported on Mg/HSAG, the bimetallic 4Cu1Ni-Mg/HSAG catalyst was also studied. Interestingly, the sample 4Cu1Ni-Mg/HSAG exhibits a sharp decrease in the percentage of strong basic sites (8%, Table 4.4.4) compared to the sample with copper and nickel alone (12 and 38%, respectively), even though the total amount of basic sites is not as lower (70 μmol CO_2/g) than the one achieved with 5Cu-Mg/HSAG (54 μmol CO_2/g). Nevertheless, the same sample after thermal treatment in helium at 723 K shows higher heats of adsorption at initial values of surface CO_2 coverage with a 18% of strong basic sites, while the total amount of basic sites remains unalterable. This strengthening of basicity also observed for the sample 5Ni-Mg/HSAG, has been associated with metal-support interaction at higher temperatures, since it is noteworthy that the samples that have been reduced or treated at 723 K are those with higher strength of basic sites. Moreover, the correlation between the strengthening of the surface basicity of magnesium oxide and metal-MgO interaction at higher temperatures has been widely reported in literature and previous studies of our group [163,164,165,166,167,183], where it was concluded that the incorporation of metals atoms in the MgO lattice, that takes place at higher temperatures, improves the basic surface of MgO. Particularly, Ueda et al. [164] observed that the surface basicity of magnesium oxide is enhanced by the addition of nickel and copper ions to the MgO, increasing the total amount of basic sites. It should be noted that Ueda's catalysts were not reduced with hydrogen and that they were pretreated in nitrogen at 873 K prior to the calorimetric analysis, while in this study only the metallic samples 5Ni-Mg/HSAG and 4Cu1Ni-Mg/HSAG have been treated at 723 K. Therefore, the metal-support interaction effect successfully explain the different basicity obtained for copper and nickel catalysts, since the 5Cu-Mg/HSAG sample has only been treated at 623 K during degasification, temperature not high enough to achieve a Cu-MgO interaction as strong as the Ni-MgO achieved at 723 K.

Table 4.4.4 CO_2 chemisorption capacities at 323 K and type of basic sites.

Sample	Total	Basic sites distribution		
	µmol CO_2/g (Q_{diff}> 40 kJ/mol)	% Strong sites (Q_{diff}>90 kJ/mol)	% Medium-strength (90>Q_{diff}>60 kJ/mol)	% Weak-strength (60>Q_{diff}>40 kJ/mol)
Mg/HSAG	65	19	55	26
Mg/HSAG*	85	21	56	23
5Cu-Mg/HSAG	54	12	62	26
5Ni-Mg/HSAG	86	38	49	13
4Cu1Ni-Mg/HSAG	70	8	77	15
4Cu1Ni-Mg/HSAG*	69	18	70	12

The ``*`` indicates that the material was thermally treated in helium at 723 K prior to reduction with hydrogen.

The results of TEM analysis are summarized in Figures 4.4.7 and 4.4.8, which depict selected TEM images of the catalysts and their corresponding histograms representing the particle size distribution. It is interesting to note that TEM cannot differentiate Cu from Ni species without an element specific signal detector; thus, the compositional information was obtained with an EDX detector coupled to the TEM/STEM setup. However, the TEM images confirm the formation of well-dispersed metal nanoparticles with a diameter ranging between 4 and 10 nm after reduction with hydrogen, which can be attributed to the formation of active Cu^0 and/or Ni^0 species. The histograms obtained after measuring a statistical meaningful number of nanoparticles, show an almost Gaussian particle size distribution for the majority of the reduced catalysts, especially the monometallic ones, whereas the bimetallic catalysts and all the samples after reaction show a long-tail distribution at higher particle size.

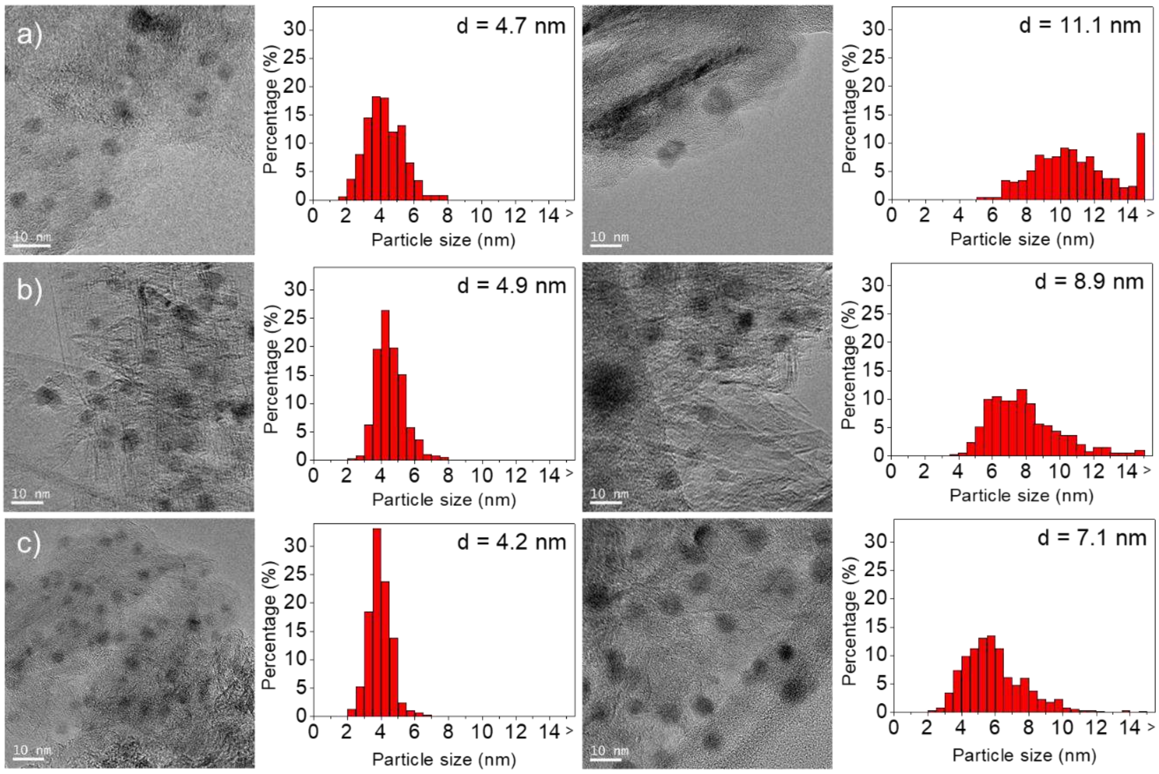

Figure 4.4.7 TEM images of catalysts reduced with hydrogen (left) and after reaction (right): a) 5Cu/HSAG, b) 5Ni/HSAG, and c) 4Cu1Ni/HSAG.

Although Cu and Ni species cannot be differentiated by observation of the TEM images, some interesting information can be drawn from the evaluation of both Figures 4.4.7 and 4.4.8. First, the presence of magnesium seems to negatively affect copper particle size, since all copper containing catalysts present bigger particle size than their reduced counterparts without magnesium, 5Cu/HSAG and 4Cu1Ni/HSAG (4.7 and 4.2 nm, Figure 4.4.7a and 4.4.7c), as the X-ray study revealed. On the other hand, the particle size of reduced 5Ni/HSAG and 5Ni-Mg/HSAG are practically the same (4.9 nm and 4.5 nm, respectively, Figure 4.4.7b and 4.4.8b), while bimetallic Cu-Ni catalysts show smaller particle size with increasing nickel content: 6.8 nm for 4.75Cu0.25Ni-Mg/HSAG, 6.6 nm for 4Cu1Ni-Mg/HSAG and 5.8 nm for 2.5Cu2.5Ni-Mg/HSAG. Furthermore, the average particle size increases for all catalysts after reaction (Figure 4.4.7 and 4.4.8, right), especially for the samples containing copper. Interestingly, all copper containing catalysts after reaction present almost 10% of particles with a diameter bigger than 15 nm, except 4Cu1Ni/HSAG (Figure 4.4.7c, right) and 4Cu1Ni-Mg/HSAG (Figure 4.4.8d, right), whose average particle size is 7.1 nm with only 0.1% and 5% of the particles bigger than 15 nm, respectively. All in all, it seems that the introduction of nickel efficiently prevents copper sintering in a certain degree, where 1 wt% is the optimal nickel content to avoid major copper agglomeration. The same sample was also studied after thermal treatment in helium at 723 K prior reduction with hydrogen and TEM analysis revealed further sintering of the particles (8.8 nm, Figure 4.4.8f left) with approximately 20% of the particles bigger than 15 nm. As it was expected, the average diameter of the particles increased to 9.7 nm (Figure 4.4.8f right) for 4Cu1Ni-Mg/HSAG* after reaction, which seems to be correlated with the decrease in conversion observed for this catalyst (Table 4.4.1).

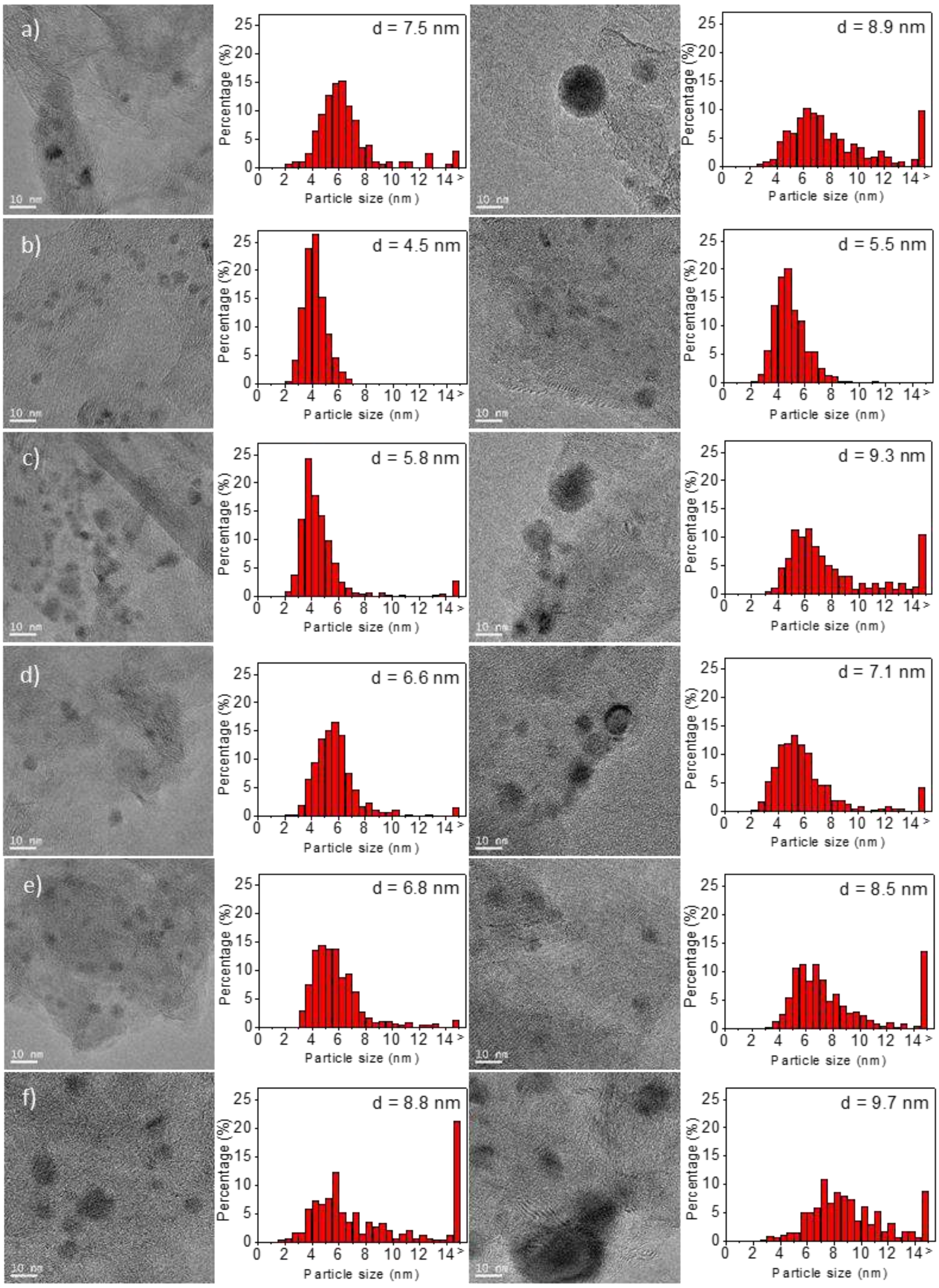
a)
d = 7.5 nm
d = 8.9 nm
b)
d = 4.5 nm
d = 5.5 nm
c)
d = 5.8 nm
d = 9.3 nm
d)
d = 6.6 nm
d = 7.1 nm
e)
d = 6.8 nm
d = 8.5 nm
f)
d = 8.8 nm
d = 9.7 nm
Percentage (%)
Particle size (nm)
0 2 4 6 8 10 12 14 >
0 5 10 15 20 25
10 nm

Figure 4.4.8 TEM images of catalysts reduced with hydrogen (left) and after reaction (right): a) 5Cu-Mg/HSAG, b) 5Ni-Mg/HSAG, c) 2.5Cu2.5Ni-Mg/HSAG, d) 4Cu1Ni-Mg/HSAG, e) 4.75Cu0.25Ni-Mg/HSAG, f) 4Cu1Ni-Mg/HSAG*. The ``\*`` indicates that the material was thermally treated in helium at 723 K prior to reduction with hydrogen.

EDX elemental mapping was performed in order to identify the interaction between Cu, Ni and Mg and the distribution of the nanoparticles on the support. The EDX images of monometallic catalysts (Figure 4.4.9) showed that the active phases (magnesium and the metal, copper or nickel) were highly dispersed on the carbonaceous support coinciding in space.

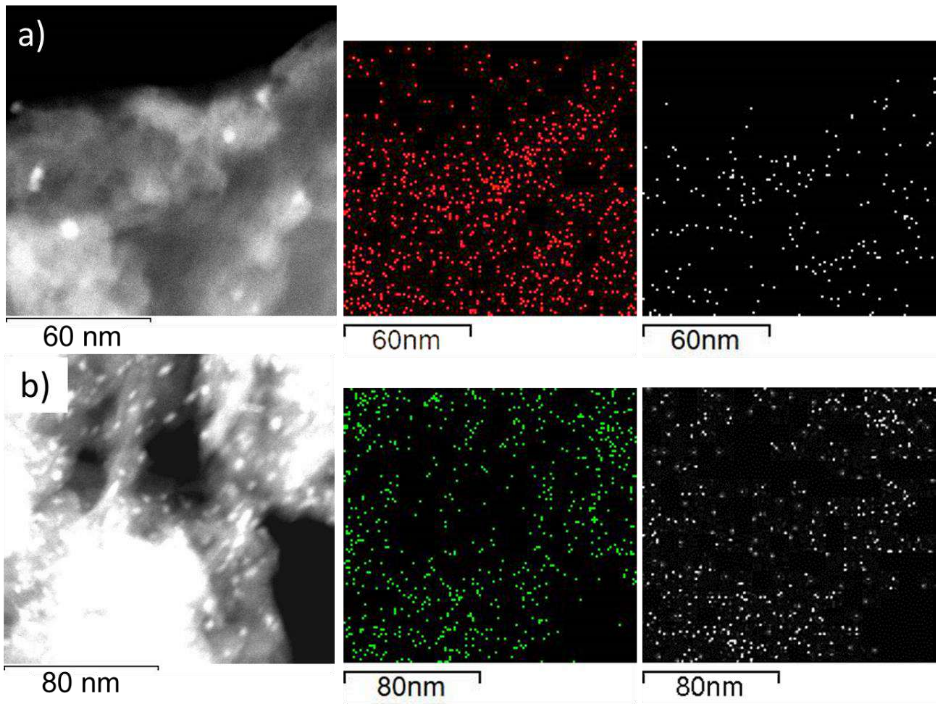

Figure 4.4.9 EDX elemental mapping of catalysts reduced in hydrogen at 573 K: a) 5Cu-Mg/HSAG, b) 5Ni-Mg/HSAG. Color code refers to the distribution of elements (Cu, red; Ni, green; Mg, white).

The bimetallic Cu-Ni catalysts reduced (Figure 4.4.10) and after reaction (Figure 4.4.11) were also analyzed by EDX to further study the interaction between copper and nickel and the likely copper sintering evidenced by XRD and BET analysis. The samples reduced at 573K showed copper particles of heterogeneous size, while nickel and magnesium appeared well dispersed. Nevertheless, copper particles, regardless of their size, coincided in space with nickel and magnesium, evidencing the formation of copper-nickel particles dispersed over Mg/HSAG. On the other hand, the samples after reaction (Figure 4.4.11) showed Cu-Ni particles of bigger size, although these big particles show a composition with a Cu/Ni ratio larger than that of the bulk chemical analysis. Even for the catalyst with the same copper and nickel content (2.5Cu2.5Ni-Mg/HSAG, Figure 4.4.11a), the bigger particles seem to be enriched in Cu. All things considered, the sintering that takes place during reaction, previously observed by XRD and TEM, could be attributed specially to copper particles. This superficial re-accommodation and agglomeration of nickel and especially copper particles seems to occur at early stages of the reaction prior to reaching the steady state conditions, since Figure 4.4.1 showed stable conversion for all catalysts after reaching a maximum at 3-4 h.

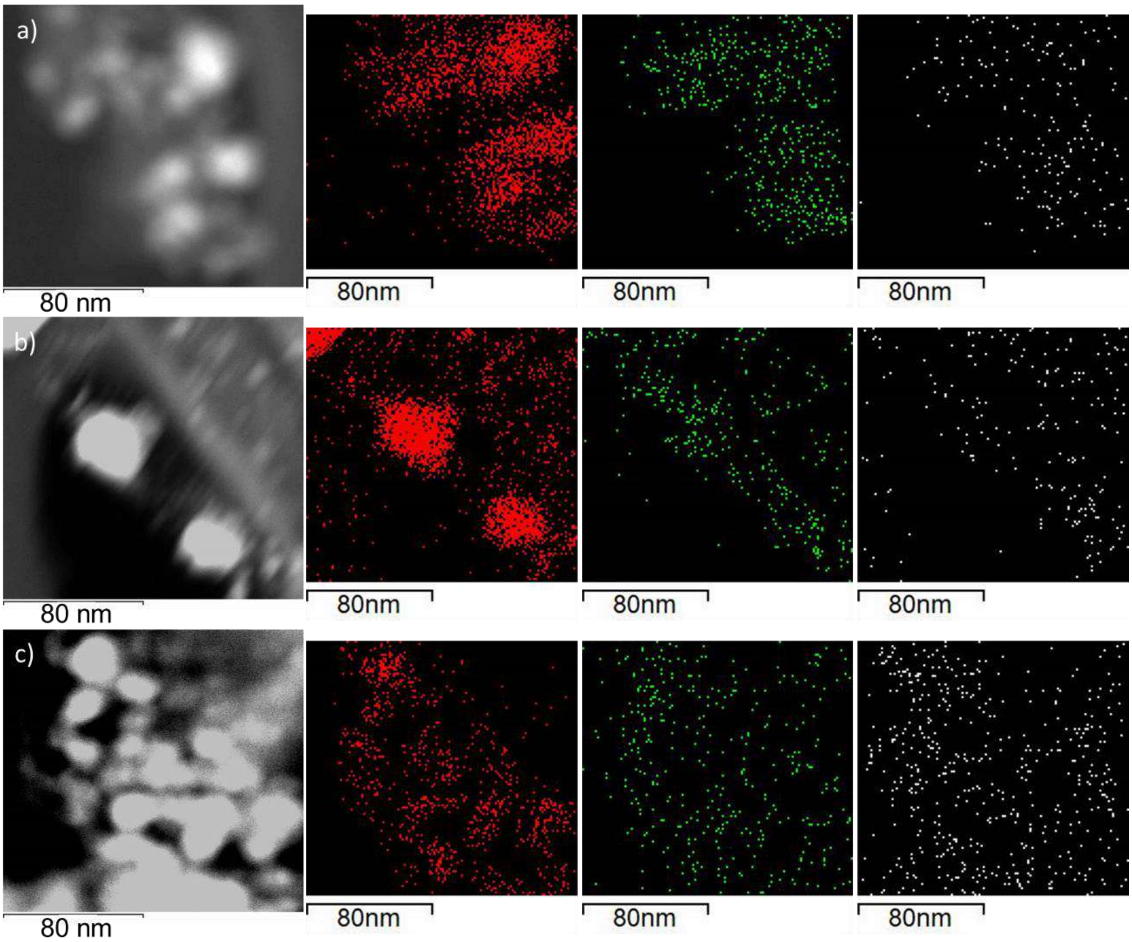
a)
80 nm
80nm
80nm
80nm
b)
80 nm
80nm
80nm
80nm
c)
80 nm
80nm
80nm
80nm

Figure 4.4.10 EDX elemental mapping of catalysts reduced in hydrogen at 573 K: a) 2.5Cu2.5Ni-Mg/HSAG, b) 4Cu1Ni-Mg/HSAG, c) 4.75Cu0.25Ni-Mg/HSAG. Color code refers to the distribution of elements (Cu, red; Ni, green; Mg, white).

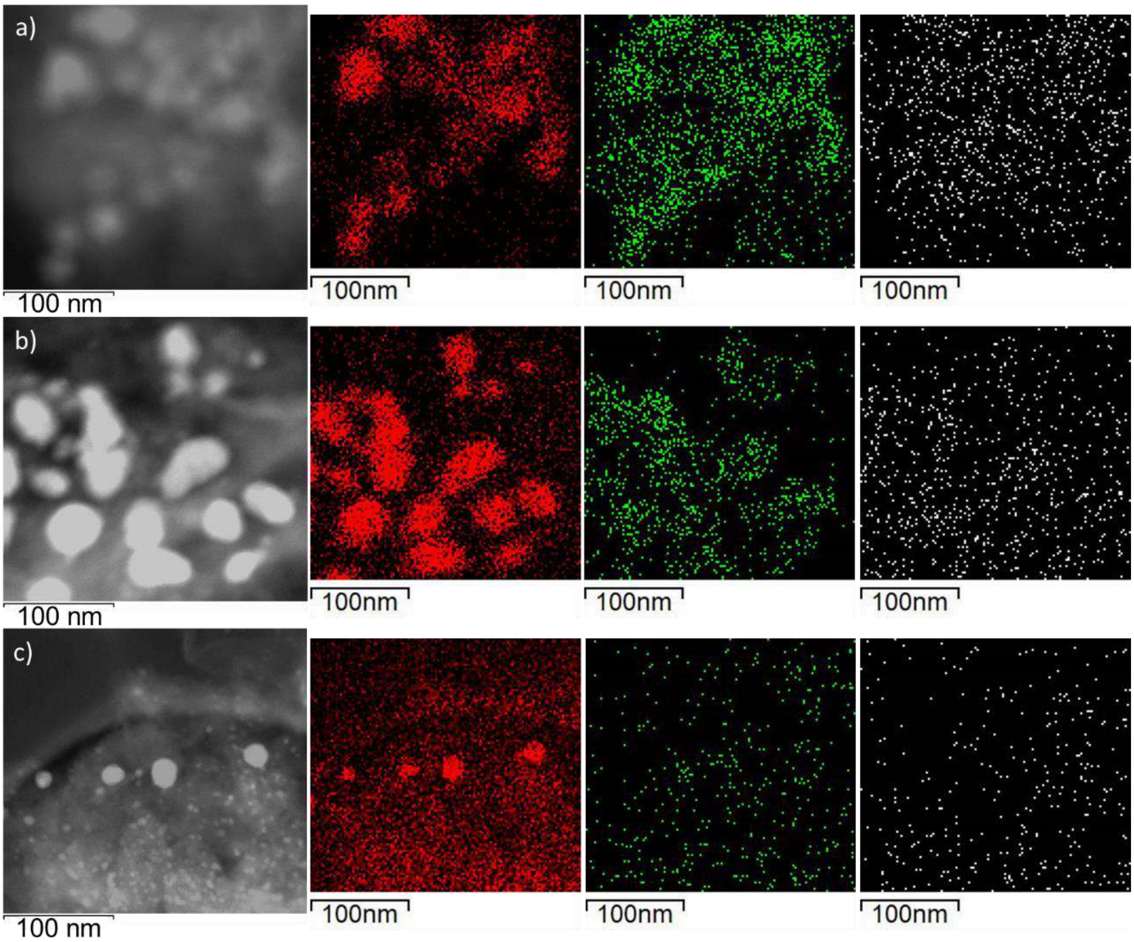

Figure 4.4.11 EDX elemental mapping of catalysts after reaction at 503 K and 50 bar: a) 2.5Cu2.5Ni-Mg/HSAG, b) 4Cu1Ni-Mg/HSAG, c) 4.75Cu0.25Ni-Mg/HSAG. Color code refers to the distribution of elements (Cu, red; Ni, green; Mg, white).

Surface analysis of the catalysts was accomplished with the aim of identifying and quantifying the different species present in the surface of the catalysts. For the sake of brevity, Figure 4.4.12 only shows the Mg 2p, Cu $2p_{3/2}$ and the Ni $2p_{3/2}$ core level spectra as well as the X-ray generated Cu LMM Auger spectra of catalyst R-4Cu1Ni-Mg/HSAG* treated in helium at 723 K before reduction in hydrogen at 573 K as an example, since all samples present similar XPS spectra as can be seen in the Annex section A3 (Figures A3.3-A3.9). The Mg 2p peak of the monometallic catalysts was deconvoluted into three components corresponding to MgO, $Mg(OH)_2$ and $MgCO_3$, which are generally associated to binding energies in the range 50.1-50.8 eV, 49.5-51.5 eV, and from 50.4 and up to 54.0 eV, respectively [209,210,211,212,213]. The surface concentration of each species is tabulated in Table 4.4.5, being MgO the most abundant. As it can be seen in Table 4.4.5 and Figure 4.4.12 (top left), the bimetallic samples only show one contribution of Mg 2p corresponding to MgO.

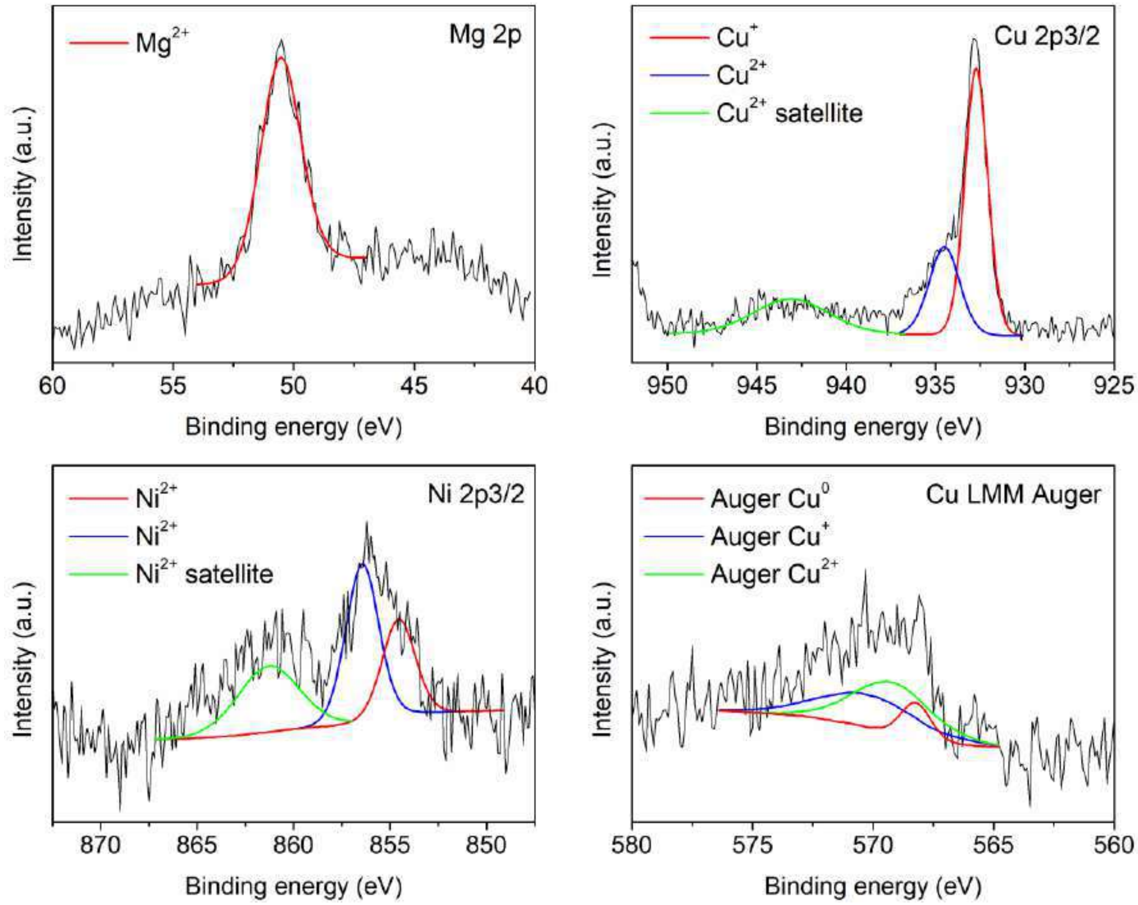

Figure 4.4.12 Mg 2p (top left), Cu $2p_{3/2}$ (top right), Ni $2p_{3/2}$ (bottom left) and X-ray generated Cu LMM Auger (bottom right) XPS spectra of sample R-4Cu1Ni-Mg/HSAG* treated in helium at 723 K before reduction in hydrogen at 573 K.

It can be observed in Table 4.4.5 that the catalysts studied show different copper oxidation states, especially comparing the reduced catalysts and their counterparts after reaction. All the reduced catalysts show a contribution at ca 934.5 eV with a characteristic satellite at the high binding energy side, indicative of the presence of Cu^{2+} [196,197,214,215]. After reaction at 503 K and 50 bar, the Cu $2p_{3/2}$ peak is shifted to lower binding energies accompanied by the reduction of the satellite peak, which indicates that the smallest copper nanoparticles become oxidized by ambient exposition. This conclusion is in agreement with the XRD results (Figure 4.4.3 and 4.4.4) previously discussed. Nevertheless, the most intense copper $2p_{3/2}$ peak appears for all catalysts at ca 932.9 eV, typical of either Cu^0 or Cu^+ [196,197], which where differentiated through examination of the L_3VV X-ray induced Auger transition and the calculation of the modified Auger parameter, α'_A, which was defined as:

$$\alpha'_A = hv + KE_{LMM} - KE\ Cu2p_{3/2} \qquad Equation\ 4.2$$

Where KE_{LMM} and KE $Cu2p_{3/2}$ are the kinetic energies of the L_3VV X-ray induced Auger-emitted electrons and the Cu $2p_{3/2}$ photo-emitted electrons, respectively [195,214]. The analysis of the Auger peak-shape confirmed the presence of Cu^{2+} in all the reduced catalysts and the samples after reaction through observation of the Cu $L_3M_{45}M_{45}$ peak at a kinetic energy of ca 917.6 eV and the estimation of the Auger parameter α'A, which resulted in the region of 1851.6-1851.9 eV, characteristic of Cu^{2+} species [196]. The main contribution of the Auger peak for all catalysts appeared at ca 916.8 eV with a α'_A in the range 1849.1-1849.6 eV, which revealed the presence of Cu^+ in all cases. Interestingly, both bimetallic samples after reaction (R-4Cu1Ni-Mg/HSAG and R-4Cu1Ni-Mg/HSAG*) exhibited a Cu $L_3M_{45}M_{45}$ peak at a kinetic energy of ca 918.5 eV with a α'A at 1851.1 and 1851.9 eV, respectively, characteristic of metallic copper [185]. The presence of Cu^{2+} could be ascribed to surface oxidation of the reduced sample under ambient air at room temperature, whereas the core must remain Cu^0 since the formation of metallic copper nanoparticles was evidenced by XRD and TEM analysis. However, the reductive atmosphere of the XPS chamber might induce the reduction of surface Cu^{2+} into Cu^+.

Table 4.4.5 Binding energies (eV) of core electrons and the Auger parameter (eV) of catalysts samples reduced in hydrogen at 573 K and after reaction (R-). *Thermally treated in helium at 723 K prior reduction with hydrogen.

	BE (eV) Mg 2p	**BE (eV) Cu 2p 3/2**		**Auger parameter**			**BE (eV) Ni 2p 3/2**
		Cu^0 / Cu^+	**Cu^{+2}**	**Cu^0**	**Cu^+**	**Cu^{+2}**	**Ni^{+2}**
5Cu-Mg/HSAG	50.4 (63)* 51.1 (31) 52.4 (6)	933.1	934.8	-	1849.1 (67)	1851.9 (33)	-
5Ni-Mg/HSAG	50.3 (81) 51.4 (13) 52.0 (6)	-	-	-	-	-	854.4 (50) 856.3 (50)
4Cu1Ni-Mg/HSAG	50.7	933.0	934.9	-	1849.6 (58)	1851.9 (42)	854.4 (42) 856.6 (58)
4Cu1Ni-Mg/HSAG*	50.7	932.8	934.6	-	1849.1 (44)	1851.6 (56)	854.6 (37) 856.5 (63)
R-5Cu-Mg/HSAG	50.4 (66) 51.1 (26) 52.2 (8)	932.8	934.6	-	1849.2 (85)	1851.9 (15)	-
R-5Ni-Mg/HSAG	50.2 (73) 51.3 (22) 52.5 (5)	-	-	-		-	853.3 (43) 856.1 (57)
R-4Cu1Ni-Mg/HSAG	50.7	932.9	934.9	1851.9 (33)	1849.1 (48)	1851.9 (19)	854.8 (36) 856.5 (64)
R-4Cu1Ni-Mg/HSAG*	50.6	932.7	934.5	1851.1 (13)	1849.1 (39)	1851.9 (47)	854.6 (38) 856.5 (62)

*The concentration of each species in atomic percent is shown in parentheses.

The analysis of Ni $2p_{3/2}$ spectra of all samples showed a main peak at ca 855 eV with a satellite peak at 861-862 eV, which is characteristic of Ni^{2+} oxidation states [203,216,217]. Taking other studies found in literature as a reference [192,198,199], the main peak was deconvoluted into two components at ca 854 eV and ca 856 eV. Moreover, the surface oxidation to Ni^{2+} might explain the absence of metallic nickel on the catalysts surface, which is evident since its corresponding peak usually appears at lower binding energies (852.6 eV) [216].

XPS atomic ratios of Metal/C, Mg/C, Cu/Ni, and Metal/Mg for the samples studied are given in Table 4.4.6. The reaction at 503 K and 50 bar is accompanied by a substantial decrease in the Cu/C, Cu/Mg and Cu/Ni atomic ratios that points to the formation of large copper nanoparticles on the catalyst surface, whereas nickel nanoparticles do not suffer intense sintering since the decrease of the Ni/C and Ni/Mg ratios after reaction is far less accentuated. This behavior clearly demonstrates once again that copper nanoparticles have more tendency to agglomerate after reaction at 503 K and 50 bar compared to nickel nanoparticles, confirming the conclusions drawn from XRD, EDX and TEM analysis. In contrast, the Mg/C ratio slightly decreases for all samples after reaction, with almost no appreciable decrease for the bimetallic catalysts. This behavior indicates that magnesium do not suffer the same agglomeration that nickel and especially copper nanoparticles, which is in agreement with the conclusions derived from the Mg mappings (Figure 4.4.11), where it can be observed that this element is well dispersed over the carbonaceous support.

It should be highlighted that the bimetallic catalyst 4Cu1Ni-Mg/HSAG shows higher Cu/Ni atomic ratio obtained by XPS (Table 4.4.6) than the nominal atomic ratio (Cu/Ni = 3.69), which indicates that the surface of the bimetallic particles is enriched by copper, due to its lower heat of sublimation compared to nickel. Surface copper enrichment has been previously reported by literature for Cu-Ni supported on Al_2O_3, ZrO_2 and CeO_2/ZrO_2 [201,202], and Cu-Ni nanostructured alloys [200].

Table 4.4.6 Atomic ratios for catalysts samples reduced in hydrogen at 573 K and after reaction (R-).

	Cu/C	Ni/C	Mg/C	Cu/Ni	Cu/Mg	Ni/Mg
5Cu-Mg/HSAG	0.0038		0.0057		0.66	
5Ni-Mg/HSAG		0.0016	0.0052			0.31
4Cu1Ni-Mg/HSAG	0.0030	0.0007	0.0069	4.01	0.43	0.11
4Cu1Ni-Mg/HSAG*	0.0021	0.0006	0.0063	3.61	0.33	0.09
R-5Cu-Mg/HSAG	0.0026		0.0048		0.54	
R-5Ni-Mg/HSAG		0.0011	0.0043			0.25
R-4Cu1Ni-Mg/HSAG	0.0013	0.0004	0.0069	3.44	0.19	0.05
R-4Cu1Ni-Mg/HSAG*	0.0015	0.0006	0.0060	2.51	0.24	0.10

4.4.3. Discussion

To rationalize the synergistic behavior of the metals and magnesium, the catalytic performance of both functions should be first analyzed separately. Foremost, the catalysts Cu/HSAG, Ni/HSAG and 4Cu1Ni/HSAG were studied in absence of magnesium, showing high activity for the conversion of ethanol but with quite low selectivity towards 1-butanol (4, 7 and 5%, respectively, Table 4.4.1). Particularly, acetaldehyde and 1,1-diethoxyethane were the principal by-products for Cu/HSAG whereas methane, carbon monoxide, diethyl ether, and acetone constituted the main undesired products of Ni/HSAG. As it was expected, 4Cu1Ni/HSAG showed an intermediate behavior in terms of conversion and product distribution when compared with the monometallic catalysts supported on HSAG, with acetaldehyde, 1,1-

diethoxyethane, methane, carbon monoxide and acetone as principal by-products. Since the dehydrogenation of ethanol towards acetaldehyde is the first step of the Guerbet reaction, it is interesting to note that the selectivity of acetaldehyde is 52% for Cu/HSAG, 24% for Ni/HSAG and 39% in the case of 4Cu1Ni/HSAG, which is in agreement with literature since copper is well-known for catalyzing the formation of acetaldehyde via ethanol dehydrogenation [52].

On the other hand, although the conversion of the Mg/HSAG sample is insignificant, the analysis of its product distribution is quite interesting even though the compounds (mainly acetaldehyde, diethyl ether and ethylene) were only traces in the product stream since more than 99% was unconverted ethanol. That is to say, catalyst Mg/HSAG is unable of upgrading ethanol to 1-butanol but given that acetaldehyde is the product of the base catalyzed dehydrogenation of ethanol, whereas diethyl ether and ethylene are both the products of the acid catalyzed dehydration of ethanol, their presence in the product stream confirms that the catalyst Mg/HSAG contains acid/base sites as it was previously concluded after the characterization analysis (Table 4.4.3 and 4.4.4). Therefore, the results point to the likelihood that the combination of the active Cu and Ni nanoparticles with the acid/base sites of Mg/HSAG would result in a synergistic effect for the upgrading of ethanol towards 1-butanol.

As expected, the bifunctional catalysts considerably improved the selectivity towards 1-butanol compared to their counterparts without magnesium, since 1-butanol selectivity rises from 4 to 26% with Cu/HSAG and 5Cu-Mg/HSAG, respectively, and it increases from 7 to 24% with Ni/HSAG and 5Ni-Mg/HSAG, respectively (Table 4.4.1). This enhancement is even more pronounced for the bimetallic Cu-Ni catalysts, since 1-butanol selectivity reaches 31% for 4.75Cu0.25Ni-Mg/HSAG, 32% for 2.5Cu2.5Ni-Mg/HSAG and 39% for 4Cu1Ni-Mg/HSAG (while 4Cu1Ni/HSAG only reached 5%), with quite comparable ethanol conversion levels. The improved 1-butanol selectivity of the bifunctional M-Mg/HSAG catalysts could be ascribed to the exposed metal sites, necessary for catalyzing the dehydrogenation/hydrogenation reactions, combined with a good equilibrium of the acid/base sites, which catalyze the dehydration of 3-hydroxybutanal (Figure 1.3.1, R3) and the aldol condensation (R2), respectively. Although it is well accepted in literature that the increase of 1-butanol selectivity is related to the presence of high strength basic sites [21,54,55,169], the results suggest that the combination of medium-high strength basicity and the presence of acid sites in medium-low concentration is preferable to achieve superior 1-butanol yields. To support this conclusion, it is important to note that 5Ni-Mg/HSAG is the least selective catalyst (23%) despite containing the largest amount of basic sites (86 µmol CO_2 chemisorbed/g, 38% of high strength, Table 4.4.4) and the most total acidity (Figure 4.4.5 and Table 4.4.3, 39% of strong acid sites) after 5Cu-Mg/HSAG (Figure 4.4.5 and Table 4.4.3, 35% of strong acid sites), which also contains the lowest amount of basic sites (54 µmol CO_2 chemisorbed/g, 12% of high strength, Table 4.4.4) and exhibits a selectivity towards 1-butanol of 26% (Table 4.4.1). In contrast, the 1-butanol selectivity improves with the sample 4Cu1Ni-Mg/HSAG (39%, Table 4.4.1) compared to the monometallic catalysts, while exhibiting intermediate basicity (70 µmol CO_2 chemisorbed/g, 8% of high strength, 77% of medium strength, Table 4.4.4) between 5Ni-Mg/HSAG and 5Cu-Mg/HSAG, and moderate amount of acid sites, 40% of weak strength (Figure 4.4.5 and Table 4.4.3).

The variable Cu-Ni loading and the presence of magnesium in the catalyst configuration have a direct impact on the acid/base sites and consequently on the product distribution. For instance, Cu/HSAG and 5Cu-Mg/HSAG produce more 1,1-diethoxyethane (31 and 15%, respectively) than the catalysts containing only nickel (Ni/HSAG and 5Ni-Mg/HSAG) given that the percentage of this compound in their product stream is less than 2%. It is noteworthy that the presence of magnesium reduces the formation of 1,1-diethoxyethane compared to Cu/HSAG, presumably due to the introduction of basic sites and that Mg covers the acid sites of HSAG needed to catalyze the acetylation of acetaldehyde with two ethanol molecules that leads to 1,1-diethoxyethane. Concerning the bimetallic Cu-Ni catalysts, the increase of nickel loading and the presence of magnesium considerably reduces the formation of this by-product since its selectivity decreases from 13% for 4Cu1Ni/HSAG to 10% for 4.75Cu0.25Ni-Mg/HSAG, 4% for 4Cu1Ni-Mg/HSAG and finally to 2% for 2.5Cu2.5Ni-Mg/HSAG (Table 4.4.1). Nevertheless, higher nickel loadings considerably intensify the formation of undesired by-products like carbon monoxide, methane and acetone. In this way, methane and carbon monoxide selectivities decrease from 25% and 15% with both Ni/HSAG and 5Ni-Mg/HSAG, to 15% and 11% with 2.5Cu2.5Ni-Mg/HSAG, to 6% and 4% with 4Cu1Ni-Mg/HSAG and finally to 2% and 2% with 4.75Cu0.25Ni-Mg/HSAG. Interestingly, the synergy between the metals and magnesium is also evidenced when comparing the methane and carbon monoxide selectivities obtained with 4Cu1Ni/HSAG (12 and 8%, respectively) and 4Cu1Ni-Mg/HSAG (6 and 4%, respectively). Particularly, in the case of acetone and the catalysts containing nickel, the presence of magnesium once again enhances the suppression of an undesired side reaction as it was previously demonstrated with the reduction of the 1,1-diethoxyethane formed by copper containing catalysts. This is well evidenced since the acetone selectivity is 9% with Ni/HSAG and 7% with 4Cu1Ni/HSAG, while it is reduced to traces for the bifunctional catalysts. Finally, taking into account the effect of the metal loading on the product distribution and the selectivity towards 1-butanol, it seems that the optimal Cu-Ni loading is 4wt.% Cu and 1wt.% Ni, that may be partly segregated and form metallic Cu and Cu–Ni alloy phases, as it has been suggested for silica-supported Cu–Ni nanoparticles with lower nickel contents [218].

Comparing the microscopy results (Figures 4.4.7 and 4.4.8) and the catalytic performance of each catalyst, metal particle size does not seem to be crucial to significantly influence on the ethanol conversion levels. Nevertheless, the reduced 4Cu1Ni-Mg/HSAG* catalyst treated in helium at 723 K exhibits the highest particle size (8.8 nm reduced and 9.7 nm after reaction) which apparently has a negative effect on conversion since it slightly decreases from 24% with 4Cu1Ni-Mg/HSAG to 20% with its counterpart thermally treated in helium. On the contrary, 1-butanol selectivity greatly improves for this catalyst in spite of the slight decrease in conversion. This behavior is in agreement with the previously introduced conclusion that the synergistic effect of the 4wt.% Cu and 1wt.% Ni as the optimal Cu-Ni loading with the medium-high strength basicity and moderate acidity of the resulting bifunctional catalyst, remarkably rises 1-butanol yields. To prove this point, it should be noted that the catalyst 4Cu1Ni-Mg/HSAG* presents mostly medium-high strength basic sites (18% of strong basic sites and 70% of medium strength, Table 4.4.4) with less total acidity (41% of high strength, Table 4.4.3) than 4Cu1Ni-Mg/HSAG (40% of weak strength, Table 4.4.3).

All in all, the results confirm the synergistic effect between the metals and the acid/base sites introduced by magnesium oxide, since appropriate copper and nickel loading, the presence of MgO and the resulting acidity and basicity of the final catalyst, influence on the product distribution and especially on the 1-butanol selectivity, inhibiting undesired side reactions and therefore improving the ethanol condensation path to 1-butanol. Taking into account the points above discussed and the fact that Mg/HSAG alone is unable to upgrade ethanol to 1-butanol, everything suggests that the metal function of the catalyst has a considerable influence on the 1-butanol yields. Consequently, the site time yield towards 1-butanol was calculated (Figure 4.4.13) for the bifunctional catalysts based on the number of metal atoms on the surface per gram. Thus, Figure 4.4.13 highlights how the 4Cu1Ni-Mg/HSAG* catalyst obtained after thermal treatment in helium at 723 K greatly favors the reaction pathway towards 1-butanol thanks to the optimal combination of copper and nickel exposed sites.

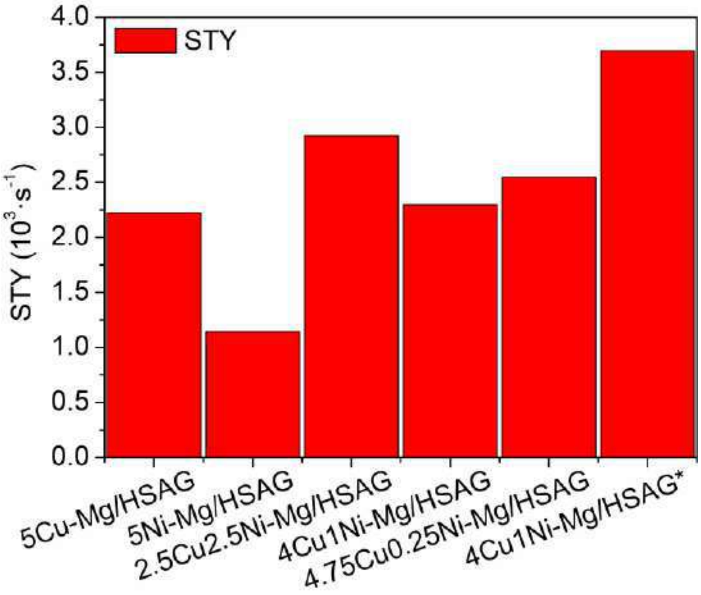

Figure 4.4.13 Site time yield (s^{-1}) for bifunctional catalyst after 7 hours of reaction.

4.4.4. Conclusions

Ethanol was continuously converted to 1-butanol on heterogeneous bifunctional catalysts based on Cu-Ni nanoparticles and magnesium oxide supported over high surface area graphite in a fixed-bed reactor operated in gas phase. All catalysts proved to be very stable, remaining active for 24 h on stream, and the analysis of the product distributions showed that the reaction follows the Guerbet route. The enhancement of the reaction path towards 1-butanol can be attributed to the exposed metal sites, required for catalyzing the dehydrogenation/hydrogenation reactions, combined with a good equilibrium of the acid/base sites, which catalyze the dehydration of 3-

hydroxybutanal and the aldol condensation, respectively. The characterization of the catalytic sites, metal nanoparticles and the acid/base sites, by TEM/EDX analysis, microcalorimetry of CO_2 chemisorption and temperature-programmed desorption of NH_3, revealed information that allowed to explain the differences between their catalytic performance. All things considered, the results endorse the synergistic effect between the acid/base sites provided by magnesium oxide and the Cu-Ni nanoparticles for the upgrading of ethanol towards 1-butanol with improved conversion and selectivity. The bimetallic Cu-Ni catalysts considerably improved the 1-butanol yield, especially 4Cu1Ni-Mg/HSAG* catalyst treated in helium at 723 K, which exhibited stable ethanol conversion of 20% and selectivity to 1-butanol of 44%. Although the sintering of its metal nanoparticles after thermal treatment seems to provide a slightly negative impact in ethanol conversion, its appropriate copper and nickel loading and the presence of medium-high strength basic sites and moderate concentration of acid sites, result in an improved catalyst for the production of 1-butanol and at the same time reducing the formation of undesired products. Comparing the TEM/EDX analysis and the catalytic performance of each catalyst, particle size does not seem to be crucial to achieve good ethanol conversion levels, but the metal function has significant effects on the resulting acidity and basicity of the bifunctional catalyst and therefore on the 1-butanol selectivity and product distribution.

CONCLUSIONS

5. CONCLUSIONS

The general objective of this Doctoral Thesis is to optimize bifunctional heterogeneous catalysts, based on metal NPs and metal oxides with different acid/base properties supported on high surface area graphite, in order to improve their performance in the continuous gas-phase condensation of ethanol into 1-butanol, namely the Guerbet reaction, in a fixed-bed reactor. In short we intended to obtain a catalytic material superior in catalytic performances to those reported in the published scientific literature. The aim is to comprehend the synergistic effect between a metal oxide combined with the metal NPs dispersed on the graphitic support that gives place to an improved catalyst, in terms of 1-butanol yield, when applied in the Guerbet process.

The purpose of this final chapter is to present the more relevant conclusions obtained, which are detailed below.

1) After analyzing the effect of temperature on ethanol conversion and 1-butanol selectivity, 503 K is considered the optimal reaction temperature since the results show that ethanol conversion increases with increasing reaction temperature, whereas the 1-butanol selectivity profile reaches a maximum at 503 K.

2) The characterization of the active metal nanoparticles along with the acidity and basicity properties of the resulting catalysts, pointed out that high 1-butanol yields can be ascribed to the synergistic effect between the acid/base sites provided by the metal oxide, which catalyze the dehydration of 3-hydroxybutanal and the aldol condensation, respectively, and the active metal nanoparticles, that catalyze the dehydrogenation/hydrogenation reactions.

3) Regarding the metal oxide, the results point out that the exposed metal sites are optimal for the catalysts with MgO, closely followed by MnO, in comparison with the catalysts containing BaO and ZnO as the metal oxide. The better catalytic performance of MgO and MnO-based catalysts are ascribed to a good equilibrium between medium-high strength basic sites and medium-weak strength acid sites of the resulting bifunctional catalyst.

4) Regarding the metal NPs, even though Pd/Mg catalysts supported on graphite showed high selectivity to 1-butanol, a combination of Cu-Ni as the metal function is preferred, independently of the metal oxide, since the activity and selectivity achieved with the latter catalysts are very similar to those obtained with Pd-based catalysts. In addition, it should be highlighted that the catalysts with Pd contain bulk MgO while the catalysts with Cu and/or Ni contain considerable less amount of metal oxide. Considering also the higher cost of palladium precursors compared to those of copper and nickel, Cu-Ni catalysts were considered the optimal metal composition.

5) Copper is needed since it considerably speeds up the rate of ethanol dehydrogenation that leads to acetaldehyde, while nickel's activity and less disposition to sintering favored the ethanol conversion. Thus, bimetallic Cu-Ni catalysts proved to combine the best characteristics of both metals, remarkably reducing the formation of unwanted products, being 2.5 wt.% Cu and 2.5 wt.% Ni the optimal metal loading for MnO-based catalysts and 4 wt.% and 1 wt.% the optimal loading for MgO-based catalysts.

6) Comparing the TEM/EDX analysis and the catalytic performance of each catalyst, particle size does not seem to be crucial to achieve good butanol yield levels even though the sintering of metal nanoparticles seems to provide a slightly negative impact in ethanol conversion.

Nevertheless, the metal function has significant effects on the resulting acidity and basicity of the bifunctional catalyst and therefore on the 1-butanol selectivity and product distribution. Thus, a compromise between both parameters must be reached to further optimize these catalysts.

7) For all catalysts, the analysis of the product streams indicated that the reaction pathway follows typical Guerbet route and relevantly is demonstrated the good stability of the here developed catalytic materials, remaining stable and active for 24 h on stream.

BIBLIOGRAPHY

6. BIBLIOGRAPHY

[1] R. Sheldon. Green and sustainable manufacture of chemicals from biomass: State of the art. Green Chem. 16 (2014) 950–963.

[2] B. Valle, A. Remiro, N. García-Gómez, A.G. Gayubo, J. Bilbao. Recent research progress on bio-oil conversion into bio-fuels and raw chemicals: a review. J Chem Technol Biotechnol 94 (2019) 670–689.

[3] P.T. Anastas, J.C. Warner. Green chemistry: theory and practice. Oxford University Press (1998).

[4] A. Camia, N. Robert, R. Jonsson, R. Pilli, S. García-Condado, R. López-Lozano, M. van der Velde, T. Ronzon, P. Gurría, R. M'Barek, S. Tamosiunas, G. Fiore, R. Araujo, N. Hoepffner, L. Marelli, J. Giuntoli. Biomass production, supply, uses and flows in the European Union. First results from an integrated assessment, EUR 28993 EN, Publications Office of the European Union, Luxembourg, 2018.

[5] C.O. Tuck, E. Pérez, I.T. Horváth, R.A. Sheldon, M. Poliakoff. Valorization of biomass: Deriving more value from waste. Science 337 (2012) 695–699.

[6] G. Centi, P. Lanzafame, S. Perathnoer. Analysis of the alternative routes in the catalytic transformation of lignocellulosic materials, Catal. Today 167 (2011) 14–30.

[7] P. Dürre. Biobutanol: An attractive biofuel. Biotechnol. J. 2 (2007) 1525–1534.

[8] P. Dürre. Fermentative Butanol Production. Bulk Chemical and Biofuel. Ann. N.Y. Acad. Sci. 1125 (2008) 353–362.

[9] M. Uyttebroek, W. Van Hecke, K. Vanbroekhoven. Sustainability metrics of 1- butanol. Catal Today 239 (2015) 7–10.

[10] World Bioenergy Association. Global Biomass Potential Towards 2035. Stockholm, 2016.

[11] M.F. Demirbas. Biorefineries for biofuel upgrading: A critical review. Applied Energy 86 (2009) S151–S161.

[12] J. Moncada, J.A. Tamayo, C.A. Cardona. Integrating first, second, and third generation biorefineries: Incorporating microalgae into the sugarcane biorefinery. Chemical Engineering Science 118 (2014) 126-140.

[13] C. Angelici, B. M. Weckhuysen, P.C.A. Bruijnincx. Chemocatalytic Conversion of Ethanol into Butadiene and Other Bulk Chemicals. ChemSusChem 6 (2013) 1595-1614.

[14] O. Casanova, S. Iborra, A. Corma. Biomass into chemicals: One pot-base free oxidative esterification of 5-hydroxymethyl-2-furfural into 2,5-dimethylfuroate with gold on nanoparticulated ceria. Journal of Catalysis 265 (2009) 109–116.

[15] K.J. Ptasinski. Efficiency of Biomass Energy: An Exergy Approach to Biofuels, Power, and Biorefineries. John Wiley & Sons, 2016.

[16] J.J. Bozell, G.R. Petersen. Technology development for the production of biobased products from biorefinery carbohydrates - The US Department of Energy's "top 10" revisited. Green Chem. 12 (2010) 539.

[17] T. Werpy, G. Petersen. Top Value Added Chemicals from Biomass; 2004; Vol. 1.

[18] J.A. Posada, A.D. Patel, A. Roes, K. Blok, A.P.C. Faaij, M.K. Patel. Potential of bioethanol as a chemical building block for biorefineries: preliminary sustainability assessment of 12 bioethanol-based products. Bioresour. Technol. 135 (2013) 490-499.

[19] K. Shimizu. Heterogeneous catalysis for the direct synthesis of chemicals by borrowing hydrogen methodology. Catal. Sci. Technol. 5 (2015) 1412–1427.

[20] P.T. Anastas, M.M. Kirchhoff, T.C. Williamson. Catalysis as a foundational pillar of green chemistry. Applied Catalysis A: General 221 (2001) 3–13.

[21] G. Onyestyák. Carbon supported alkaline catalysts for guerbet coupling of bioethanol. Period. Polytech. Chem. Eng. 62 (2018) 91–96.

[22] X. Zhang, Z. Liu, X. Xu, H. Yue, G. Tian, S. Feng. Hydrothermal synthesis of 1-butanol from ethanol catalyzed with commercial cobalt powder. ACS Sustain. Chem. Eng. 1 (2013) 1493–1497.

[23] J. Sun, Y. Wang. Recent Advances in Catalytic Conversion of Ethanol to Chemicals. ACS Catal. 4 (2014) 1078−1090.

[24] B. Ndaba, I. Chiyanzu, S. Marx. N-Butanol derived from biochemical and chemical routes: A review. Biotechnology Reports 8 (2015) 1–9.

[25] P. Dürre. Fermentative Butanol Production. Bulk Chemical and Biofuel. Ann. N.Y. Acad. Sci. 1125 (2008) 353–362.

[26] B. Ernst, Butyl Alcohols, In: Kirk-Othmer Encyclopedia of Chemical Technology, Wiley-VCH, 2001.

[27] P. Nigam, A. Singh. Production of liquid biofuels from renewable resources. Progress in Energy and Combustion Science. 37 (2011) 52–68.

[28] R.K. Rathour, V. Ahuja, R.K. Bathia, A. K. Bhatt. Biobutanol: New era of biofuels. Int J Energy Res. 42 (2018) 4532–4545.

[29] A. Prakash, V. Sharma, D. Kumar, A. Kuila, A.K. Sharma. Utilization of lignocellulosic biomass for biobutanol production. Lignocellulosic Biomass Production and Industrial Applications, Scrivener Publishing LLC, 2017.

[30] N. Mishra, A. Dubey. Biobutanol: An Alternative Biofuel. Advances in Biofeedstocks and Biofuels: Production Technologies for Biofuels, II. Chapter 6 2017 Scrivener Publishing LLC

[31] A. Ranjan, V.S. Moholkar. Biobutanol: science, engineering, and economics. International journal of energy research 36 (2012) 277–323.

[32] J.K. Fink. The Chemistry of Bio-based Polymers. Biofuels. Scrivener Publishing LLC. Published 2014 by John Wiley & Sons, Inc.

[33] J.T. Bartis, F. Camm, D.S. Ortiz. Producing Liquid Fuels from Coal: Prospects and Policy Issues. Rand Corporation, 2008.

[34] D. Verma, E. Fortunati, S. Jain, X. Zhang. Biomass, Biopolymer-Based Materials, and Bioenergy: Construction, Biomedical, and other Industrial Applications. Woodhead Publishing, 2019.

[35] A. Milbrandt, R.P. Overend. National Renewable Energy Laboratory. The Future of Liquid Biofuels for APEC Economies, 2008.

[36] M. Brito, F. Martins. Life cycle assessment of butanol production. Fuel 208 (2017) 476–482.

[37] A. Chauvel, G. Lefebvre. Petrochemical Processes. Institut français du pétrole publications Editions OPHRYS, 2003.

[38] J. Zhang, S. Wang, Y. Wang. Biobutanol Production from Renewable Resources: Recent advances. Advances in Bioenergy, Volumen 1. Academic Press, 2016.

[39] D. Gabriëls, W.Y. Hernández, B. Sels, P. Van Der Voort, A. Verberckmoes. Review of catalytic systems and thermodynamics for the Guerbet condensation reaction and challeges for biomass conversion. Catal. Science Technol. 5 (2015) 3876-3902.

[40] A.J. O'Lenick. Guerbet Chemistry. Journal of Surfactants and Detergents, 4 (2001) 311–315.

[41] C.M. Moore, O. Staples, R.W. Jenkins, T.J. Brooks, T.A. Semelsberger, A.D. Sutton. Acetaldehyde as an ethanol derived bio-building block: An alternative to Guerbet chemistry. Green Chem. 19 (2017) 169–174.

[42] H. Aitchison, R.L. Wingad, D.F. Wass. Homogeneous Ethanol to Butanol Catalysis - Guerbet Renewed. ACS Catalysis 6 (2016) 7125–7132.

[43] Q. Zhang, J. Dong, Y. Liu, Y. Wang, Y. Cao. Towards a green bulk-scale biobutanol from bioethanol upgrading. Journal of Energy Chemistry 25 (2016) 907–910.

[44] S. Cimino, L. Lisi, S. Romanucci. Catalysts for conversion of ethanol to butanol: Effect of acid-base and redox properties. Catalysis Today 304 (2018) 58–63.

[45] H.S. Ghaziaskar, C. Xu. One-step continuous process for the production of 1-butanol and 1-hexanol by catalytic conversion of bio-ethanol at its sub-/supercritical state. RSC Advances 3 (2013) 4271–4280.

[46] C.R. Ho, S. Shylesh, A.T. Bell. Mechanism and Kinetics of Ethanol Coupling to Butanol over Hydroxyapatite. ACS Catal. 6 (2016) 939−948.

[47] L. Silvester, J.F. Lamonier, C. Lamonier, M. Capron, R.N. Vannier, A.S. Mamede, F. Dumeignil. Guerbet Reaction over Strontium-Substituted Hydroxyapatite Catalysts Prepared at Various (Ca+Sr)/P Ratios. ChemCatChem 9 (2017) 2250 –2261.

[48] C. Yang, Z.Y. Meng. Bimolecular Condensation of Ethanol to 1-Butanol Catalyzed by Alkali Cation Zeolites. Journal of Catalysis 142 (1993) 37–44.

[49] C. Chuck. Biofuels for Aviation: Feedstocks, Technology and Implementation. Academic Press, 2016.

[50] J. Scalbert, F. Thibault-Starzyk, R. Jacquo, D. Morvan, F. Meunier. Ethanol condensation to butanol at high temperatures over a basic heterogeneous catalyst: How relevant is acetaldehyde self-aldolization? J. Catal. 311 (2014) 28–32.

[51] J.T. Kozlowski, R.J. Davis. Heterogeneous catalysts for the guerbet coupling of alcohols. ACS Catal. 3 (2013) 1588−1600.

[52] Z. Sun, A.C. Vasconcelos, G. Bottari, M.C.A. Stuart, G. Bonura, C. Cannilla, F. Frusteri, K. Barta. Efficient catalytic conversion of ethanol to 1-butanol via the guerbet reaction over copper- and nickel-doped porous. ACS Sustain. Chem. Eng. 5 (2) (2017) 1738–1746.

[53] F.C. Meunier, J. Scalbert, F. Thibault-Starzyk. Unraveling the mechanism of catalytic reactions through combined kinetic and thermodynamic analyses: Application to the condensation of ethanol. Comptes Rendus Chimie 18 (2015) 345-350.

[54] I.C. Marcu, D. Tichit, F. Fajula, N. Tanchoux. Catalytic valorization of bioethanol over Cu-Mg-Al mixed oxide catalysts. Catal. Today 147 (2009) 231−238.

[55] M. León, E. Díaz, S. Ordóñez. Ethanol catalytic condensation over Mg-Al mixed oxides derived from hydrotalcites. S. Catal. Today 164 (2011) 436− 442.

[56] M. Almohalla, E. Gallegos-Suarez, A. Arcoya, I. Rodríguez-Ramos, A. Guerrero-Ruiz. Comparative study of bioethanol transformation catalyzed by Ru or Pt nanoparticles supported on KL zeolite. Catal. Sci. Technol. 6 (2016) 521–529.

[57] E. Makshina, M.Dusselier, W. Janssens, J. Degrève, P. Jacobs, B. Sels. Review of old chemistry and new catalytic advances in the on-purpose synthesis of butadiene. Chem. Soc. Rev. 43 (2014) 7917–7953.

[58] L. Zhang, T.N. Pham, J. Faria, D. Santhanaraj, T. Sooknoi, Q. Tan, Z. Zhao, D.E. Resasco. Synthesis of C4 and C8 Chemicals from Ethanol on MgO-Incorporated Faujasite

Catalysts with Balanced Confinement Effects and Basicity. ChemSusChem 9 (2016) 736-748.

[59] T. Jordison, C. Lira, D. Miller. Condensed-Phase Ethanol Conversion to Higher Alcohols. Ind. Eng. Chem. Res. 54 (2015) 10991–11000.

[60] P. Benito, A. Vaccari, C. Antonetti, D. Licursi, N. Schiarioli, E. Rodriguez-Castellon, A.. Raspolli Galletti. Tunable copper-hydrotalcite derived mixed oxides for sustainable ethanol condensation to n-butanol in liquid phase. Journal of Cleaner Production 209 (2019) 1614−1623.

[61] J. Pang, M. Zheng, L. He, L. Li, X. Pan, A. Wang, X. Wang, T. Zhang. Upgrading ethanol to n-butanol over highly dispersed Ni–MgAlO catalysts. J. Catal. 344 (2016) 184–193.

[62] O.M. Perrone, F. Lobefaro, M. Aresta, F. Nocito, M. Boscolo, A. Dibenedetto. Butanol synthesis from ethanol over CuMgAl mixed oxides modified with palladium (II) and indium (III). Fuel Processing Technology 177 (2018) 353-357.

[63] X. Wu, G. Fang, Z. Liang, W. Leng, K. Xu, D. Jiang, J. Ni, X. Li. Catalytic upgrading of ethanol to n-butanol over M-CeO2/AC (M = Cu, Fe, Co, Ni and Pd) catalysts. Catalysis Communications 100 (2017) 15-18.

[64] A.S. Ndou, N. Plint, N.J. Coville. Dimerisation of ethanol to butanol over solid-base catalysts. Appl. Catal., A 251 (2003) 337−345.

[65] J.I. Di Cosimo, V.K. Díez, M. Xu, E. Iglesia, C.R. Apesteguía. Structure and surface and catalytic properties of Mg-Al basic oxides. Journal of Catalysis 178 (1998) 499–510.

[66] T.W. Birky, J.T. Kozlowski, R.J. Davis. Isotopic transient analysis of the ethanol coupling reaction over magnesia. Journal of Catalysis 298 (2013) 130–137.

[67] A. Chieregato, J. Velasquez Ochoa, C. Bandinelli, G. Fornasari, F. Cavani, M. Mella. On the chemistry of ethanol on basic oxides: Revising mechanisms and intermediates in the lebedev and guerbet reactions. ChemSusChem 8 (2015) 377 – 388.

[68] W. Ueda, T. Kuwabara, T. Ohshida, Y. Morikawa. A Low-pressure Guerbet Reaction over Magnesium Oxide Catalyst. Journal of the Chemical Society, Chemical Communications, 1990, 1558-1559.

[69] F. Cavani, F. Trifirò, A.Vaccari. Hydrotalcite-type anionic clays: preparation, properties and applications. Catal. Today 11 (1991) 173–301.

[70] A.E. Bessudnov, L.M. Kustov, I.V. Mishin, M.N. Mikhailov. Phase composition of Mg-Al mixed oxides, their activity and selectivity in the ethanol condensation reaction. Russian Chemical Bulletin International Edition 66 (2017) 666—672.

[71] J.I. Di Cosimo, C.R. Apesteguía, M.J.L. Ginés, E. Iglesia. Structural requirements and reaction pathways in condensation reactions of alcohols on MgyAlOx catalysts. Journal of Catalysis 190 (2000) 261–275.

[72] M. León, E. Díaz, A. Vega, S. Ordóñez, A. Auroux. Consequences of the iron–aluminium exchange on the performance of hydrotalcite-derived mixed oxides for ethanol condensation. Applied Catalysis B: Environmental, 2011, 102, 590-599.

[73] D. L. Carvalho, R. R. de Avillez, M. T. Rodrigues, L. E. P. Borges, L. G. Appel. Mg and Al mixed oxides and the synthesis of n-butanol from etanol. Appl. Catal. A 415–416 (2012) 96–100.

[74] A. D. Patel, S. Telalović, J. H. Bitter, E. Worrell, M. K. Patel. Analysis of sustainability metrics and application to the catalytic production of higher alcohols from ethanol. Catalysis Today 239 (2015) 56-79.

[75] G. Zhang, H. Hattori, K. Tanabe. Aldol Addition of Acetone, Catalyzed by Solid Base Catalysts: Magnesium Oxide, Calcium Oxide, Strontium Oxide, Barium Oxide, Lanthanum (III) Oxide and Zirconium Oxide. Applied Catalysis 36 (1988) 189-197.

[76] A. Corma, S. Iborra. Optimization of Alkaline Earth Metal Oxide and Hydroxide Catalysts for Base-Catalyzed Reactions. Adv. Catal. 49 (2006) 239–302.

[77] N. La-Salvia, J.J Lovón-Quintana, G.P. Valença. Vapor-phase catalytic conversion of ethanol into 1,3-butadiene on Cr-Ba/MCM-41 catalysts. Brazilian J. Chem. Eng. 32 (2015) 489–500.

[78] M.D. Jones, C.G. Keir, C. Di Iulio, R.A.M. Robertson, C.V. Williams, D.C. Apperley. Investigations into the conversion of ethanol into 1,3-butadiene. Catal. Sci. Technol. 1 (2011) 267–272.

[79] I.C. Marcu, N. Tanchoux, F. Fajula, D. Tichit. Catalytic conversion of ethanol into butanol over M-Mg-Al mixed oxide catalysts (M = Pd, Ag, Mn, Fe, Cu, Sm, Yb) obtained from LDH precursors. Catal. Lett. 143 (2013) 23–30.

[80] N.V. Kulkarni, W.W. Brennessel, W.D. Jones. Catalytic Upgrading of Ethanol to n-Butanol via Manganese-Mediated Guerbet Reaction. ACS Catal. 8 (2018) 997−1002.

[81] S. Fu, Z. Shao, Y. Wang, Q. Liu. Manganese-Catalyzed Upgrading of Ethanol into 1-Butanol. J. Am. Chem. Soc. 139 (2017) 11941–11948.

[82] Y. Kitayama, A. Michishita. Catalytic activity of fibrous clay mineral sepiolite for butadiene formation from ethanol. J. Chem. Soc. Chem. Commun. (1981) 401–402.

[83] F. Engelhardt, W. Schritt. US Patent 3558716 A; 1971.

[84] V. Nagarajan, N.R. Kuloor. Indian J. Technol. 4 (1966) 46−54.

[85] T. Tsuchida, S. Sakuma, T. Takeguchi, W. Ueda. Direct Synthesis of n-Butanol from Ethanol over Nonstoichiometric Hydroxyapatite. Industrial & Engineering Chemistry Research 45 (2006) 8634-8642.

[86] T. Tsuchida, J. Kubo, T. Yoshioka, S. Sakuma, T. Takeguchi, W. Ueda. Reaction of ethanol over hydroxyapatite affected by Ca/P ratio of catalyst. J. Catal. 259 (2008) 183–189.

[87] S. Ogo, A. Onda, Y. Iwasa, K. Hara, A. Fukuoka, K. Yanagisawa. 1-Butanol synthesis from ethanol over strontium phosphate hydroxyapatite catalysts with various Sr/P ratios. Journal of Catalysis 296 (2012) 24–30.

[88] S. Ogo, A. Onda, K. Yanagisawa. Selective synthesis of 1-butanol from ethanol over strontium phosphate hydroxyapatite catalysts. Applied Catalysis A: General 402 (2011) 188-195.

[89] J. Kubo, S. Sakuma,T. Tsuchida, T. Yoshioka. Method for producing alcohol by Guerbet reaction, WO2012035772A1 patent, 2011.

[90] J. T. Kozlowski, R. J. Davis. Sodium modification of zirconia catalysts for ethanol coupling to 1-butanol. Journal of Energy Chemistry 22 (2013) 58-64.

[91] X. Wu, G. Fang, Y. Tong, D. Jiang, Z. Liang, W. Leng, L. Liu, P. Tu, H. Wang, J. Ni, X. Li. Catalytic Upgrading of Ethanol to n-Butanol: Progress in Catalyst Development. ChemSusChem 11 (2018) 71– 85.

[92] M.J.L. Gines, E. Iglesia. Bifunctional Condensation Reactions of Alcohols on Basic Oxides Modified by Copper and Potassium. Journal of Catalysis 176 (1998) 155-172.

[93] K. Kourtakis, R. Ozer. Lanthanum-promoted supported metal catalysts and process for producing Guerbet alcohols using same. US20100160692A1 patent, 2009.

[94] J.W. Van Hal, R.J.H. Grisei. Process for preparing β-alkylated alcohols. WO/2014/137212 patent, 2014.

[95] R. Olcese, M.M. Bettahar. Thermodynamics conditions for Guerbet ethanol reaction, MATEC Web of Conferences 3 (2013) 01060.

[96] R. Arjona, J.L. Sanz, A. Corma, M. E. Domine. WO2014001595, 2014.

[97] E.S. Olson, R.K. Sharma, T.R. Aulich (2004) Higher-Alcohols Biorefinery. In: M. Finkelstein, J.D. McMillan, B.H. Davison, B. Evans. Proceedings of the Twenty-Fifth Symposium on Biotechnology for Fuels and Chemicals Held. Biotechnology for Fuels and Chemicals (The Twenty-Fifth Symposium), 2003. Humana Press, Totowa, NJ.

[98] F. Hosoglu, J. Faye, K. Mareseanu, G. Tesquet, P. Miquel, M. Capron, O. Gardoll, J.-F. Lamonier, C. Lamonier, F. Dumeignil. High resolution NMR unraveling Cu substitution of Mg in hydrotalcites–ethanol reactivity. Applied Catalysis A: General 504 (2015) 533-541.

[99] S. Veibel, J. I. Nielsen. On the mechanism of the Guerbet reaction. Tetrahedron 23 (1967) 1723-1733.

[100] M. A. Landau, V. V. Shchekin. Difference in mechanisms of dehydrogenation on oxides and metals. Russ Chem Bull 9 (1960) 885-887.

[101] T. Riittonen, K. Eränen, P. Mäki-Arvela, A. Shchukarev, A-R. Rautio, K. Kordas, N. Kumar, T. Salmi, J-P. Mikkola. Continuous liquid-phase valorization of bio-ethanol towards bio-butanol over metal modified alumina. Renew. Energ. 74 (2015) 369–378.

[102] P. Dziugan, K.G. Jastrzabek, M. Binczarski, S. Karski, A.Witonska, B. Kolesinska, Z.J.Kaminski. Continuous catalytic coupling of raw bioethanol into butanol and higher homologues. Fuel 158 (2015) 81–90.

[103] T. Riittonen, E. Toukoniitty, D.K. Madnani , A-R. Leino, K. Kordas, M. Szabo, A. Sapi, K. Arve, J. Wärnå, J-P. Mikkola. One-Pot Liquid-Phase Catalytic Conversion of Ethanol to 1-Butanol over Aluminium Oxide—The Effect of the Active Metal on the Selectivity. Catalysts 2 (2012) 68-84.

[104] R. Miller, G. Bennett. Producing 2-Ethylhexanol by the Guerbet Reaction. Ind. Eng. Chem. 53 (1961) 33–36.

[105] E. Pratt, D. Kubler. Disproportionative Condensations. I. Modified Guerbet Reactions. J. Am. Chem. Soc. 76 (1954) 52–56.

[106] I.C. Freitas, S. Damyanova, D.C. Oliveira, C.M.P. Marques, J.M.C. Bueno. Effect of Cu content on the surface and catalytic properties of Cu/ZrO2 catalyst for ethanol dehydrogenation. Journal of Molecular Catalysis A: Chemical 381 (2014) 26– 37.

[107] F.-W. Chang, H.-C. Yang, L.S. Roselin, W.-Y. Kuo. Ethanol dehydrogenation over copper catalysts on rice husk ash prepared by ion exchange. Appl. Catal. A: Gen. 304 (2006) 30–39.

[108] F. Zaccheria, N. Scotti, N. Ravasio. The Role of Copper in the Upgrading of Bioalcohols. ChemCatChem 10 (2018) 1526 –1535.

[109] F. Cheng, H. Guo, J. Cui, B. Hou, H. Xi, L. Jia, D. Li. Coupling of methanol and ethanol over CuMgAlOx catalysts: the roles of copper species and alkalinity. Reaction Kinetics, Mechanisms and Catalysis. DOI: 10.1007/s11144-018-1476-z.

[110] J.A. Barrett, Z.R. Jones, C. Stickelmaier, N. Schopp, P.C. Ford. A Pinch of Salt Improves n-Butanol Selectivity in the Guerbet Condensation of Ethanol over Cu-Doped Mg/Al Oxides. ACS Sustainable Chem. Eng. 6 (2018) 15119−15126.

[111] J. Franckaerts, G.F. Froment. Kinetic study of the dehydrogenation of ethanol. Chemical Engineering Science 19 (1964) 808–819.

[112] J.H. Earley, R.A. Bourne, M.J. Watson, M. Poliakoff. Continuous catalytic upgrading of ethanol to n -butanol and >C4 products over Cu/CeO_2 catalysts in supercritical CO_2. Green. Chem. 17 (2015) 3018–3025.

[113] D.D. Petrolini, N. Eagan, M.R. Ball, S.P. Burt, I. Hermans, G.W. Huber, J.A. Dumesic, L. Martins. Ethanol condensation at elevated pressure over copper on AlMgO and AlCaO porous mixed-oxide supports. Catal. Sci. Technol. 9 (2019) 2032–2042.

[114] J. Quesada, L. Faba, E. Díaz, S. Ordóñez. Tuning the selectivities of Mg-Al mixed oxides for ethanol upgrading reactions through the presence of transition metals. Applied Catalysis A, General 559 (2018) 167–174.

[115] K.W. Yang, X.Z. Jiang, W.C. Zhang. One-step Synthesis of n-Butanol from Ethanol Condensation over Alumina-supported Metal Catalysts. Chinese Chem. Lett. 15 (2004) 1497-1500.

[116] K. Kourtakis, M.B. D'Amore, L.E. Manzer. Catalytic conversion of ethanol to a 1-butanol-containing reaction product using a thermally decomposed hydrotalcite catalyst. Patent US20090054705, 2009.

[117] K. Kourtakis, R. Ozer, M.B. D'Amore. Process for producing Guerbet alcohols using water tolerant basic catalysts. Patent US008318989B2, 2012.

[118] W.Y. Hernández, K. De Vlieger, P. Van Der Voort, A. Verberckmoes. Synthesis of Guerbet alcohols by self and cross condensation reactions of a variety of fatty alcohols and terpenes over Ni/Cu hydrotalcite-derived mixed oxides. Poster GB reaction GREN 2017 Conference Berlin. http://hdl.handle.net/1854/LU-8552646

[119] W.Y. Hernández, K. De Vlieger, P. Van Der Voort, A. Verberckmoes. Ni−Cu Hydrotalcite-Derived Mixed Oxides as Highly Selective and Stable Catalysts for the

Synthesis of β-Branched Bioalcohols by the Guerbet Reaction. ChemSusChem 9 (2016) 3196 –3205.

[120] M. Matsuda, M. Horio. Patent US4518810, 1985.

[121] V. Dwarakanath, R. Shong, T. E. Weksberg. Mixed carbon length synthesis of primary Guerbet alcohols. Patent WO/2014/149419, 2014.

[122] G.E. Bennett, R. E. Miller. Patent US2862013, 1958.

[123] C. Zhang, M. Borlik, H. Weiner. Coated hydrotalcite catalysts and processes for producing butanol. Patent WO/2014/100131, 2014.

[124] C. Carlini, A. Macinai, A. Maria, R. Galletti, G. Sbrana. Selective synthesis of 2-ethyl-1-hexanol from n-butanol through the Guerbet reaction by using bifunctional catalysts based on copper or palladium precursors and sodium butoxide. Journal of Molecular Catalysis A: Chemical 212 (2004) 65-70.

[125] A. Wick, E.U. Mahnke. Method for Producing Guerbet Alcohols. Patent US20120220806A1, 2012.

[126] J. Hagen. Industrial Catalysis: A Practical Approach. 2015 Wiley-VCH Verlag GmbH & Co. KGaA.

[127] E. Santacesaria, G. Carotenuto, R. Tesser, M. Di Serio. Ethanol dehydrogenation to ethyl acetate by using copper and copper chromite catalysts. Chemical Engineering Journal 179 (2012) 209–220.

[128] L. Faba, E. Díaz, S. Ordoñez. Improvement on the catalytic performance of Mg-Zr mixed oxides for furfural-acetone aldol condensation by supporting on mesoporous carbons. ChemSusChem 6 (2013) 463–473.

[129] Q.N. Wang, L. Shi, A.H. Lu. Highly selective copper catalyst supported on mesoporous carbon for the dehydrogenation of ethanol to acetaldehyde. ChemCatChem 7 (2015) 2846-2852.

[130] O.N. Stavinskaya, E.I. Oranskaya, V.K. Imshennik. On the effect of surface oxygen complexes on iron-catalyzed carbon hydrogenation. Carbon 39 (2001) 291-294.

[131] C. Moreno-Castilla, M.A. Ferro-Garcia, J.P. Joly, I. Bautista-Toledo, F. Carrasco-Marin, J. Rivera-Utrilla. Activated carbon surface modifications by nitric acid, hydrogen peroxide, and ammonium peroxydisulfate treatments. Langmuir 11 (1995) 4386-4392

[132] J.L. Eslava, X. Sun, J. Gascon, F. Kapteijn, I. Rodríguez-Ramos. Ruthenium particle size and cesium promotion effects in Fischer-Tropsch synthesis over high-surface-area graphite supported catalysts. Catal. Sci. Technol. 7 (2017) 1235–1244.

[133] E. Díaz, S. Ordónez, .F. Bueres, E. Asedegbega-Nieto, H. Sastre. High-surface area graphites as supports for hydrodechlorination catalysts: Tuning support surface chemistry for an optimal performance. App. Catal. B 99 (2010) 181–190.

[134] L. Faba, E. Díaz, S. Ordoñez. Gas phase acetone self-condensation over unsupported and supported Mg–Zr mixed-oxides catalysts. Appl. Catal. B 142–143 (2013) 387–395.

[135] S. Ardizzone, C.L. Bianchi, B. Vercelli. MgO powders: interplay between adsorbed species and localisation of basic sites. Applied Surface Science 126 (1998) 169–175.

[136] S. Ardizzone, C.L. Bianchi, M. Fadoni, B. Vercelli. Magnesium salts and oxide: An XPS overview. Applied Surface Science 119 (1997) 253-259.

[137] W. Gao, T. Zhoua, Q. Wang. Controlled synthesis of MgO with diverse basic sites and its CO_2 capture mechanism under different adsorption conditions. Chemical Engineering Journal 336 (2018) 710–720.

[138] A.O. Menezes, P.S. Silva, E.P. Hernández, L.E.P. Borges, M.A. Fraga. Tuning surface basic properties of nanocrystalline MgO by controlling the preparation conditions. Langmuir 26 (5) (2010) 3382–3387.

[139] G. A. H. Mekhemer, S. A. Halawy, M. A. Mohamed, M. I. Zaki. Qualitative and Quantitative Assessments of Acid and Base Sites Exposed on Polycrystalline MgO Surfaces: Thermogravimetric, Calorimetric, and in-Situ FTIR Spectroscopic Study Combination. J. Phys. Chem. B 108 (2004) 13379-13386.

[140] O. Karslıoglu, L. Trotochaud, I. Zegkinoglou, H. Bluhm. X-Ray Spectroscopic Characterization of BaO, Ba(OH)2, BaCO3, and Ba(NO3)2. Journal of Electron Spectroscopy and Related Phenomena 225 (2018) 55–61.

[141] D. Pang, H. Tan, R. Zhu, F. Ouyang. Producing biodiesel from waste animal oil by modified ZnO. International Journal of Green Energy. 14 (2017) 703–711.

[142] C. Shi, H. Chang, C. Wang, T. Zhang, Y. Peng, M. Li, Y.Wang, J. Li. Improved Activity and H_2O Resistance of Cu-Modified MnO_2 Catalysts for NO Oxidation. Ind. Eng. Chem. Res. 57 (3) (2018) 920–926.

[143] R. Jenkins, R.L. Snyder. Introduction to X-ray powder diffractometry New York, 1996.

[144] A.G. Marangoni, M.F. Peyronel. X-Ray Powder Diffractometry; 2013.

[145] M. Thommes, K. Kaneko, A.V. Neimark, J.P. Olivier, F. Rodriguez-Reinoso, J. Rouquerol, K.S. W. Sing. Physisorption of gases, with special reference to the evaluation of surface area and pore size distribution (IUPAC Technical Report). Pure Appl Chem 87 (2015) 1051-1069.

[146] K.S.W. Sing. Reporting physisorption data for gas/solid systems with special reference to the determination of surface area and porosity (Recommendations 1984). Pure Appl. Chem., 57 (1985) 603-619.

[147] J. Rouquerolt, D. Avnir, C.W. Fairbridge, D.H. Everett, J.H. Haynes, N. Pernicone, J.D.F. Ramsay, K.S.W. Sing, K.K. Unger. Recommendations for the characterization of porous solids. Pure Appl. Chem. 1994, 66 (8), 1739–1758.

[148] M. Che, J.C. Vedrine. Characterization of Solid Materials and Heterogeneous Catalysts; Wiley-VCH Verlag & Co. KGaA: Weinheim, 2012.

[149] E. P. Barrett, L. G. Joyner, P.P. Halenda. The determination of pore volume and area distributions in porous substances. I. Computations from nitrogen isotherms. J. Am. Chem. Soc. 73 (1951) 373-380.

[150] F. Rodríguez-Reinoso. Problemas más habituales en el uso de la adsorción física como técnica de caracterización de sólidos porosos. Materiales en Adsorción y Catálisis 0 (2010) 1-37.

[151] M. Pellerano, P. Pré, M. Kacem, A. Delebarre. CO_2 capture by adsorption on activated carbons using pressure modulation. Energy Procedia 1 (2009) 647-653.

[152] S.L. Suib. New and Future Developments in Catalysis: Activation of Carbon Dioxide. Elsevier (2013).

[153] http://www.ltp-oldenburg.de/index.php/caloric-properties.html

[154] D. B. Williams, C. B. Carter, Transmission Electron Microscopy I, Basics, New York (1996).

[155] P. Serp, K. Philippot. Nanomaterials in Catalysis. Wiley-VCH Verlag & Co. KGaA: Weinheim, 2013; pp 443–471.

[156] J.W. Niemantsverdriet, Spectroscopy in Catalysis, An Introduction, Wiley-VCH, Weinheim, 2000.

[157] I. Chorkendorff, J. W. Niemantsverdriet. Concepts of Modern Catalysis and Kinetics. 2003 WILEY-VCH Verlag GmbH & Co. KGaA, Weinheim

[158] J. R. Anderson. Structure of metallic catalysts. Academic Press (1975).

[159] S. E. Wankeki, R.M.J. Fiedorow. The influence of preparation methods on surface area, porosity and crystallinity of magnesium oxide. K.K. Unger et al. (Editors), Characterization of Porous Solids, 1988 Elsevier Science Publishers B.V., Amsterdam - Printed in The Netherlands.

[160] M. Estrada, V.V. Costa, S. Beloshapkin, S. Fuentes, E. Stoyanov, E.V. Gusevskaya, A. Simakov. Aerobic oxidation of benzyl alcohol in metanol solutions over Au nanoparticles: Mg(OH)2 vs MgO as the support. Appl. Catal. A: Gen. 473 (2014) 96-103.

[161] S.A.C. Carabinero, N. Bogdanchikova, A. Pestryakov, P.B. Tavares, L.S.G. Fernandes, J.L. Figueiredo. Gold nanoparticles supported on magnesium oxide for CO oxidation. Nanoscale Res. Let. 6 (2011) 435-440.

[162] K. Refson, R. A. Wogelius, and D. G. Fraser. Water chemisorption and reconstruction of the MgO surface. Physical Review B, 52 (15) (1995) 10823-10827.

[163] W. Ueda, H. Kurokawa, Y. Morooka, T. Ikawa. Coupling reaction between methylpropionate and methanol to form methylmethacrylate over metal ion-contained magnesium-oxide catalysts. Chemistry Letters, 6 (1985) 819-820.

[164] W. Ueda, T. Yokoyama, Y. Morooka, T. Ikawa. Enhancement of Surface Base Property of Magnesium Oxide by the Combination of Metal Ion. Chem. Lett., 14C (1985) 1059-1062.

[165] W. Ueda, T. Yokoyama, Y. Morooka, T. Ikawa. Catalytic synthesis of vinyl ketones over metal oxide catalysts using methanol as the vinylating agent. Chem. Lett., 1 (1984) 39-40.

[166] B. Wang, R. Yan, H. Liu. Effects of interactions between NiM (M = Mn, Fe, Co and Cu) bimetals with MgO (1 0 0) on the adsorption of CO_2. Applied surface science, 258 (22) (2012) 8831-8836.

[167] R. Ferrando, A. Fortunelli. Diffusion of adatoms and small clusters on magnesium oxide surfaces. Journal of Physics Condensed Matter, 21 (26) (2009).

[168] M.C. Abelló, M.F. Gómez, L.A. Arima. Synthesis of 1,1-diethoxyethane from bioethanol. Influence of catalysts acidity. React. Kinet. Catal. Lett. 73 (2001) 143-149.

[169] A. Galadima, O. Muraza. Catalytic Upgrading of Bioethanol to Fuel Grade Biobutanol: A Review. Ind. Eng. Chem. Res. 2015, 54, 7181–7194.

[170] S. Hanspal, Z.D. Young, J. Tyler, P. Robert, J.Davis. Influence of surface acid and base sites on the Guerbet coupling of ethanol to butanol over metal phosphate catalysts. Journal of Catalysis. 352 (2017) 182-190.

[171] C.L. Kibby, W. K. Hall. Studies of acid-catalyzed reactions: XII. Alcohol decomposition over hydroxyapatite catalysts. J. Catal. 29(1) (1973) 144-159.

[172] T. Kamsuwan, P. Praserthdam, B. Jongsomjit. Diethyl Ether Production during Catalytic Dehydration of Ethanol over Ru- and Pt- modified H-beta Zeolite Catalysts. J Oleo Sci. 66 (2017) 199-207.

[173] S. Yuvaraj, L. Fan-Yuan, C. Tsong-Huei, Y. Chuin-Tih. Thermal Decomposition of Metal Nitrates in Air and Hydrogen Environments. J. Phys. Chem. B 107 (2003) 1044-1047.

[174] D. Lopes, F. Zotin, L.A. Palacio. Copper-nickel catalysts from hydrotalcite precursors: The performance in NO reduction by CO. App. Catal., B 237 (2018) 327–338.

[175] B. Dragoi, A. Ungureanu, A. Chirieac, C. Ciotonea, C. Rudolf, S. Royer, E. Dumitriu. Structural and catalytic properties of mono- and bimetallic nickel-copper nanoparticles derived from MgNi(Cu)Al-LDHs under reductive conditions. Applied Catalysis A: General 504 (2015) 92–102.

[176] D.H. Kim, Y-H Chin, J.H. Kwak, J. Szanyi, C.H.F. Peden. Changes in Ba Phases in BaO/Al_2O_3 upon Thermal Aging and H_2O Treatment. Catalysis Letters 105 (2005) 259–268.

[177] I. Arvanitidis, D. Sichen, S. Seetharaman. A Study of the Thermal Decomposition of BaCO3. Metallurgical and Materials Transactions B. 27B (1996) 409-416.

[178] Y. Jeong, I. Kim, J.Y. Kang, H. Jeong, J.K. Park, J.H. Park, J.C. Jung. Alcohol-assisted low temperature methanol synthesis from syngas over Cu/ZnO catalysts: Effect of pH value in the co-precipitation step. Journal of Molecular Catalysis A: Chemical 400 (2015) 132–138.

[179] S. Hajduk, V.D.B.C. Dasireddy, B. Likozar, G. Drazic, Z.C. Orel. COx-free hydrogen production via decomposition of ammonia over Cu–Zn-based heterogeneous catalysts and their activity/stability. Applied Catalysis B: Environmental 211 (2017) 57–67.

[180] P.T. Patil, D. Liu, Y. Liu, J. Chang, A. Borgna. Improving 1,3-butadiene yield by Cs promotion in ethanol conversion. Appl. Catal., A 543 (2017) 67–74.

[181] W. Biemolt, P.R. Davies, A.P.J. Jansen, R.A. van Santen. The adsorption site of ammonia at copper surfaces. Catalysis Today, 12 (1992) 421-432.

[182] P. Baumgärtel, R. Lindsay, T. Giessel, O. Schaff, A. M. Bradshaw, D. P. Woodruff. Structure Determination of Ammonia on Cu (111). J. Phys. Chem. B 104 (2000) 3044-3049.

[183] C. López-Olmos, M.V. Morales, A. Guerrero-Ruiz, C. Ramirez-Barria, E. Asedegbega-Nieto, I. Rodríguez-Ramos. Continuous Gas-Phase Condensation of Bioethanol to 1-Butanol over Bifunctional Pd/Mg and Pd/Mg–Carbon Catalysts. ChemSusChem 11 (2018) 3502–3511.

[184] V. Thyssen, T. Maia, E. Assaf. Cu and Ni Catalysts Supported on γ-Al_2O_3 and SiO_2 Assessed in Glycerol Steam Reforming Reaction. J. Braz. Chem. Soc. 26 (2015) 22–31.

[185] A. B. Dongil, B. Bachiller-Baeza, I. Rodríguez-Ramos, J.L.G. Fierro, N. Escalona. The effect of Cu loading on Ni/carbon nanotubes catalysts for hydrodeoxygenation of guaiacol. RSC Adv. 6 (2016) 26658–26667.

[186] G. Peng, F. Gramm, C. Ludwig, F. Vogel. Effect of carbon surface functional groups on the synthesis of Ru/C catalysts for supercritical water gasification. Catal. Sci. Technol. 5 (2015) 3658–3666.

[187] L. Gonzalo-Chacón, M. Almohalla, E. Gallegos-Suarez, A. Guerrero-Ruiz, I. Rodríguez-Ramos. Effects of the reduction temperature over ex-chloride Ru Fischer–Tropsch catalysts supported on high surface area graphite and promoted by potassium. Appl. Catal., A 480 (2014) 86–92.

[188] A. Guerrero-Ruiz, A. Sepúlveda-Escribano, I. Rodríguez-Ramos. Carbon monoxide hydrogenation over carbon supported cobalt or ruthenium catalysts. Promoting effects of magnesium, vanadium and cerium oxides. Appl. Catal., A 120 (1994) 71–83.

[189] M. Cerro-Alarcon, A. Guerrero-Ruiz, I. Rodriguez-Ramos. Stereoselective hydrogenation of Paracetamol to trans-4-acetamidocyclohexanol on carbon-supported Ru-M (M = Co, Ni) bimetallic catalysts. Catal. Today 93–95 (2004) 395–403.

[190] M. Cerro-Alarcón, B. Bachiller-Baeza, A. Guerrero-Ruiz, I. Rodríguez-Ramos. Effect of the reduction–preparation method on the surface states and catalytic properties of supported-nickel particles. J. M. Catal. A: Chem. 258 (2006) 221–230.

[191] M. León, E. Díaz, S. Bennici, A. Vega, S. Ordónez, A. Auroux. Adsorption of CO_2 on Hydrotalcite-Derived Mixed Oxides: Sorption Mechanisms and Consequences for Adsorption Irreversibility. Ind. Eng. Chem. Res. 49 (8) (2010) 3663–3671.

[192] M.C. Biesinger, B.P. Payne, A.P. Grosvenor , L.W.M. Lau, A.R. Gerson, R. St.C. Smart. Resolving surface chemical states in XPS analysis of first row transition metals, oxides and hydroxides: Cr, Mn, Fe, Co and Ni. Appl. Surf. Sci. 257 (2011) 2717–2730.

[193] H.W. Nesbitt, D. Banerjee. Interpretation of XPS Mn(2p) spectra of Mn oxyhydroxides and constraints on the mechanism of MnO_2 precipitation. Am. Mineral. 83 (1998) 305–315.

[194] O. A. Bulavchenko, Z. S. Vinokurov, T. N. Afonasenko, P. G. Tsyrul’nikov, S. V. Tsybulya, A. A. Saraev, V. V. Kaichev. Reduction of mixed Mn-Zr oxides: In situ XPS and XRD studies. J. Chem. Soc., Dalton Trans. 44 (2015) 15499–15507.

[195] J.M. Campos-Martín, J. L. G. Fierro, A. Guerrero-Ruiz, R. G. Herman, K. Klier. Promoter Effect of Cesium on C–C Bond Formation during Alcohol Synthesis from CO/H_2 over Cu/ZnO/Cr_2O_3 Catalysts. J. Catal. 163 (1996) 418–428.

[196] M.C. Biesinger. Advanced analysis of copper X-ray photoelectron spectra. Surf. Interface Anal. 49 (2017) 1325–1334.

[197] M.C. Biesinger, L.W.M. Lau, A.R. Gerson, R. St.C. Smart. Resolving surface chemical states in XPS analysis of first row transition metals, oxides and hydroxides: Sc, Ti, V, Cu and Zn. Appl. Surf. Sci. 257 (2010) 887–898.

[198] A.P. Grosvenor, M.C. Biesinger, R. St.C. Smart, N.S. McIntyre. New interpretations of XPS spectra of nickel metal and oxides. Surf. Sci. 600 (2006) 1771–1779.

[199] A. Davidson, J. F. Tempere, M. Che. Spectroscopic studies of nickel(II) and nickel(III) species generated upon thermal treatments of nickel/ceria-supported materials. J. Phys. Chem. 100 (1996) 4919–4929.

[200] A.C. Carreras, M.A. Cangiano, M.W. Ojeda, M.C. Ruiz. Characterization of Cu-Ni nanostructured alloys obtained by a chemical route. Influence of the complexing agent content in the starting solution. Mater. Charact. 101 (2015) 40–48.

[201] B.C. Miranda, R.J. Chimentão, J. Szanyi, A.H. Braga, J.B.O. Santos, F. Gispert-Guirado, J. Llorca, F. Medina. Influence of copper on nickel-based catalysts in the conversion of glycerol. Appl. Catal., B 166–167 (2015) 166–180.

[202] A. Kitla, O.V. Safonova, K. Föttinger. Infrared studies on bimetallic copper/nickel catalysts supported on zirconia and ceria/zirconia. Catal. Lett. 143 (2013) 517–530.

[203] A. Ungureanu, B. Dragoi, A. Chirieac, C. Ciotonea, S. Royer, D. Duprez, E. Dumitriu. Composition-dependent morphostructural properties of Ni-Cu oxide nanoparticles confined within the channels of ordered mesoporous SBA-15 silica, ACS Appl. Mater. Interfaces 5 (8) (2013) 3010-3025.

[204] Y. Lv, J. Li, S. Feng, P. Liu, F. Hao, W. Xiong, H. Luo. Multi-walled carbon nanotubes supported nickel nanoparticles doped with magnesia and copper for adiponitrile

hydrogenation with high activity and chemoselectivity under mild conditions. Chemical Engineering Journal 346 (2018) 203–216.

[205] Q. Guo, M. Wu, K. Wang, L. Zhang, X. Xu, Catalytic hydrodeoxygenation of algae bio-oil over bimetallic Ni-Cu/ZrO2 catalysts, Ind. Eng. Chem. Res. 54 (3) (2015) 890–899.

[206] J. Ashok, M. Subrahmanyam, A. Venugopal, Hydrotalcite structure derived Ni-Cu- Al catalysts for the production ofH2 by CH4 decomposition, Int. J. Hydrogen Energy 33 (11) (2008) 2704–2713.

[207] A. Chattopadhyay, H. Yang, J.L. Whitten. Adsorption of Ammonia on Ni (111). J. Phys. Chem. 94 (1990) 6379-6383.

[208] Y-X Liu, H-H Wang, T-J Zhao, B. Zhang, H. Su, Z-H Xue, X-H Li, J-S Chen. Schottky Barrier Induced Coupled Interface of Electron-Rich N-Doped Carbon and Electron-Deficient Cu: In-Built Lewis Acid−Base Pairs for Highly Efficient CO2 Fixation. J. Am. Chem. Soc. 141 (2019) 38−41.

[209] V. Rheinheimer, C. Unluer, J. Liu , S. Ruan, J. Pan, P.J.M. Monteiro. XPS study on the stability and transformation of hydrate and carbonate phases within MgO systems. Materials 10 (2017) 1-16.

[210] J.S. Corneille, J.W. He, D.W. Goodman. Use of an Auger parameter for characterizing the Mg chemical state in different materials. Surface Science 306 (1994) 269-278.

[211] C. Fotea, J. Callaway, M.R. Alexander. Characterisation of the surface chemistry of magnesium exposed to the ambient atmosphere. Surf. Interface Anal. 38 (2006) 1363–1371.

[212] M. Santamaria, F. Di Quarto, S. Zanna, P. Marcus. Initial surface film on magnesium metal: A characterization by X-ray photoelectron spectroscopy (XPS) and photocurrent spectroscopy (PCS). Electrochimica Acta 53 (2007) 1314–1324.

[213] A. Sasahara, T. Murakami, M. Tomitori. Hydration of MgO(100) surface promoted at <011> steps. J. Phys. Chem. C 119 (2015) 8250−8257.

[214] S.W. Goh, A.N. Buckley, R.N. Lamb, R.A. Rosenberg, D. Moran. The oxidation states of copper and iron in mineral sulfides, and the oxides formed on initial exposure of chalcopyrite and bornite to air. Geochimica et Cosmochimica Acta 70 (2006) 2210–2228.

[215] E. Pál, R. Kun, C. Schulze, V. Zöllmer, D. Lehmhus, M. Bäumer, M. Busse. Composition-dependent sintering behaviour of chemically synthesised CuNi nanoparticles and their application in aerosol printing for preparation of conductive microstructures. Colloid Polym Sci 290 (2012) 941–952.

[216] M.V. Bykova, D.Yu. Ermakov, V.V. Kaichev, O.A. Bulavchenko, A.A. Saraev, M.Yu. Lebedev, V.A. Yakovlev. Ni-based sol-gel catalysts as promising systems for crude bio-oil upgrading: Guaiacol hydrodeoxygenation study. Applied Catalysis B: Environmental 113– 114 (2012) 296– 307.

[217] N. Weidler, J. Schuch, F. Knaus, P. Stenner, S. Hoch, A. Maljusch, R. Schäfer, B. Kaiser, W. Jaegermann. X-ray Photoelectron Spectroscopic Investigation of Plasma-Enhanced Chemical Vapor Deposited NiOx, NiOx(OH)y, and CoNiOx(OH)y: Influence of the Chemical Composition on the Catalytic Activity for the Oxygen Evolution Reaction. J. Phys. Chem. C 121 (2017) 6455−6463.

[218] Q. Wu, L.D.L. Duchstein, G.L. Chiarello, J.M. Christensen, C.D. Damsgaard, C.F. Elkjær, J.B. Wagner, B. Temel, J-D Grunwaldt, AD. Jensen. In Situ Observation of Cu–Ni Alloy Nanoparticle Formation by X-Ray Diffraction, X-Ray Absorption Spectroscopy, and Transmission Electron Microscopy: Influence of Cu/Ni Ratio. ChemCatChem 6 (2014) 301–310.

ANNEX

ANNEX A1

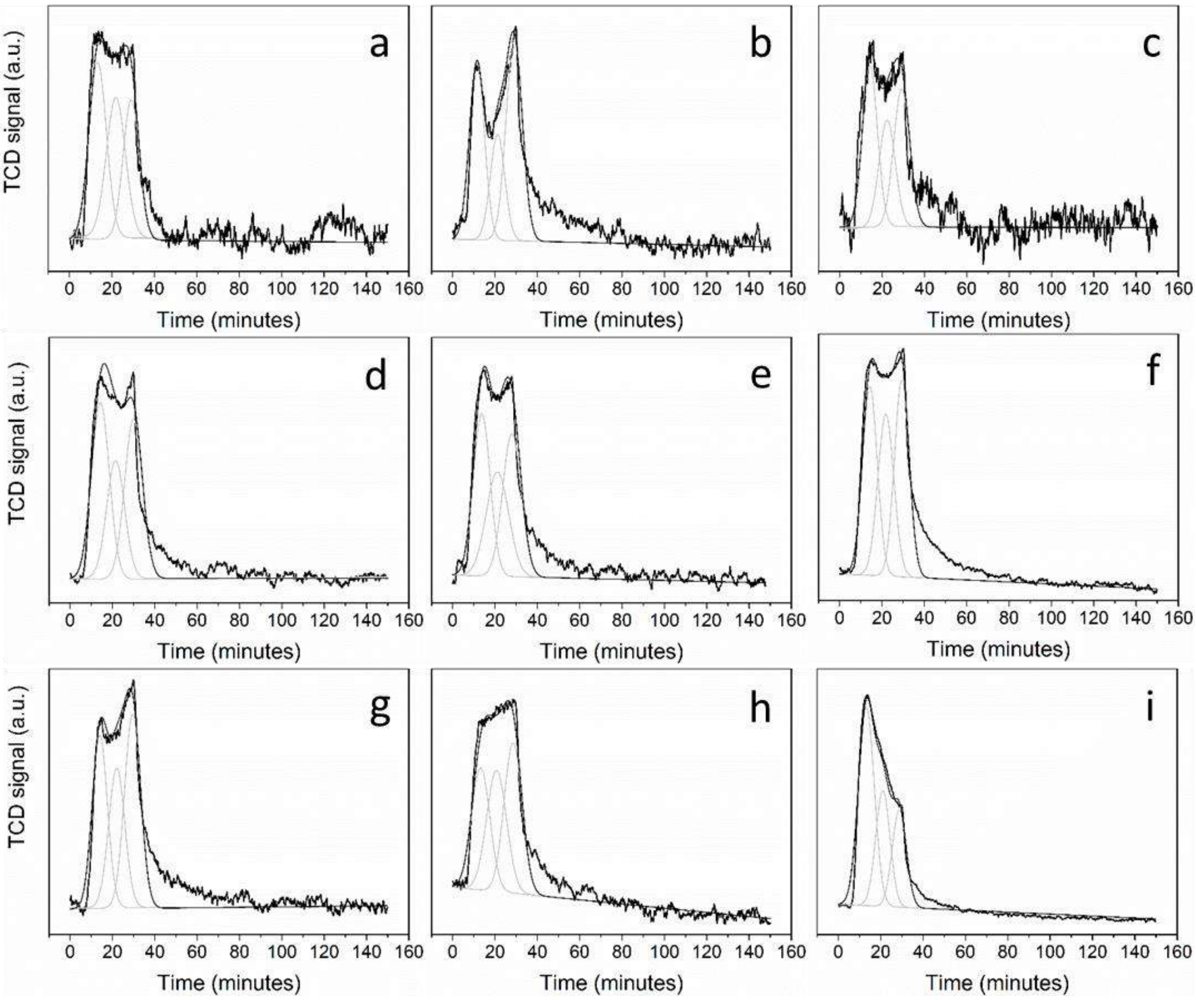

Figure A1.1 NH$_3$-TPD fitted profiles of samples a) Mg/HSAG, b) Ba/HSAG, c) Zn/HSAG, d) Mn/HSAG, e) 5Cu/HSAG, f) 5Cu-Mg/HSAG, g) 5Cu-Ba/HSAG, h) 5Cu-Zn/HSAG, i) 5Cu-Mn/HSAG.

ANNEX A2

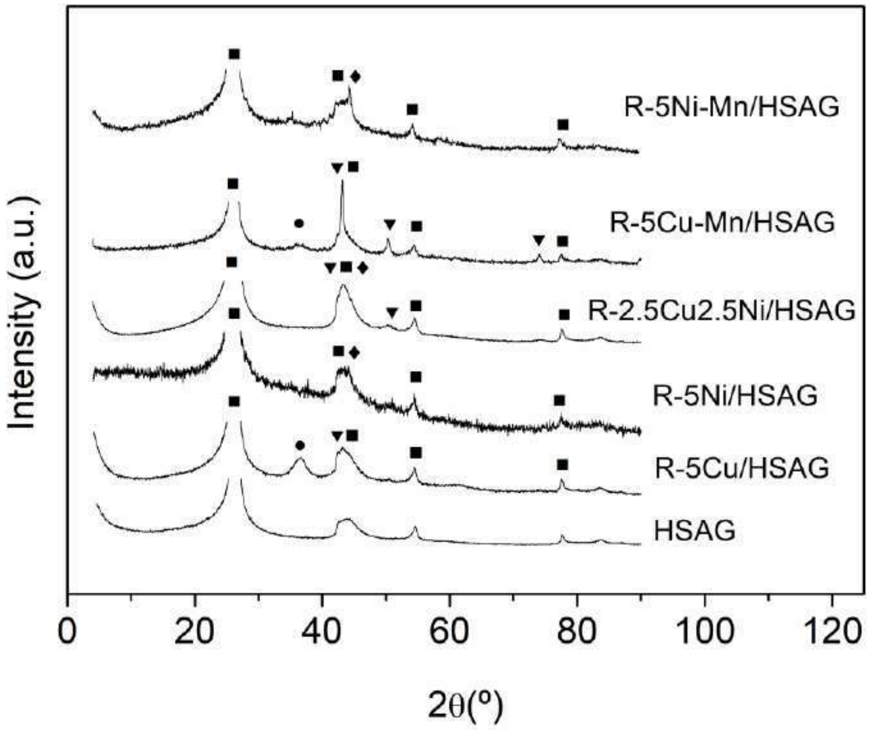

Figure A2.1 XRD patterns of the support HSAG and the catalysts after reaction. (■) HSAG, (▼) Metallic Cu, (♦) Metallic Ni, (●)CuO.

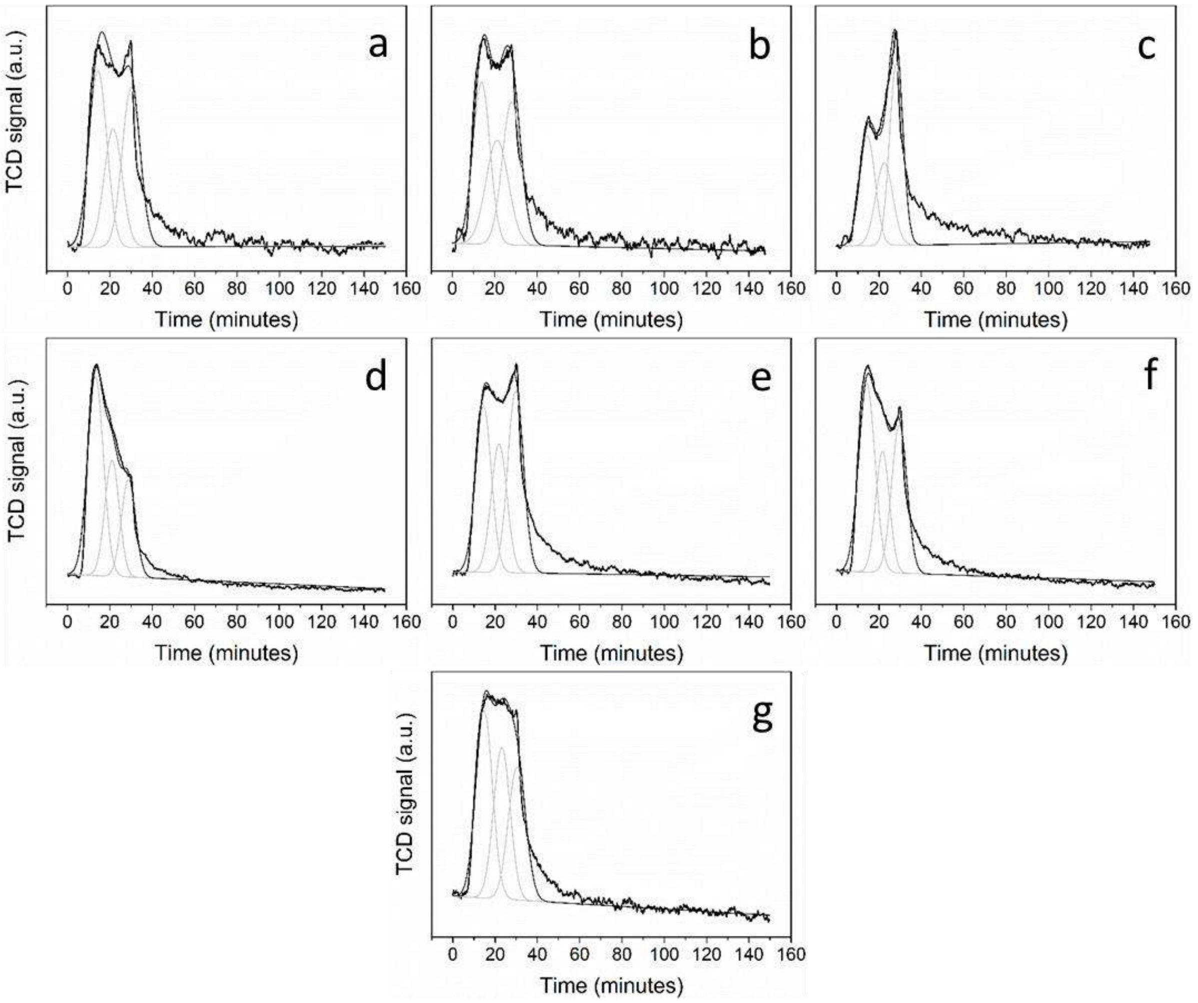

Figure A2.2 NH_3-TPD fitted profiles of samples a) Mn/HSAG, b) 5Cu/HSAG, c) 5Ni /HSAG, d) 5Cu-Mn/HSAG, e) 5Ni-Mn/HSAG, f) 2.5Cu2.5Ni-Mn/HSAG, g) 2.5Cu2.5Ni-Mn/HSAG*.

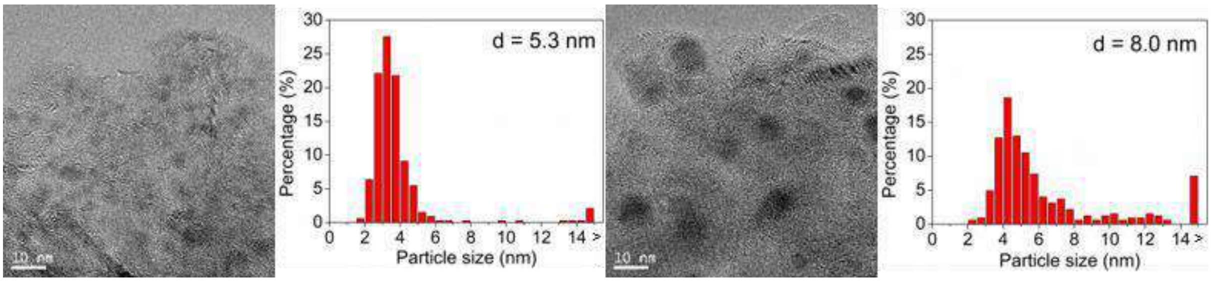

Figure A2.3 TEM images of catalysts reduced with hydrogen (left) and after reaction (right): 4Cu1Ni-Mn/HSAG.

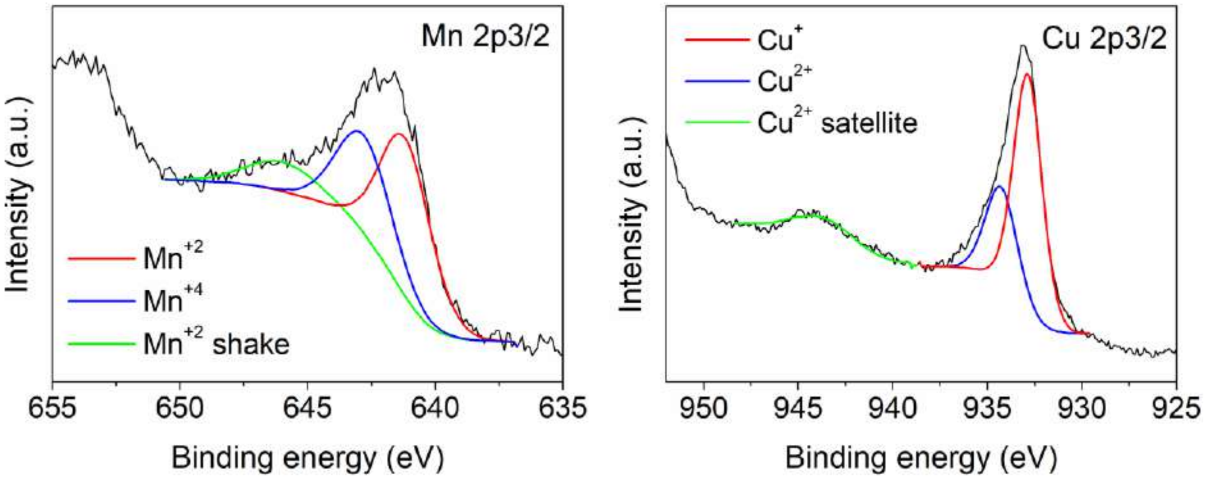

Figure A2.4 Mn 2p$_{3/2}$ (left), Cu 2p$_{3/2}$ (right) XPS spectra of sample 5Cu-Mn/HSAG reduced in hydrogen at 573 K.

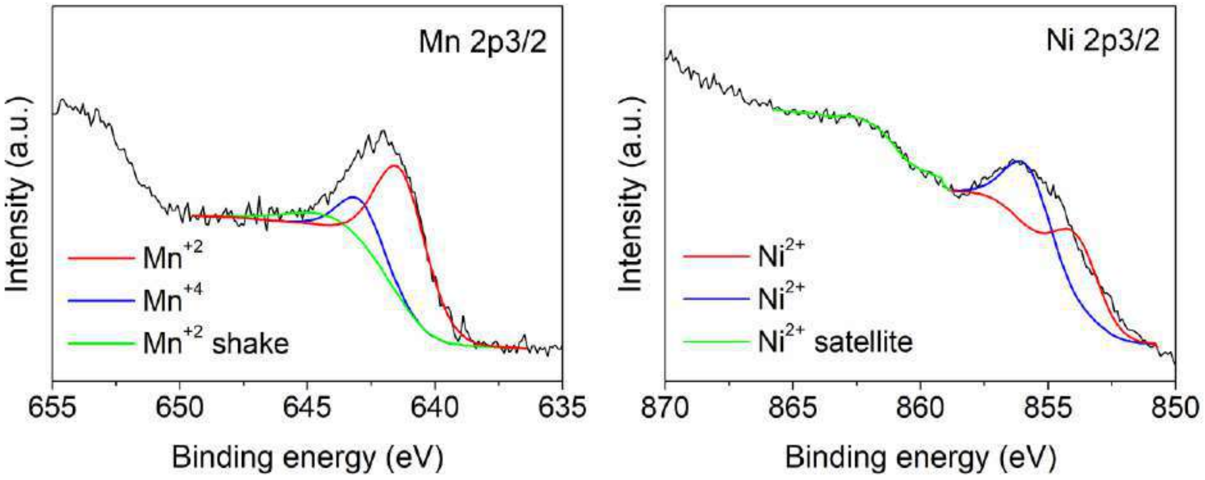

Figure A2.5 Mn 2p$_{3/2}$ (left), Ni 2p$_{3/2}$ (right) XPS spectra of sample 5Ni-Mn/HSAG reduced in hydrogen at 723 K.

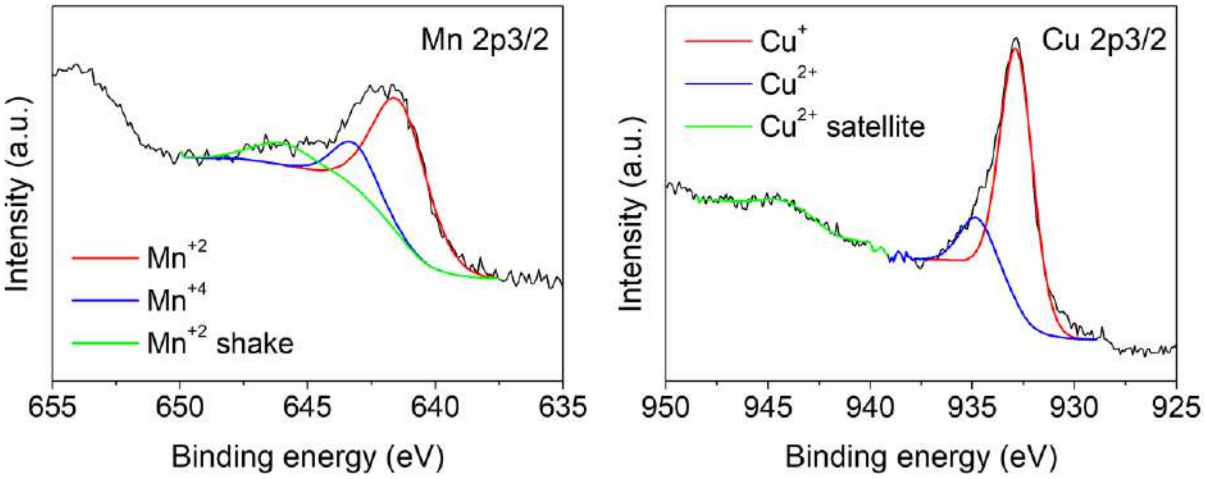

Figure A2.6 Mn 2p$_{3/2}$ (left), Cu 2p$_{3/2}$ (right) XPS spectra of sample R-5Cu-Mn/HSAG.

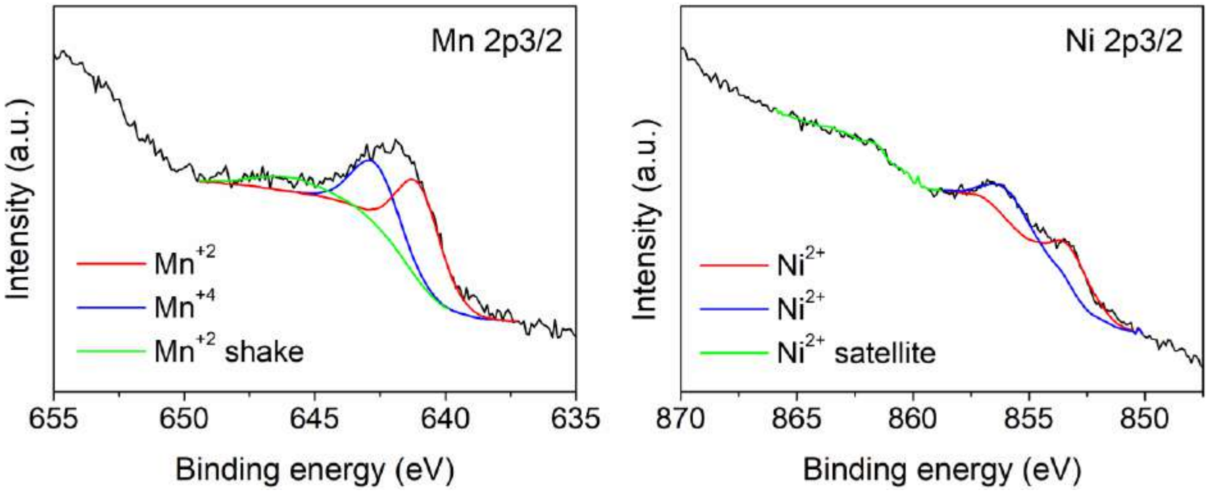

Figure A2.7 Mn 2p$_{3/2}$ (left), Ni 2p$_{3/2}$ (right) XPS spectra of sample R-5Ni-Mn/HSAG.

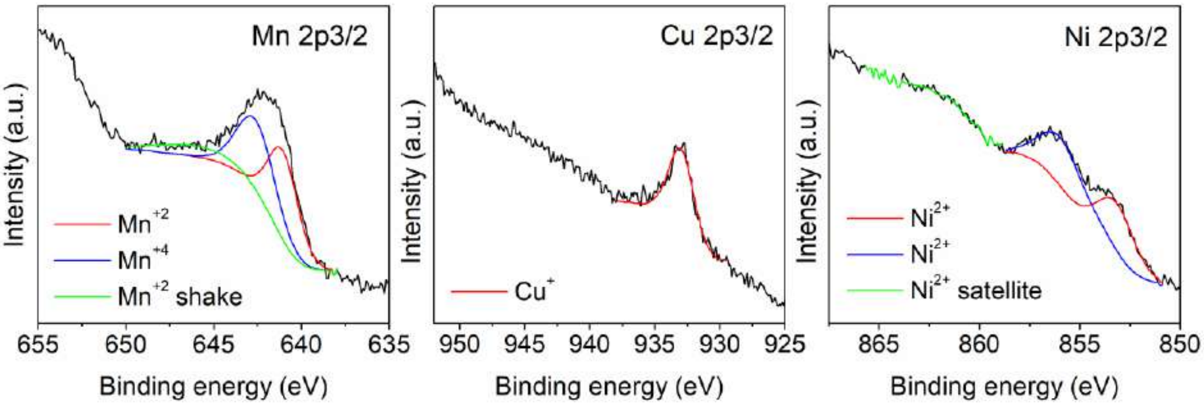

Figure A2.8 Mn $2p_{3/2}$ (left), Cu $2p_{3/2}$ (center) and Ni $2p_{3/2}$ (right) XPS spectra of sample R-2.5Cu2.5Ni-Mn/HSAG.

ANNEX A3

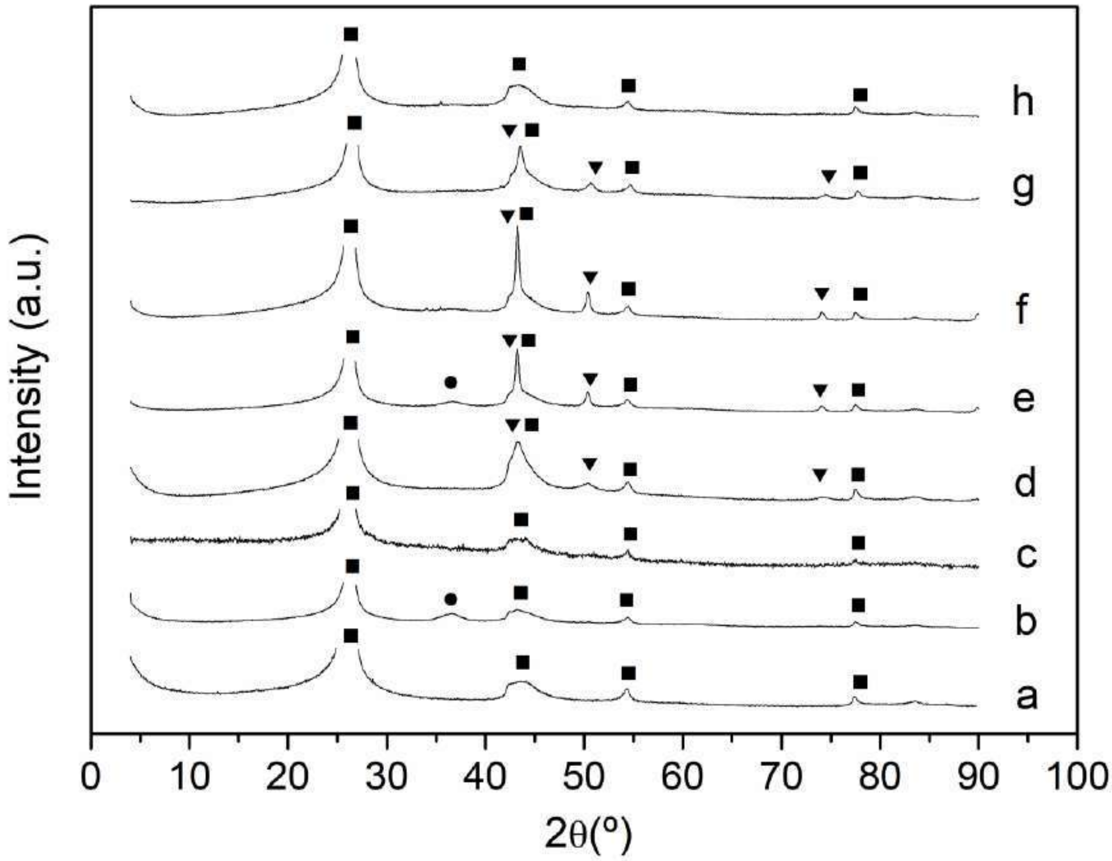

Figure A3.1 XRD patterns of the support and the catalysts after reaction (R-), where a) HSAG, b) R-Cu/HSAG, c) R-Ni/HSAG, d) R-4Cu1Ni-HSAG, e) R-5Cu-Mg/HSAG, f) R-4.75Cu0.25Ni-Mg/HSAG, g) R-2.5Cu2.5Ni-Mg/HSAG, h) R-5Ni-Mg/HSAG. (■) HSAG, (▼) Metallic Cu, (●) CuO.

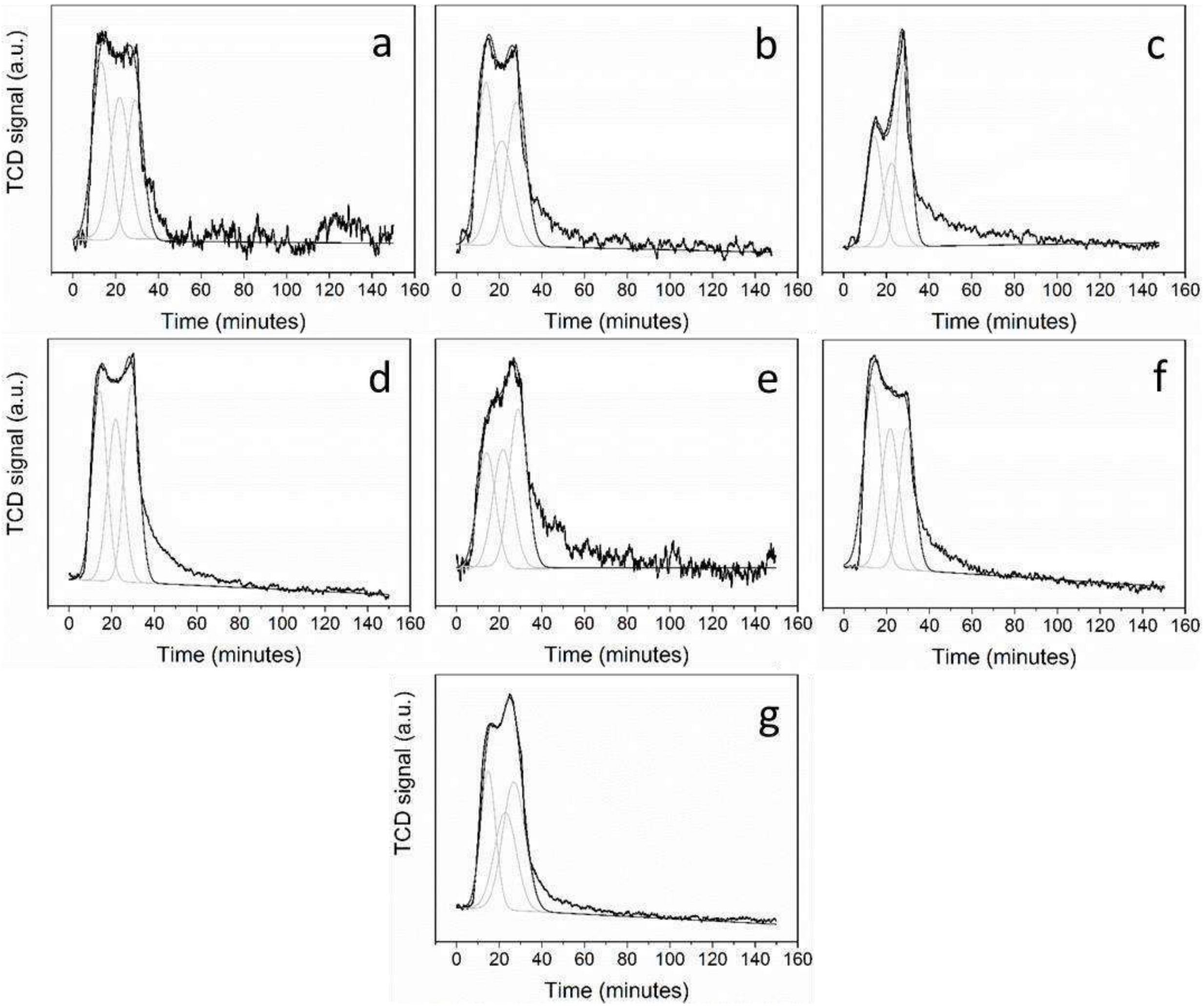

Figure A3.2 NH$_3$-TPD fitted profiles of samples a) Mg/HSAG, b) 5Cu/HSAG, c) 5Ni /HSAG, d) 5Cu-Mg/HSAG, e) 5Ni-Mg/HSAG, f) 4Cu1Ni-Mg/HSAG, g) 4Cu1Ni-Mg/HSAG*.

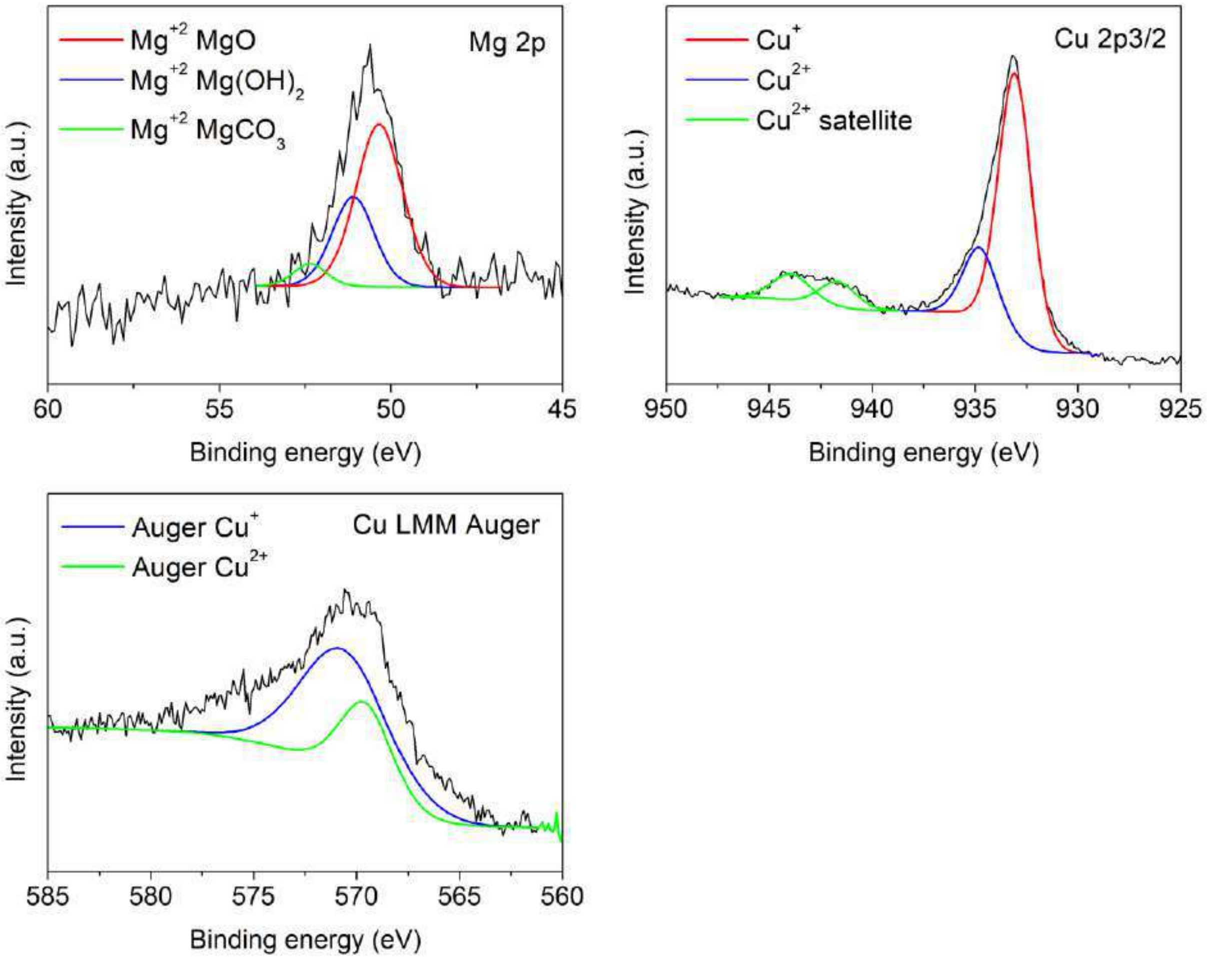

Figure A3.3 Mg 2p (top left), Cu 2p$_{3/2}$ (top right), and X-ray generated Cu LMM Auger (bottom) XPS spectra of sample 5Cu-Mg/HSAG reduced in hydrogen at 573 K.

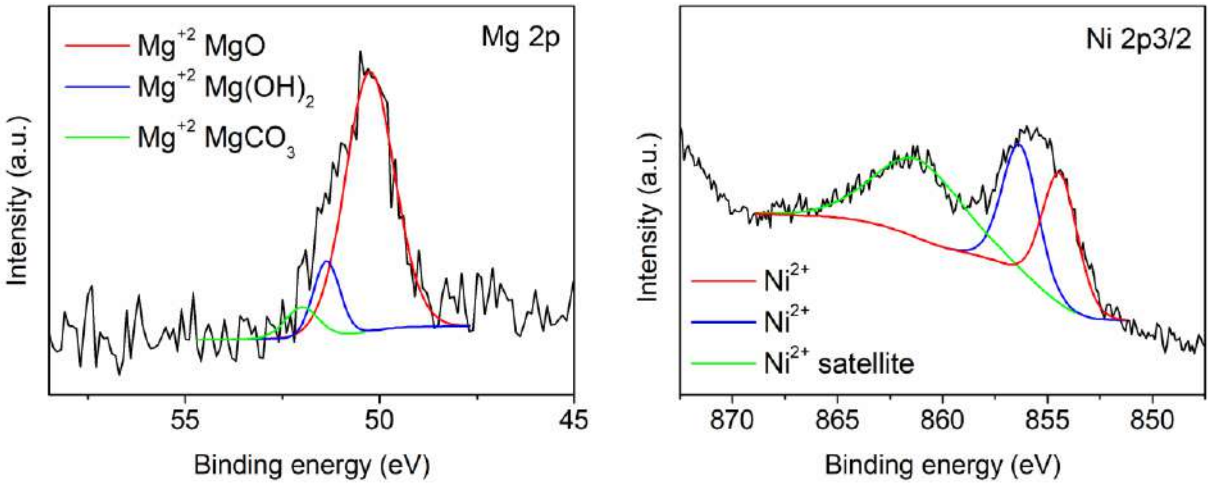

Figure A3.4 Mg 2p (left), Ni 2p$_{3/2}$ (right) XPS spectra of sample 5Ni-Mg/HSAG reduced in hydrogen at 723 K.

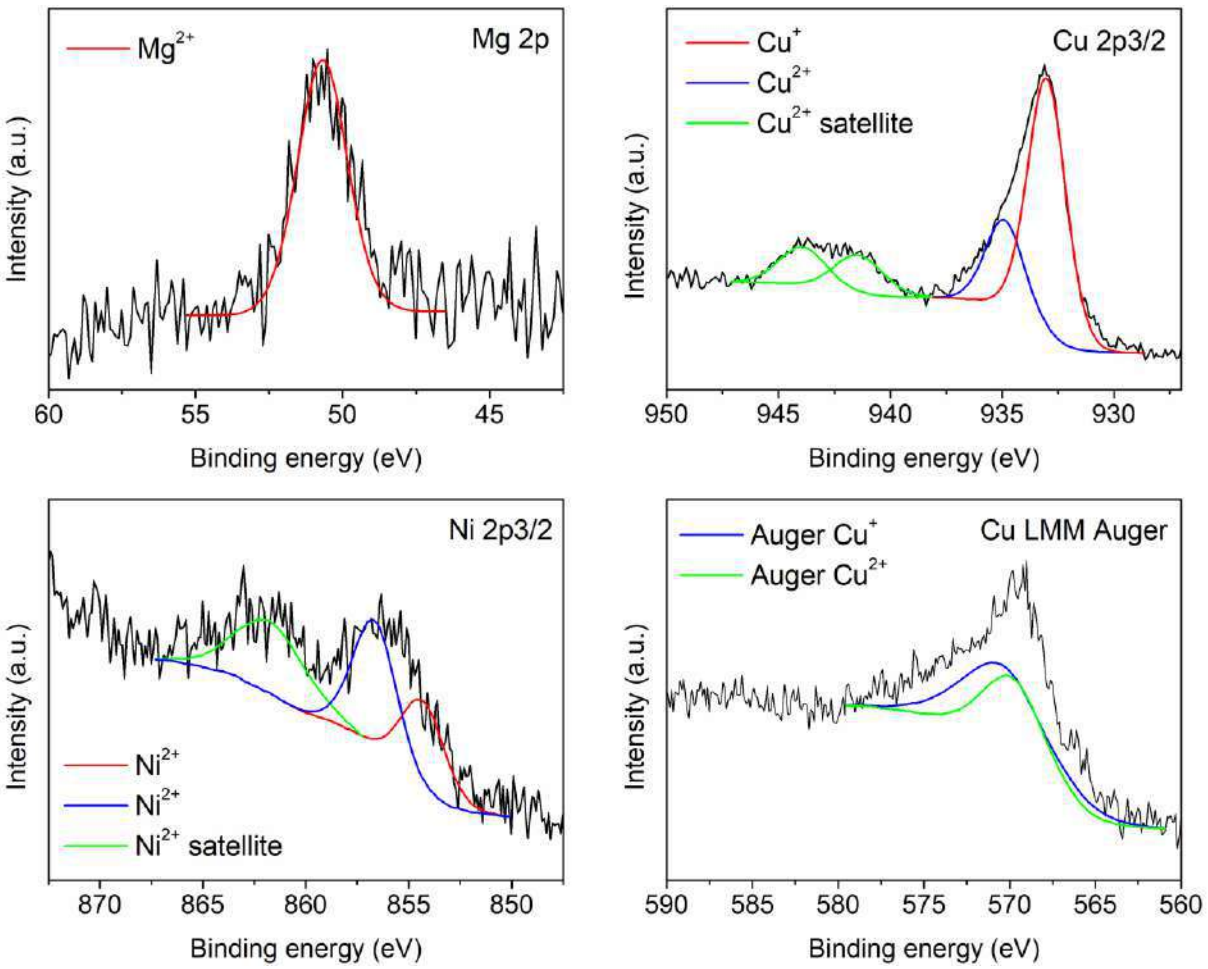

Figure A3.5 Mg 2p (top left), Cu $2p_{3/2}$ (top right), Ni $2p_{3/2}$ (bottom left) and X-ray generated Cu LMM Auger (bottom right) XPS spectra of sample 4Cu1Ni-Mg/HSAG reduced in hydrogen at 573 K.

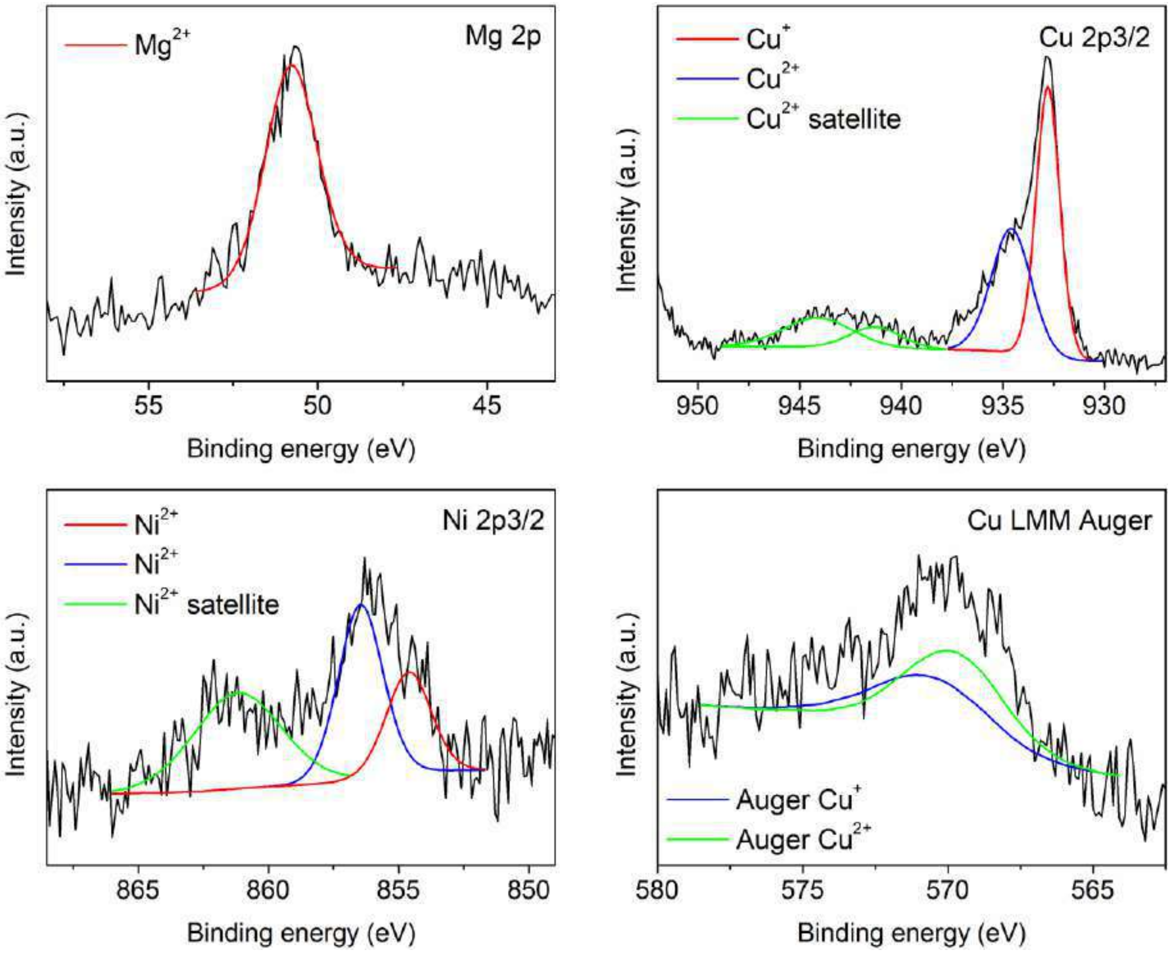

Figure A3.6 Mg 2p (top left), Cu 2p$_{3/2}$ (top right), Ni 2p$_{3/2}$ (bottom left) and X-ray generated Cu LMM Auger (bottom right) XPS spectra of sample 4Cu1Ni-Mg/HSAG* treated in helium at 723 K before reduction in hydrogen at 573 K.

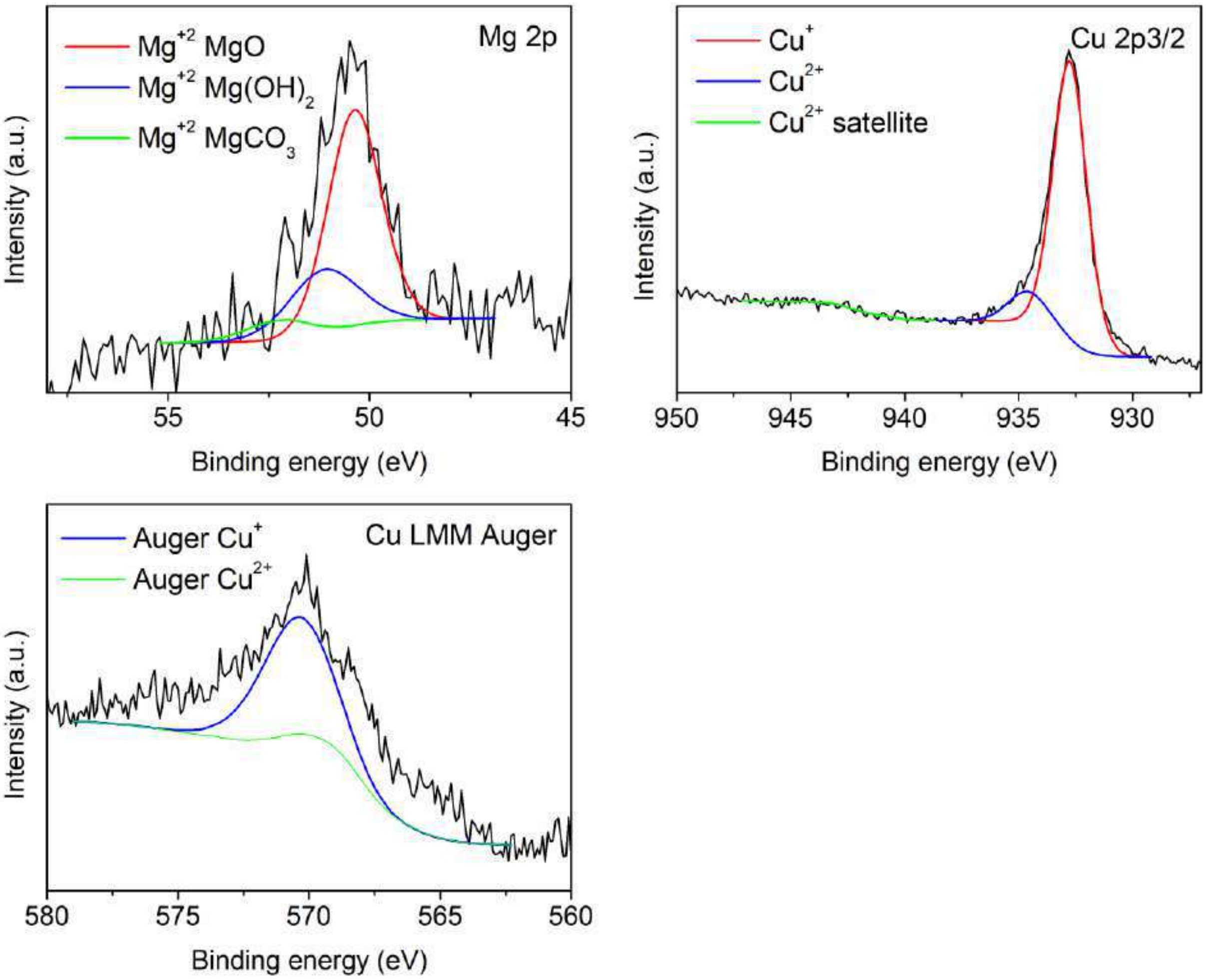

Figure A3.7 Mg 2p (top left), Cu 2p$_{3/2}$ (top right), and X-ray generated Cu LMM Auger (bottom) XPS spectra of sample R-5Cu-Mg/HSAG.

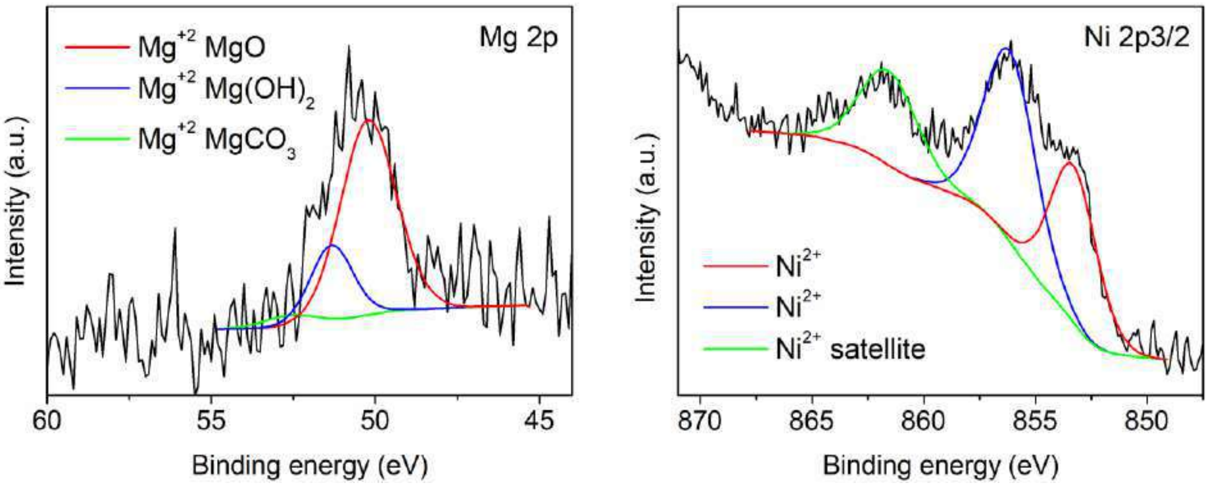

Figure A3.8 Mg 2p (left), Ni $2p_{3/2}$ (right) XPS spectra of sample R-5Ni-Mg/HSAG.

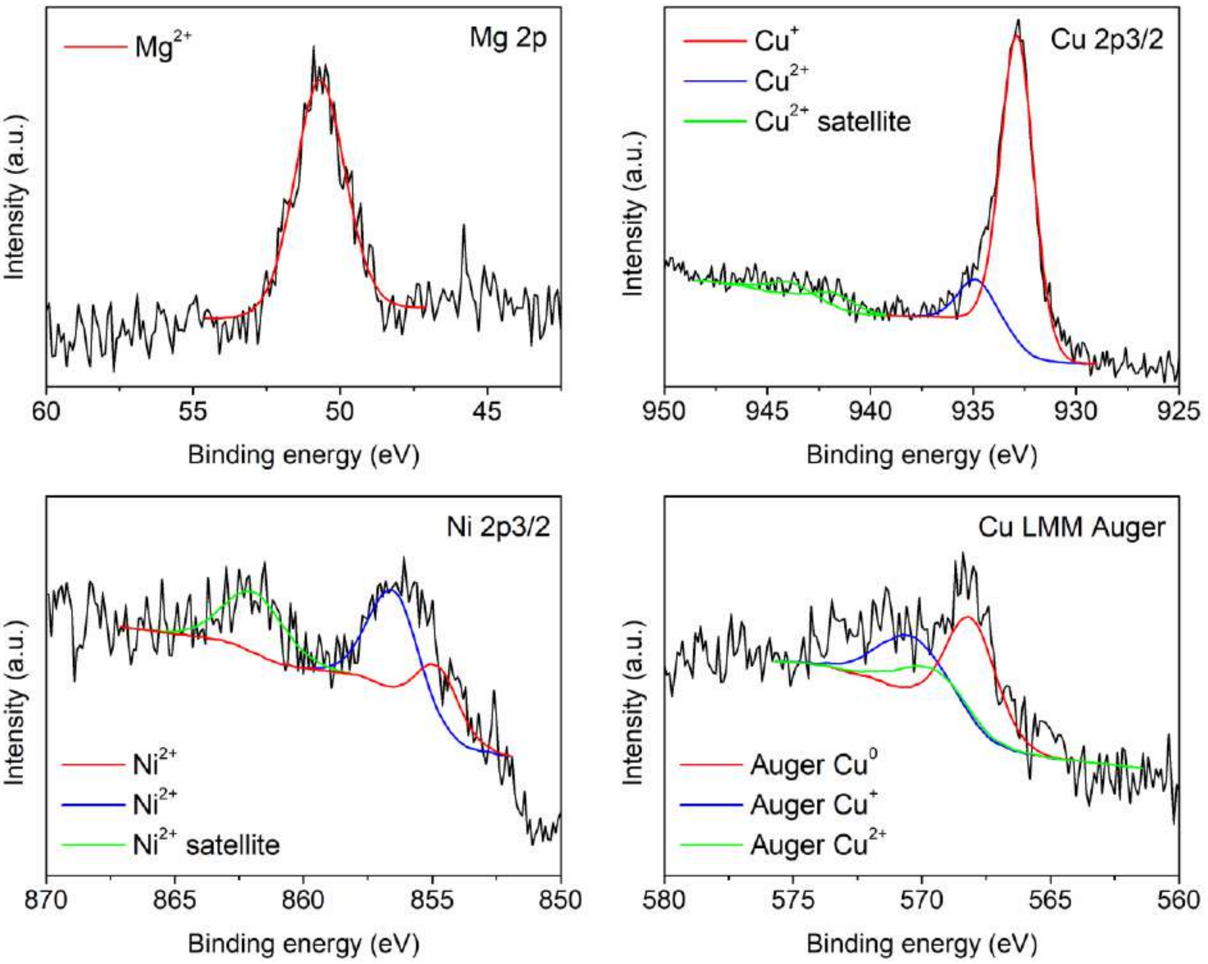

Figure A3.9 Mg 2p (top left), Cu $2p_{3/2}$ (top right), Ni $2p_{3/2}$ (bottom left) and X-ray generated Cu LMM Auger (bottom right) XPS spectra of sample R-4Cu1Ni-Mg/HSAG.

ANNEX A4

Publications derived from this Doctoral Thesis

Publications:

C. López-Olmos, M.V. Morales, A. Guerrero-Ruiz, C. Ramirez-Barria, E. Asedegbega-Nieto, I. Rodríguez-Ramos. Continuous Gas-Phase Condensation of Bioethanol to 1-Butanol over Bifunctional Pd/Mg and Pd/Mg–Carbon Catalysts. ChemSusChem 11 (2018) 3502 –3511.

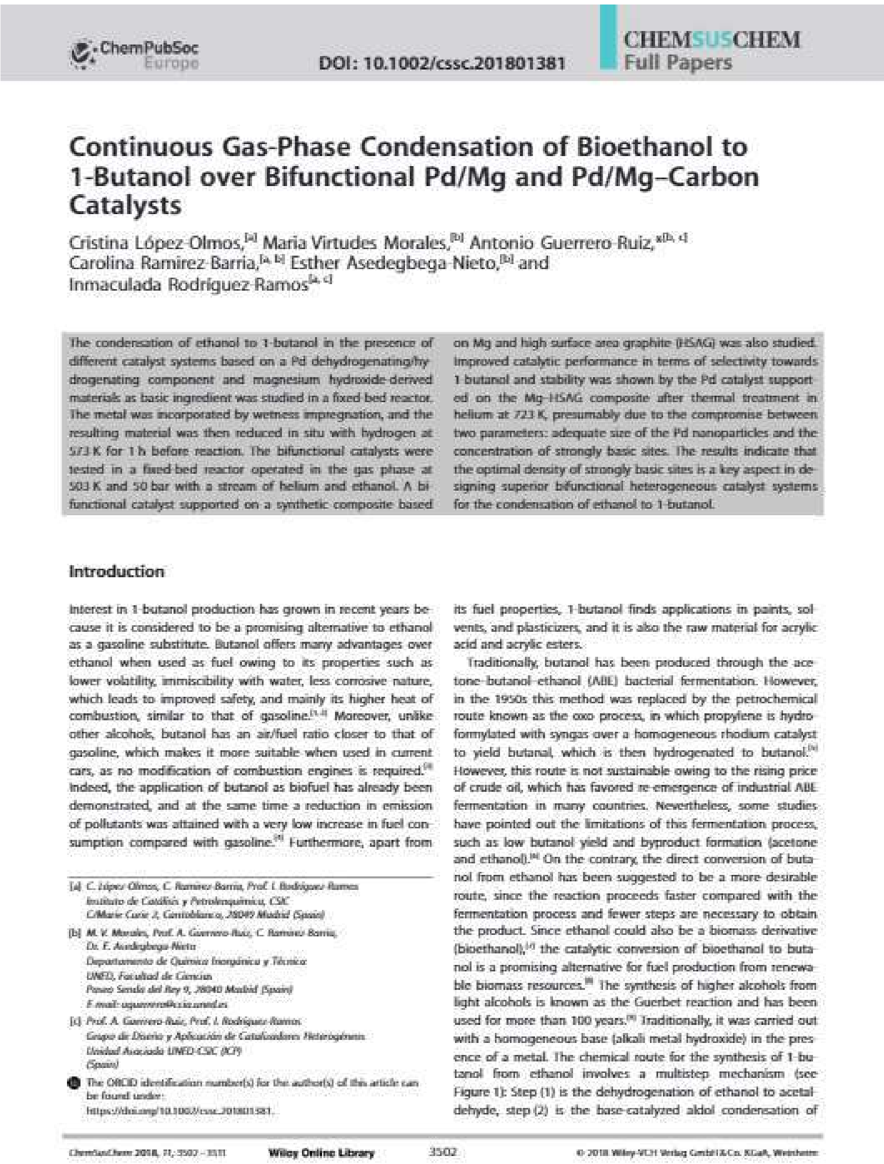

ChemPubSoc Europe
DOI: 10.1002/cssc.201801381
CHEMSUSCHEM
Full Papers

Continuous Gas-Phase Condensation of Bioethanol to 1-Butanol over Bifunctional Pd/Mg and Pd/Mg–Carbon Catalysts

Cristina López-Olmos,[a] Maria Virtudes Morales,[b] Antonio Guerrero-Ruiz,*[b, c]
Carolina Ramirez-Barria,[a, b] Esther Asedegbega-Nieto,[b] and
Inmaculada Rodríguez-Ramos[a, c]

The condensation of ethanol to 1-butanol in the presence of different catalyst systems based on a Pd dehydrogenating/hydrogenating component and magnesium hydroxide-derived materials as basic ingredient was studied in a fixed-bed reactor. The metal was incorporated by wetness impregnation, and the resulting material was then reduced in situ with hydrogen at 573 K for 1 h before reaction. The bifunctional catalysts were tested in a fixed-bed reactor operated in the gas phase at 503 K and 50 bar with a stream of helium and ethanol. A bifunctional catalyst supported on a synthetic composite based on Mg and high surface area graphite (HSAG) was also studied. Improved catalytic performance in terms of selectivity towards 1-butanol and stability was shown by the Pd catalyst supported on the Mg–HSAG composite after thermal treatment in helium at 723 K, presumably due to the compromise between two parameters: adequate size of the Pd nanoparticles and the concentration of strongly basic sites. The results indicate that the optimal density of strongly basic sites is a key aspect in designing superior bifunctional heterogeneous catalyst systems for the condensation of ethanol to 1-butanol.

Introduction

Interest in 1-butanol production has grown in recent years because it is considered to be a promising alternative to ethanol as a gasoline substitute. Butanol offers many advantages over ethanol when used as fuel owing to its properties such as lower volatility, immiscibility with water, less corrosive nature, which leads to improved safety, and mainly its higher heat of combustion, similar to that of gasoline.[1–3] Moreover, unlike other alcohols, butanol has an air/fuel ratio closer to that of gasoline, which makes it more suitable when used in current cars, as no modification of combustion engines is required.[4] Indeed, the application of butanol as biofuel has already been demonstrated, and at the same time a reduction in emission of pollutants was attained with a very low increase in fuel consumption compared with gasoline.[5] Furthermore, apart from its fuel properties, 1-butanol finds applications in paints, solvents, and plasticizers, and it is also the raw material for acrylic acid and acrylic esters.

Traditionally, butanol has been produced through the acetone–butanol–ethanol (ABE) bacterial fermentation. However, in the 1950s this method was replaced by the petrochemical route known as the oxo process, in which propylene is hydroformylated with syngas over a homogeneous rhodium catalyst to yield butanal, which is then hydrogenated to butanol.[3] However, this route is not sustainable owing to the rising price of crude oil, which has favored re-emergence of industrial ABE fermentation in many countries. Nevertheless, some studies have pointed out the limitations of this fermentation process, such as low butanol yield and byproduct formation (acetone and ethanol).[6] On the contrary, the direct conversion of butanol from ethanol has been suggested to be a more desirable route, since the reaction proceeds faster compared with the fermentation process and fewer steps are necessary to obtain the product. Since ethanol could also be a biomass derivative (bioethanol),[7] the catalytic conversion of bioethanol to butanol is a promising alternative for fuel production from renewable biomass resources.[8] The synthesis of higher alcohols from light alcohols is known as the Guerbet reaction and has been used for more than 100 years.[9] Traditionally, it was carried out with a homogeneous base (alkali metal hydroxide) in the presence of a metal. The chemical route for the synthesis of 1-butanol from ethanol involves a multistep mechanism (see Figure 1): Step (1) is the dehydrogenation of ethanol to acetaldehyde, step (2) is the base-catalyzed aldol condensation of

---

[a] C. López-Olmos, C. Ramirez-Barria, Prof. I. Rodríguez-Ramos
Instituto de Catálisis y Petroleoquímica, CSIC
C/Marie Curie 2, Cantoblanco, 28049 Madrid (Spain)
[b] M. V. Morales, Prof. A. Guerrero-Ruiz, C. Ramirez-Barria,
Dr. E. Asedegbega-Nieto
Departamento de Química Inorgánica y Técnica
UNED, Facultad de Ciencias
Paseo Senda del Rey 9, 28040 Madrid (Spain)
E-mail: aguerrero@ccia.uned.es
[c] Prof. A. Guerrero-Ruiz, Prof. I. Rodríguez-Ramos
Grupo de Diseño y Aplicación de Catalizadores Heterogéneos
Unidad Asociada UNED-CSIC (ICP)
(Spain)

The ORCID identification number(s) for the author(s) of this article can be found under:
https://doi.org/10.1002/cssc.201801381.

ChemSusChem 2018, 11, 3502 – 3511 Wiley Online Library 3502
© 2018 Wiley-VCH Verlag GmbH & Co. KGaA, Weinheim

C. López-Olmos, A. Guerrero-Ruiz, I. Rodríguez-Ramos. Optimization of Cu-Ni-Mn-catalysts for the conversion of ethanol to butanol. doi.org/10.1016/j.cattod.2019.05.058

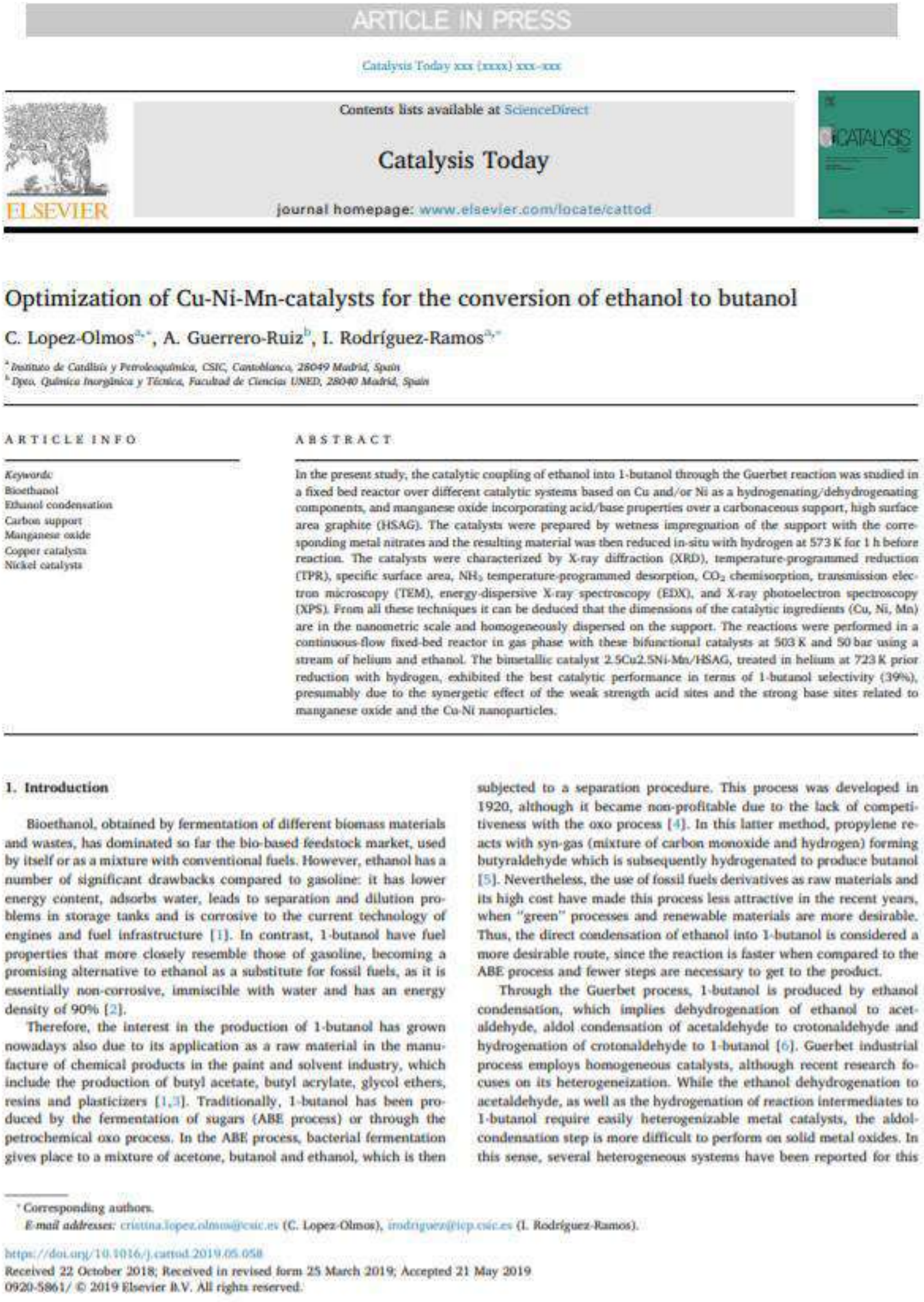

ARTICLE IN PRESS

Catalysis Today xxx (xxxx) xxx–xxx

Contents lists available at ScienceDirect

Catalysis Today

journal homepage: www.elsevier.com/locate/cattod

Optimization of Cu-Ni-Mn-catalysts for the conversion of ethanol to butanol

C. Lopez-Olmos[a,*], A. Guerrero-Ruiz[b], I. Rodríguez-Ramos[a,*]

[a] Instituto de Catálisis y Petroleoquímica, CSIC, Cantoblanco, 28049 Madrid, Spain
[b] Dpto. Química Inorgánica y Técnica, Facultad de Ciencias UNED, 28040 Madrid, Spain

ARTICLE INFO

Keywords:
Bioethanol
Ethanol condensation
Carbon support
Manganese oxide
Copper catalysts
Nickel catalysts

ABSTRACT

In the present study, the catalytic coupling of ethanol into 1-butanol through the Guerbet reaction was studied in a fixed bed reactor over different catalytic systems based on Cu and/or Ni as a hydrogenating/dehydrogenating components, and manganese oxide incorporating acid/base properties over a carbonaceous support, high surface area graphite (HSAG). The catalysts were prepared by wetness impregnation of the support with the corresponding metal nitrates and the resulting material was then reduced in-situ with hydrogen at 573 K for 1 h before reaction. The catalysts were characterized by X-ray diffraction (XRD), temperature-programmed reduction (TPR), specific surface area, NH_3 temperature-programmed desorption, CO_2 chemisorption, transmission electron microscopy (TEM), energy-dispersive X-ray spectroscopy (EDX), and X-ray photoelectron spectroscopy (XPS). From all these techniques it can be deduced that the dimensions of the catalytic ingredients (Cu, Ni, Mn) are in the nanometric scale and homogeneously dispersed on the support. The reactions were performed in a continuous-flow fixed-bed reactor in gas phase with these bifunctional catalysts at 503 K and 50 bar using a stream of helium and ethanol. The bimetallic catalyst 2.5Cu2.5Ni-Mn/HSAG, treated in helium at 723 K prior reduction with hydrogen, exhibited the best catalytic performance in terms of 1-butanol selectivity (39%), presumably due to the synergetic effect of the weak strength acid sites and the strong base sites related to manganese oxide and the Cu-Ni nanoparticles.

1. Introduction

Bioethanol, obtained by fermentation of different biomass materials and wastes, has dominated so far the bio-based feedstock market, used by itself or as a mixture with conventional fuels. However, ethanol has a number of significant drawbacks compared to gasoline: it has lower energy content, adsorbs water, leads to separation and dilution problems in storage tanks and is corrosive to the current technology of engines and fuel infrastructure [1]. In contrast, 1-butanol have fuel properties that more closely resemble those of gasoline, becoming a promising alternative to ethanol as a substitute for fossil fuels, as it is essentially non-corrosive, immiscible with water and has an energy density of 90% [2].

Therefore, the interest in the production of 1-butanol has grown nowadays also due to its application as a raw material in the manufacture of chemical products in the paint and solvent industry, which include the production of butyl acetate, butyl acrylate, glycol ethers, resins and plasticizers [1,3]. Traditionally, 1-butanol has been produced by the fermentation of sugars (ABE process) or through the petrochemical oxo process. In the ABE process, bacterial fermentation gives place to a mixture of acetone, butanol and ethanol, which is then subjected to a separation procedure. This process was developed in 1920, although it became non-profitable due to the lack of competitiveness with the oxo process [4]. In this latter method, propylene reacts with syn-gas (mixture of carbon monoxide and hydrogen) forming butyraldehyde which is subsequently hydrogenated to produce butanol [5]. Nevertheless, the use of fossil fuels derivatives as raw materials and its high cost have made this process less attractive in the recent years, when "green" processes and renewable materials are more desirable. Thus, the direct condensation of ethanol into 1-butanol is considered a more desirable route, since the reaction is faster when compared to the ABE process and fewer steps are necessary to get to the product.

Through the Guerbet process, 1-butanol is produced by ethanol condensation, which implies dehydrogenation of ethanol to acetaldehyde, aldol condensation of acetaldehyde to crotonaldehyde and hydrogenation of crotonaldehyde to 1-butanol [6]. Guerbet industrial process employs homogeneous catalysts, although recent research focuses on its heterogeneization. While the ethanol dehydrogenation to acetaldehyde, as well as the hydrogenation of reaction intermediates to 1-butanol require easily heterogenizable metal catalysts, the aldol-condensation step is more difficult to perform on solid metal oxides. In this sense, several heterogeneous systems have been reported for this

---

[*] Corresponding authors.

E-mail addresses: cristina.lopez.olmos@csic.es (C. Lopez-Olmos), irodriguez@icp.csic.es (I. Rodríguez-Ramos).

https://doi.org/10.1016/j.cattod.2019.05.058
Received 22 October 2018; Received in revised form 25 March 2019; Accepted 21 May 2019
0920-5861/ © 2019 Elsevier B.V. All rights reserved.

In preparation:

C. López-Olmos, M.V. Morales, A. Guerrero-Ruiz, I. Rodríguez-Ramos. Comparative study on the acidity and basicity of metal oxides for the catalytic conversion of ethanol into 1-butanol.

C. López-Olmos, A. Guerrero-Ruiz, I. Rodríguez-Ramos. Improvement of Cu based catalyst for ethanol conversion into butanol.

ANNEX A5

Curriculum Vitae

Education:

UNED – Instituto de Catálisis y Petroleoquímica

PhD Student, FPU Fellow

2015-current Supervisor: Prof. Inmaculada Rodriguez-Ramos and Antonio Guerrero-Ruiz. Thesis title: Producción catalítica de compuestos químicos a partir de materiales renovables.

UNED

Master of Science (M.Sc.) Master´s degree in Inorganic Chemistry and Chemical Engineering

(2014 – 2015) Supervisor: Prof. María Luisa Rojas Cervantes

Research Project: Encapsulación via sol-gel y su aplicación para la industria alimenticia. Defense on October 2015 obtaining the maximum grade with Honours.

Universidad de Málaga

Bachelor's degree, Chemical Engineering (First Class Honours)

(2008 – 2014) Research Supervisor: Prof. Dietmar Leinen

Research Project: Capas selectivas sobre acero galvanizado. Defense on April 2014 obtaining the maximum grade with Honours.

Publications:

C. Ramirez-Barria, C. López-Olmos, A. Guerrero-Ruiz, I. Rodríguez Ramos. Direct catalytic effect of nitrogen functional groups exposed on graphenic materials when acting cooperatively with Ru nanoparticles. RSC Advances, 7 (2017) 44568-44577.

C. López-Olmos, M.V. Morales, A. Guerrero-Ruiz, C. Ramirez-Barria, E. Asedegbega-Nieto, I. Rodríguez-Ramos. Continuous Gas-Phase Condensation of Bioethanol to 1-Butanol over Bifunctional Pd/Mg and Pd/Mg–Carbon Catalysts. ChemSusChem 11 (2018) 3502 –3511.

J.M. Conesa, M.V. Morales, C. López-Olmos, I. Rodríguez-Ramos, A. Guerrero-Ruiz. Comparative study of Cu, Ag and Ag-Cu catalysts over graphite in the ethanol dehydrogenation reaction: catalytic activity, deactivation and regeneration. Applied Catalysis A, 576 (2019) 54-64.

C. López-Olmos, A. Guerrero-Ruiz, I. Rodríguez-Ramos. Optimization of Cu-Ni-Mn-catalysts for the conversion of ethanol to butanol. Catal. Today, doi.org/10.1016/j.cattod.2019.05.058

Conferences and Presentations:

SECAT'19: Catalysis for the future: Advances in structures, processes and applications.

Poster communication: Optimización de catalizadores basados en Cu-Ni-MgO para la conversión de etanol a butanol.

CarboCat–VIII: 8th International Symposium on Carbon for Catalysis.

Poster communication: Optimization of Mn promoted Cu-Ni catalysts for the conversion of ethanol to butanol.

SECAT'17: Catalysis for a more sustainable world.

Oral communication: Optimización de catalizadores de Cu para la conversión de etanol a butanol.

Europacat 2017: Catalysis - A bridge to the future.

Poster communication: Improvement of Cu based catalyst for ethanol conversion into butanol

Awards, fellowships and Grants:

FPU Ph.D Fellowship (2017-2019).

Universidad de Málaga. Award for the Outstanding Graduate of the Year 2013/2014.